Alloys of Pt and Rare Earths for the Oxygen Electroreduction Reaction

Malacrida, Paolo; Horch, Sebastian; Chorkendorff, Ib

Publication date:
2014

Document Version
Peer reviewed version

Alloys of Pt and Rare Earths for the Oxygen Electroreduction Reaction

A Ph.D. thesis by

Paolo Malacrida

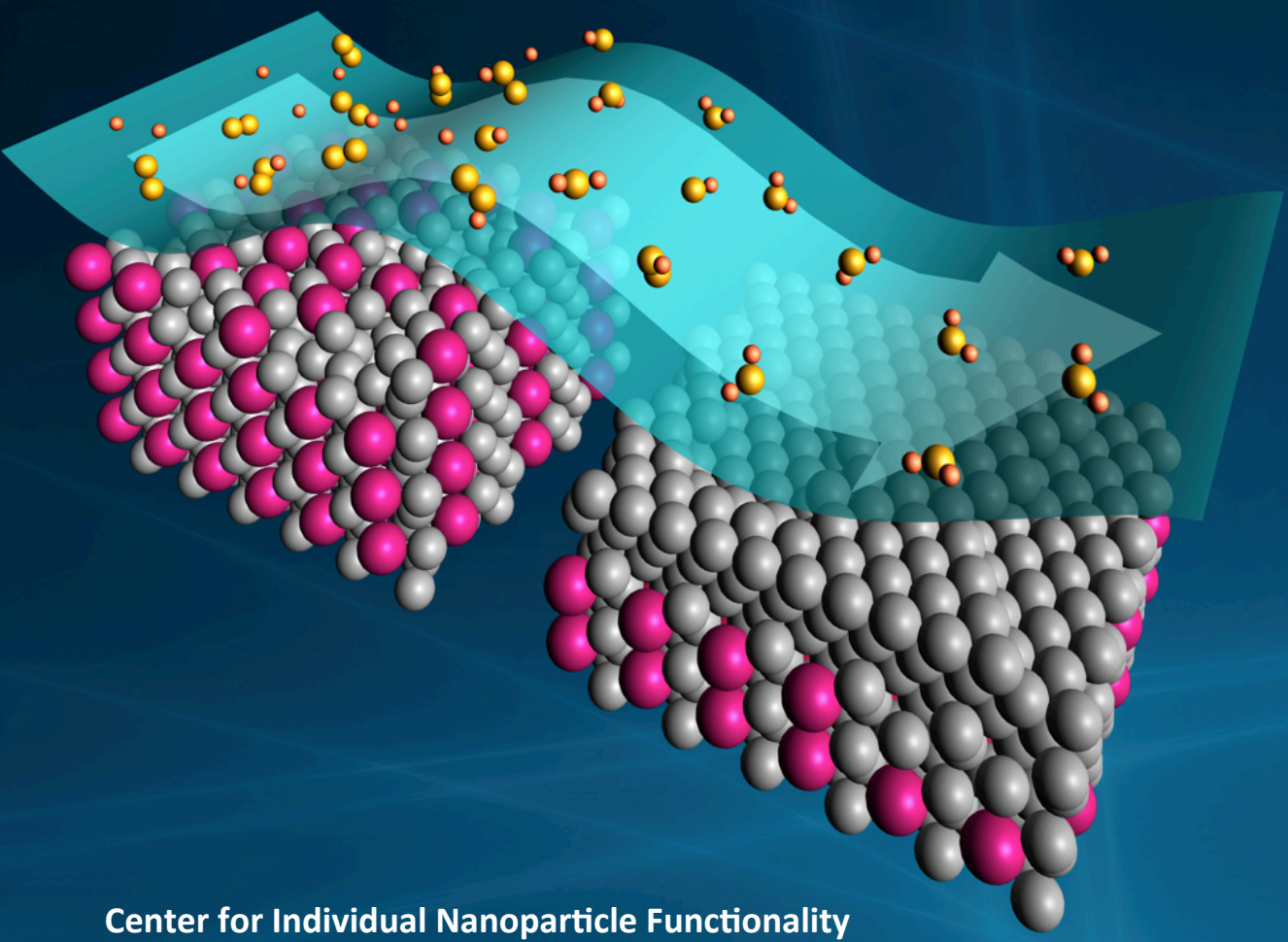

Center for Individual Nanoparticle Functionality
Department of Physics

Alloys of Pt and Rare Earths for the Oxygen Electroreduction Reaction

A Ph.D. thesis by

Paolo Malacrida

April 2014

Center for Individual Nanoparticle Functionality
Technical University of Denmark

Contents

Preface

This work was accomplished at the Center for Individual Nanoparticle Functionality (CINF) under the Department of Physics of the Technical University of Denmark (DTU). CINF is funded by the Danish National Research Foundation which is greatly acknowledged for its support. This Ph.D. project was also funded by the Danish Ministry of Science through the UNIK initiative CAtalysis for Sustainable Energy (CASE). The experimental activities were carried out in the period between April 2011 and April 2014 under the supervision of Professor Ib Chorkendorff and of Professor Søren Dahl and with Professor Sebastian Horch as co-supervisor. I would like to thank all of them for the excellent supervision and in particular Ib Chorkendorff for his ideas and the always motivating discussions. Special thanks are also directed to Assistant Professor Ifan E. L. Stephens for assisting me everyday as if he also was one of my supervisors.

Among my colleagues I am most grateful to Maria Escudero-Escribano who performed good part of the electrochemical measurements presented in this thesis. I express her my sincere thanks for the fruitful collaboration and the inspiring conversations. Particular thanks also to all the other colleagues I have been collaborating with, especially Arnau Verdaguer-Casadevall, Patricia Hernandez-Fernandez, Ana Sofia Varela and Anders B. Laursen who also performed electrochemical measurements, Christian Schlaup, Lone Bech, Robert Jensen and Kenneth Nielsen who helped me in the development of the EC-XPS setup, Tobias Johansson and Elisabeth Therese Ulrikkeholm for their work on single crystals, Federico Masini and David N. McCarthy for the preparation of nanoparticles, Ulrik Grønbjerg and Vladimir Tripković for the theoretical modeling and Hernan Sanchez-Casalongue with whom I performed the Ambient-Pressure X-ray Photoelectron Spectroscopy measurements (AP-XPS) of this thesis.

In general I thank all the staff of CINF and of all my friends at the Department of Physics. Their agreeable company, the pleasant conversations and our afternoon

teas contributed to the creation of an informal enjoyable working environment. Finally I thank all my friends who supported me in this period of time and most importantly, my parents who have always been with me even though living far away.

Kgs. Lyngby, 14th April 2014
Paolo Malacrida

Abstract

This thesis presents the development and characterization of a new class of Pt alloys for catalyzing the Oxygen Reduction Reaction (ORR), in perspective of a future substitution of traditional Pt-based catalysts at the cathode of Polymer Electrolyte Membrane Fuel Cells (PEMFCs). Focused on spectroscopic techniques such as Angle-Resolved X-Ray Photoelectron Spectroscopy (AR-XPS), Ambient Pressure X-Ray Photoelectron Spectroscopy (AP-XPS) and Ion Scattering Spectroscopy (ISS), it takes part in a broader context of studies pursuing the combination of these physical techniques with electrocatalysis. A number of bimetallic alloys based on Pt and a rare earth, like the Pt-Y system or more recently proposed Pt-lanthanide phases, have been tested and characterized.

Polycrystalline Pt_5La and Pt_5Ce exhibited more than a factor of 3 enhancement in specific activity relative to state-of-the-art polycrystalline Pt. They maintain at least 90% of this activity after accelerated stability tests (10 000 cycles between 0.6 and 1.0 V *vs.* the Reversible Hydrogen Electrode (RHE) in 0.1 M $HClO_4$ electrolyte). A combination of AR-XPS and ISS measurements allowed to elucidate the active surface phase and structure of these materials, consisting of a $\approx$1 nm thick pure Pt overlayer on top of the bulk alloy, the stable overlayer providing kinetic stability against further dissolution of the lanthanides. We hypothesize that this high stability is related to the very negative heat of formation of their intermetallic phases, that would prevent La and Ce diffusion to the surface. For this structure only strain effects can explain the activity enhancement.

Other alloys of the same class (*e.g.* Pt_5Gd and Pt_5Tb) exhibit even higher specific activities, up to 6 times the one of polycrystalline Pt in the case of Pt_5Tb, a record activity among polycrystalline alloys. On the basis of their similar crystal structures, the ORR activity of this class of alloys is correlated to the lattice parameter of the bulk, which is expected to define the Pt-Pt distance in the overlayer. The compression of this Pt-Pt distance in the overlayer originates a volcano-shape

trend in activity. However, the most active alloys experience higher activity losses during stability tests, suggesting that high levels of compression might not favour the long-term stability of the Pt overlayers. This hypothesis is supported by Density Functional Theory (DFT) calculations and by AR-XPS. A model for the quantitative estimate of the Pt overlayer thickness from AR-XPS measurements indicates a correlation between the thickening of the Pt overlayers and the activity losses, supporting the concept that more compressed overlayers have lower physical stability.

The application of these materials in a fuel cell requires the fabrication in nanoparticulate form. Through the combination of a gas aggregation technique and a time-of-flight mass spectrometer size-selected Pt-Y nanoparticles are produced. With a mass activity of 3.05 A mg_{Pt}^{-1} at 0.9 V *vs.* RHE, 9 nm Pt-Y nanoparticles are among the most active ORR catalysts ever reported, although they lose 37 % of this activity after stability test. Similar to the case of polycrystals, after immersion in the acidic electrolyte and testing the active phase consists of a Pt shell surrounding an alloyed core. Also in this case the compressed Pt-Pt distance explains the ORR activity enhancement of these catalysts.

The deposition of these 9 nm Pt-Y nanoparticles on the cathode side of a Membrane Electrode Assembly (MEA), part of a specifically prepared fuel cell, allows AP-XPS measurements under operation conditions. As a consequence of potential cycling, Y oxidizes due to the dealloying process which is observed *in-situ*. The adsorbed species can be also probed and correlated to the electrochemical potential. Near the open circuit potential (OCP) conditions the oxygenated species consist, to a good extent, of non-hydrated OH, similar to the case of pure Pt nanoparticles.

Resume

Denne afhandling omhandler udvikling og karakterisering af en ny klasse af Pt-legeringer, der kan benyttes som katalysatorer for Oxygen Reduktion Reaktionen (ORR). Det langsigtede mål er at erstatte de traditionelle Pt-katalysatorer ved katoden i Polymer Elektrolyt Membran brændselsceller (PEMFCs). Med fokus på spektroskopiske teknikker såsom vinkelopløst røntgen fotoelektronspektroskopi (AR-XPS), atmosfærisk tryk røntgen fotoelektronspektroskopi (AP-XPS) og ionspredningsspektroskopi (ISS), er denne afhandling en del af en større række af undersøgelser udført med henblik på at kombinere fysiske teknikker med elektrokatalyse.

Polykrystallinske legeringer bestående af Pt og et lanthanidemetal (Pt_5La og Pt_5Ce) demonstrerede mere end en faktor 3 forøgelse i specifik aktivitet i forhold til state-of-the-art polykrystallinsk Pt. De fastholder mindst 90% af denne aktivitet efter accelererede stabilitetsforsøg (10 000 cykler mellem 0,6 og 1,0 V ift. den Reversible Hydrogen Elektrode (RHE) i 0,1 M $HClO_4$ elektrolyt). En kombination af AR-XPS og ISS målinger muliggjorde at den aktive overflade fase og struktur af disse materialer kunne bestemmes. Målingerne viser at de består af et ca. 1 nm tykt rent platinoverlag oven på legeringen. Det stabile platinoverlag leverer kinetisk stabilitet mod yderligere opløsning af lanthanider. Vi antager, at denne høje stabilitet er relateret til den meget negative dannelsesvarme for deres intermetalliske faser, der forhindre La og Ce i at diffunderer til overfladen. For denne struktur kan kun komprimeringseffekter forklarer den forøgede aktivitet.

Andre legeringer af samme klasse (f.eks. Pt_5Gd og Pt_5Tb) udviser endnu højere specifikke aktiviteter. I tilfælde af Pt_5Tb op til 6 gange den af polykrystallinsk Pt, en rekordhøj aktivitet blandt polykrystallinske legeringer. På basis af deres tilsvarende krystalstrukturer er ORR aktiviteten af denne klasse af legeringer korreleret til gitterparameteren af den bulk legering, som forventes at definere Pt-Pt afstanden i Pt overlaget. Komprimeringen af Pt-Pt afstanden i overlaget giver anledning til en ”vulkanformig” tendens i aktiviteten. Men de mest aktive legeringer oplever

størst aktivitetstab under stabilitetstest, hvilket tyder på at en høj grad af kompression kompromitterer den langsigtede stabilitet af Pt overlagene. Denne hypotese understøttes af tæthedsfunktionalteori (DFT) beregninger og AR-XPS. En model til kvantitativ vurdering af tykkelsen af Pt overlaget fra AR-XPS målinger indikerer en sammenhæng mellem størrelsen af Pt overlagene og tab i aktivitet. Dette støtter hypotesen om at mere komprimerede overlag har lavere fysisk stabilitet. Anvendelsen af disse materialer i en brændselscelle kræver at de fremstilles som nanopartikler.

Gennem en kombination af en gas aggregeringsteknik og et "time-of-flight" massespektrometer produceres størrelsesudvalgte Pt-Y nanopartikler. Med en masseaktivitet på 3,05 A *per* mg Pt ved 0,9 V ift. RHE, er 9 nm Pt-Y nanopartikler blandt de mest aktive ORR katalysatorer nogensinde målt. De mister dog 37% af denne aktivitet efter stabilitetstest. Efter nedsænkning i den sure elektrolyt og udførsel af elektrokemiske test består den aktive fase af en ren Pt-skal ovenpå en legeret kerne, svarende til strukturen af de polykrystallinske prøver. Også i dette tilfælde kan den forøgede ORR aktivitet forklares af den komprimerede Pt-Pt afstand.

Deponeringen af disse 9 nm Pt-Y nanopartikler på katodesiden af en Membran Elektrode Assembly (MEA) , en del af en specialforberedt brændselscelle, muliggør AP-XPS målinger under driftsbetingelser. Som følge af spændingscykling, oxiderer Y på grund af aflegeringsprocessen, der observeres *in-situ*. De adsorberede molekyler kan også probes og korreleres med det elektrokemiske potentiale. Tæt på det åbne kredsløb potentiale (OCP) består de iltholdige molekyler hovedsageligt af ikke-hydreret OH , svarende til tilfældet for rene Pt nanopartikler.

List of publications

Included publications

Paper 1:

Pt_5Gd as a Highly Active and Stable Catalyst for Oxygen Electroreduction.
María Escudero-Escribano, Arnau Verdaguer-Casadevall, Paolo Malacrida, Ulrik Grønbjerg, Brian P. Knudsen, Anders K. Jepsen, Jan Rossmeisl, Ifan E. L. Stephens, and Ib Chorkendorff. *Journal of the American Chemical Society*, 134(40): 16476 – 16479, October 2012.

Paper 2:

Pt Skin Versus Pt Skeleton Structures of Pt_3Sc as Electrocatalysts for Oxygen Reduction.
Tobias Peter Johansson, Elisabeth Therese Ulrikkeholm, Patricia Hernandez-Fernandez, Paolo Malacrida, Heine A. Hansen, Aliaksandr S. Bandarenka, Jens K. Nørskov, Jan Rossmeisl, Ifan E. L. Stephens, and Ib Chorkendorff. *Topics in Catalysis*, 57(1-4): 245 – 254, February 2014.

Paper 3:

Enhanced activity and stability of Pt–La and Pt–Ce alloys for oxygen electroreduction: the elucidation of the active surface phase.
Paolo Malacrida, María Escudero-Escribano, Arnau Verdaguer-Casadevall, Ifan E. L. Stephens, and Ib Chorkendorff. *Journal of Materials Chemistry A*, 2(12): 4234 - 4243, February 2014.

Paper 4:

Towards the elucidation of the high oxygen electroreduction activity of PtxY: surface science and electrochemical studies of Y/Pt(111).
Tobias Peter Johansson, Elisabeth Therese Ulrikkeholm, Patricia Hernandez-Fernandez, María Escudero-Escribano, Paolo Malacrida, Ifan E. L. Stephens, and Ib Chorkendorff. *Physical Chemistry Chemical Physics*, DOI: 10.1039/C4CP00319E, April 2014.

Paper 5:

Mass-selected nanoalloys as model catalysts: Pt_xY nanoparticles for oxygen electroreduction.
Patricia Hernandez-Fernandez, Federico Masini, David N. McCarthy, Christian E. Strebel, Daniel Friebel, Davide Deiana, Paolo Malacrida, Anders Nierhoff, Anders Bodin, Anna M. Wise, Jane H. Nielsen, Thomas W. Hansen, Anders Nilsson, Ifan E. L. Stephens, Ib Chorkendorff. *Submitted*, manuscript included.

Paper 6:

Understanding the trends in activity and stability of Pt-based cathode electrocatalysts for low-temperature fuel cells.
María Escudero-Escribano, Paolo Malacrida, Ulrik Grønbjerg, Vladimir Tripković, Jan Rossmeisl, Ifan E. L. Stephens, Ib Chorkendorff. *in preparation*, abstract included.

Other publications of this Ph.D. project

Paper 7:

Enabling direct H_2O_2 production through rational electrocatalyst design.
Samira Siahrostami, Arnau Verdaguer-Casadevall, Mohammadreza Karamad, Davide Deiana, Paolo Malacrida, Björn Wickman, María Escudero-Escribano, Elisa A. Paoli, Rasmus Frydendal, Thomas W. Hansen, Ib Chorkendorff, Ifan E. L. Stephens, and Jan Rossmeisl. *Nature Materials*, 12: 1137 – 1143, November 2013.

Paper 8:

Trends in the Electrochemical Synthesis of H_2O_2: enhancing Activity and Selectivity by Electrocatalytic Site Engineering.

Arnau Verdaguer-Casadevall, Davide Deiana, Mohammadreza Karamad, Samira Siahrostami, Paolo Malacrida, Thomas W. Hansen, Jan Rossmeisl, Ib Chorkendorff, and Ifan E. L. Stephens. *Nano Letters*, 14(3): 1603 – 1608, February 2014.

Paper 9:

CO_2 Electroreduction on Well-Defined Bimetallic Surfaces: Cu Overlayers on Pt(111) and Pt(211).
Ana Sofia Varela, Christian Schlaup, Zarko P. Jovanov, Paolo Malacrida, Sebastian Horch, Ifan E. L. Stephens, and Ib Chorkendorff. *Journal of Physical Chemistry C*, 117(40): 20500 – 20508, September 2013.

Paper 10:

MoS_2—an integrated protective and active layer on n^+p^-Si for solar H_2 evolution.
Anders B. Laursen, Thomas Pedersen, Paolo Malacrida, Brian Seger, Ole Hansen, Peter C. K. Vesborg, and Ib Chorkendorff. *Physical Chemistry Chemical Physics*, 15: 20000 - 20004, October 2013.

Paper 11:

Highly dispersed supported ruthenium oxide as an aerobic catalyst for acetic acid synthesis.
Anders B. Laursen, Yury Y. Gorbanev, Filippo Cavalca, Paolo Malacrida, Alan Kleiman-Schwarsctein, Søren Kegnæs, Anders Riisager, Ib Chorkendorff, Søren Dahl. *Applied Catalysis A: General*, 433 - 434, 243 – 250, August 2012.

List of abbreviations

AES	Auger Electron Spectroscopy
AP-XPS	Ambient-Pressure X-Ray Photoelectron Spectroscopy
AR-XPS	Angle-Resolved X-Ray Photoelectron Spectroscopy
CV	Cyclic Voltammetry
C-O-H	Carbon-Oxygen-Hydrogen Contamination Layer
DFT	Density Functional Theory
EC-STM	Electrochemical Scanning Tunneling Microscopy
EC-XPS	Electrochemical X-Ray Photoelectron Spectroscopy
ECSA	Electrochemically Active Surface Area
EDS	Energy Dispersive X-Ray Spectroscopy
EPU	Elliptically Polarized Undulator
EXAFS	Extended X-ray absorption fine structure
FCC	Face Centered Cubic
FEAL	Fast Entry Air Lock
FWHM	Full Width at Half Maximum
FTIR	Fourier Transform Infrared Spectroscopy
HAADF	High Angle Annular Dark Field
ICP-MS	Inductively Coupled Plasma Mass Spectroscopy
ISS	Ion Scattering Spectroscopy
LEED	Low Energy Electron Diffraction
LEIS	Low Energy Ion Spectroscopy
Ln	Generic Lanthanide metal

M	Generic metal
MEA	Memabrane Electrode Assembly
OCP	Open Circuit Potential
ORR	Oxygen Reduction Reaction
PEMFC	Polymer Electrolyte Membrane Fuel Cell
QCM	Quartz Crystal Microbalacane
RDE	Rotating Disk Electrode
RHE	Reversible Hydrogen Electrode
RRDE	Rotating Ring Disk Electrode
SHE	Standard Hydrogen Electrode
SIMS	Secondary Ion Mass Spectroscopy
SEM	Scanning Electron Microscopy
SLA	Straight Line Approximation
SSRL	Stanford Synchrotron Radiation Lightsource
STEM	Scanning Transmission Electron Microscopy
STM	Scanning Tunneling Microscopy
SXS	Surface X-Ray Scattering
TEM	Transmission Electron Microscopy
TPD	Temperature Programmed Desorption
TPP-2M	Tanuma-Powell-Penn Formula
TSP	Titanium Sublimation Pump
UHV	Ultra High Vacuum
UPD	Underpotential deposition
UPS	Ultraviolet Photoelectron Spectroscopy
XAS	X-Ray Absorption Spectroscopy
XPS	X-Ray Photoelectron Spectroscopy
XRD	X-Ray Diffraction

List of symbols

U	Electrochemical potential
U_0	Equilibrium potential
E_k	Photoelectron kinetic energy
E_b	Electron binding energy
h	Planck's constant
ν	Photon's frequency
ϕ_s	Material work function
ϕ_a	Analyzer work function
λ	Inelastic electron mean free path
λ_{eff}	Effective inelastic electron mean free path
θ	XPS photoemission angle calculated from the surface normal
x, y	Coordinates parallel to the sample surface
z	Coordinate normal to the sample surface
T	Detection efficiency (transmission function) of photoelectrons
Φ	XPS Photon flux
I_A	XPS intensity from a photoelectron transition of element A
E_A	Kinetic energy from a photoelectron transition of element A
σ_A	Cross section for a photoelectron transition of element A
N_A	Atomic concentration of element A
$N_A(\%)$	Relative atomic concentration in percent of element A
S_A	XPS sensitivity factor for a photoelectron transition of element A

$\hat{I}_A$	Normalized XPS intensity from a transition of element A
N_A^0	Atomic concentration of element A in a reference material
λ^0	Inelastic electron mean free path in a reference material
T^0	Analyzer transmission function of Wagner's sensitivity factors
$d_{sput.}$	Thickness of the sputtered region
I_i	Sputtering ion current
Y	Sputter yield
M	Molar mass
e	Electron charge
A	Sputtered surface area
ρ	Mass density
N_a	Avogadro's number
t_s	Total sputtering time
M_i	ISS ion mass
M_s	ISS mass of the probed atom
$\vec{v}_0$	ISS initial velocity of the ion
$\vec{v}_1$	ISS final velocity of the ion
$\vec{v}_s$	ISS final velocity of the probed atom
φ	ISS scattering angle
j_k	Kinetic current density
j	Total measured current density
j_d	Diffusion limited current density
λ_A	Inelastic electron mean free path through element A
I_A^∞	XPS intensity from an infinitely thick layer of element A
d	Thickness of the Pt overlayer
t	Thickness of the contamination (C-O-H) layer
$N_{Pt,alloy}$	Atomic concentration of Pt in the Pt_nM_m alloy
$N_{M,alloy}$	Atomic concentration of M in the Pt_nM_m alloy
$I_{Pt,alloy}^\infty$	Pt XPS intensity from an infinitely thick Pt_nM_m alloy
$I_{M,alloy}^\infty$	M XPS intensity from an infinitely thick Pt_nM_m alloy

Alloys of Pt and Rare Earths for the Oxygen Electroreduction Reaction

CHAPTER 1

Introduction

1.1 Low temperature fuel cells

Proton Exchange Membrane Fuel Cells (PEMFCs) represent one of the most promising alternatives to traditional power sources. The requirements of new technologies for storing energy into fuels, for instance through electrolysis of water, also involve the development of efficient ways for the re-conversion of fuels into electrical energy. In a PEMFC hydrogen is used as a fuel and combined with oxygen to produce water and electricity. Comprehensive reviews about fuel cells can be found in [1, 2]. Since the conversion of chemical energy to electrical energy can be performed in a clean and potentially very efficient way, PEMFCs might represent one of the fundamental progresses towards a future sustainable society [3, 4]. They would play a particularly important role for transportation applications, where the need of high energy density has so far limited the use of batteries. At the same time other kinds of fuel cells requiring high temperatures (*e.g.* Solid Oxide Fuel Cells) would not be practical due to their long start-up times.

Figure 1.1 shows a schematic drawing of a PEMFC. H_2 is introduced from the anode side where it is converted to protons and electrons through the Hydrogen Oxidation Reaction (HOR). The central part of the fuel cell consists of a proton conductive membrane, typically made of nafion; it allows the transfer of protons to the cathode side, but not the transfer of electrons which are collected into an external circuit producing electricity. Once the protons reach the cathode side they react with oxygen and electrons to produce water in the so called Oxygen Reduction

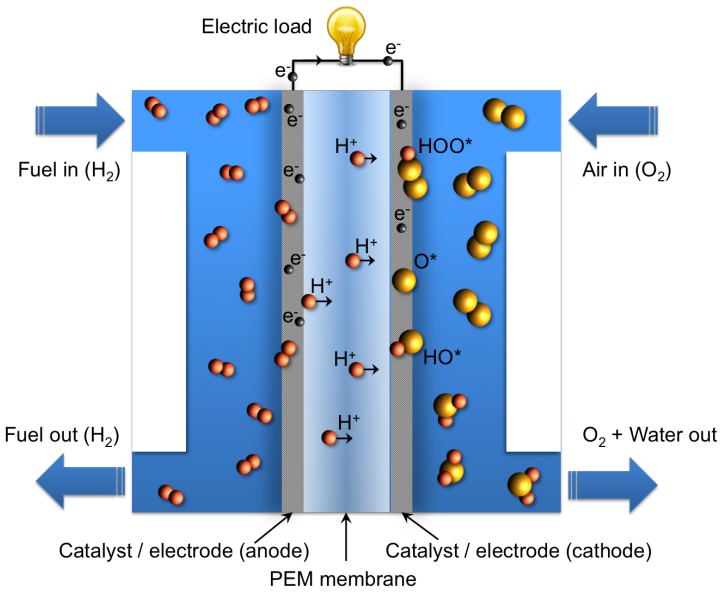

Figure 1.1: Schematic drawing of a PEMFC. Orange spheres represent hydrogen atoms (or protons), yellow spheres represent oxygen atoms and small black spheres represent electrons.

Reaction (ORR). The overall reaction is:

$$2H_2 + O_2 \longrightarrow 2H_2O. \tag{1.1}$$

Although PEMFCs have been known and intensively studied for about fifty years, their high production costs and their relatively low performances have so far inhibited their widespread commercialization. The reason for this can be primarily ascribed to the requirement of proper materials to catalyze both the HOR at the anode and the ORR at the cathode. In the current state-of-the-art PEMFCs both these catalysts are based on Pt, which strongly raises the costs of fabrication. At the same time it introduces problems related to the scarce availability of this material [5], indeed the current loadings are not really suited for a global utilization [3, 6]. To give an idea Stephens *et al.* estimated that a 100 kW vehicle would currently require about 50 g of Pt state-of-the-art catalysts: to be economically viable and scalable this quantity should probably be reduced to a level similar to that used in catalytic converters for internal combustion engines: $\approx$ 3.4 g per vehicle as an average [6].

With this objective modern research has primarily focused on the improvement of ORR catalysts at the cathode. A direct explanation for this can be easily visualized in Figure 1.2, where the overall efficiency of a PEMFC is shown. Although the

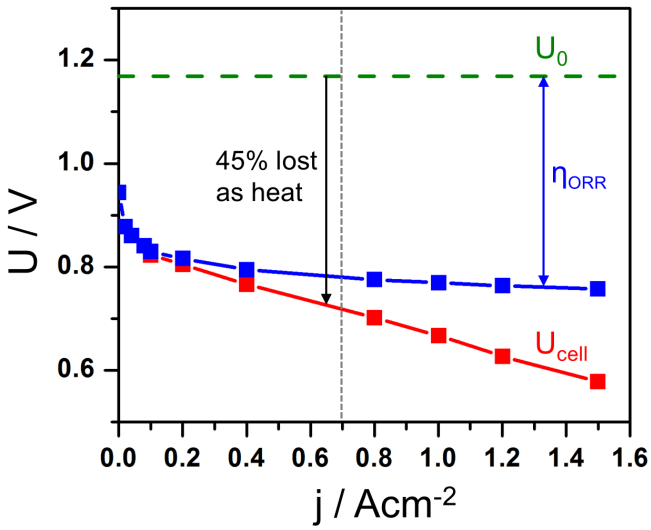

Figure 1.2: Potential (U) *vs.* current density (j) relationship of a state-of-the-art PEMFC with a typical ORR catalyst consisting of carbon supported Pt nanoparticles (red line). The reversible potential U_0 is shown for comparison (green dotted line). The kinetics of the ORR is responsible for most of the potential losses (blue line). Figure adapted from [3].

reversible thermodynamic cell potential for the reaction of equation 1.1 is 1.169 V at 80 °C (a typical operation temperature for PEMFCs), major losses occur. At a typical current density of 0.7 A cm^{-2} 45% of this chemical energy is lost as heat. According to Gasteiger *et al.* about 75 % of this efficiency loss can be assigned to the slow kinetics of the ORR at the cathode [3]. The rest is accounted by the losses due to the kinetics of the HOR, to the omhic resistance and to mass transport limitations.

Even the best state-of-the-art catalysts, all based on precious metals such as Pt or Pd, are still far from optimal and they exhibit considerable overpotentials for the ORR, which ultimately raises the loading of precious metals in PEMFCs [6, 7]. This means that the catalytic ORR mass activity, defined as the current density at a given potential per mass of precious metal, must be improved. This project enters in a broad research for the development of new Pt-based catalysts for the ORR whose main achievements will be introduced in the following sections of this chapter. An alternative approach focuses on non-precious metals cathode catalysts. The challenge here is to find materials that can be stable at the highly oxidizing acidic conditions (pH $\approx$ 0) of the cathode. Among the metals, only Ir, Pt and Au are thermodynamically stable at potentials higher than 0.9 V *vs.* the Reversible Hydrogen Electrode (RHE) [8] and even Pt corrodes at potentials close to 1 V *vs.*

RHE [9–11]. Although a number of important advances have been made, particularly promising those on pyrolyzed transition metal nitrogen-containing complexes supported on carbon materials (*e.g.* Fe– and Co–N/C), these catalysts still suffer insufficient activity and/or low stability in acidic conditions [12, 13].

1.2 Oxygen reduction reaction

Before introducing the most promising state-of-the-art Pt-based catalysts for the ORR, it is worth describing this reaction in more detail. As already anticipated the overall oxygen reduction reaction is:

$$O_2 + 4H^+ + 4e^- \longrightarrow 2H_2O, \tag{1.2}$$

with the total transfer of four electrons and four protons. According to the Sabatier principle [14], finding the catalyst with the highest activity for this reaction will correspond to identify a catalyst with the right compromise of reactivity [15]; meaning that the optimal catalyst should be sufficiently reactive to activate the O_2 gas molecule and at the same time sufficiently noble to release oxygen and the reaction products in the form of H_2O [16, 17]. In this view the trends in activity of pure metal surfaces can be well explained [18]. Pt is the pure metallic element with the highest ORR activity. More reactive metals as for instance Pd, Cu or Ir bind oxygen or some of the reaction intermediates too strongly while more noble metals as Ag or Au bind oxygen too weakly. This results in a typical volcano plot illustrated in Figure 1.3 where the experimental activities of different metal surfaces is plotted *vs.* the theoretical O adsorption energy.

The reasons why the O adsorption energy is such a good descriptor of the catalytic activity can be to a good extent clarified once the reaction mechanism is studied in more detail. Although this has been the focus of numerous studies for several decades and it is still quite controversial [19–21]: also due to the difficulties of performing experiments allowing a direct and possibly in-situ observation of the reaction intermediates [22–24]. A theoretical treatment of the ORR mechanism is also highly complex, in particular the modeling of the electrochemical environement, including the effects of the solvent on the adsorbed species, the electric field in the double layer region and the free energies of electrons in the solid and of the reactants, as a function of the electrochemical potential [25–28]. The general trends can be addressed through a somewhat easier approach, by referring to heterogeneous catalysis. Density Functional Theory (DFT) calculations can provide accurate values of the chemical potentials and adsorption energies of the reaction intermediates at the gas-solid interface [19, 29, 30]. By calculating the adsorption energies of all the possible intermediates (*i.e.* HOO^*, HO^* and O^*), the overall free energy pathway of the ORR can be derived as a function of potential.

In the rest of this section the following reaction mechanism will be considered:

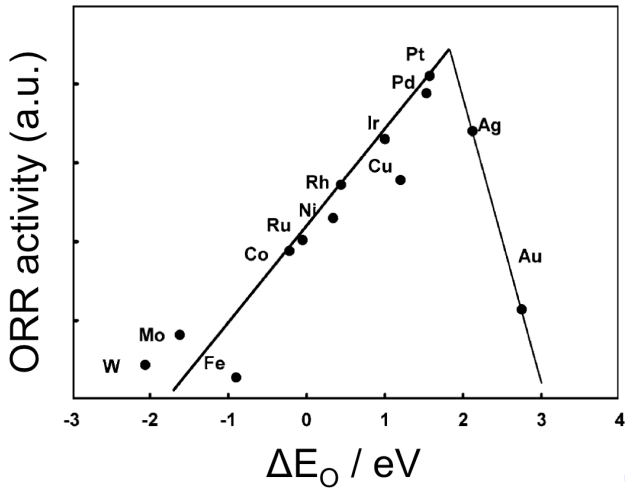

Figure 1.3: Volcano-shape trend of the ORR experimental activity plotted as a function of the calculated oxygen binding energy ΔE_O. Figure adapted from [19].

$$O_2\,(g) + H^+ + e^- + * \longrightarrow HOO^* \tag{1.3a}$$
$$HOO^* + H^+ + e^- + * \longrightarrow O^* + H_2O\,(l) \tag{1.3b}$$
$$O^* + H^+ + e^- + * \longrightarrow HO^* \tag{1.3c}$$
$$HO^* + H^+ + e^- + * \longrightarrow * + H_2O\,(l), \tag{1.3d}$$

where $*$ indicates the active site on a catalytic surface and the adsorbed intermediates in the case of HOO^*, HO^* and O^*, all bound through an oxygen atom. The first step is particularly controversial as the dissociative mechanism, involving the direct dissociation of the oxygen molecule ($O_2\,(g) \longrightarrow 2O^*$), could also occur [19, 31]. However, in the relevant range of potentials this was shown to play a minor role on Pt surfaces, which are the main interest of this work [18, 32].

The presence of three different intermediates explains the higher level of complexity with respect for instance to the HOR (with the single intermediate H^*) and therefore the difficulties of finding good catalysts. Indeed an efficient ORR catalyst should bind each of these intermediates optimally, neither too strongly nor too weakly [17]. Figure 1.4 illustrates the calculated free energy pathway on a Pt(111) surface at a potential of 0.9 V *vs.* RHE. The four reaction steps of equations 1.3a-1.3d can be distinguished. Two of them, namely the formation of OOH^* (equation 1.3a) and the protonation of HO^* with desorption of a H_2O molecule (equation 1.3d) are uphill in free energy; these are the possible candidates for the potential determining step.

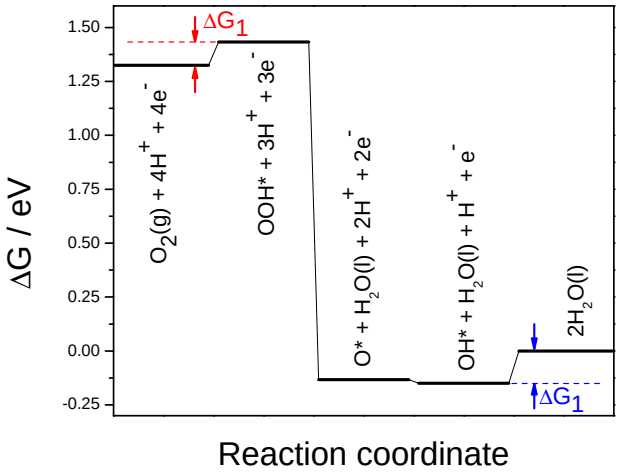

Figure 1.4: Free energy diagram corresponding to the ORR steps of equations 1.3a-1.3d on a Pt(111) surface at an applied potential of 0.9 V *vs.* RHE. Figure adapted from [17].

The ORR activity can be related to this kind of free energy diagrams under two main assumptions. The maximum activity per active site at very high overpotentials is assumed to be the same for all kinds of site and materials and the actual activity is only dependent on the free energy difference of the potential determining step. This last assumption implicates that this will also coincide with the rate determining step: its validity was confirmed by more detailed theoretical models for the ORR including the effects of reaction barriers [32, 33].

Figure 1.4 also shows that the Pt(111) surface is still far from the optimal catalytic surface for the ORR. A better catalyst would bind HOO^* more strongly and OH^* more weakly so that all the free energy steps would be downhill. In particular an ideal catalyst would exhibit a flat free energy diagram at the equilibrium potential: 1.23 V at standard conditions. This would result in considerable ORR currents at slightly more negative potentials and negligible kinetic losses would occur. Unfortunately, it turns out that it is in general not possible to tune the binding energy of the three ORR intermediates independently of each other [34]. It is quite intuitive, for instance, that a surface binding strongly to HO^* will also bind strongly to HOO^*, due to the similarity of these species and to the fact that they both bind through an O atom. DFT calculations suggest that the binding energies of the ORR intermediates all scale linearly with each other [19, 34]. Therefore, each of these binding energies can be employed as a single descriptor of the ORR activity, explaining the volcano relationship of Figure 1.3 where the binding energy

of O was used. In this view, the only possible way of enhancing the activity of a Pt(111) surface is to find a catalyst for which, the two uphill steps in Figure 1.4, are equal: this would correspond to a surface binding HO* about 0.1 eV weaker than Pt(111).

1.3 Pt alloys for oxygen reduction

In the previous section it was theorized that on a metal surface the optimal ORR catalyst would bind the ORR intermediates slightly weaker than pure Pt. The traditional approach for tuning the binding energy of Pt and enhance its activity involves the alloying of Pt with other metals. In the last couple of decades, extended bimetallic surfaces of Pt and late transition metals such as Fe, Co, Ni and Cu have been studied extensively [35–41]. Various of these surfaces exhibited an increased ORR activity with respect to pure Pt. It should be noted that in all these cases the less noble *solute* metal is not thermodynamically stable under the acidic conditions of a PEMFC at the typical cathode potentials [8]. Therefore these metals tend to dissolve into the electrolyte via a process known as dealloying [41–43]. The resulting surface of these catalysts is Pt enriched and it typically consists of a Pt overlayer protecting the bulk alloy from the dissolution of the solute metal. A precise characterization of these structures is challenging as the level of Pt enrichment and the thickness of the Pt overlayers varies for different alloys, preparation techniques and electrochemical treatments.

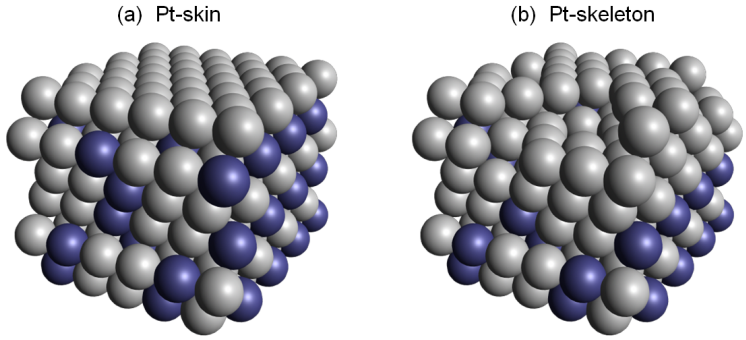

Figure 1.5: Schematic representation of a Pt-skin (a) and of a Pt-skeleton (b) surface structure.

In general two kinds of surface structures can be distinguished: denoted by Stamenkovic *et al.* as *Pt-skeleton* and *Pt-skin* structures [37, 44]: their schematic representation is illustrated in Figure 1.5. In the first case their polycrystalline alloys are prepared in vacuum by sputter-cleaning and later immersed into an acidic

electrolyte. The skeleton structure is the result of the dissolution of the solute atoms; these leached surfaces typically exhibit a 1-2 nm thick Pt overlayers containing negligible amounts of other metals [6, 35, 37]. Although in principle these Pt overlayers could exhibit some level of roughness and be to some extent disordered, there is in-situ experimental evidence of the formation of ordered (111) facets under electrolyte exposure [45]. In the second case the sputter-cleaned alloys are annealed in vacuum inducing Pt segregation, the reason for this being the lower surface energy of Pt with respect to the solute metals. This Pt-skin structures are highly ordered and typically composed of a single Pt monolayer on top of the bulk alloy. According to some reports the concentration profile would exhibit a oscillatory behaviour in the surface layers, with a certain enrichment of the solute metal in the second layer [37, 46]. Some of these Pt-skin alloys have shown the highest activities ever reported on extended surfaces. In particular, the annealed surface of $Pt_3Ni(111)$ holds the record in activity [39]. Figure 1.6 shows the measured ORR activities of various alloys of Pt and late transition metals with a Pt-skin structure, including $Pt_3Ni(111)$: they are plotted as a function of the oxygen binding energy and compared to the theoretical volcano trend.

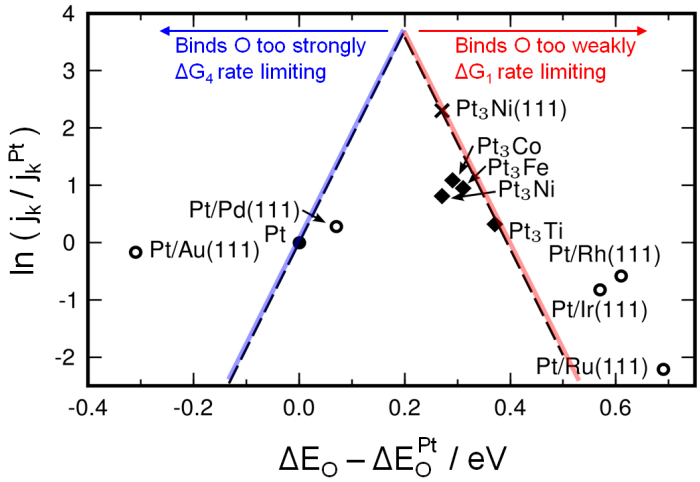

Figure 1.6: Experimental ORR activity (expressed as kinetic current density) of various Pt alloys exhibiting a Pt-skin structure, as a function of the calculated oxygen binding energy ΔE_O. All data are shown relative to Pt. Experimental point refer to: Pt monolayers on single crystal metal substrates (circles) [47], Ultra High Vacuum (UHV) annealed polycrystalline alloys (diamonds) [38] and $Pt_3Ni(111)$ single crystal alloy (cross) [39]. Dashed lines represent the theoretical predictions from [17, 19]. Figure adapted from [16].

It should be noted that all these kind of surfaces are thermodynamically unstable. The Pt overlayer provides kinetic stability against rapid dissolution of the

solute metal from the bulk. However, the process of dealloying will ultimately define the lifetime of these surfaces and it is considered as the main reason of long-term deactivation. Since stability, together with ORR activity, is one of the main requirements for cathode catalysts of PEMFCs, this translates in the need of surfaces that will be sufficiently stable over the particular time and conditions of practical use of a certain application. The annealing treatments originating these Pt-skin structures stabilize the surface layers allowing to obtain stable CVs and a complete electrochemical characterization in acidic conditions over these surfaces. This is the case of $Pt_3Ni(111)$ whose structure was probed in-situ by Surface X-Ray Scattering (SXS) demonstrating its complete stability in the potential range of 0.05-1.00 V *vs.* RHE in 0.1 M $HClO_4$ electrolyte [39]. However also these surfaces will ultimately evolve towards structures that resemble a Pt-skeleton. As an example, Todoroki *et al.* recently studied the stability of Pt-enriched (Pt-skin) Ni/Pt(111) catalysts [48]. Although their initial ORR activity was 8 times higher than that of pure Pt(111), after only 1000 potential cycles between 0.6 and 1.0 V *vs.* RHE, 75% of this activity was lost as a consequence of Ni dissolution. It should be also anticipated that the stabilization of these Pt-skin structures on the large surface area catalysts required for the application in PEMFCs, either in the nanoparticulate or in the nanostructured thin film form, will be challenging. Some of the most promising results in this perspective will be presented in the next section.

Various studies on alloys of Pt and late transition metals have aimed at elucidating the mechanisms of activity enhancement with respect to Pt. The presence of two different metals could tempt into explaining the high activity in terms of bifunctional effects [49–51]. Indeed, if the solute metal was effectively present on the surface different catalytic sites could catalyze different steps of the ORR, for instance with the less noble metal facilitating the O_2 dissociation or the removal of OH radicals from the more noble Pt sites. In this view the scaling relations among the ORR intermediates could be bypassed, potentially providing very high activities. However, as explained above, the thermodynamic instability of the solute metal in the typical range of pH and potentials of a PEMFC does not allow their stabilization on the surface of the alloy which is in all cases constituted by Pt overlayers. Therefore, the observed activity enhancement must be related to a modification of the electronic structure of these Pt overlayers, which finally results in a weakening of its binding to the ORR intermediates (HOO^*, HO^* and O^*): this is typically achieved through either *ligand* or *strain* effects. Ligand effects are caused by the direct electronic interactions of the surface Pt atoms with a different solute metal. They are usually obtained by subsurface alloying as this kind of interactions exhibit a very short spatial range and they would vanish if the solute atoms are not present in the second atomic layer [52]. Strain effects occur when the Pt overlayer is either compressed or expanded laterally: a lateral compression in particular would result in downshift of the d-band center of Pt and a weaker binding to the ORR intermediates [53–55]. This compression is typically achieved by imposing the Pt overlayer over a substrate with different lattice parameter. Figure 1.7 shows a schematic rep-

resentation of two alloyed surface structures subjected to pure ligand effects and pure strain effects.

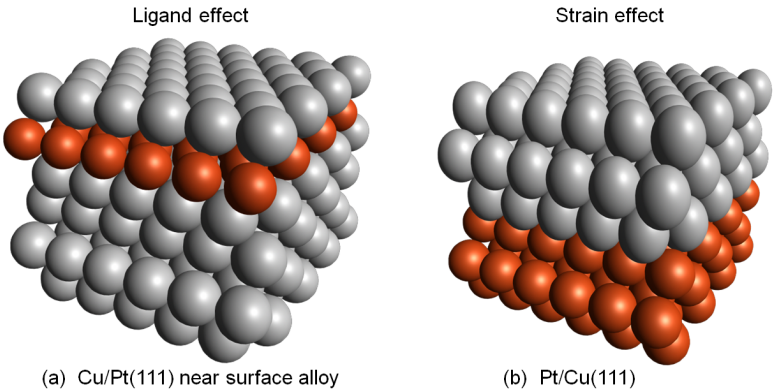

Figure 1.7: Schematic representation of a Cu/Pt(111) near surface alloy [56] where ligand effects prevail (a) and of a three layers thick Pt overlayer deposited on a Cu(111) (b) [31]: in this case the smaller lattice parameter of the Cu atoms induce lateral compressive strain on the Pt overlayer. Grey and orange spheres represent Pt and Cu atoms respectively.

On a real surface the two effects often coexist and it is difficult to separate them. For instance, the enhanced activity of Pt_3Co and Pt_3Ni could be explained by strain effects as these alloys present the same closed packed bulk structure of Pt, but with a compressed lattice parameter, induced by the smaller covalent radius of Co and Ni [57]. However, the higher ORR activity reported on their annealed Pt-skin structures with high solute metal concentrations in the second atomic layer [37], and in particular the extremely high activity of $Pt_3Ni(111)$ [39] suggest that ligand effects also play an important role. Two recent studies on Pt-Cu alloys have been able to separate ligand and strain effects. In the study of our group, a Pt(111) surface was modified by subsurface alloying: a so called near surface alloy, with a similar structure as in Figure 1.7 a, was prepared through a combination of Cu underpotential deposition and annealing [56]. Since the bulk of the alloy still consists of pure Pt and Cu is only present in the second atomic layer strain effects should be negligible. Increasing amounts of Cu in the second layer originated a shift towards lower OH^* binding energies, mainly ascribed to ligand effects: the ORR activity was found to vary accordingly and a volcano relationship in good agreement with the one in Figure 1.6 appeared. In the work of Strasser *et al.* Pt-Cu nanoparticles as well as Pt overlayers on a Cu(111) single crystal were studied [31]. Since the nanoparticles exhibited a rather thick ($\approx$ 1 nm) Pt overlayer, for which ligand effects should already be vanished at the surface, their high activity was associated to pure strain effects. In order to elucidate these effects they deposited controlled amounts of Pt on a Cu(111) substrate, whose lattice parameter induces compres-

sive strain on the surface Pt. Despite some strain relaxation effects, after deposition of 5 Pt monolayers a certain level of compressive strain was still observed at the surface; this was correlated to the experimentally observed downshift of the d-band center and, in agreement with the d-band theory [53–55], to a weaker OH^* binding, explaining the enhanced activity of the Pt-Cu nanoparticles.

1.4 Large surface area catalysts

The vast majority of the ORR catalysts described so far consisted of extended surfaces, typically single crystals or polycrystalline alloys. These kind of samples could never be employed in a fuel cell where the need of high power densities and sufficiently low costs imposes the use of high surface area catalysts. These are typically Pt, or Pt based, nanoparticles supported on a large surface area carbon support (Pt/C), although an alternative could be represented by thin films of a catalytic material (typically Pt or Pt alloys) deposited on nanostructured substrates [58–62]. In all these cases the relevant quantity for the design of a better catalyst is the mass activity, that is the amount of ORR current at a given potential per amount of precious metal. Higher mass activities can be achieved either by raising the level of catalyst dispersion (*i.e.* number of active sites per mass of catalyst) or by raising the the intrinsic activity per active site (specific activity). Unfortunately, in most cases these two quantities cannot be tuned indipendently. In the case of pure Pt nanoparticles, for instance, a higher dispersion can be reached by decreasing the particle size. However, while the catalyst dispersion increases for smaller sizes, so does the number of under-coordinated active sites on the surface of the nanoparticles. On these sites (*e.g.* steps, edges and kinks) the ORR intermediates (for instance HO^*) bind more strongly, causing higher overpotentials and lower specific activities. The combination of these two opposite trends generates a maximum of mass activity at a particle size of about 3 nm [3, 63, 64], which is not optimal in terms of catalyst stability [9, 65].

Given this optimal particle size, the only possible way of further enhancing the performance of ORR catalysts is to tune their specific activity. Although there might be some way of raising these specific activities without involving different materials, for instance by engineering the morphology of the particles [66–69] or by tuning the intra-particle distance at high coverages as recently proposed by Nesselberger *et al.* [70], the traditional approach consists of alloying Pt with other transition metals.

The promising results of their correspondent extended surfaces motivated the interest towards testing carbon supported nanoparticles based on alloys of Pt and late transition metals such as Fe, Co, Ni and Cu. Some of these systems have been studied for at least two decades [3, 43, 71–74] typically exhibiting 2-3 times higher specific activities than that of Pt/C state-of-the-art catalysts [75]. However, the same tendency towards dealloying of the solute metal observed on extended

surfaces is also observed on these nanoparticles, generally limiting their stability in acidic conditions [10, 76, 77]. The same process leading to the formation of a Pt-skeleton typically produced an acid-leached core-shell structure consisting of Pt enriched shell and an alloyed core [31, 43]. It should be noted that in comparison with extended surfaces, the issue of stability for supported nanoparticles is much more complex and even Pt/C catalysts typically degrade considerably over time [6, 9, 78]. However, in the case of Pt bimetallic nanoparticles the dealloying process is considered as the main reason of degradation [10, 76].

Since the presence of dissolved metal cations can easily affect the activity of these catalysts, particularly in PEMFCs due to poisoning of the membrane[77], the particles are often pre-leached in a liquid electrolyte [3]. Complex procedures combining acid leaching and annealing have been optimized in order to stabilize the Pt overlayers on top of these particles and ensure more ordered structures [79–82]. The idea is to reproduce the superior properties of Pt-skin extended surfaces; this strategy lead to improvements both in terms of stability and activity, in some cases approaching 4-fold activity enhancements relative to state-of-the-art Pt/C catalysts [82]. An alternative approach for the formation of ordered Pt-skin structures consisted of exposing the surface to controlled atmospheres, for instance by electrochemical cycling in a CO-saturated electrolyte [83].

Another interesting approach was proposed by Adzic and co-workers; they formed Pt overlayers onto a core containing significant amounts of another noble metal such as Ir, Au or Pd [84, 85]. These materials are also very expensive and scarce, with no relevant long term advantage in terms of cost with respect to Pt [5]. The obtained mass activities once normalized for the total amount of precious metals are also lower than for other alloys. However the nanoparticles prepared with this method exhibited highly enhanced stability. As a very recent example they reported only 8 % of loss in mass activity after 100 000 potential cycles between 0.6 and 1.0 V *vs.* RHE in a PEMFC [86].

Probably the most promising perspective is the one inspired by studies on single-crystalline samples: by controlling the nanoparticle shape and morphology it is possible to model their surface and to selectively expose particular crystal facets [87–90]. Various attempts have been performed in order to synthesize octahedral alloy nanoparticles dominated by (111) facets, especially with the aim of reproducing the record specific activity of $Pt_3Ni(111)$. The highest mass activities ever reported have been achieved with this method [91, 92], although the stability of these octahedra still appear to be a critical issue. However, Stamenkovic and co-workers have just reported a record breaking activity on so called Pt_3Ni nanoframes. The fabrication starts from $PtNi_3$ polyhedra: these are transformed through a process of internal erosion that preserves the edges of the nanoparticles forming a peculiar shape with three-dimensional molecular accessibility [93]. The mass activity of these nanoframes showed an extraordinary factor of 10 enhancement with respect to state-of-the-art Pt/C. Their stability test consisting of 10 000 potential cycles between 0.6 and 1.0 V *vs.* RHE indicated that these structures are

also highly stable.

1.5 Alloys of Pt and early transition metals

In the previous sections it was shown how alloys of Pt and late transition metals with their promising ORR activities, solve some of the problems involved in the development of efficient PEMFCs. However, the stabilization of the Pt overlayers against dealloying that would ensure the necessary long-term stability of the cathode is still a big challenge. These observations motivated our group to carry out a theoretical DFT screening study in search of new Pt alloys for the ORR [16]. In order to account for both ORR activity and stability, the candidate alloys, all in the form of Pt_3M or Pd_3M (with M indicating a generic transition metal), had to fulfill two requirements. First, they had to form Pt (or Pd) overlayers (Pt-skin structure) with binding energy to OH^* about 0.1 eV weaker than the one of pure Pt. Secondly, the heat of alloy formation, defined as the amount of energy gained during the bulk alloy formation by its constituents, had to be as negative as possible. This quantity was taken as a measure of the alloy stability.

As a result of the DFT screening two promising candidates were chosen: Pt_3Y and Pt_3Sc. This new class of catalysts, constituted by Pt and an *early* transition metal, is characterized by extremely negative heats of alloying formation; this is a consequence of the filling degree of their d-bands: only one electron for Sc and Y and nine electrons in the case of Pt. In the so formed alloys the d-band is half filled, meaning that all the bonding states are full, and anti-bonding states are empty [94, 95]. Similar to the well studied Pt-skin structures of Pt_3Co and Pt_3Ni, the OH^* binding energy of Pt_3Y and Pt_3Sc is rather close to the theoretical optimal value. Interestingly, the heat of alloy formation of Pt_3Co and Pt_3Ni, as for most of the alloys of Pt and late transition metals, is basically negligible. This could explain their tendency towards dealloying. Although all these alloys, including Pt_3Y and Pt_3Sc, are thermodynamically unstable, the more negative heats of alloy formation are expected to raise higher kinetic barriers against the diffusion of the solute metals to the surface, ultimately improving the surface stability.

The electrochemical testing of sputter-cleaned polycrystalline Pt_3Y and Pt_3Sc lead in both cases to enhanced activities with respect to Pt [16]. In particular, the ORR activity of Pt_3Y measured in O_2-saturated 0.1 M $HClO_4$ electrolyte at 0.9 V *vs.* RHE was about 5 times higher than for polycrystalline Pt. At that time, this promoted Pt_3Y as the most active polycrystalline surface ever tested, although consisting of a Pt-skeleton. More recently, Kim and co-workers have also tested Pt-Y catalysts in the form of sputter-deposited thin films [96, 97]. Their results show even higher specific activities. Interestingly, they also performed accelerated stability tests consisting of 3 000 cycles between 0.6 and 1.1 V *vs.* RHE.: no significant activity losses were measured. This was a first indication of the stability of Pt-Y alloys in electrochemical environment, further motivating the interest towards the

investigation of these new class of catalysts. However, we anticipate that a proper test of stability should be conducted on nanoparticles and in a fuel cell if possible. Furthermore there is so far no direct comparison between the stability of Pt alloys based on early transition metals and late transition metals. A proper test should be strictly performed under the same conditions and with similar preparation techniques.

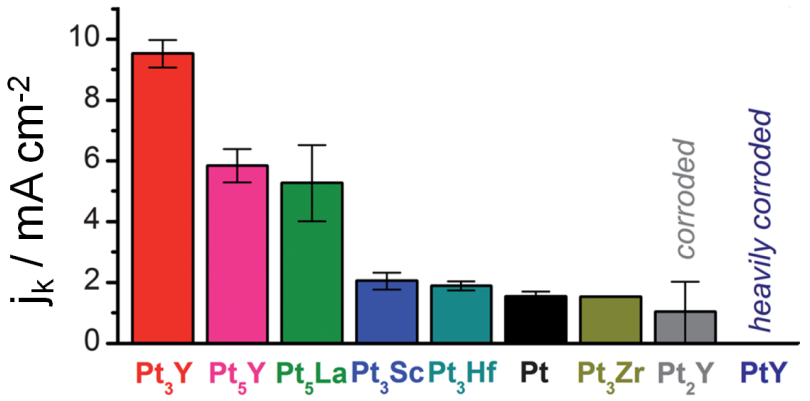

Figure 1.8: Experimental ORR activity (expressed as kinetic current density at 0.9 V *vs.* RHE normalized per geometric surface area) of various polycrystalline alloys of Pt and early transition metals. ORR polarization curves were acquired at 20 mV s^{-1}, while they were acquired at 50 mV s^{-1} for the other activities reported in the following chapters of this thesis. Figure adapted from [6].

On the basis of the encouraging results on Pt_3Y and Pt_3Sc surfaces, other polycrystalline alloys of Pt and early transition metals have been tested with the same methodology [6, 98]. Figure 1.8 summarizes the ORR activities of all the alloys of Pt and early transition metals tested in our group prior to the work of this thesis: following the rank of activities, Pt_3Y, Pt_5Y, Pt_5La, Pt_3Sc, Pt_3Hf, Pt_3Zr, Pt_2Y, PtY. Among these, the Pt-Y phases with very high Y content (Pt_2Y, PtY) were found to corrode in acid; Pt_3Hf, Pt_3Zr exhibited the formation of Hf oxide and Zr oxide on the surface of Pt, explaining the low activity enhancement compared to Pt. Pt_3Sc also showed a rather small increase. On the other hand, both Pt_5Y and Pt_5La were at least 3 times more active than polycrystalline Pt and considerably more active than alloys such as Pt_3Co and Pt_3Ni prepared in similar conditions [37]. Pt_5La in particular was the first alloy of Pt and a lanthanide metal tested as an ORR catalyst. Together with the results of Kim and co-workers on Pt-La thin films [99] that also exhibited high activity and stability, it motivated the study of a large number of other Pt_5Ln alloys (with Ln indicating a generic lanthanide metal) in the present work.

Given the high activity and stability measured on these alloys, all exhibiting a Pt-skeleton structure, the physical and electrochemical characterization of their correspondent Pt-skin surfaces would be highly interesting. Possibly, the stabilization by annealing of a single Pt monolayer on top of these alloys could lead to activities that are close or even higher than those of $Pt_3Ni(111)$ [39]. Very recently we reported the formation of Pt-skin structures on polycrystalline Pt_3Sc [100] and on Y modified Pt(111) single crystal [101] (Paper 2 and 4 in the end of this thesis). CO Temperature Programmed Desorption (TPD) experiments demonstrated that these surfaces bind CO considerably weaker than pure Pt: on a Pt surface this can be associated to a decrease of the OH^* binding energy [100]. In both cases, despite the formation of a Pt-skin structure, some level of solute metal oxidation was observed after air-exposure, indicating that the Pt overlayer was not completely stable. Accordingly, their ORR activities resembled those of sputter-cleaned Pt_3Sc and sputter-cleaned Pt_3Y in the Pt-skeleton form. Furthermore a clear increase of the Pt to solute metal ratios after ORR testing indicated a thicker Pt overlayer and the evolution of these ordered annealed surfaces towards Pt-skeleton structures. The stabilization of Pt-skin structures on alloys of Pt and early transitions metals therefore remains a challenge.

Finally it should be remarked that the biggest challenge regarding these alloys of Pt and early transition metals is the synthesis of large surface area catalysts, for instance in the form of supported nanoparticles. The application into fuel cells would indeed require a fabrication method that is suitable for large scale production. The sputter-deposition technique employed by Kim and co-workers [96, 97, 99] might be promising if applied onto large surface area nanostructured substrates. A chemical method for the production of nanoparticles would probably be more economically feasible. However, all these early transition metals, as well as all the lanthanides, are highly reactive and oxophilic. Therefore, reducing them into the form of an alloy is very difficult. Although some groups have recently attempted the fabrication of Pt-Y nanoparticles by using chemical-electrochemical methods [102, 103], there is so far no solid evidence that a metallic Pt-Y phase could be produced and that it would exhibit superior catalytic performance. In this thesis a physical method based on the gas aggregation technique will be used for the fabrication of size-selected Pt-Y nanoparticles. This will be the first report of the ORR activity on a similar kind of large surface area catalysts, although this fabrication method is certainly not suited for a large scale production.

1.6 Thesis outline

In the next chapter of this thesis (Chapter 2) the employed experimental setups and correspondent experimental methods of this work will be introduced. A particular attention will be given to the X-ray Photoelectron Spectroscopy (XPS) and Ion Scattering Spectroscopy (ISS) techniques, as they constituted the central part of this

Ph.D. project. Later on, these techniques will be applied to various polycrystalline Pt alloys: their electrochemical behaviour will be also presented both in terms of ORR activity and stability. In Chapter 3 the application of XPS and ISS to Pt-La and Pt-Ce alloys will elucidate their active surface phase and surface structure: general considerations will allow to extend these properties to the other alloys of Pt and rare earths. In Chapter 4 the electrochemical results from this class of materials as well as from a new class of Pt and alkaline earths alloys, will be collected showing clear trends in activity and stability. A model for the quantitative interpretation of Angle-Resolved X-ray Photoelectron Spectroscopy (AR-XPS) results will correlate their electrochemical stability to their physical (structural) stability. Chapter 5 will focus on the study of Pt-Y nanoparticles. Their ORR activity and stability will be presented. XPS and ISS, together with other experimental techniques such as Transmission Electron Microscopy (TEM) and Extended X-ray Absorption Fine Structure (EXAFS), will show that the mechanisms of activity enhancement are similar to those of polycrystalline surfaces. In Chapter 6 Ambient-Pressure X-ray Photoelectron Spectroscopy (AP-XPS) will be used for the *in-situ* characterization of these Pt-Y nanoparticles in a specifically prepared fuel cell. The design and construction of a new experimental setup for combining XPS measurements and electrochemistry will be also described. General conclusions and perspectives of this work will be given in Chapter 7. Published papers and manuscripts related to this work or to this Ph.D. project may be found in the end of this thesis after the bibliography.

CHAPTER 2

Experimental setups and methods

This chapter describes the experimental setups as well as the experimental methods that were used during this project. The first sections will be focused on the Theta-Probe, since this is the setup which was mainly employed and developed during this Ph.D. project and where most of the presented analyses were made. Starting from an overview of the system some of the single components will be treated in more detail. The correspondent experimental techniques will then be described in detail. The last section of the chapter introduces some of the other experimental setups connected to this project.

2.1 The Theta-Probe system

The Theta-Probe setup is a Ultra High Vacuum (UHV) system provided by Thermo Scientific and specifically intended for state-of-the-art surface analysis and in particular X-Ray Photoelectron Spectroscopy (XPS) analysis. Figure 2.1 a represents a side view of the Theta-Probe, the corresponding schematic drawing (Figure 2.1 b) illustrates the main components. The system consists of two main chambers separated by a gate valve: a main analysis chamber and a Fast Entry Air Lock (FEAL) for the quick loading and unloading of samples. The analysis chamber is equipped with an X-ray gun with correspondent monochromator, an UV Helium lamp and a hemispherical analyzer for X-Ray Photoelectron Spectrocopy (XPS) and Ultraviolet Photoelectron Spectroscopy (UPS) measurements; Figure 2.1 also shows the

ion gun for sample cleaning and Ion Scattering Spectroscopy (ISS). A flood gun for charge neutralization of the non-conductive samples is available. A camera is mounted on top of the analysis chamber: in combination with a three axis motorized stage in the middle of this chamber it allows a precise alignment of the samples. The most relevant of these components will be described in more detail in the following paragraphs.

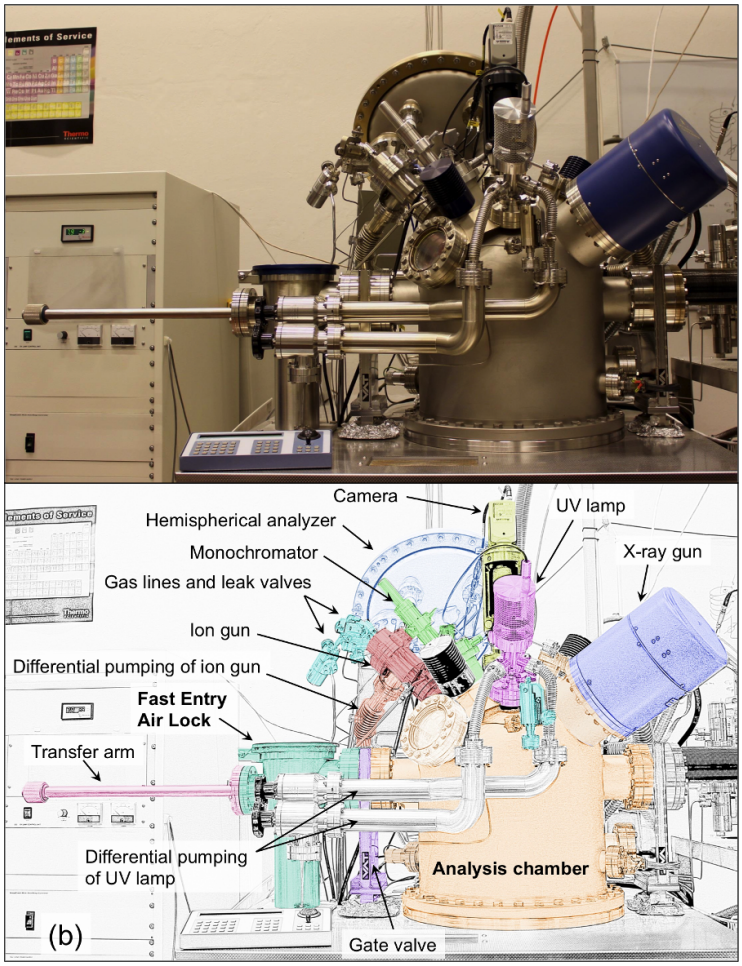

Figure 2.1: Side view of the Theta-probe setup which was used for most of the spectroscopic measurements of this work (a) and correspondent schematic representation with indications of the main components (b).

2.1.1 Pumping system and gas lines

The pumping system consisted originally of three turbopumps: two 270 l s^{-1} turbopumps dedicated to the FEAL and the analysis chamber respectively and a smaller 80 l s^{-1} turbopump for the differential pumping of the ion gun and of the flood gun. Two extra 80 l s^{-1} turbopumps have been mounted during this project in order to provide differential pumping of the UV helium lamp and to improve the cleanliness of the gas lines. The analysis chamber is also provided with a Titanium Sublimation Pump (TSP) that allows to reach a base pressure of 5×10^{-10}mbar and improves the pumping rate of reactive gases. This pressure was allowed to increase up to about 5×10^{-9}mbar during some of the measurements, due to degassing from the samples. The gas system comprehends five separated lines containing N60 purity He, Ne, Ar, CO, H_2 respectively, each separated from the analysis chamber through manually controlled leak valves.

2.1.2 Sample types and mounting

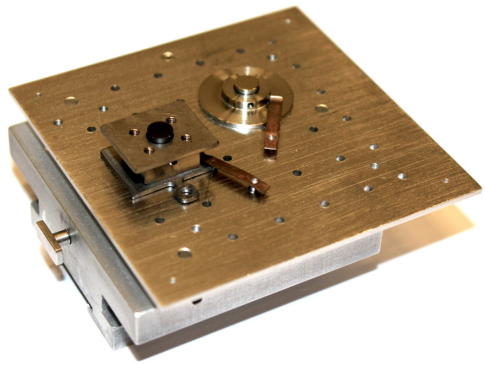

Figure 2.2: Most used sample carrier of the Theta-Probe setup. Two clamps keep in place two of the typical sample holders: they respectively carry size-selected Pt-Y nanoparticles deposited on glassy carbon (left) and polycrystalline Pt_5Tb (right).

Three different sample carriers can be loaded in the FEAL and transferred onto the three axis sample stage in the analysis chamber. The samples are typically hold through metallic clamps as shown for the most commonly used carrier in Figure 2.2. The measurements reported in this thesis have been typically carried out on two different kinds of samples. A number of polycrystalline Pt alloys represent the first typology: the nominal compositions were Pt_3Sc, Pt_3Y, Pt_5Y, Pt_3La, Pt_5Ce, Pt_5Sm, Pt_5Gd, Pt_5Tb, Pt_5Dy, Pt_5Tm, Pt_5Sr and Pt_5Ca. All these polycrystalline alloys (5 mm in diameter disks) were provided by Mateck GmbH, Germany. Their bulk structure was investigated by X-Ray Diffraction (XRD), their surface composition

was also regularly checked after sputter-cleaning by XPS. The second kind of sample consisted of size selected Pt-Y nanoparticles fabricated by a cluster source (see Section 2.5.2) and deposited onto a glassy carbon substrate. Examples of these two kinds of samples are also visible in Figure 2.2.

2.1.3 X-ray gun and monochromator

The X-ray gun apparatus (see Figure 2.1) is one of the main instruments equipped on the Theta-Probe chamber which is primarily dedicated to X-Ray Photoelectron Spectroscopy (XPS) measurements. The main component of the X-ray gun is a MXR1 electrostatic electron gun from Thermo Scientific. This is constituted of a resistively heated LaB_6 cathode combined with an extractor electrode to control the electron emission; an asymmetric electrostatic lens focuses the electron beam towards a water cooled Al anode. The AlKα (1486.7 eV) X-ray radiation produced by electron bombardment of the anode is monochromatized by a bent quartz crystal X-ray monochromator of Johan geometry bonded to a toroidal surface that provides point to point imaging of the X-rays onto the sample. Depending on the operation mode and supplied power, the X-ray beam spot size can be varied between 20 μm and 400 μm.

2.1.4 Ion gun

The Theta-Probe UHV chamber is equipped with a EX05 differentially pumped ion gun from Thermo Scientific (see Figure 2.1). It is suitable for use as an etching source in X-Ray Photoelectron Spectroscopy (XPS) or Auger Electron Spectroscopy (AES) depth profiles. It also allows Secondary Ion Mass Spectroscopy (SIMS) and Ion Scattering Spectroscopy (ISS) measurements. It can be operated in a number of different modes with typical ion energies between 0.5 keV and 4 keV and ion currents between few nA and few μA. The beam spot dimensions can be tuned by rastering over areas of different sizes (*i.e.* between 1 mm × 1 mm and 10 mm × 10 mm) depending on the application. For the ionization of high-purity noble gases three separated gas lines were installed during this project, respectively reserved to N60 purity He, Ne and Ar. In this work the ion gun was mainly used for two purposes: sputter-cleaning of polycrystalline Pt-based alloys and ISS measurements on different samples.

2.1.5 Hemispherical analyzer

The energy analysis of the Theta-Probe system is provided by a Theta hemispherical analyzer from Thermo Scientific equipped with a two-dimensional channelplate detector. It is a multi-channel detector with 112 energy channels and 96 angle channels allowing to acquire XPS spectra in a reduced amount of time and with

angular resolution. The total acceptance angle of the analyzer is 60°, between 20° and 80° from the normal to the surface of the sample. By distinguishing the XPS signals at various angles in this range Angle-Resolved X-Ray Photoelectron Spectroscopy (AR-XPS) measurements are possible. The energy resolution of the analyzer during XPS measurements is a function of the employed pass energy but also of the X-ray beam spot size and it will be discussed in the XPS Section 2.2.

2.2 X-ray photoelectron spectroscopy

X-ray photoelectron spectroscopy is one of the most popular and powerful spectroscopy techniques used in this thesis and in general in surface science. Indeed, by providing information on the elemental composition of a material as well as on the chemical state of the elements and on the surface structure it is one of the most complete surface sensitive techniques.

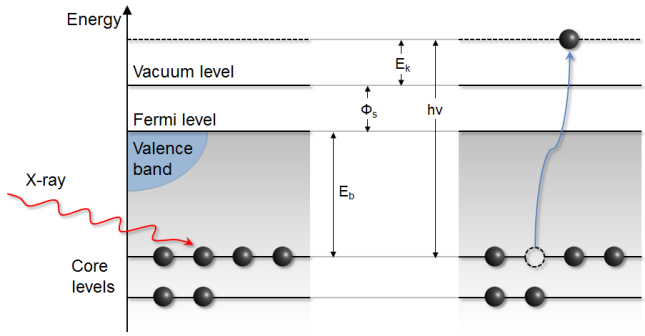

Figure 2.3: Illustrative representation of the photoelectric effect. An X-ray of energy $h\nu$ excite an electron with binding energy E_b. This is emitted with a kinetik energy E_k.

It relies on the Photoelectric effect that is the emission of an electron from an atom due to absorption of a photon. If the absorbed energy of the photon $h\nu$ is sufficient for the electron to overcome its binding energy E_b (*i.e.* its energy relative to the Fermi level of the material) and the work function of the material ϕ_s, electron emission can occur (see Figure 2.3). The kinetic energy E_k of the emitted electron is related to its initial binding energy which is characteristic of a certain element and of a certain chemical state. In XPS, the distribution of kinetic energies of the emitted electrons is measured, typically by a hemispherical analyzer; their binding energies are calculated from the equation:

$$E_k = h\nu - E_b - \phi_a, \tag{2.1}$$

where ϕ_a is the work function of the analyzer. From the binding energies it is possible to differentiate different elements and their chemical state. The surface

sensitivity of XPS is ensured by the strong interactions of the emitted electrons with the material itself, meaning that typical electron mean free paths λ are in the range of 5-20Å and only electrons emitted from atoms very close to the surface can be detected. In Angle-Resolved X-Ray Photoelectron Spectroscopy (AR-XPS) measurements, the energy distribution of the emitted electrons is measured as a function of the emission angle θ (calculated from the surface normal). Since the effective electron mean free path is a function of this emission angle, $\lambda_{eff} = \lambda \cos(\theta)$, the XPS signals collected at different angles will have different surface sensitivities: information on the surface structure and depth profiles can be extrapolated.

In the Theta-Probe XPS setup the photon source is monochromatized AlKα (1486.7 eV) X-ray radiation. The energy resolution was estimated from the Full Width at Half Maximum (FWHM) of the Ag $3d_{5/2}$ peak on a sputter-cleaned Ag foil. A maximum energy resolution below 0.5 eV was achieved using an X-ray beam spot size of 50 µm and a pass energy of the analyzer of 25 eV. However, unless differently specified the spectra of this thesis were acquired with beam spot size of 400 µm at a pass energy of 100 eV: this gave an energy resolution slightly better than 1 eV. By separating the intensity of the emitted electrons at different emission angles, the analyzer allows AR-XPS measurements. These were taken in parallel, without tilting the sample, from 16 different channels covering all the acceptance angles of the analyzer (*i.e.* from 20° to 80° from the surface normal).

2.2.1 Quantification of XPS

Since the analysis and quantification of XPS measurements represent a substantial part of this thesis, this section provides further details about the employed methods. While most of the commonly used softwares for the analysis of XPS data can provide an almost immediate quantification of the elemental species of a sample, such an immediate quantification will often lead to wrong interpretations. Therefore, any kind of XPS quantification requires a good knowledge of the principles of this technique and of the involved physical assumptions; this will also allow, depending on the different cases and samples, to choose the best method and achieve the most meaningful quantification.

In the typical Straight-Line Approximation (SLA) [15, 104, 105], the photoelectrons travel along straight trajectories until they are either emitted from a sample, or scattered. The total number of photoelectrons detected per second from a chosen orbital of an element A is given by the equation :

$$I_A = \sigma_A(h\nu)\, T\left(E_A\right) \Phi \int_z N_A(z)\, e^{\frac{-z}{\lambda\left(E_A\right)\cos(\theta)}}\, dz, \tag{2.2}$$

where σ_A is the photoelectric cross section for this particular transition at the excitation energy $h\nu$, T is the efficiency of detection of the emitted photoelectrons

(transmission function) at a characteristic kinetic energy E_A, Φ is flux of photons impinging on the sample and N_A is the atomic concentration of the element A in the probed material, as a function of the depth z from the surface (under the assumption that this is not dependent on the in-plane coordinates x and y). The exponential accounts for the probability that an electron at depth z will be emitted. It should be noticed that equation 2.2 is based on the assumption that the X-ray beam spot on the surface is small enough to neglect the dependence on x and y and that the angular asymmetry of photoemission is also negligible. The problem can be further simplified by assuming that the sample is homogeneous:

$$I_A = \sigma_A(h\nu)\, T\left(E_A\right) \Phi N_A \lambda\left(E_A\right) \cos(\theta). \tag{2.3}$$

However, this is rarely the case as the surface composition will typically vary from the one of the bulk. In Chapter 4 a more general model for homogeneously thick layers will be introduced and applied to a real system. The idea of quantifying the atomic composition by XPS comes from the inversion of equation 2.3, allowing the determination of N_A:

$$N_A = \frac{I_A}{\sigma_A(h\nu)\, T\left(E_A\right) \Phi \lambda\left(E_A\right) \cos(\theta)}. \tag{2.4}$$

The first challenge here is to perform a proper measurement of the XPS intensity I_A, which requires a proper integration of the XPS signals corresponding to the chosen orbital of the element A. The crucial part of this procedure is the background subtraction, which is often somewhat arbitrary. Various background expressions of different levels of complexity have been reported in literature but no general agreement is found; for all the measurements of this thesis a Shirley-type background was chosen. The application of such background to the proper energy range is also crucial; in this work the same energy range was always consistently chosen for peaks corresponding to the same orbital.

Concerning the other factors of equation 2.4, only Φ and $\cos(\theta)$ are element independent. This means that, as long as the interest is to evaluate the *relative* atomic concentrations, these terms disappear; namely, the idea is to determine the atomic concentrations in percent with the formula:

$$N_A(\%) = \frac{N_A}{\sum_i N_i} = \frac{I_A/S_A}{\sum_i I_i/S_i}, \tag{2.5}$$

where i is an index accounting for all the present elements. S_A is the so called *sensitivity factor*: a parameter that should summarize the element dependent terms in the bottom of equation 2.4 and that could easily be tabulated. In equation 2.5 this was defined with the most obvious definition: $S_A = \sigma_A(h\nu)\, T\left(E_A\right) \lambda\left(E_A\right)$. However this choice is usually not practical because T also contains information about the particular setup and E_A depends on the particular excitation energy $h\nu$. De-

pending on the particular definition of S three different approaches to XPS quantification are described in the following paragraphs. It should be noticed that in equation 2.4, the cross section σ_A is the most important normalization factor as it varies strongly for different elements and orbitals. T and λ exhibit in general a lower variability, most of all if it is possible to compare XPS peaks with a similar kinetic energy E_A.

2.2.2 Sensitivity factors and quantification approaches

Before describing the three approaches, in equation 2.5 it is convenient to define a *normalized intensity* $\hat{I}_A = I_A/S_A$, so that the problem of XPS quantification now coincide with the determination of all the $\hat{I}_i$ for all the elements of a probed sample:

$$N_A(\%) = \frac{\hat{I}_A}{\sum_i \hat{I}_i}. \tag{2.6}$$

Method 1. Scofield sensitivity factors

In this first approach the sensitivity factor includes the minimum amount of information, namely it is equal to the simple cross section:

$$S_i = \sigma_i(h\nu). \tag{2.7}$$

Theoretical values for these cross sections for the different elemental orbitals and different excitation energies are easily accessible in literature, the most popular being those calculated by Scofield in the single-potential Hartree-Slater atomic model [106]. The normalized intensities will be:

$$\hat{I}_i = \frac{I_i}{S_i T\left(E_i\right) \lambda\left(E_i\right)}, \tag{2.8}$$

The other terms of equation 2.8 need to be determined individually; the transmission function T can usually be precisely measured on each particular XPS setup. The mean free path λ, instead, has to be estimated through semi-empirical formulas. In the last paragraph of this section (see Section 2.2.4) some examples of these formulas are discussed.

Once a proper choice of the mean free path is made, this first approach provides a quite simple quantification. The main limit consists in the accuracy of the theoretical cross sections since large discrepancies with experimental data have been reported in literature [107]. These differences are probably mainly ascribed to the experimental difficulties of choosing energy ranges and backgrounds effectively corresponding to the calculated cross sections. The need of overcoming these limits leads to the other two approaches discussed in the following paragraphs.

Method 2. Measured sensitivity factors

This second approach is diametrically opposed to the first one, meaning that the sensitivity factors are determined experimentally (typically on each individual XPS setup) and they include the maximum possible information. Namely, they are determined by acquiring an XPS spectrum of a clean reference material, for instance a clean foil of a single element, and by determining the intensity I_i of a certain orbital. Referring to equation 2.3, S_i will therefore be equal to:

$$S_i = I_i^0 = \sigma_i(h\nu)\, T\left(E_i\right) \Phi N_i^0 \lambda^0\left(E_i\right) \cos(\theta). \tag{2.9}$$

It should be noticed that the superscript 0 specifies that a reference material is probed: N_i^0 now identifies the well known atomic density for the pure element i and λ^0 is the electron mean free path in such pure element. With this definition the normalized intensities can be calculated as:

$$\hat{I}_i = \frac{I_i}{S_i}\left(N_i^0 \frac{\lambda^0\left(E_i\right)}{\lambda\left(E_i\right)}\right). \tag{2.10}$$

The factor in parenthesis is basically a correction of the sensitivity factors. The reason why it appears is related to the fact that according to the definition of equation 2.9, the sensitivity factors contain information that is proper of the reference material. The atomic concentration N_i^0 has nothing to do with the probed material of unknown composition. The mean free path $\lambda^0\left(E_i\right)$ is also in principle different, because of the different properties of the material the electrons need to travel through. As an example, relevant for this thesis, it is quite intuitive that the mean free path of the electrons from the Y 3d XPS peak will be different if the electrons are traveling through an Y foil or a much more dense Pt-Y alloy. In the end of this section (see Section 2.2.4), some of the empirical expressions for the estimate of the mean free path will take into account these differences allowing to evaluate the terms in parenthesis of equation 2.10.

Although, if properly applied, this second method leads to the most precise XPS quantification [105, 108] it should be noticed that there are also various drawbacks. First, it requires careful measurements of the sensitivity factors that in some cases might be experimentally complicated. For instance, it might be difficult to perfectly clean the reference materials. It is also important that different sensitivity factors are measured in the same conditions, for instance with the same photon flux Φ, since this might typically vary after a certain amount of time. The remarkable advantage of this method is that both the cross section σ_i and the transmission function T are directly taken into account. Even more importantly, the huge difficulties of selecting the proper energy range and background are usually canceled by applying consistent choices for both the reference material and the probed sample.

Method 3. Wagner sensitivity factors

In this third approach the definition of sensitivity factor is somewhat intermediate with respect to the two previous choices. Namely it is defined as:

$$S_i = \sigma_i(h\nu)\, T^0\left(E_i\right) \lambda^0\left(E_i\right) \tag{2.11}$$

and these values have been tabulated by Wagner [109] by measuring on an extended group of reference materials. T^0 is now the transmission function of the XPS setup that was used during the collection of these XPS data. Compared to the reference materials mentioned in the previous method, these measurements were taken on powders, typically fluorides or carbonates. With this choice of sensitivity factors the normalized intensities become:

$$\hat{I}_i = \frac{I_i}{S_i}\left(\frac{T^0\left(E_i\right)\lambda^0\left(E_i\right)}{T\left(E_i\right)\lambda\left(E_i\right)}\right). \tag{2.12}$$

Also in this case the term in parenthesis is a correction of the sensitivity factor. It is due to the different mean free path $\lambda^0\left(E_i\right)$ of the electrons in the reference materials and to the different transmission function T^0. The semi-empirical formulas for the estimate of the mean free path (see Section 2.2.4) could in principle provide the first correction. However, the values provided by Wagner are an average obtained on different materials and the estimate of λ^0 would be difficult. In practice this first correction is usually neglected. The reason is that most of the reference materials in this case are powders with rather similar mass densities, so that the relative values of the sensitivity factors S_i should still hold. Focusing now on the transmission function correction, this is usually performed by assuming that $T^0 \propto E^{-1}$ which is a good approximation for the XPS system used by Wagner [109].

This method basically combines some of the advantages of the previous two approaches; the sensitivity factors are easily found in literature [109] with no need to obtain clean reference samples and to measure on them. At the same time the experimental nature of these values allow to directly take into account the experimental cross sections σ_i. Also a proper definition of energy ranges and backgrounds should be easier, even though a direct comparison with Wagner's spectra would be desirable. Main drawbacks are related to the presence of the mentioned correcting factors and to the fact that values for some elements are not available.

2.2.3 Application to Pt alloys

In this particular study XPS was generally used for quantifying the surface composition of Pt alloys, either in the polycrystalline form or as supported nanoparticles. This means that for each sample the most relevant XPS signals were the one of Pt (Pt 4f peak) and of the secondary component of the alloy, typically a rare earth. C

(C 1s peak) and O (O 1s peak) signals were usually present either as surface contaminations or as part of the support in the case of nanoparticles. To gain a general idea of the composition *method 1*, based on the tabulated Scofield cross sections was used, due to its simple and fast applicability.

However, the quantification of Pt to rare earth ratios in the alloys is particularly important for the characterization of these materials and other approaches have been in general preferred. *Method 2* probably leads to the most precise quantification and it was used, in particular, for all Pt-Y alloys (Chapters 5 and 6). Reference signals were measured on sputter-cleaned foils of Pt and Y. This method was not considered practical in the case of lanthanides, due to the large amount of materials tested and the difficulties in achieving perfectly clean foils of such reactive materials. Scofield cross sections often produced some discrepancies between the composition of sputter-cleaned polycrystals and their nominal composition. As discussed in more detail in Chapter 4 this is probably due to the difficulties of a proper background subtraction and of a proper choice of energy ranges. Indeed, the quite complex XPS structure of the lanthanide core levels and the appearance of numerous shake-up satellites complicate these operations. In general *method 3*, with the choice of experimental sensitivity factors, provided quite good agreement and it will be preferred in Chapter 3 for the quantification of the Pt to La and Pt to Ce ratios.

In Chapter 4 the composition of these polycrystalline alloys and their surface structure will be studied in particular detail. A model will be introduced in order to derive quantitative information about these structures from the XPS intensities. The comparison between these quantification methods will be addressed in more detail with a direct test of their applicability. Different interpretations to the observed discrepancies in composition with respect to the nominal stoichiometric ratios of the alloys will be presented and discussed.

2.2.4 Inelastic electron mean free path

All three quantification methods described in the previous section involved at least an estimate of the inelastic electron mean free path λ for each present element. Hence the importance of determining as precise values as possible: as in the case of sensitivity factors, the relative values are more important than the absolute ones as they will finally determine the relative concentrations. It is well known that λ is a function of the electron kinetic energy which is typical of each XPS peak, once the photon energy is fixed. However, it is quite intuitive that electrons at the same kinetic energy traveling through different materials might also be differently scattered. In particular, these so-called *matrix effects* can be very significant if the materials have very different mass densities. Unfortunately, this means that the best estimate of λ, and therefore the best XPS quantification, can be only achieved when some of the properties of the probed material are known in advance, which

is often not the case.

A first possibility for the quantification of λ would be to directly choose experimentally measured values from literature. This approach has two main problems. The former is the scarce availability of large databases reporting the values for different elements measured under the same conditions. The latter is related to the low flexibility of this method: for instance, it does not allow to estimate the mean free path of the electrons from a certain XPS peak traveling through different materials. The difficulties of including such matrix effects strongly limits the applicability to the quantification methods described previously: most of all because the values reported in literature are typically measured on samples whose mass densities can be very different.

Another option is to define semi-empirical formulas based on different databases of experimental values, that can easily generalize the estimate to arbitrary energies and matrices. The simplest of these, defines λ as: $\lambda \propto E^{\alpha}$ where α is a numerical value typically chosen between 0.5 and 1.0 [110]. Although it does not provide numerical values of the mean free path, this expression might give sufficiently good estimates of the relative values for different XPS signals. It should be noticed that this formula makes sense in the case of a homogeneous sample; in this case the mass density will be the same for all photoemitted electrons and λ can be quite well considered as a pure function of the kinetic energy. More quantitative estimates are provided by the so called Tanuma-Powell-Penn (TPP-2M) formula [111] or by the one proposed by Cumpson and Seah [112]. These expressions also take into considerations some of the properties of the matrix and the mass density in particular. The TPP-2M and the Cumpson-Seah formulas will assume particular importance in Chapter 4, where the case of inhomogeneous samples will be considered. In the rest of this thesis, for general quantification purposes, the relative concentrations have been achieved by simply assuming $\lambda \propto E^{0.6}$ (0.6 is the standard value used in Thermo Avantage and Eclipse data systems).

2.2.5 Angle resolved XPS depth profiles

The quantification of the AR-XPS measurements was carried out by applying the same principles described in the previous sections for each individual emission angle. In brief, detailed XPS spectra of all relevant elements were acquired at 16 different emission angles between 20° to 80° from the surface normal; Shirley type backgrounds were subtracted in order to quantify their intensities. These were normalized according to one of the three methods described in 2.2.2. Once the relative concentration of each element was determined as function of the emission angle, the depth profiles were calculated using the simulation tool ARProcess (Thermo Avantage software), which uses a maximum entropy method combined with a genetic algorithm. Relative concentrations at emission angles higher than 65° were omitted in order to reduce the influence of diffraction effects and elastic scattering.

The electron mean free path was approximated by the TPP-2M formula.

It should be noticed that the fitting procedure requires some assumptions about the substrate composition and the density and conductance of the overlayers. The composition of the substrate in particular was assumed to be equal to the nominal bulk composition of the alloy, which in general was in quite good agreement with the composition measured by XPS on the sputter-cleaned alloys. Because of these assumptions the depth-profiles should be mainly considered as qualitative. A more quantitative approach to the definition of the surface structure from the AR-XPS measurement will be discussed in Chapter 4.

2.3 Sputter-cleaning procedure

Prior to any electrochemical measurement the surface of the polycrystalline samples was cleaned by sputtering; mild sputtering conditions were preferred in order not to excessively roughen the surface. The ion energy was set to 0.5 keV with a current of 1μA Ar^+ ions; a rastering area of 7 mm × 7 mm was typically chosen in order to homogeneously clean the samples. In order to better understand the results on these polycrystalline samples a rough estimate of the sputtered thickness at the mentioned conditions is given by:

$$d_{sput.} = \frac{I_i Y M}{eA\rho N_a} t_s, \tag{2.13}$$

where I_i is the ion current, Y is the sputter yield, M is the molar mass, e is the electron charge, A is the area of the beam spot, ρ is the mass density, N_a is the Avogadro number and t_s is the total sputtering time. For pure Pt, a sputter yield of $Y = 1.8$ [113] and a typical sputtering time of 20 min, the thickness of the sputtered region is of the order of $d_{sput.} = 3.2$nm. This treatment was usually sufficient to clean the surface from C and O adventitious contamination without inducing a roughening of the surface that could affect the electrochemical measurements (see Section 3.2.2).

2.4 Ion scattering spectroscopy

Ion Scattering Spectroscopy (ISS), also known as Low Energy Ion Spectroscopy (LEIS), is a physical high vacuum technique relying on the elastic scattering of ions over the surface of a sample. An ion gun is typically used to ionize a gas and accelerate the ions; after collision with the atoms of the probed material the kinetic energy of the scattered ions is measured, for instance by a hemispherical analyzer, allowing the identification of the surface atoms. The main advantage of this method compared to other surface science techniques is the extreme surface sensitivity,

which even allows to probe a single atomic layer of the surface. This is due to the very strong interactions of the ions with the surface atoms (scattering cross section $\approx 1\text{Å}^2$); the neutralization probability is also close to unity, meaning that the few ions penetrating into the material or undergoing multiple scattering events usually won't survive the collision as ions and therefore they won't be detected.

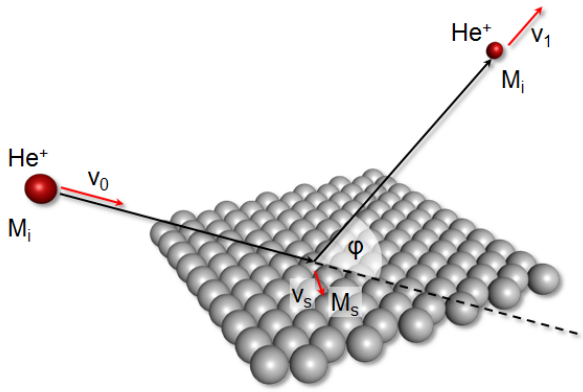

Figure 2.4: Illustrative representation of the ISS principle. An ion (*e.g.* He^+) of initial velocity $\vec{v}_0$ is scattered on the surface and loses kinetic energy depending on the mass of the probed atom, finally leaving with a final velocity $\vec{v}_1$.

Figure 2.4 illustrates the principle of ISS. The elastic scattering events between the probing ions and the probed atoms can be described by the equations of momentum and energy conservation [105]:

$$M_i\vec{v}_0 = M_i\vec{v}_1 + M_s\vec{v}_s \tag{2.14}$$

$$\frac{1}{2}M_i v_0^2 = \frac{1}{2}M_i v_1^2 + \frac{1}{2}M_s v_s^2, \tag{2.15}$$

where M_i is the mass of the ion and M_s is the mass of the surface atom. $\vec{v}_0$, $\vec{v}_1$ and $\vec{v}_s$ are respectively the initial velocity of the ion, the final velocity of the ion and the final velocity of the surface atom. By combining these equations it is possible to derive the following relationship:

$$\frac{E_1}{E_0} = \left(\frac{\sqrt{M_s^2 - M_i^2 \sin^2(\varphi)} + M_i \cos(\varphi)}{M_s + M_i} \right)^2, \tag{2.16}$$

where φ is the scattering angle defined as the angle between the incoming ion (ion beam from the ion gun) and the scattered ion (energy analyzer). Given an ion with a known mass M_i and initial energy E_0, equation 2.16 allows to derive the unknown mass of the surface ion M_s from the measured energy of the scattered ion

E_1.

The choice of the gas and of the accelerating potential is essential for a proper characterization. Generally, noble gases (*e.g.* He, Ne, Ar) are chosen in order to avoid reactions with the probed atoms. Ion energies of a few hundreds eV up to a few keV, are typically used. The choice of heavier ions and higher kinetic energies helps to increase the resolution of the measurement and distinguish masses that are closer to each other. However, these choices also result in a faster damaging of the surface due to sputtering. If this removal of surface atoms is sufficiently fast, the probed masses will also originate from the sub-surface layers and the surface sensitivity of the measurement might be lowered. Therefore, depending on the application, a precise compromise of these parameters might be necessary.

For the experiments of this study, unless differently stated, ISS spectra were acquired with He^+ ions at 1 keV energy. The beam was generally rastered over a sample area of approximately 2 mm × 2 mm. Ne^+ or Ar^+ ions at the same energy were occasionally used to distinguish the ISS peaks of Pt and some of the rare earths (ex. Ce). In these cases a particular optimization of the setup was necessary in order to minimize the destructive effects induced by ion sputtering: in particular the ion beam was rastered over a larger sample area, 4 mm × 4 mm. Further details will be given in the correspondent sections. Typical residual pressures of the noble gases were between 3×10^{-9}mbar and 1×10^{-8}mbar, resulting in ion currents between 10nA and 60nA. The scattering angle was 125° and the incidence angle of the ion beam was 45°.

2.5 Other setups and methods

The Theta-Probe setup has been primarily employed in the physical characterization by XPS and ISS of the materials presented in this thesis. This was the primary focus of this project, together with the development of a new experimental setup that will be introduced in Chapter 6. The preparation of the alloyed nanoparticles, the electrochemical measurements and the application of some other techniques such as X-Ray Diffraction (XRD), Transmission Electron Microscopy (TEM) and Extended X-ray Absorption Fine Structure (EXAFS) were not a direct part of this Ph.D. project and, in general, they have been performed by other researchers of our group. Their role in these measurements will be specified in the corresponding figures of this thesis. Due to their importance, the experimental setups and methods for the electrochemical measurements and for the deposition of the Pt-Y nanoparticles will be briefly described in this section. Concerning the other techniques, further details are available in the publications attached in the end of this thesis as it will be indicated in the correspondent sections.

2.5.1 Electrochemical experiments

The electrochemical measurements were taken in the electrochemical cell of Figure 2.5, or analogous one. A standard two-compartment glass cell with the typical three electrode configuration was used. The cell was furnished with a water jacket attached to a hot water bath to control the temperature: all reported electrochemical measurements were preformed at 23 °C. The experiments were carried out with a VMP2 potentiostat (Bio-Logic Instruments), controlled by a computer. All glassware was cleaned for 24 h in a "piranha" solution consisting of a 3 to 1 mixture of 96% H_2SO_4 and 30% H_2O_2, followed by multiple cycles of heating and rinsing with ultrapure water (Millipore Milli-Q, 18.2 MΩ cm^{-1}) to remove residual sulphates. For all measurements the electrolyte consisted of a 0.1 M $HClO_4$ (Merck Suprapur) electrolyte also prepared with ultrapure water. The working electrode was mounted on a rotating ring-disk electrode (RRDE) assembly provided by Pine Instruments Corporation. A Pt wire was used as counter electrode while the reference electrode was a Hg/Hg_2SO_4 electrode, separated from the working electrode compartment using ceramic frits. All potentials of this thesis are referred to the reversible hydrogen electrode (RHE) and are corrected for ohmic losses. After each experiment, the potential of the reference electrode was calibrated with respect to 0 V *vs.* RHE, by carrying out the hydrogen oxidation and hydrogen evolution reactions on Pt.

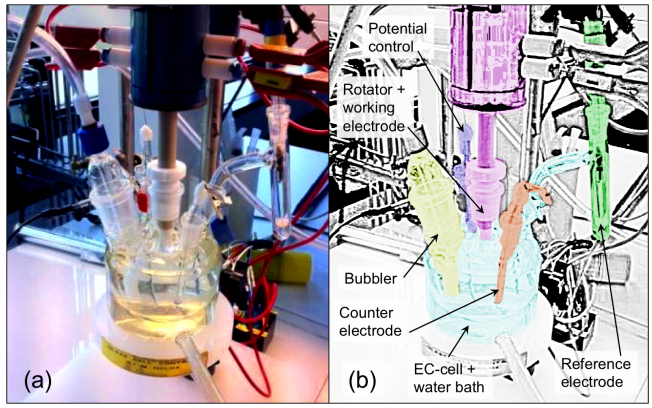

Figure 2.5: Photograph of the RRDE setup employed for most of the electrochemical measurements of this thesis (a) and correspondent schematic representation with indications of the main components (b).

All the tested electrodes, once mounted into the arbor of a RRDE, were immersed into the electrochemical cell under potential control of 0.1 V *vs.* RHE into a N_2 (N5, Air Products) saturated electrolyte. The electrodes were cycled between 0.05 V and 1.00 V at 1600 rpm and a sweep rate of 50 mV s^{-1} until stable cyclic voltammograms (CVs) were obtained: typically within 100-200 cycles. After acqui-

sition of these stable CVs, the Oxygen Reduction Reaction (ORR) activity measurements were conducted by taking CVs in an electrolyte saturated with O_2 (N55, Air Products). The kinetic current densities j_k (*i.e.* the current densities in absence of any mass-transfer effects) were determined from the equation:

$$\frac{1}{j} = \frac{1}{j_d} + \frac{1}{j_k}, \tag{2.17}$$

where j is the total measured current density and j_d is the diffusion limited current density. In order to give a general definition of *ORR activity* and facilitate the comparison between different catalysts, the kinetic current density at 0.9 V *vs.* RHE, measured under the mentioned conditions, was chosen. It should be noticed that a proper comparison requires that these currents are normalized by the Electrochemically Active Surface Area (ECSA). Once this normalization is performed the term *specific activity* will be generally used. In the case of nanoparticles (see Chapter 5) the kinetic currents will be alternatively normalized by the total Pt mass in the catalyst, providing a more valuable comparison between different catalysts: the term *mass activity* will be used in this case. As a graphic comparison of the catalytic activities, the logarithm of the kinetic current will be sometimes plotted against the RHE potential in the so called Tafel plot.

Stability tests

In order to test the long-term electrochemical stability of the catalysts of this thesis, an accelerated stability test based on potential cycling was chosen. This typically consisted of potential cycles between 0.6 and 1.0 V *vs.* RHE in an O_2-saturated 0.1 M $HClO_4$ electrolyte at 100 mV s^{-1} and 23 °C. This choice was based on the protocols of the U.S. Department of Energy [114] and of the Fuel Cell Commercialization Conference of Japan [115]. 10 000 cycles have been chosen for testing of the polycrystalline alloys while 9 000 cycles were chosen in the case of nanoparticles: corresponding to about 24 hours of experiment. Before and after these cycles CVs were taken at 50 mV s^{-1} in order to measure and compare the ORR activities.

Electrochemically active surface area

A proper comparison of the ORR activities can only be performed with a proper determination of the specific activities (*i.e.* a proper estimate of the electrochemically active surface area). Various methods have been described in literature for achieving a good estimate of the electrochemically active surface area on surfaces of Pt and Pt alloys. Hereby we mention three of them: the Hydrogen underpotential deposition method, the CO-stripping method and the Cu underpotential deposition method. These methods are of course essential when comparing the activity of high surface area electrocatalysts, whose areas are originally unknown, as in the case of

nanoparticles in Chapter 5. It should be noticed that all these methods rely on approximations; therefore they don't necessarily give equivalent results and they are not necessarily the best choice in the case of extended surfaces. Hence a few comments are advisable.

The three methods rely on the adsorption of different species on the active sites of an electrode and on the total desorption of these species from the surface while raising the applied potential [75, 116]. In the case of hydrogen the number of active sites is calculated by integrating the adsorption-desorption charge of an adsorbed layer in the so-called hydrogen underpotential deposition (H_{upd}) region. The CO-stripping involves the adsorption of a monolayer of CO and the measurement of its potentiodynamic (or chronoamperometric) oxidation charge. The third method relies on the under-potential deposition of a layer of Cu (Cu_{upd}) and its oxidation to Cu^{2+}. In all cases the measured adsorption-desorption charges are expected to be proportional to the number of active sites and therefore to the ECSA. All these methods can give satisfactory results for establishing the active surface area of Pt catalysts. The H_{upd} is probably the most common choice as it can be directly derived from the stable CVs. When the CO oxidation reaction is studied, CO-stripping is also often performed as a further estimate of the ECSA. However, it is well known that the saturation coverages of H and CO might vary depending on the chemical properties of a surface; for instance they are highly dependent on the exposed Pt facets. For the same reason the saturation coverages might strongly differ in the case of Pt alloys whose surface chemistry is different from pure Pt [73, 117–119].

2.5.2 Deposition of Pt-Y nanoparticles

Although a good part of this thesis presents fundamental studies on new materials for the ORR, mainly performed on extended surfaces, Chapters 5 and 6 will focus on Pt-Y alloys in the more technologically relevant form of nanoparticles. These were fabricated in a cluster source under UHV conditions as described in this section. The preparation relies on a magnetron sputter gas aggregation source (Birmingham Instruments Inc.), combined with time-of-flight mass filtering. The gas aggregation method consists in the Ar^+ sputtering of an Pt-Y alloy target to produce an atomic vapor that is subsequently condensed into nanoparticles through collissions with a liquid nitrogen cooled Ar and He gas. For the particles of this work the alloy target was purchased from Kurt J. Lesker Inc. with nominal composition of Pt_9Y. Compared to chemical or electrochemical methods this technique has the advantage of forming the particles under UHV conditions where the oxygen pressure is negligible. Indeed, the high reactivity and oxophilicity of Y (or any other rare earth) and the very negative standard reduction potentials are the main challenges for a chemical-electrochemical synthesis. At the same time the particles produced through this gas aggregation technique are generally ionized, allowing the mass selection through a time-of-flight filter selecting the desired mass to charge ratio.

Narrow size distributions can be achieved, typically within a 20% of relative uncertainty for average particle diameters between 1 nm and 10 nm. Once the particles have been formed and mass-selected, they are directed towards a planar glassy carbon support in a separate UHV chamber (Omicron, Multiscan Lab) with a base pressure of 1×10^{-10} mbar. The acceleration of the nanoparticles occurs through a system of Einzel lenses that allows to control the position and width of the particle beam and therefore the density of nanoparticles on the support. In combination with the mass filter a measurement of the nanoparticle beam current provides an estimate of the amount of catalyst deposited onto the glassy carbon: a quantity needed for defining the mass activity. At the same time a Maxtek Inc. quartz crystal monitor is used in parallel for estimating the deposition rate. These two indipendent measurements typically agreed within 10 %. This Omicron chamber is also equipped with various UHV techniques as XPS, ISS and Scanning Electron Microscopy (SEM) for a first characterization of the as-deposited nanoparticles.

CHAPTER 3

Pt-La and Pt-Ce alloys: the active chemical phase

3.1 Introduction

On the wake of the results achieved for the Pt-Y and Pt-Sc systems, alloys of Pt and lanthanide metals were also considered as potentially promising ORR catalysts. Some of their intermetallic compounds, such as Pt_5La, Pt_5Ce and Pt_5Gd, also exhibit very negative heats of alloy formation, as shown in Figure 3.1. The experimental values found in literature approach the exceptionally negative value of Pt_3Y ($\Delta H \approx$ -4 eV). They could potentially be more stable than alloys of Pt and late transition metals whose alloying energies, also reported for comparison, are much less negative ($\Delta H \approx$ -0.5 eV). We note that despite their denomination as "rare earths", good part of these elements, and in particular La and Ce, are much more inexpensive and much more abundant than Pt [5]. This chapter focuses on Pt-La and Pt-Ce alloys: indeed, Pt_5La was the first material of this kind to be tested and characterized [6]. In general, Pt-La and Pt-Ce alloys exhibit very similar properties and for the peculiar structure of their 3d core level XPS spectra, they represent a very good case study in order to identify the active chemical state of these catalysts. This turned out to be a controversial issue after the recent work of Kim and co-workers who also focused on alloys of Pt and early transition metals [96, 97] and more recently on alloys of Pt and lanthanides [99].

The ORR activity of their Pt_3La catalyst is similar to the one we measured on Pt_5La [6]. However some of their experimental evidences and particularly the

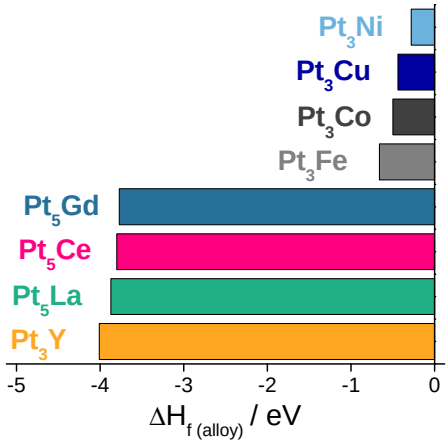

Figure 3.1: Experimental enthalpies of alloy formation specified per formula unit. The values for the different alloys are respectively taken from: Pt_3Ni [120], Pt_3Cu [121], Pt_3Co [122], Pt_3Fe [122], Pt_5Gd [123], Pt_5Ce [123, 124], Pt_5La [123, 124] and Pt_3Y [123].

interpretation of this high activity are quite different. By performing AR-XPS measurements, they claim that the surface structure and composition of Pt_3La is unaltered before and after electrochemical measurements. On the basis of their DFT calculations, they also suggest that, in vacuum, La atoms would spontaneously tend to segregate to the surface of the compound. In their view, the very negative alloying energy would be sufficient to make them *thermodynamically* stable during reaction, without any La oxidation or dissolution. As these conclusions differed considerably from our own, we decided to revisit the issues of the active chemical state and surface structure of Pt-La alloys. This discussion takes part in a broader debate about the possible stabilization of the more reactive metals on the surface of Pt and Pd alloys, including some more widely studied systems as the Pt-Ni and Pt-Co alloys [37, 51, 118, 125]. If possible, this notion would be of fundamental interest, as the higher activity of these materials could be also explained by bifunctional effects; meaning that both metals would provide active sites during ORR, with the more reactive atoms facilitating the O_2 dissociation or the removal of OH radicals from the more noble Pt sites [49, 50].

Due to the similar chemical properties of the lanthanides, most of the considerations of this chapter will then be extended to Chapter 4 where other alloys of Pt and lanthanides will be introduced; the observed trends in activity and stability will help us to answer other fundamental questions about the origin of the activity enhancement and the mechanism of long-term deactivation. The content of this chapter is based on the results of Paper 3 in the end of this thesis [126]. The

electrochemical experiments have been performed by María Escudero-Escribano as indicated in the corresponding figures.

3.1.1 Initial characterization and sample preparation

All the reported measurements have been carried out on three polycrystalline samples with nominal stoichiometry: Pt_5La, Pt_5Ce and Pt_3La. Their bulk structure was investigated by XRD: details of the measurements and of the experimental apparatus can be found in [126] (Paper 3 in the end of this thesis). For Pt_5La and Pt_5Ce no closed-packed structure exist as it will be further discussed in Chapter 4. They exhibit a hexagonal structure of the Cu_5Ca-type, with the space group P6/mmm. Their lattice parameters were found to be: $a = b = (0.5378 \pm 0.0005)$ nm, $c = (0.4187 \pm 0.0008)$ nm for Pt_5Ce, and $a = b = (0.5393 \pm 0.0003)$ nm, $c = (0.4381 \pm 0.0004)$ nm for Pt_5La, in good agreement with the literature values [127]. Concerning the sample with nominal composition of Pt_3La, two different crystal structures were identified: Pt_2La and Pt_5La. This is consistent with the previously reported phase diagrams of Pt-La alloys, where no stable Pt_3La phase exists [128, 129].

The surface composition of the polycrystals was regularly checked by XPS. In particular, XPS measurements were taken before all electrochemical measurements to ensure that the Pt to La and Pt to Ce ratios were reproducible and no change in the overall surface composition occurred. In order to do that the polycrystalline samples were sputter-cleaned under UHV conditions as described in the Section 2.3. In brief, an ion beam consisting of Ar ions at 0.5 keV was rastered over an area of 7×7 mm^2. Typically, 20 minutes of such cleaning procedure allowed to reduce the total amount of C and O contaminations below 5%. After this cleaning procedure the Pt to lanthanide ratios were estimated from the Pt 4f, La 3d and Ce 3d XPS peaks: 4.9 ± 0.4 for Pt_5La, 4.8 ± 0.1 for Pt_5Ce and 3.2 ± 0.2 for Pt_3La. The presence of these residual contaminations is mainly due to the extremely high reactivity of La, Ce and of the other rare earths in general. This means that the sticking coefficient of molecules like O_2 or CO will likely be close to unity [130], and even at such low pressures, relevant C and O signals might arise during the time needed for XPS characterization (typically about one hour). The small variations of the Pt to lanthanide ratios for different experiments might also be related to this partial oxidation of the lanthanides, as it could induce a rearrangement of the surface atoms (*e.g.* surface segregation). In order to avoid this uncertainty the ratios reported in the rest of this chapter for sputter-cleaned samples were measured while continuing the sputter cleaning. This allowed to maintain the C and O contaminations below 1%.

3.2 Electrochemical characterization

After the cleaning procedure, the polycrystals were readily transferred to the RRDE apparatus. (details of the transfer procedure and about the electrochemical measurements can be found in Section 2.5.1 and [126] (Paper 3 in the end of this thesis). After mounting the polycrystalline alloys were immersed into a N_2 saturated 0.1 M $HClO_4$ electrolyte and cycled between 0.05 V and 1.00 V until stable CVs were obtained, typically 100-150 cycles. This procedure is required in order to clean the surface from the impurities accumulated during the transfer. At the same time, chemical and structural modifications of the surface might occur (*e.g.* dealloying), until a stable phase is reached.

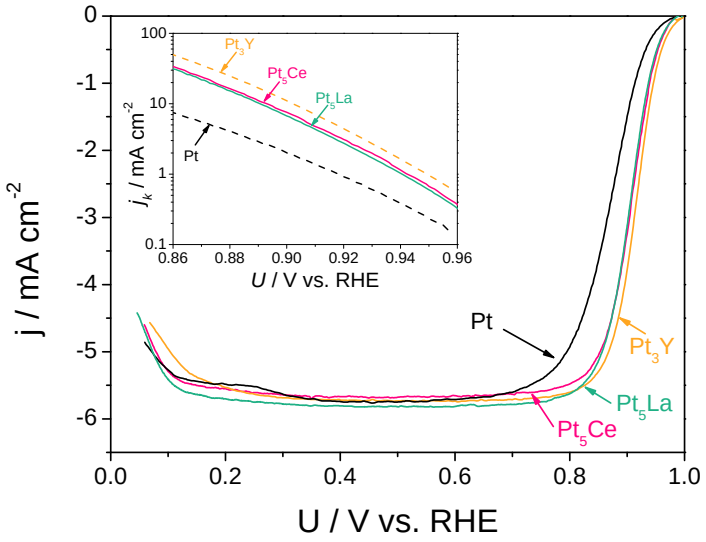

Figure 3.2: RRDE polarization curves at 1 600 rpm and 50 mV s^{-1} for the ORR on Pt_5La, Pt_5Ce and Pt polycrystalline electrodes in O_2-saturated 0.1 M $HClO_4$: in the inset, Tafel plot with the corresponding kinetic currents. Polarization curve and Tafel plot of Pt_3Y are also shown for comparison [16]. Measurements performed by María Escudero-Escribano.

Once stable CVs had been obtained the catalytic activity of the electrodes was tested in O_2-saturated 0.1 M $HClO_4$. Figure 3.2 shows the polarization curves of Pt_5La and Pt_5Ce in comparison with polycrystalline Pt and, in the inset, their Tafel plots. Data for Pt_3Y are also shown for comparison as this was the polycrystalline alloy with the highest ORR activity reported prior to this work. Pt_5La and Pt_5Ce exhibit a lower overpotential for the oxygen reduction than pure Pt. Their specific activities, defined as the kinetic current densities at 0.90 V *vs.* RHE, are (6.8 $\pm$ 0.3) mA cm^{-2} and (7.4 $\pm$ 0.4) mA cm^{-2}, respectively: meaning that the ORR

activity enhancements for Pt_5La and Pt_5Ce are 3.4 and 3.7. Alloys of Pt and late transition metals prepared under similar conditions (Pt_3Fe, Pt_3Co and Pt_3Ni) exhibited a considerably lower activity, with about a factor of 2 enhancement relative to polycrystalline Pt [37, 73]. It is important to specify that the measured activity of polycrystalline Pt is in agreement with the values recently proposed by reputable groups under the same conditions [44, 75, 116].

3.2.1 Stability test

Once stable CVs were obtained and the ORR activity was measured, accelerated stability tests were conducted in order to test the long-term durability of the samples. 10 000 consecutive cycles between 0.6 and 1.0 V *vs.* RHE in an O_2-saturated 0.1 M $HClO_4$ electrolyte at 100 mVs^{-1} were chosen as a standard stability test (see Section 2.5.1 for further details). Kinetic currents of Pt_5La and Pt_5Ce were measured before and after cycling; in both cases they experienced remarkably low losses: around 8% for Pt_5La and 10% for Pt_5Ce. This is a good evidence of the long-term electrochemical stability of these alloys. Figure 3.3 shows the ORR activity of Pt_5La and Pt_5Ce: the activity of pure polycrystalline Pt and of Pt_3Y is also plotted for comparison. Both activities before and after stability test are reported. Interestingly, after 10 000 cycles both alloys maintain a specific activity which is more than 3 times higher than for pure Pt.

Although a complete stability test should be carried out on large surface area catalysts and possibly in a fuel cell, the results on polycrystalline Pt_5La and Pt_5Ce are a good indication of the resistance to de-alloying, which is considered as the main cause of degradation for alloys of Pt and late transition metals [76]. Recently, Todoroki *et al.* studied the stability of Pt-enriched Ni/Pt(111) catalysts whose initial activity is 8 times higher than for pure Pt(111). After a stability test of only 1 000 cycles between 0.6 and 1.0 V *vs.* RHE in analogous conditions, they measured activity losses close to 75% [48]. State-of-the-art Pt-Co ORR catalysts also exhibited a substantial degradation under fuel-cell operating conditions, primarily due to de-alloying [76, 77]. The high electrochemical stability of Pt_5La and Pt_5Ce suggests them as promising materials for the cathode catalysts of PEMFCs. This motivates the interest towards the fabrication of large surface area catalysts based on these alloys and towards more extended stability tests under the technologically relevant conditions of a fuel cell. However, it should be anticipated that the chemical (or electrochemical) synthesis of Pt-La or Pt-Ce alloyed nanoparticles will be particularly challenging due to the high reactivity of the lanthanides and to the difficulties of reducing them to a metallic state.

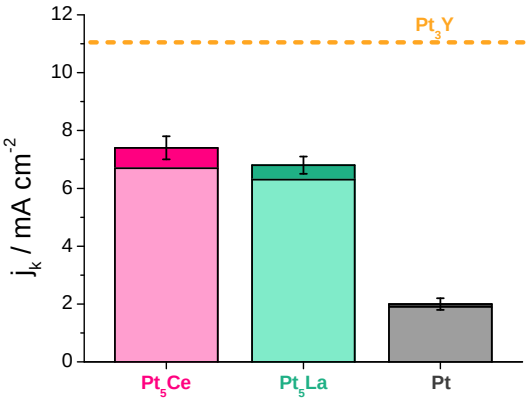

Figure 3.3: ORR activity expressed in terms of kinetic current density at 0.9 V *vs.* RHE for polycrystalline Pt_5La, Pt_5Ce and Pt. The activities are reported both before and after stability test consisting of 10 000 cycles between 0.6 and 1.0 V *vs.* RHE in an O_2-saturated 0.1 M $HClO_4$ electrolyte at 100 mV s^{-1}. The dotted line represents the ORR activity of polycrystalline Pt_3Y for comparison. Measurements performed by María Escudero-Escribano.

3.2.2 Electrochemically active surface area

It is important to mention that all the currents presented so far are normalized by the geometric surface area (0.196 cm^2) under the assumption that the surface of the polycrystals is smooth, with a roughness factor $\approx$ 1 cm^2 / cm^2. This might seem a rough approximation since the definition of specific activity often requires a measurement of the electrochemically active surface area (ECSA), particularly when a study aims at comparing specific activities of different materials. However, our choice of using the geometrical surface area is supported by a number of experimental evidences.

For both Pt_5La and Pt_5Ce, as well as for the other alloys of this work unless differently stated, the voltammetric currents and charges did not increase during successive measurements on the same surface; the CVs and in particular the double layer capacitance were also reproducible for successive experiments, suggesting that the sputter-cleaning procedure did not induce a continuous roughening of the surface. CO-stripping experiments were also performed. The integrated CO-stripping charges were $\approx$ 310 $\mu C\ cm^{-2}$ on Pt_5La and $\approx$ 300 $\mu C\ cm^{-2}$ on Pt_5Ce. These values are similar to those measured on other Pt-alloys [118, 119] and lower than that measured on polycrystalline Pt $\approx$ 360 $\mu C\ cm^{-2}$, in good agreement with literature values [119]. The lower CO-stripping charge could be explained by a weaker binding of CO to the Pt surface of the alloys; a reduced CO bind-

ing energy was already shown for other Pt-alloys with a Pt overlayer [100, 119], and in particular for the Cu/Pt(111) near surface alloys, both prepared in electrochemical [118] and in UHV environment [131]. On the basis of these lower CO-stripping charges we considered the geometric surface area to be a more reliable and more conservative estimate of the microscopic surface area; a normalization to the CO-stripping charge could introduce further uncertainty in the comparison of the specific activities and would not be consistent with our recent publications [6, 16, 98, 100, 126, 132].

It should be also noted that, in general, the H_{upd} method did not provide reliable measurements of the ECSA on these polycrystalline alloys. This was due to the observation of H absorption in the bulk of some alloys (*e.g.* Pt_5Ce). Further details about the CO stripping experiments and about the evidences of H absorption on Pt_5Ce can be found in [126] (Paper 3 in the end of this thesis).

3.3 X-ray photoelectron spectroscopy

The catalytic surfaces of Pt_5La, Pt_5Ce and Pt_3La were systematically studied by AR-XPS in order to follow all the modifications of chemical state and surface structure. Such measurements were carefully repeated during the sputter-cleaning procedure, in order to characterize the samples *as-prepared*. Subsequently the same measurements were repeated *after air-exposure* in order to verify their stability in presence of oxygen, *after ORR* activity test to verify the stability in electrochemical environment and *after stability* test to verify their long-term stability during potential cycling.

The XPS features of the core level spectra of the lanthanide metals are in general quite complex. In the case of La and Ce atoms some of these characteristic features are similar, allowing a common description. Due to the presence of localized electrons in the 5d or 4f shells, distinctive shake-up satellites arise in the 3d region of their spectra. Since their relative intensity and energy position is highly dependent on the chemical state, these satellites provide useful information on the oxidation state and can be used as a diagnostic tool [133]. The origin of the satellites and the explanation of their behaviour has been discussed in various studies: among these the Schönhammer-Gunnarsson treatment provides a general good description of the system [134]. The initial state of La and Ce atoms and their final state, excited by photoelectron emission, cannot be described with a single electron approximation and a many-body description is needed. Each state is given by the linear combination of different f_n states, where n represents the electron occupancy of the 4f shell. Since the level of occupancy n of these valence orbitals will drastically change the level of screening of the core-hole and, consequently, the measured energy position of the 3d peaks, different n values will correspond to different f_n satellites. A higher number of electrons in the 4f shell (higher n) better screens the photo-emitted electron from the core hole, resulting in a higher

kinetic energy. Concerning the different chemical states, these will be characterized by different coefficients in the linear combination and, therefore, different relative intensities of the f_n satellites.

All the La 3d and Ce 3d spectra of this chapter (Figure 3.4 and 3.10) were fitted according to the same assignment of the f_n satellites reported before [135–137]. A complete summary of the peaks energy positions and relative intensities can be found in Appendix A. If we consider a La atom in its elemental state (valence electron configuration 5d16s2) the 4f shell is empty, meaning that the predominant f_n component of the ground state will be the one with $n = 0$. For Ce (valence electron configuration 4f15d16s2) it will be the one with $n = 1$. From here on the corresponding peaks (f_0 for La and f_1 for Ce) will be defined as *main peaks* and denoted as f_N. Notably, these turn out to be the most intense components of the metallic state and of intermetallic compounds: smaller satellites correspond to the f_1 state in the case of La to the f_0 and f_2 states in the case of Ce [135]. The charge transfer occurring during oxidation shifts the position of all these states to higher binding energies, in the same way as for most metals. At the same time it results in a strong intensification of the f_1 satellite for La, and of the f_0 and f_2 satellites for Ce providing a clear diagnostic tool [130, 133, 137].

Figure 3.4 a,b shows the XPS signals of the La 3d and Ce 3d core level regions acquired during sputtering of Pt_5La and Pt_5Ce respectively (*i.e. as-prepared* samples). When compared to the spectra found in literature the shape of the 3d peaks is metallic. The main f_N peaks are the most intense as expected, although rather intense f_{N+1} satellites are clearly distinguished at lower binding energies. It is well known that these f_{N+1} components are strengthened in intermetallic compounds compared to La or Ce in their pure phases; indeed the spectra of Figure 3.4 a,b are very similar to those reported for similar compounds as Pd_3La, Ni_5La, Pd_5Ce, Pd_5Ce and Ni_5Ce [135, 138–140].

The spectra of Figure 3.4 c,d were acquired *after air-exposure* of the samples for one hour. Compared to Figure 3.4 a,b the La 3d and Ce 3d peaks have undergone serious modifications. These spectra demonstrate that, at least after the sputter-cleaning procedure, the chemical state of La and Ce cannot be maintained in presence of O_2. This is understood in terms of the high reactivity and oxophilicity of lanthanide metals. The fit of figures 3.4 c,d provides further information; a new set of f_n peaks overlaps to the metallic phases observed during sputter-cleaning which are still present. These new peaks are all shifted towards higher binding energies as expected from an oxidized phase; the relative intensity of the f_n components varies in favor of the f_{N+1} and f_{N-1} satellites that might even become more intense than the main peaks. All these evidences are typical of La and Ce oxides with close resemblance to literature spectra [137, 141]. Since analogous but less pronounced effects were also observed after exposure to air for shorter times, and even in UHV after sufficiently long waiting times, we should expect that the surfaces of these catalysts are always partially oxidized before electrochemical measurements; even if protected by a drop of Milli-Q water. It should be noted that

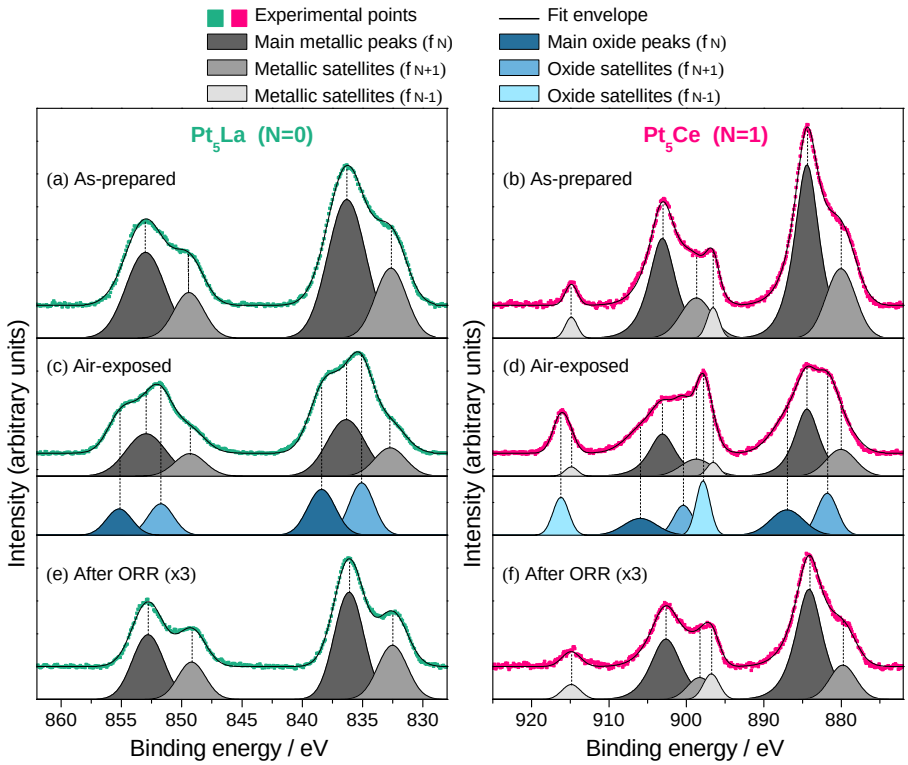

Figure 3.4: La 3d (left) and Ce 3d (right) XPS spectra of Pt_5La and Pt_5Ce respectively after background subtraction, at an average emission angle of 45°. The spectra were acquired in three different sample conditions: *as-prepared* (*i.e.* during sputter-cleaning) (a,b), *air-exposed* (c,d) and *after ORR* testing (e,f). The measurements after electrochemical measurements were magnified three times due to the lower signal intensity. The fitted spectra of the metallic peaks (grey) and of the oxidized peaks (blue) appear under the experimental points. Detailed information about the peak positions and relative intensities are found in Table A.1.

while La has only one stable oxide phase (*i.e.* La_2O_3), the fit of the Ce oxide phase is complicated by the possible coexistence of trivalent Ce from Ce_2O_3 and tetravalent Ce from CeO_2 overlapping to the metallic peaks. However, the strong intensification of the f_0 components, which are absent for trivalent Ce [137, 142], suggests CeO_2 as the main oxide phase. For simplicity, only the CeO_2 phase was considered in the fit of Figure 3.4 d; this allowed to achieve a set of f_n peaks whose position and intensity resembles the one of other reported fits for CeO_2 [136, 137]. A comprehensive description and quantification of the oxide components is hampered by the possible presence of sub-oxides and beyond the interest of this study.

The XPS spectra acquired *after ORR* activity tests are shown in Figure 3.4 e,f. On the basis of the previous considerations, it can easily be concluded that they represent La and Ce in a completely metallic state: the spectra are very similar to those measured during sputtering. The absence of any oxide phase indicates that La and Ce oxides are all unstable under ORR conditions and that they dissolve in the acidic electrolyte. It is worth noting that, according to the measurements after air-exposure, this metallic phases could not be conserved if the lanthanides were directly exposed to oxygen during the transfer from the electrochemical cell to the XPS setup. Some kind of protective layer must prevent the lanthanides from oxidation. The Pt enriched surface originated from the dissolution of the oxides is expected to provide such protection. This hypothesis is consistent with the much lower intensity of the La 3d and Ce 3d XPS signals after ORR testing: the AR-XPS profiles in the end of this section will further support this idea. A closer look at the fitted spectra shows minor differences between the spectra after ORR testing and during sputter-cleaning. After electrochemistry a slight intensification of the f_{N+1} satellites of La and of the f_{N-1} satellites for Ce can be observed (see Appendix A.1). As such intensification is typical of La and Ce alloys [135, 139], it could be explained by the removal of surface La (or Ce) atoms that would be under-coordinated to Pt atoms. It is worth noting that the spectra of Figure 3.4 e,f actually represent the chemical state of La and Ce in the active catalyst, as no chemical modifications are expected during the transfer to the XPS setup. This also means that no La or Ce should be expected on the active surface of these catalysts. Instead, no conclusive information about the chemical state of the catalyst could be obtained from the spectra of Figure 3.4 a-d; this emphasizes the importance of a proper catalysts characterization, that should be performed after testing and possibly in-situ, unless, as in this case, there are clear indications about the conservation of the active catalytic phase. Although in-situ XPS measurements are in general quite rare and only applicable to few experiments, mainly due to the difficulties related to the short mean free path of photoelectrons in any realistic reaction environment, important advances have been made and will be discussed in Chapter 6.

3.3.1 Angle-resolved experiments

While the spectra of Figure 3.4 have been obtained as an average over all the acceptance angles of the analyzer, by distinguishing the XPS signal at different angles a depth profile can be constructed; in this way the active surface structure of the catalyst was also studied. Figure 3.5 a,b shows how the relative composition of Pt and lanthanides varies for Pt_5La and Pt_5Ce as a function of the acceptance angle. The Pt to La and Pt to Ce ratios are close to the nominal composition of the alloys during sputtering. However, a clear increase of these ratios is observed after ORR testing. This increase is particularly pronounced at higher angles (*i.e.* further from the surface normal), where the measurements are more surface sensitive. Figure 3.5 c,d shows the calculated depth profiles of Pt_5La and Pt_5Ce after ORR

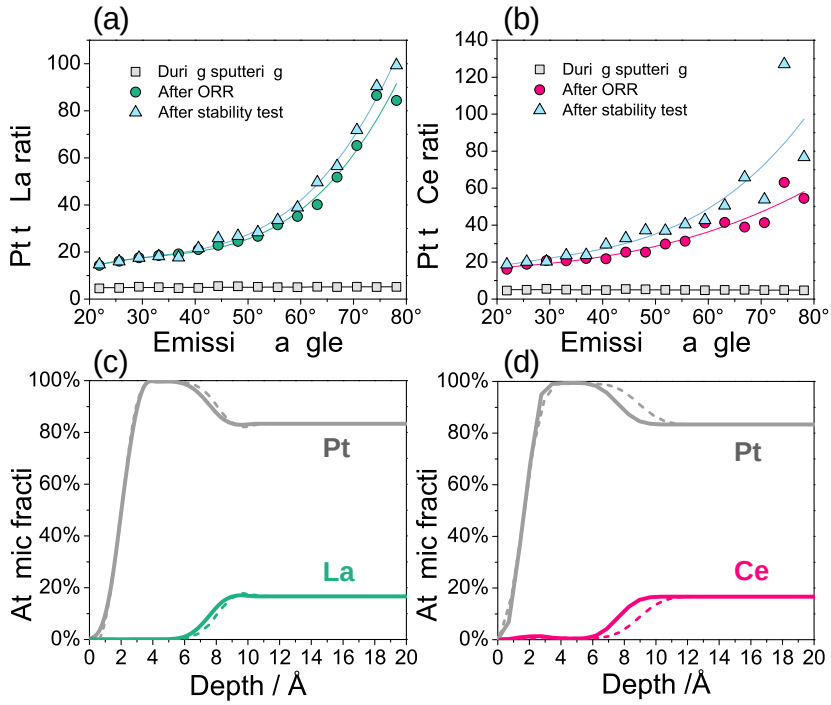

Figure 3.5: Pt to lanthanide atomic ratios in Pt_5La (a) and Pt_5Ce (b) as determined from AR-XPS in three different conditions: *as-prepared*, *after ORR* activity test and *after stability* test. All ratios were calculated as the average of at least two independent measurements, giving a standard deviation lower than 3 for all angles lower than 60°. Corresponding AR-XPS depth profiles of Pt_5La (c) and Pt_5Ce (d), *after ORR* activity test (solid line) and *after stability* test (dashed line).

testing. On both surfaces a thick Pt overlayer was formed as a consequence of the exposure to the electrolyte and electrochemical cycling. Similar structures have already been reported for other de-alloyed surfaces as Pt_3Co, Pt_3Ni, Pt_3Y, Pt_5Y and Pt_5Gd [37, 38, 98, 132, 143].

After stability test new AR-XPS measurements were taken. The idea was to investigate the compositional or structural changes occurred during potential cycling. The La 3d and Ce 3d spectra (not shown) completely resembled those of Figure 3.4 e,f indicating no modifications of the active chemical state of the lanthanides. This also suggests that a Pt overlayer is still present and prevents them from oxidation. The comparison of the Pt to La and Pt to Ce ratios in Figure 3.5 a,b provides more interesting information. A further increase of these ratios is observed, meaning that Pt enrichment proceeded further. In agreement with this higher values, the AR-XPS depth profiles of Pt_5La and Pt_5Ce in Figure 3.5 c,d exhibit a slight thickening of the

Pt overlayer. For both alloys, and in particular for Pt_5La, these changes are very modest, demonstrating that these surfaces are highly stable under these cycling conditions and no bulk de-alloying occurs.

3.4 Ion scattering spectroscopy

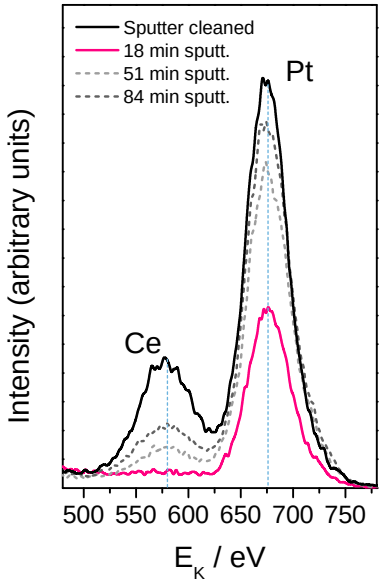

Figure 3.6: ISS spectra on polycrystalline Pt_5Ce after ORR testing for different sputtering times. The ISS spectrum acquired on a sputter-cleaned (as-prepared) sample is also reported for comparison.

The AR-XPS depth profiles of Figure 3.4 seem to indicate that, *after ORR* testing, the surfaces of Pt_5La and Pt_5Ce consist of pure Pt. As it will be better discussed in Chapter 4, their significance is mostly qualitative: the XPS measurements represent an average over a 400 μm wide region of the surface and over a depth of a few electron mean free paths ($\lambda \approx 10$ Å [111]). This means that they don't necessarily give a comprehensive description of the surface structure that could in principle be inhomogeneous due to the polycrystalline nature of the samples. Therefore, ion scattering spectroscopy (ISS) was employed as an even more surface sensitive tool to further investigate the surface structure of these catalysts. By only probing the composition of the topmost layer, it allows to exclude the presence of residual La and Ce atoms on the surface after ORR testing: in this case the possibility of

bifunctional effects would also be ruled out.

Since the atomic masses of Ce and Pt are quite similar, it was not possible to distinguish their peaks by using He^+ ions. A beam of Ne^+ ions at 1 keV was used instead. Since Ne atoms are heavier a careful optimization was required in order to achieve a sufficiently good signal, without causing too fast sputtering damages to the surface. The ion beam was rastered over a large 4 mm × 4 mm sample area, the currents were decreased to values between 10 and 16 nA at a residual Ne pressure in the UHV chamber of 5×10^{-9} mbar and the analyzer lenses were optimized for maximum sensitivity. Figure 3.6 shows the ISS spectra acquired on Pt_5Ce after ORR testing for different measuring times: each scan took approximately 2 minutes. The spectrum of the sputter-cleaned surface is also reported for comparison, showing that the peaks of Pt and Ce could be clearly separated at $E_K \approx 680$ eV and $E_K \approx 580$ eV respectively. Around 10-15 minutes of ISS sputtering were required in order to clean the surface from the surface contaminations occurred during the electrochemical measurements and the transfer. These very first scans (not shown) are dominated by the background originating from adventitious O and C. At around 18 minutes a very clear Pt peak appears while no Ce signal can be seen. At increasing times and further sputtering a weak peak from Ce appears and the Pt to Ce signals progressively approach those measured on sputter-cleaned Pt_5Ce.

In order to further quantify the Pt to Ce ratio from these ISS measurements, a Shirley-type background was subtracted and the peaks were fitted. Despite the slight intrinsic asymmetry of the ISS peaks, the product of a Gaussian and a Lorentzian curve provided a rather good fit of the experimental data. In figure 3.7 the areas of the Pt and Ce peaks are shown as a function of the total sputtering time; the Pt to Ce ratio is also plotted. For the first 10 minutes of measurement, the areas were not calculated due to the predominance of the background related to surface contaminations. After this period of time, the Pt peak appears and its area increases rapidly while the Ce peak is absent or barely visible, proving the clear Pt enrichment at the surface. At around 20 minutes of total sputtering also the Ce peak appears. As expected, the Pt to Ce ratio progressively diminishes until it starts stabilizing at about 80-100 minutes of total sputtering time. At these times the Pt to Ce ratio slowly approaches the one of the bulk, as measured from the ISS spectrum of a sputter-cleaned sample. These data seem to indicate that the Pt to Ce ratio diverges for sputtering times between 15 and 20 minutes: higher than 10 000 at 18 minutes of sputtering. When the estimated level of noise in the measurement is also considered the maximum significative ratio for this measurement is still around 800. This evidence together with the AR-XPS depth profiles and the fact that Ce (or La) appears in a completely metallic state, contribute to the conclusion that no Ce (or La) atoms are present on the surface of these catalysts and no bifunctional effects can occur.

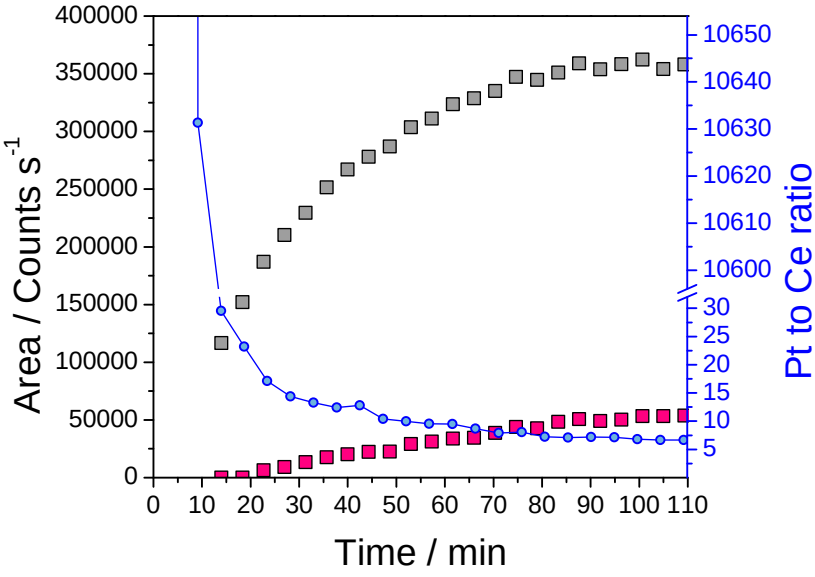

Figure 3.7: Fitted areas of Ce (red) and Pt (grey) peaks from ISS spectra as a function of the total sputtering time on Pt_5Ce after ORR. The Pt to Ce ratio of the areas (blue) is also plotted.

3.5 The case of Pt_3La

Since the electrochemical behaviour of polycrystalline Pt_3La was largely different from the one of Pt_5La and Pt_5Ce a dedicated section is hereby introduced. The sample was prepared by sputter-cleaning in totally similar conditions as for the other alloys (see Section 3.1.1); the conditions of electrochemical characterization were also identical (see Section 3.2). However, Figure 3.8 shows various CVs in N_2 saturated 0.1 M $HClO_4$ electrolyte. Starting from cycle 1, the voltammetric currents increased continuously as can be observed after 30 and 60 cycles; no stable CVs could be obtained. This is an indication of continuous roughening from the initially polished surface and of a progressive increase of the active surface area. After 60 cycles ORR activity measurements were performed in the same conditions as for Pt_5La and Pt_5Ce. After ORR testing, new CVs were acquired in N_2 saturated solution. As apparent from Figure 3.8 the voltammetric currents increased even further reaching very high values. The double layer capacitance was also much higher. All these evidences can be ascribed to the corrosion of this sample, consisting in the dissolution of metallic La to La^{3+} and the formation of H_2.

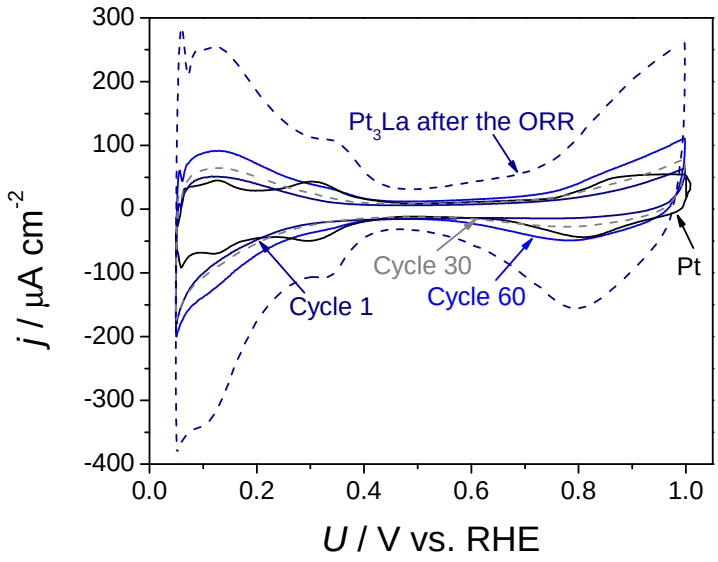

Figure 3.8: CVs of Pt_3La in a N_2-saturated 0.1 M $HClO_4$ electrolyte at 50 mV s^{-1}. Cycles 1, 30, 60 were acquired readily after transfer of the as-prepared sample to the elctrochemical cell. The stable CV of polycrystalline Pt is also plotted for comparison. Measurements performed by María Escudero-Escribano.

Figure 3.9 a presents the Tafel plot of Pt_3La in O_2 saturated 0.1 M $HClO_4$ electrolyte. The kinetic current densities of Pt_5La and polycrystalline Pt are also plotted for comparison; the ORR current of Pt_3La resembles closely the one of pure Pt with no noticeable activity enhancements, probably as a result of the fast corrosion. To further elucidate this corrosion ICP-MS measurements were performed after these ORR activity tests: details are given in [126] (Paper 3 in the end of this thesis). 5 mL of electrolyte were extracted from the 0.1 M $HClO_4$ solutions and transferred to the ICP-MS setup. Internal standards for the calibration were used. A reference spectrum was also taken on a clean 0.1 M $HClO_4$ solution (free of Pt and La) and no La and Pt signals appeared above the background level. Figure 3.9 b shows the total signal of La (atomic mass: 139 amu) and Pt (atomic masses: 194, 195, 196 and 198 amu) acquired after the ORR activity tests on Pt_3La and Pt_5La. For both electrolyte samples small Pt signals appear. Interestingly, Mayrhofer and co-workers studied the dissolution of Pt on pure Pt electrodes by combining an electrochemical scanning flow cell and an ICP-MS setup [11]. However, they did not observe any significant Pt dissolution in this potential region (up to 1.0 V vs RHE). Focusing on the La signals, a much higher concentration of La was measured in the solution from the Pt_3La electrode. This is in agreement with the hypothesis

of strong corrosion of this alloy.

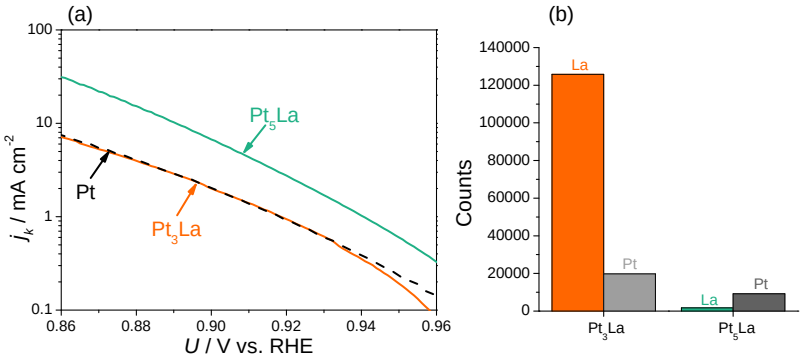

Figure 3.9: Tafel plot (a) representing the kinetic current densities of Pt_3La, Pt_5La and polycrystalline Pt as a function of potential. Corresponding ICP-MS analysis (b) of the amount of dissolved La and Pt from Pt_3La and Pt_5La electrodes in 0.1 M $HClO_4$ electrolytes. The same measurement was performed on a clean 0.1 M $HClO_4$ electrolyte and produced much lower signals of La and Ce (negligible on the chosen scale). Measurements performed by María Escudero-Escribano and Arnau Verdaguer-Casadevall.

Contrary to these results, Kim and co-workers [99] observed a considerable enhancement of specific activity relative to pure Pt on their Pt_3La thin films: as well as high stability during potential cycling. Possible reasons for the corrosion of our Pt_3La polycrystal and a comparison with Pt_5La, together with a broader discussion about the stability of these surfaces, will be assessed in the following section.

As for the other alloys, analogous XPS characterization was performed on Pt_3La. For the close similarity of the spectra with those of Pt_5La (see Figure 3.4) the results are described briefly. The fitted spectra of Pt_3La *as-prepared* (*i.e.* during sputter-cleaning), *air-exposed* and *after ORR* testing are presented in Figure 3.10. Similar to Pt_5La the La 3d XPS peaks of the sputtered sample are completely metallic and very different from those measured by Kim and co-workers for thin films of the same stoichiometry (*i.e.* Pt_3La) [99]. After air-exposure the level of oxidation was also similar to the one of Pt_5La, demonstrating the same tendency of La atoms towards oxidation. After ORR testing small La 3d signals could still be measured and appeared to be completely metallic, indicating that La_2O_3 dissolved in the electrolyte. For all spectra the energy position and relative intensity of the f_n components was similar to Pt_5La (see table of Appendix A). Due to the fast corrosion no long-term stability tests were conducted on Pt_3La. At the same time, no AR-XPS depth profiles will be presented for Pt_3La due to the increased roughness that could easily affect such measurements.

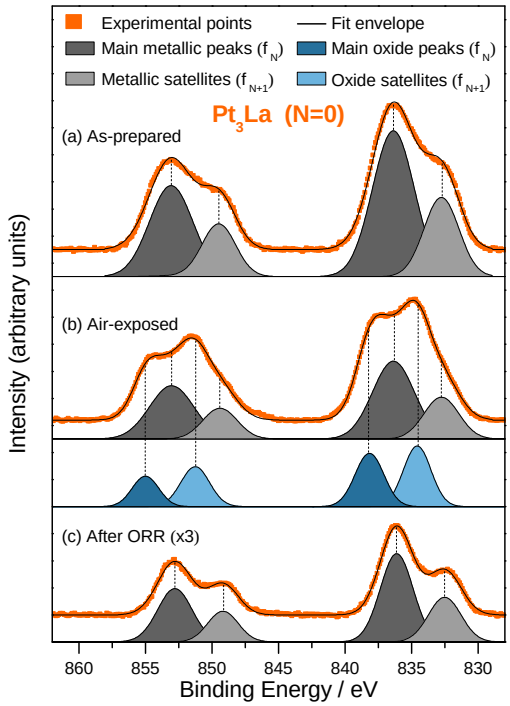

Figure 3.10: La 3d XPS spectra of Pt_3La after background subtraction, at an average emission angle of 45°. The spectra were acquired in three different sample conditions: *as-prepared* (*i.e.* during sputter-cleaning) (a), *air-exposed* (b) and *after ORR* testing (c). The measurements after electrochemical measurements were magnified three times due to the lower signal intensity. The fitted spectra of the metallic peaks (grey) and of the oxidized peaks (blue) appear under the experimental points. Detailed information about the peak positions and relative intensities are found in Table A.1.

3.6 Discussion on the active chemical phase and surface stability

Evidently, the XPS results of Sections 3.3 and 3.5 have highlighted a strong tendency towards the La and Ce oxidation. The surface of these Pt-La and Pt-Ce alloys is intrinsically unstable under air-exposure. The very negative alloying energies (see Figure 3.1) which are typical of these alloys are insufficient to prevent such oxidation. It should be noted, however, that these alloying energies might still play a role against oxidation. The spectra of Figures 3.4 and 3.10 and the correspondent data of Appendix A show that the metallic components of the La 3d and Ce 3d spectra still account for most of the XPS signal. This indicates that the alloys still create kinetic barriers against deep oxidation, while pure La or Ce would immediately

form a thick oxide layer [144, 145].

Our experimental evidences are in clear discrepancy with the results and interpretation of Kim and co-workers for Pt_3La [99]. On the basis of their DFT calculations on a closely packed structure of Pt_3La they claim that La atoms would be present on the surface without forming any Pt overlayer. The alloying energy would stabilize this structure not only in vacuum but also under reaction conditions: no oxidation or dissolution of La would occur. They support this interpretation with AR-XPS measurements, showing that La atoms are present on the surface and that their chemical phase does not vary before and after electrochemical measurements. However, the peak shape and position of their La 3d XPS peaks does not appear as metallic: it is instead similar to those we observed for La oxide in Figure 3.4 c,d. In general, these spectra are typical of compounds where La is in an oxidized state, with very intense f_{N+1} components, almost as intense as the main La 3d peaks [130, 141, 146]. This observation together with the fact that no explicit details about the purity of their fabricated alloys or any surface cleaning procedures are described in their work [99] suggest the formation of a rather thick La oxide layer.

It should be noted that the XRD measurements reported by Kim and co-workers exhibit the same crystal structure of pure Pt with the presence of some lattice strain. This indicates that their Pt_3La phase should consist of a *solid solution* [147, 148], meaning that the overall bulk composition might still be constant and close to the stochiometry of Pt_3La, but with a random substitution of Pt and La atoms at any given atomic coordinate. Solid solutions are typical of metal compounds with weak interactions between its constituents, as in the case of Pt_3Co, in particular when the annealing temperatures are not sufficiently high [147]. In the case of Pt and La these interactions should be strong, providing a significant driving force towards the formation of an ordered *intermetallic compound*. In this case, the energetically unfavorable La-La bonds would be minimized resulting in a compound with the highest possible number of Pt-La nearest neighbours. Interestingly, the phase diagrams found in literature for the Pt-La intermetallic compounds do not report the existence of any stable Pt_3La phase [128, 129]. The XRD measurements on our polycrystalline sample with nominal composition of Pt_3La are in agreement with these diagrams; they allowed to identify two coexisting phases: Pt_2La and Pt_5La that are both reported as stable intermetallic compounds. In our view, Kim and co-workers obtained a meta-stable solid solution due to their particular preparation conditions: they fabricated thin films of Pt_3La by magnetron sputtering at room temperature, without any heat treatment that could facilitate the formation of an ordered intermetallic compound. For such a meta-stable phase the low stability of their Pt_3La sample to oxidation in air is unsurprising.

Focusing now on Pt_5La and Pt_5Ce, and in particular on the AR-XPS results after ORR testing (see Figures 3.4 e,f and 3.5 c,d), it is clear that both the La and Ce oxides, as well as their metallic phases to some extent, are dissolved from the near-surface region in acid. This tendency can be understood in terms of simple thermodynamic considerations. First considering the Pt_5La case, La_2O_3 is not ther-

modynamically stable at pH 0 and it will clearly dissolve to La^{3+} [8]. Metallic La is also unstable for similar reasons: the standard dissolution potential of a La atom to La^{3+} is -2.38 V *vs.* the standard hydrogen electrode (SHE) [149]. Since the reaction involves three electrons the correspondent Gibbs free energy of dissolution is ≈ -7.1 eV at 0 V SHE. The presence of the alloy will partially stabilize each La atom for an amount of energy given by the standard Gibbs free energy of formation (ΔG_{Pt_5La} = -3.8 eV [124]). This results in a residual standard Gibbs free energy of dissolution ≈ -3.3 eV, or in terms of standard reduction potential ≈ -1.1 V *vs.* SHE. Due to the very similar chemical properties of Pt_5Ce analogous considerations apply, giving a standard reduction potential of Ce^{3+} to Ce ≈ -1.1 V *vs.* SHE, approximately the same as for Pt_5La. At the cathode of a fuel cell typical potentials of around 1 V can be reached during shut down, these values are 2.1 V higher than those needed for stabilizing metallic La or Ce. In other words, these simple calculations predict a huge driving force of about 6.3 eV for the dissolution of each La or Ce atom: this is despite the very negative alloying energy. Such analysis supports the concept the that no La or Ce atoms can be expected on the surface of these catalysts. Although the preparation technique employed by Kim and co-workers is different from the one of our sample, and the structures are also different, it is very unlikely that any kind of metallic Pt-La phase could resist to this huge driving force towards the dissolution of La atoms at the surface, especially without any annealing treatment. This tendency towards dissolution is probably independent on the bulk structure of the alloys.

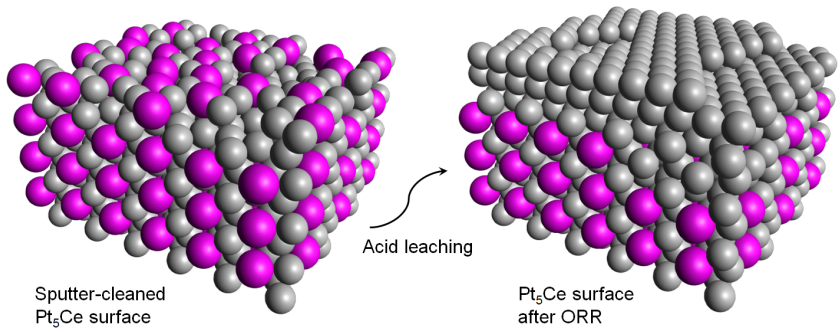

Figure 3.11: Illustrative three-dimensional view of the Pt_5Ce structure after sputter-cleaning (left) and after ORR activity test with the formation of a Pt overlayer on top of the Pt_5Ce bulk alloy (right). Grey and magenta spheres represent Pt and Ce atoms respectively.

Despite the instability of the lanthanides on the surface of the alloys the AR-XPS depth profiles of Figure 3.5 c,d show that La and Ce are still present under a few monolayers thick Pt overlayer. With a mean free path of photoelectrons of

the order of $\lambda \approx 10$ Å [111] their presence is certain within few nanometers from the surface: an illustrative view showing the effect of acid leaching on Pt_5Ce and the formation of such overlayer is found in Figure 3.11. The Pt overlayer provides kinetic stability against the dissolution of the lanthanides from the bulk. The very negative alloying energies are still expected to play a role: the very strong Pt-La and Pt-Ce interactions are expected to obstruct and slow down the diffusion of La and Ce through the overlayer. A different case is the one of Pt_3La that continuously corrodes as described in Section 3.5. We ascribe the origin of such instability to the presence of multiple phases in its XRD trace. The importance of stoichiometry for the stability of the Pt_xY alloys was already investigated in a previous publication [98]: different intermetallic compounds exhibited completely different behaviours. The Y-rich phases (PtY and Pt_2Y), in particular, heavily corroded while both Pt_3Y and Pt_5Y were stable under ORR conditions. We anticipate that La-rich phase (Pt_2La) might be the one corroding on the Pt_3La polycrystalline sample. Other groups have reported similar evidences for alloys of Pt and late transition metals [58, 150]: it is particularly difficult to stabilize the Pt alloys when the less noble metal overcomes a certain percentage of the total composition. For percentages higher than 60% the dissolution directly occurs from the bulk of the alloy. The very high activity and good stability of Pt_5La and Pt_5Ce, compared to the poor results of Pt_3La, underlines how essential the identification of the right phase is for this kind of compounds, and for this purpose how important physical techniques as XPS, XRD and LEIS might be.

Chapter 4

Trends in activity and stability

4.1 Introduction

In the previous chapter some of the first alloys of Pt and a lanthanide metal (La, Ce) have been introduced. In particular, detailed AR-XPS and ISS analyses were performed on Pt_5La and Pt_5Ce. These model polycrystalline alloys allowed to elucidate the active chemical phase of this kind of samples when exposed to acidic electrolytes and subjected to ORR conditions. The presence of a thick Pt overlayer providing kinetic protection against deep dealloying was demonstrated. With a similar structure it was theorized that neither bifunctional effects or ligand effects could explain the enhanced ORR activity relative to pure Pt, and that only strain effects could be the explanation. This chapter will focus on this particular point, with the purpose of explaining the origin of the strain and how this strain is related to the ORR activity of these catalysts and their durability. A number of polycrystalline alloys all exhibiting the nominal stoichiometry of Pt_5Ln (with Ln indicating a generic lanthanide metal) were tested. Similar to the Pt_5La and Pt_5Ce intermetallic phases, the heat of alloy formation of these new materials is also very negative [123], indicating the high thermodynamic stability of the alloys. Their chemical states and surface structures also present the same characteristic features allowing a direct comparison of the catalytic performances of all these materials. Indeed, their electrochemical characterization will be presented showing clear trends both in terms of ORR activity and stability. A new class of alloys for catalyzing the ORR

will also be introduced: alloys of Pt and some alkaline earths exhibit promising activities.

The XRD characterization shows that all these materials have similar bulk structures and it will allow to give an interpretation of these trends on the basis of the nearest neighbour Pt-Pt distance in the bulk, although strain relaxation effects are expected to occur in the Pt overlayer. Investigating the nanoscale properties of these Pt overlayers, (*e.g.* their crystal structure, orientation and level of ordering) is a fundamental step towards a full understanding of their catalytic properties. The thickness of the overlayer in particular is an important parameter defining the level of strain relaxation and providing details about the dealloying mechanism. A model for estimating these thicknesses on the basis of the AR-XPS measurements will be introduced.

This work enters in the context of various other studies that in the last two decades tried to establish experimental trends in the ORR activity of Pt alloys. Mukerjee *et al.* studied the activity of carbon supported alloyed nanoparticles (PtM/C with M = Cr, Mn, Fe, Co, Ni): they related it to the nearest neighbour Pt-Pt distance and to the level of Pt d-band vacancy [72]. Instead, Stamenkovic *et al.* reported trends in activity of various polycrystalline extended surfaces (namely Pt_3Ti, Pt_3V, Pt_3Fe, Pt_3Co and Pt_3Ni) more similar to those studied here; they chose the experimental (or theoretical) d-band center position as a descriptor of the activity [38, 44]. More recently, Hwang and coworkers also correlated the position of the d-band center with the activities of various sputter-deposited thin films, including some alloys of Pt and early transition metals as Pt_3Y and Pt_3Zr [151]. We anticipate that, in agreement with the d-band model [53–55] and with the d-band shift observed by Strasser *et al.* on strained Pt overlayers [31], an analogous trend could be also observed for the alloys tested in this chapter. However, it will be experimentally challenging to perform accurate measurements of the d-band on these alloys. Indeed, these should be carried out after ORR testing, when the Pt-skeleton structures are formed as a consequence of surface dealloying. The presence of C and O contaminations and of the 4f states of the lanthanides overlapping to the d-band would highly complicate the analysis of the XPS-UPS spectra. A number of trends based on the DFT calculated binding energies to one of the ORR intermediates (HOO^*, HO^* and O^*) have also been reported [16, 38, 47, 56, 152].

On the basis of the results of this chapter a manuscript about the trends in activity and stability of these alloys is currently in preparation: the abstract can be found in the end of this thesis (included Paper 6). All electrochemical measurements have been performed by María Escudero-Escribano. DFT calculations were performed by Vladimir Tripković.

4.2 Bulk structure and Pt-Pt distance

All the Pt_5Ln polycrystalline alloys have been investigated by XRD in order to identify their bulk structure and confirm the presence of the right phases. For most of these alloys the XRD patterns with correspondent lattice constants have already been reported in literature. Nevertheless for a good part of them there is only a single reference article [127]. It should be noted that in all cases these combinations of Pt and lanthanides lead to the formation of intermetallic compounds whose structure is considerably different from the typical closed packed structure (face centered cubic) of pure Pt. In this sense these structures are all very different from those of more widely studied alloys of Pt and and late transition metals such as Pt_3Co, Pt_3Ni [36, 147], and also from the structure of Pt_3Y or Pt_3Sc which all exhibit closed packed structures similar to Pt [16, 98].

For the first lanthanide metals of the periodic table (La, Ce, Pr, Nd) the reported structure is hexagonal with the well characterized prototype of the Cu_5Ca phase and space group P6/mmm [127, 153]. While moving towards the right of the periodic table the covalent radius of the lanthanides decreases [57] and as a consequence the unit cell of this phase contracts as indicated, in particular, by the lower *a* lattice constants. For alloys with most of the other lanthanides (Sm, Gd, Tb, Dy, Ho, Er, Tm,) this contraction exceeds a critical value causing the appearance of a different orthorhombic structure [127]. The lattice parameter *a* is still the same and it continues its contraction while moving towards lanthanides with higher atomic number, but the *b* and *c* lattice constants are considerably different due to the different re-organization of the atoms. Despite the availability of these lattice constants measured by XRD, the stack of the atoms and the space group of this structure has not been fully characterized. However, the two structures are expected to closely resemble each other [127].

The XRD patterns of the alloys tested in this work were found to be in agreement with the structures reported in [127]. In the case of Pt_5Gd the two mentioned structures (*i.e.* hexagonal and orthorhombic) were found to coexist [132] suggesting that this material could somehow define the boundary between these two phases. The hexagonal Cu_5Ca type structure for Pt_5Gd was also reported previously [155]. The numerical values of lattice constants also agree quite well with literature.

In the previous chapter the enhanced ORR activity of the Pt_5Ln alloys with respect to Pt was ascribed to strain effects. In this view the catalytic properties are related to the level of strain in the Pt overlayer and in particular to the level of strain of the most superficial surface atoms. This strain must be induced by the properties of the bulk and be correlated to some of its lattice parameters. It was recently proposed that the Pt overlayer would predominantly consist of a closely packed Pt layer, resembling pure Pt, with a lattice parameter imposed by the nearest neighbour Pt-Pt distance in the alloy. This idea was suggested by the DFT calcu-

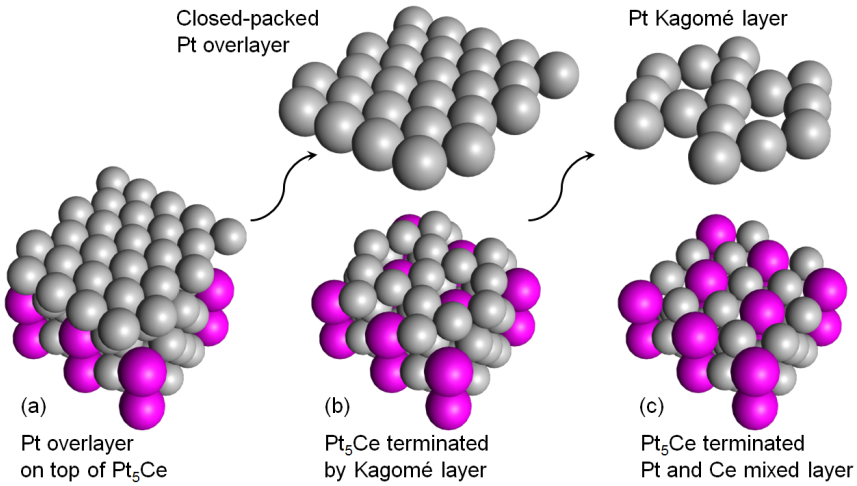

Figure 4.1: Illustrative structure of a closely packed Pt monolayer on top of Pt_5Ce with the typical hexagonal (Cu_5Ca prototype) unit cell (a). In (b) the Pt overlayer has been removed revealing the structure of Pt_5Ce: this is terminated by a Pt Kagomé layer [154] resembling the structure of closed packed Pt but with vacancies corresponding to the Ce atoms underneath. In (c) the Kagomé layer has also been removed revealing a Pt and Ce mixed layer. The continuous alternation of these two layers originates the bulk structure of Pt_5Ce.

lations conducted on a Pt slab superimposed to the structure of Pt_5La [6]. Figure 4.1 helps to intuitively understand this concept by showing how different atomic layers parallel to the (001) plane overlap with each other on this hexagonal Cu_5Ca structure. The alloy is basically constituted of alternating layers of pure Pt and Pt and La. The pure Pt layers have vacancies at the positions where La atoms lie below, forming a so called Kagomé layer [154]. DFT calculations suggested that a closed-packed Pt overlayer would form on this Kagomé layer by occupying its vacancies with Pt atoms. The formation of a closely packed Pt layer on top of these alloys is also supported by experimental evidences. It was proven on a Y modified Pt(111) single crystal: after deposition of Y, upon annealing in vacuum, it forms a Pt-Y alloyed phase (exhibiting the structure of Pt_5Y) covered by a compressed Pt-skin [101, 156] (Paper 4 in the end of this thesis). In-situ STM studies of Pt-Fe alloys have also exhibited the formation of a closely packed Pt overlayer, similar to Pt (111), in acidic electrolyte [45].

As already anticipated, with this structure of the overlayer the Pt-Pt at the surface of the catalyst would be defined by the nearest neighbour Pt-Pt distance in the bulk. In the case of the Cu_5Ca hexagonal structure this turns out to be half of the a parameter: $d_{Pt-Pt} = a/2$. In the rest of this chapter it will be assumed that for the orthorhombic structure the same relationship applies. Although this cannot

be verified due to the unknown space group, the similarity of the two structures, exhibiting the same a lattice parameter, supports this assumption. Since the a parameter decreases monotonically while moving towards lanthanides with higher atomic number, also the Pt-Pt distance in the overlayer is expected to follow the same trend.

4.2.1 Alloys of Pt and alkaline earths

On the basis of theoretical DFT calculations [157] a new class of Pt alloys for catalyzing the ORR was also studied as part of this project. Alloys of Pt and alkaline earth metals such as Pt_5Ca and Pt_5Sr also form stable intermetallic compounds. Although their heat of alloy formation is not as negative as for the Pt_5Ln alloys [158], the very low costs and vast availability of alkaline earth metals promotes the interest towards the characterization of these materials. At the same time the reason why it is worth introducing them in this chapter comes from the fact that they also exhibit the same structure of Pt_5La and Pt_5Ce, with the typical hexagonal phase (Cu_5Ca prototype) [159, 160]. The high reactivity of the alkaline earth metals and their very negative standard reduction potentials [149] suggests that they would also tend to dissolve from the surface of the alloy in acidic electrolytes. The structure of the Pt overlayer is also expected to be the same, with the Pt-Pt distance dictated by the nearest neighbour Pt-Pt distance of the bulk, as for the other alloys of this chapter $d_{Pt-Pt} = a/2$. Under these assumptions it will be possible to directly compare these alloys with those of the other Pt_5Ln polycrystalline samples.

4.3 Trends in activity

For all the polycrystalline alloys the preparation procedure was the same as described in the experimental section of this work (see Section 2.3) and as applied to the Pt-La and Pt-Ce alloys. Sputter-cleaning was performed in UHV conditions until no C and O contaminations were observed. Following the cleaning procedure, the samples were transferred first to a fast-entry air lock, vented in dry nitrogen, protected by a drop of H_2 saturated Millipore water and then transferred to the RRDE setup. The electrochemical characterization was also carried out under nominally the same conditions (see Section 2.5.1). They were cycled between 0.05 V and 1 V at a sweep rate of 50 mV s^{-1} until stable CVs were obtained, typically 100-150 cycles. Once stable CVs were obtained the catalytic activity of the electrodes was tested in O_2-saturated 0.1 M $HClO_4$. The ranking of the resulting ORR activities is plotted in Figure 4.2.

Proceeding in the order of lanthanide atomic number the following alloys were tested: Pt_5La, Pt_5Ce, Pt_5Sm, Pt_5Gd, Pt_5Tb, Pt_5Dy and Pt_5Tm. Among these materials polycrystalline Pt_5Tb exhibited the highest ORR activity, exceeding the one of

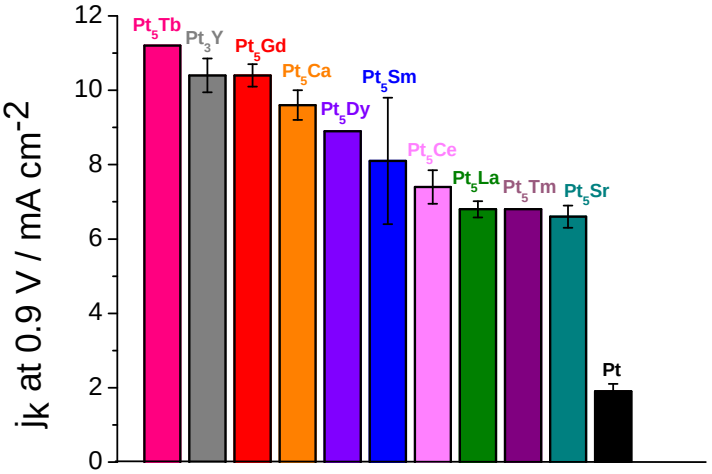

Figure 4.2: Rank of the experimental ORR activities (kinetic current densities per geometric surface area at 0.9 V *vs.* RHE) of various Pt_5Ln alloys *vs.* the lattice parameter a of the alloys as determined from XRD measurements. The ORR activities of Pt_5Ca and Pt_5Sr and for comparison, of polycrystalline Pt and Pt_3Y, are also plotted. On the basis of the considerations about the ECSA of Section 3.2.2 all the specific activities have been calculated by normalization to the geometrical surface area. Measurements and figure made by María Escudero-Escribano.

Pt_3Y and therefore, being the polycrystalline alloy with the highest ever reported activity. Its kinetic current density at 0.90 V *vs.* RHE is 11.2 mA cm^{-2} about 6 times higher than that of pure Pt; even more interestingly, all the reported Pt_5Ln alloys show more than a 3-fold enhancement in activity with respect to Pt. The ORR activities of Pt_5Ca and Pt_5Sr are also very high, with a factor of 5 enhancement relative to Pt in the case of Pt_5Ca. In comparison, similarly prepared alloys of Pt and late transition metals (Pt_3Fe, Pt_3Co and Pt_3Ni) exhibited lower activities with about a factor of 2 enhancement [37, 73].

For most of these alloys the qualitative surface structure of the active phases after ORR was studied by AR-XPS. In all cases the AR-XPS depth profiles confirmed similar structures as the ones shown for Pt_5La and Pt_5Ce in Section 3.3 and in particular in Figure 3.5 and similar to the surface structure already reported for Pt_5Gd [132]. The presence of a thick Pt overlayer suggests that in all cases the ORR activity should be related to strain effects and, in some way, to the lattice parameters a measured in Section 4.2. In Figure 4.3 the activities of the tested

Pt_5Ln alloys are plotted as a function of the lattice parameter a, and on the top axis, as a function of the nearest neighbour Pt-Pt distance (*i.e.* $a/2$) in the bulk of the alloys. The activity of polycrystalline Pt is also plotted for comparison by considering on the top axis the typical Pt-Pt distance in pure Pt. Interestingly, a volcano shape relationship appears. The activities of Pt_5Ca and Pt_5Sr are also inserted in the plot since they both exhibit the Cu_5Ca type structure. Notably, their position fits very well into the same trend.

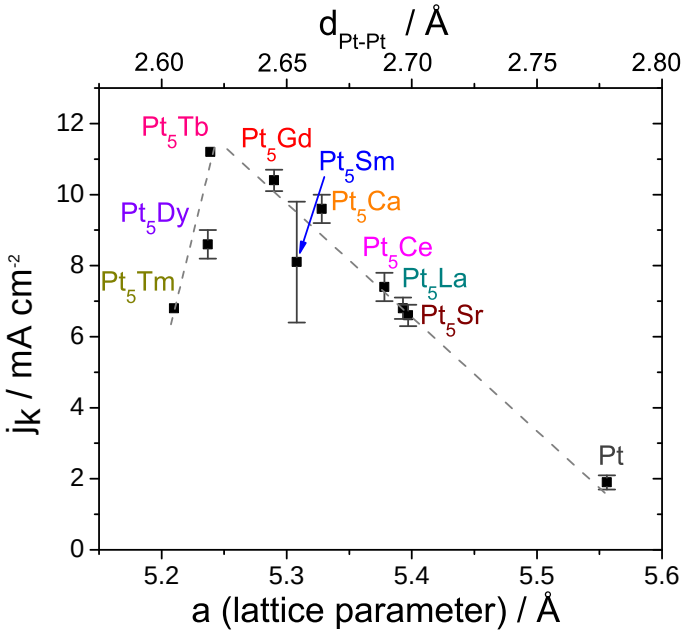

Figure 4.3: Experimental ORR activity from Figure 4.2 of various Pt_5Ln and Pt-alkaline earths alloys *vs.* the lattice parameter a of the alloys as determined from XRD measurements. On the top axis the nearest neighbour Pt-Pt distance in the bulk, which is assumed to define the Pt-Pt distance in the Pt overlayer, is also indicated: $d_{Pt-Pt} = a/2$. The activity of polycrystalline Pt, referred to its typical Pt-Pt lattice distance (top axis), is also reported. Measurements and figure made by María Escudero-Escribano.

The appearance of a clear volcano trend is explained in terms of strain effects. Both DFT calculations [54] and experimental results [31, 126, 132] agree on the concept that compressive strain should weaken the binding energy of Pt to oxygenated species such as O, OH or OOH. This weakening should result in a higher ORR activity [16, 17, 19]. In agreement with this concept, the reduction of the lattice parameter a in Figure 4.3, or alternatively of the derived Pt-Pt nearest neighbour distance, results in a higher ORR activity. This would explain the right side of the volcano with activities that increase constantly until Pt_5Tb. A similar re-

lationship was found by Strasser and coworkers on core-shell Pt-Cu nanoparticles [31]. Also in their case, higher levels of compressive strain in the bulk correspond to higher ORR activites: according to their considerations the presence of strain relaxations in the Pt shell of the particles did not allow them to reach the left side of the volcano.

It should be noted that according to DFT calculations the optimal ORR catalyst should bind OH $\approx$ 0.1 eV weaker than pure Pt [16]. This optimal binding energy should correspond to a compressive strain of about 2 % relative to pure Pt [31]. However, in the case of Pt_5Tb the contraction of the Pt-Pt distance would be approximately 6 %: this much higher level of strain supports the concept that, also in this case, strain relaxations occur in the Pt overlayer, of which only the surface atoms are actually defining the ORR activity. It is here anticipated that a higher level of compressive strain in the bulk of the alloy will result in a lower Pt-Pt distance also on the surface of the overlayer, despite the presence of strain relaxations. Under this assumption the trends in activity of Figure 4.3 would still be explained. This view is also supported by the experimental evidences of Strasser *et al.* [31]: they deposited controlled amounts of Pt on a Cu(111) surface and measured (by low energy electron diffraction (LEED)) substantial strain relaxations of the Pt overlayer for thicknesses higher than one monolayer. Clearly, establishing a direct relationship between the level of strain in the bulk and the one on the surface would be highly desirable. However, this would require a direct measurement of the structure of the overlayer and in particular of the Pt-Pt distance: the very limited thickness of the overlayer suggested by the AR-XPS measurements highly complicates such measurement. The polycrystalline nature of these samples makes it even more challenging since no diffraction techniques as XRD or LEED can be effectively employed. Ongoing synchrotron measurements are trying to elucidate these aspects on a Y modified Pt(111) single crystal [101]. The last part of this chapter, trying to quantify the thickness of the Pt overlayer for different alloys, might also contribute to elucidate this complex relationship. At the same time current theoretical models and DFT calculations are trying to answer some of these important questions.

The reason why the activity of Pt_5Dy and Pt_5Tm does not follow the same trend is also uncertain. One possible explanation is related to an excessively low Pt-Pt distance in the overlayer, exceeding the compressive strain of the optimal Pt catalyst. In this sense, these catalysts would effectively lie on the left side of the volcano. However, another possible theory could hold; it is anticipated that beyond a certain level of strain the closely packed structure of the Pt overlayer could intrinsically be unstable. This might lead to a further reorganization of the surface atoms and to a Pt-Pt distance that would collapse towards a lower level of strain.

4.4 Trends in stability

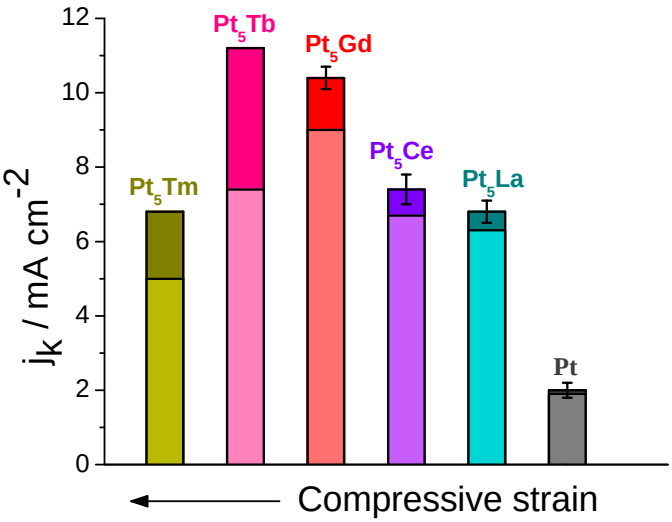

Figure 4.4: ORR activity expressed in terms of kinetic current density at 0.9 V *vs.* RHE for some Pt_5Ln polycrystalline alloys and polycrystalline Pt. The activities are reported both before and after stability test consisting of 10 000 cycles between 0.6 and 1.0 V *vs.* RHE in an O_2-saturated 0.1 M $HClO_4$ electrolyte at 100 mV s^{-1}. The arrow indicates increasing level of compression in the Pt overlayers. Measurements and figure made by María Escudero-Escribano.

After measuring the ORR activities, accelerated stability tests were conducted on the alloys by applying the same standard protocol as for Pt_5La and Pt_5Ce (see Section 2.5.1). The electrodes were subjected to 10 000 consecutive cycles between 0.6 and 1.0 V *vs.* RHE in an O_2-saturated 0.1 M $HClO_4$ electrolyte at 100 mVs^{-1}. Figure 4.4 reports the measured ORR activities before and after stability test. The various alloys have been placed in the same order as in Figure 4.3, hence the *a* lattice parameter is smaller for the alloys on the left and their Pt overlayers are expected to be more contracted. While the activity losses of Pt_5La and Pt_5Ce are very low (within 10 %) as already shown in Chapter 3, Pt_5Gd loses in average 14% of its initial activity. Even higher losses occur in the case of Pt_5Tb and Pt_5Tm, although these data are preliminary and only obtained from a single measurement. In general it looks like Pt_5Ln alloys with a higher level of contraction and higher compressive strain in the Pt overlayer are less stable. Intuitively, this trend could be explained by the fact that more compressed Pt overlayers might be intrinsically

less stable.

In order to better understand this trend in stability DFT calculations were performed. The stability of the Pt overlayer is quantified in terms of dissolution potentials *vs.* RHE: these are plotted in Figure 4.5 for various Pt_5Ln alloys. The surface of the Pt_5Ln alloys is modeled as strained Pt slab (Pt overlayer), with a level of strain induced by the experimental lattice constants of the bulk (see Figure 4.3). This strained Pt overlayer is represented by periodically repeated slabs separated by at least 12 Å of vacuum. The unit cell size of Pt was 2×2 atoms large and 4 to 5 layers thick. Two bottom layers were kept fixed, while the remaining atoms can relax, allowing to assume their minimum energy positions. When the total energies of the two slabs (with 4 and 5 layers respectively) are subtracted from each other, the resulting energy corresponds to a single layer of Pt atoms in the bulk. For non-strained Pt this energy corresponds to a dissolution potential at standard conditions of 1.23 V, taken as a benchmark value. The differences in energy in the case of strained Pt slabs are referred to this benchmark value. It should be noted that the purpose of this comparison is to illustrate a stability trend and these values should not be directly interpreted as the experimental dissolution potentials.

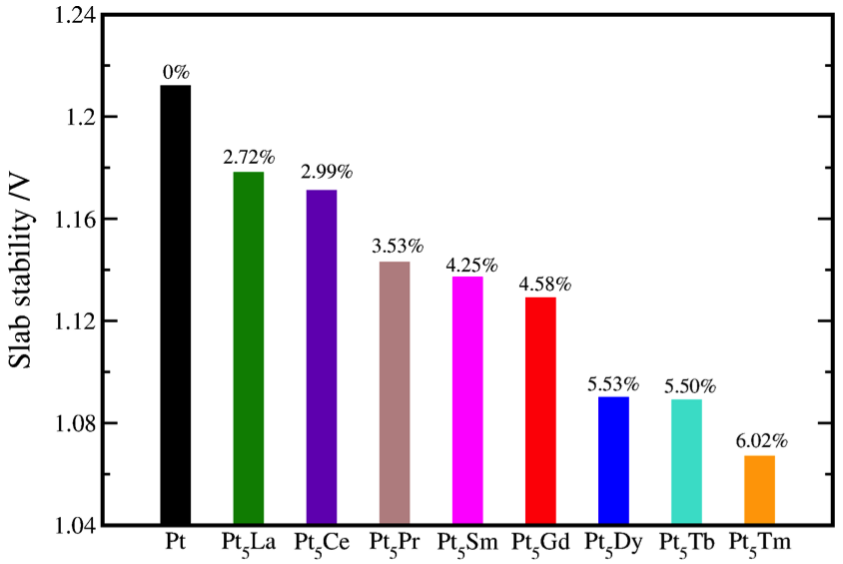

Figure 4.5: Stability of the Pt overlayers as a function of lattice strain in Pt_5Ln alloys (percentage compressive strain in the overlayer relative to pure Pt), as predicted by DFT calculations. The stability is indicated in terms of dissolution potentials *vs.* RHE. The Pt overlayers are modeled as a strained Pt slab using experimental values for the lattice parameters. Calculations and figure made by Vladimir Tripković.

Figure 4.5 clearly shows that the stability of these overlayers decreases when higher levels of compression are applied. The more strained the Pt overlayer is, the

faster the relaxation of its structure and the formation of defects. If this trend was confirmed by further measurements this would be quite unfortunate; it would mean that it is not possible to enhance both the activity and stability by tuning the Pt-Pt distance. An independent optimization of these properties would be impossible, since the trends in activity and stability go in opposite directions a compromise should be found. Taking into account both the activity and stability behaviour of these candidates, Pt_5Gd exhibits the best compromise, being more than 4 times more active than pure Pt after stability test.

4.5 Model for the Pt overlayer thickness

The previous section enlightened how important a precise knowledge of the physical properties of the Pt overlayer is. A direct measurement of the crystal structure and in particular of the nearest neighbour Pt-Pt distance in the overlayer would be highly desirable. By quantifying the level of strain relaxation relative to the bulk of these alloys, it would probably allow to directly relate the strain to the enhanced activity and to enable a comparison with theoretical DFT calculations: more precise explanations to the appearance of the volcano shape of Figure 4.3 could be found.

As apparent from the previous section, the thickness of the Pt overlayer also carries important information. As suggested by the experiments on Pt overlayers over a Cu(111) single crystal [31], it is expected to define the level of strain relaxation of the overlayer and as a consequence the activity of these polycrystalline alloys. The observed thickening of the Pt overlayer after stability tests (see Figure 3.5) might also explain, to a good extent, the ORR activity loss during potential cycling. Most importantly, the thickness of the Pt overlayer is the result of the dealloying process: differences in the Pt overlayer thickness for different alloys might provide notions about its mechanisms and help to establish principles for confining this process and improve the long term stability of these samples. Although the fitting algorithm used for the AR-XPS depth profiles (see Section 2.2.5) provides a qualitative image of the surface structure, a proper quantification of the overlayer thickness requires precise explicit approximations. Herein, a simple model based on the basic equation for XPS quantification (equation 2.2) is introduced, with the particular aim of estimating the Pt overlayer thickness for different alloys. In this way the simple approximations and involved assumptions can be varied in order to demonstrate the consistency of the method and to ensure more quantitative results.

4.5.1 Single overlayer

The method for the estimate of the thickness of a single layer over a substrate of a different material from AR-XPS measurements is well established in literature [112]. Starting from the basic equation for the intensity of the XPS signal from a

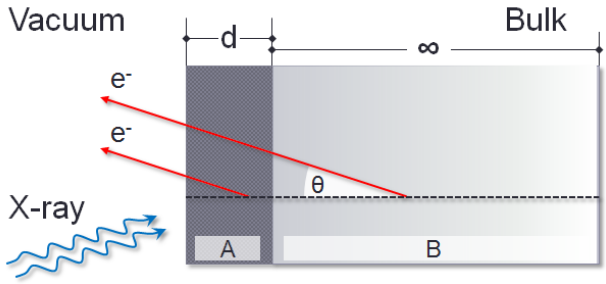

Figure 4.6: Sketch of a single overlayer (element A) of thickness d on top of an infinitely thick substrate (element B). The emitted photoelectrons are emitted along straight lines with an angle θ with respect to the surface normal.

certain orbital of element A (see equation 2.2):

$$I_A = \sigma_A(h\nu)\, T\left(E_A\right) \Phi \int_z N_A(z)\, e^{\frac{-z}{\lambda\left(E_A\right)\cos(\theta)}}\, dz, \tag{4.1}$$

the integral over the depth z easily allows to take into consideration the presence of a layered structure. It is convenient to define the XPS intensity generated by a homogeneous infinitely thick layer as:

$$I_A^{\infty} = \sigma_A(h\nu)\, T\left(E_A\right) \Phi N_A \lambda_A\left(E_A\right) \cos(\theta), \tag{4.2}$$

where it should be noticed that a subscript has been added to the mean free path $\lambda_A\left(E_A\right)$: since the materials will not in general be homogeneuos, this expression will indicate the mean free path of the photoelectrons from element A traveling through element A. Considering now the presence of a single overlayer (element A) of thickness d over an infinitely thick substrate (element B) as in Figure 4.6 and assuming the layers to be uniform and flat, their XPS intensities become:

$$I_A = I_A^{\infty}\left(1 - e^{\frac{-d}{\lambda_A\left(E_A\right)\cos(\theta)}}\right) \tag{4.3a}$$

$$I_B = I_B^{\infty}\left(e^{\frac{-d}{\lambda_A\left(E_B\right)\cos(\theta)}}\right). \tag{4.3b}$$

These equations can be seen as if the terms in parentheses modified (reduced) the intensity of some infinitely thick layers I_A^{∞} and I_B^{∞} respectively. In the first

case (equation 4.3a), this reducing factor takes into account the finite thickness d of the A layer. In the second case (equation 4.3b), the factor represents the attenuation that a signal from an infinite layer B experiences due to the scattering events occurring through the layer A. It should be noticed that, if the values of I_A^∞ and I_B^∞ are known, and the mean free paths are estimated through one of the semi-empirical formulas mentioned in Section 2.2.4, each of equations 4.3a and 4.3b can provide an estimate of d. In practice it is usually more convenient to measure the ratio of the intensities:

$$\frac{I_A}{I_B} = \frac{I_A^\infty}{I_B^\infty} \left(\frac{1 - e^{\frac{-d}{\lambda_A(E_A)\cos(\theta)}}}{e^{\frac{-d}{\lambda_A(E_B)\cos(\theta)}}} \right). \tag{4.4}$$

By doing so, all the material independent terms of the equation like the photon flux Φ will cancel out. Furthermore the final value of d will now depend on the relative values of I_A^∞ and I_B^∞ instead of their absolute values whose uncertainty is much higher. More importantly, the absolute values of I_A^∞ and I_B^∞ can be measured on reference samples as already described in *method 2* of Section 2.2.2, but these measurements are not always practical. Alternatively, the ratio I_A^∞ / I_B^∞ can be easily calculated from Scofield cross sections or Wagner sensitivity factors as in *method 1* and *method 3*.

If the orbitals of element A and B can be properly chosen, so that the kinetic energies $E_A \approx E_B$ and $\lambda_A(E_A) \approx \lambda_A(E_B)$ equation 4.4 can be simplified. Thus the thickness d can be written in the explicit form:

$$d = \lambda_A(E_A)\cos(\theta) ln\left(1 - \frac{I_A/I_A^\infty}{I_B/I_B^\infty}\right). \tag{4.5}$$

It is sometimes convenient to write this equation in the form:

$$ln\left(1 - \frac{I_A/I_A^\infty}{I_B/I_B^\infty}\right) = \frac{d}{\lambda_A(E_A)\cos(\theta)}, \tag{4.6}$$

so that the quantity on the left can be plotted in a graph as a function of $1/(\lambda_A(E_A)\cos(\theta))$ for measurements taken at different angles θ: the slope of the graph will represent the estimate of d.

4.5.2 Polycrystalline alloys

In the case of polycrystalline alloys the structure is more complicated, but the describing equations are based on the same principles as in the previous section. After

electrochemical measurements a pure Pt overlayer of thickness d is imposed over a bulk alloy indicated in general as Pt_nM_m: where M will typically stand for one of the lanthanide metals of this chapter. Organic contaminations mainly consisting of C, O and H are taken into account as a further overlayer of thickness t. All three layers are assumed to be uniform and flat as illustrated in Figure 4.7.

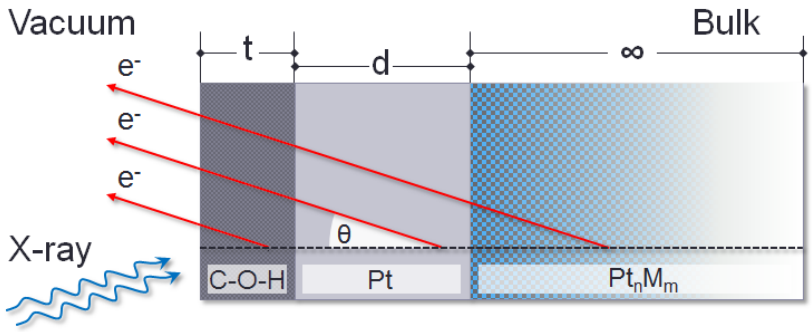

Figure 4.7: Sketch of typical layered structure of a Pt_nM_m alloy after ORR activity test. A layer of C, O and H contaminations (C-O-H layer) of thickness t lies on top of all samples. This is followed by a pure Pt overlayer of thickness d over an infinitely thick bulk alloy with stoichiometry Pt_nM_m. The emitted photoelectrons are emitted along straight lines with an angle θ with respect to the surface normal.

The information about the thickness of the Pt overlayer d will be provided by the signals of Pt and M. These will be expressed as:

$$I_{Pt} = \left[I^{\infty}_{\substack{Pt,\\ alloy}} \left(e^{\frac{-d}{\lambda_{Pt}(E_{Pt})\cos(\theta)}} \right) + I^{\infty}_{Pt} \left(1 - e^{\frac{-d}{\lambda_{Pt}(E_{Pt})\cos(\theta)}} \right) \right] A \quad (4.7a)$$

$$I_{M} = \left[I^{\infty}_{\substack{M,\\ alloy}} \left(e^{\frac{-d}{\lambda_{Pt}(E_{M})\cos(\theta)}} \right) \right] B, \quad (4.7b)$$

where the terms $I^{\infty}_{Pt,alloy}$ and $I^{\infty}_{M,alloy}$ represent the XPS intensities of Pt and M respectively from an infinitely thick Pt_nM_m alloy; both these terms are attenuated in parentheses by the presence of the Pt overlayer. The second term in the sum of 4.7a represents the contribution to the Pt signal from the Pt overlayer. The constants A and B take into account the attenuation of the two signals in the C-O-H

contamination layer, and are respectively equal to:

$$A = e^{\frac{-t}{\lambda_{COH}\left(E_{Pt}\right)\cos(\theta)}} \tag{4.8a}$$

$$B = e^{\frac{-t}{\lambda_{COH}\left(E_{M}\right)\cos(\theta)}}, \tag{4.8b}$$

with λ_{COH} representing the mean free path of the electrons in the C-O-H layer. In general the parameters A and B are expected not to affect dramatically the values of d. Indeed, A and B only differ for the values of the mean free paths that will also be similar as long as we can choose $E_M \approx E_{Pt}$; meaning that they will to a good extent cancel out when considering the intensity ratio I_{Pt}/I_M. It should be noticed that the contaminations are mainly due to water and adsorbed organic species whose mass density is very low in comparison with the one of Pt. This means that the mean free paths of the electrons traveling through this layer will be rather high and that the attenuation factors A and B will not usually be much lower than 1: most of all when the samples are treated carefully and readily transferred between the XPS system and the EC cell. In these cases the amount of contamination does not vary abruptly, typically corresponding to a thickness of 4-12 Å. The estimate of these values and the influence of t on the determination of the Pt overlayer thickness d when the approximation $E_M \approx E_{Pt}$ is not verified will be discussed later for a particular case (see Section 4.5.3).

In order to solve equations 4.7a and 4.7b and determine d the crucial point is the choice of the three quantities: I^{∞}_{Pt}, $I^{\infty}_{Pt,alloy}$ and $I^{\infty}_{M,alloy}$. These are explicitly defined as:

$$I^{\infty}_{Pt} = \sigma_{Pt}(h\nu)\, T\left(E_{Pt}\right) \Phi N_{Pt} \lambda_{Pt}\left(E_{Pt}\right) \cos(\theta) \tag{4.9a}$$

$$I^{\infty}_{\substack{Pt,\\ alloy}} = \sigma_{Pt}(h\nu)\, T\left(E_{Pt}\right) \Phi N_{\substack{Pt,\\ alloy}} \lambda_{alloy}\left(E_{Pt}\right) \cos(\theta), \tag{4.9b}$$

$$I^{\infty}_{\substack{M,\\ alloy}} = \sigma_{M}(h\nu)\, T\left(E_{M}\right) \Phi N_{\substack{M,\\ alloy}} \lambda_{alloy}\left(E_{M}\right) \cos(\theta). \tag{4.9c}$$

Since I^{∞}_{Pt} and $I^{\infty}_{Pt,alloy}$ are related by the simple relation:

$$I^{\infty}_{Pt} = \left(\frac{N_{Pt}\lambda_{Pt}\left(E_{Pt}\right)}{N_{\substack{Pt,\\ alloy}} \lambda_{alloy}\left(E_{Pt}\right)} \right) I^{\infty}_{\substack{Pt,\\ alloy}} = C I^{\infty}_{\substack{Pt,\\ alloy}}, \tag{4.10}$$

with the definition of this coefficient C, whose terms are known or easily estimated, two quantities are sufficient for calculating d: for instance $I^{\infty}_{Pt,alloy}$ and $I^{\infty}_{M,alloy}$. As in the case of a single overlayer (see Section 4.5.1) employing the ratio I_{Pt}/I_M

allows to simplify the calculation and cancel the material independent terms:

$$\frac{I_{Pt}/I^{\infty}_{Pt,\,alloy}}{I_M/I^{\infty}_{M,\,alloy}} = \frac{\left(e^{\frac{-d}{\lambda_{Pt}(E_{Pt})\cos(\theta)}} \right) + C\left(1 - e^{\frac{-d}{\lambda_{Pt}\left(E_{Pt}\right)\cos(\theta)}} \right)}{\left(e^{\frac{-d}{\lambda_{Pt}\left(E_M\right)\cos(\theta)}} \right)} \frac{A}{B}, \tag{4.11}$$

which is the relevant formula for the numerical determination of d. Also in this case, if the energies of the Pt and M XPS peaks can be chosen so that $E_M \approx E_{Pt}$, then $A \approx B$ and the other exponentials in equation 4.11 are all similar: substituting them by the term x, equation 4.11 can be written in a more compact form.

$$R^{\star} = \frac{I_{Pt}/I^{\infty}_{Pt,\,alloy}}{I_M/I^{\infty}_{M,\,alloy}} = \frac{x + C\,(1-x)}{x}, \tag{4.12}$$

with the definition of this ratio of normalized intensities $R^{\star}$ including all the necessary XPS data. This expression leads to:

$$ln\left[1 + \frac{1}{C}\left(1 - R^{\star}\right)\right] = \frac{d}{\lambda_{Pt}\left(E_{Pt}\right)\cos(\theta)}. \tag{4.13}$$

Equation 4.13 allows to explicitly write the expression of d and to plot the left term as a function of $1/(\lambda_{Pt}\left(E_{Pt}\right)\cos(\theta))$: the slope of this graph represents the thickness d, similar to the single overlayer case 4.5.1.

As already mentioned, the last requirement for the calculation of d is the actual determination of the terms I^{∞}_{Pt}, $I^{\infty}_{Pt,alloy}$ and $I^{\infty}_{M,alloy}$ (equations 4.9a-4.9c). By employing the three quantification methods described in 2.2.2 to determine these quantities, three different approaches can be distinguished. Since the approximations and assumptions involved in the methods are substantially different, two of these possibilities will be introduced in the following paragraphs.

Method 1. Scofield sensitivity factors

With this choice the theoretical Scofield cross sections σ can be easily found in literature and substituted in the expressions 4.9a-4.9c. Of the remaining terms, Φ and $\cos(\theta)$ are element independent and they cancel out when calculating the ratio I_{Pt}/I_M. The transmission function T is known, the atomic densities N can be easily calculated from the known structures of Pt and of the polycrystalline alloys

and the mean free paths λ can be estimated by the TPP-2M or the Cumpson-Seah semi-empirical formulas of Section 2.2.4.

The main limit of this theoretical approach is the uncertainty on the cross sections σ, both due to the intrinsic limits of the theoretical models and, most importantly, to the experimental difficulties of choosing backgrounds and energy ranges correctly. In the case of lanthanide metals this issue is even more important as a number of satellites might arise from the interactions with the f orbitals (see Section 3.3) and the choice of backgrounds and energy ranges is to some extent arbitrary. The importance of this point is highlighted when the XPS measurements taken on sputter-cleaned polycrystalline alloys are considered. The measured Pt to M ratios quite often differ from the expected nominal ratios of the alloys. The appearance of the correct XRD patterns suggests that in the bulk of the alloys the composition is quite close to the nominal one. Apart from the mentioned uncertainty on the cross sections and on the definition of the proper XPS intensities, these discrepancies could also be related to a surface effect: in particular, they might be produced by preferential sputtering of the elements Pt and M during the cleaning procedure. It should be noticed that AR-XPS experiments usually did not show any clear angular dependency of the Pt to M ratios after sputter-cleaning (see for instance Figure 3.5 a,b), suggesting that the surface composition is uniform after cleaning.

For the purpose of this section (*i.e.* determining the thickness of the Pt overlayer) it is important to keep in mind two possibilities. If these discrepancies on sputter-cleaned samples are related to a real surface enrichment (*e.g.* due to preferential sputtering) this method will still successfully describe the alloy after electrochemical measurements. Indeed the estimate of d will not incorporate any information from the XPS measurements acquired during sputtering. On the contrary, if these discrepancies are due to errors in the cross sections or in the background subtraction, they will result in an underestimate (or overestimate) of d: depending on the fact that the measured ratios on sputter-cleaned samples are respectively lower (or higher) than the nominal ratio.

Method 2. Measured sensitivity factors

The idea of this second approach is to avoid using tabulated data of sensitivity factors and substitute them with experimental values. The choice of the sensitivity factors, however, is original of this work and it comes from the observation that the values $I^{\infty}_{Pt,alloy}$ and $I^{\infty}_{M,alloy}$ are exactly the XPS intensities of Pt and M measured on a sputter-cleaned alloy. This is true under the assumption that the sputter-cleaned samples are effectively representing a homogeneous alloy with the correct nominal stoichiometry: basically the opposite assumption of *method 1*. In this sense, the two methods complement each other because in this case, a real surface enrichment of one element would lead to an incorrect estimate of d but no errors in

the estimate of the cross sections or in the definition of the backgrounds can easily occur. Furthermore, the measurement of the sensitivity factors is considerably easier then on clean foils, due to the difficulties of cleaning foils of lanthanides for instance, due to their high reactivity and oxophilicity. Furthermore, the Pt and M signals are measured under exactly the same conditions (*e.g.* same photon flux and exact same geometry of the XPS setup) that would be harder to reproduce when measuring on different reference samples.

The third necessary parameter is I_{Pt}^{∞} that could also be measured on a clean Pt reference sample. However, in order to maintain the simplicity of this method and avoid the introduction of further experimental errors a different approach was chosen. Namely, I_{Pt}^{∞} was directly derived from the value of $I_{Pt,alloy}^{\infty}$ according to equation 4.10. Consistent to the previous choice, the assumption here is that the atomic concentration in the alloy $N_{Pt,alloy}$ is the one expected from a Pt_nM_m stoichiometric compound.

4.5.3 Test on Pt_5Gd

In this section the model will be applied to the particular case of Pt_5Gd in order to elucidate the fitting procedure and to verify some of the involved assumptions: in particular, the two quantification methods will be tested in order to find the most reliable. The choice of this polycrystalline alloy is related to the fact that in terms of activity and stability it is probably the most promising material reported in this work and a particularly extensive characterization was performed. Furthermore, from an XPS point of view it represents a good model case as it allows to choose at least two XPS peaks for quantification: Gd 4d at a binding energy $\approx$ 141 eV and Gd $3d_{5/2}$ at $\approx$ 1187 eV. This will not be always the case for the other lanthanides due to the low intensity of some core level peaks and their overlap with the Pt peaks. The kinetic energies E of the photoelectrons from the Gd 4d and Gd $3d_{5/2}$ core levels are also very different: $\approx$ 1341 eV and $\approx$ 295 eV respectively. In the case of Pt, the Pt 4f peak was always chosen: binding energy $\approx$ 71 eV and kinetic energy $\approx$ 1411 eV. The distance in energy of the Gd 4d and Gd $3d_{5/2}$ is important for verifying the validity of the model at different energies. Indeed, it will always be easier and the model will in general work better, when quantifying the Pt to Gd ratios using the Gd 4d peak, since the condition $E_{Pt} \approx E_{Gd}$ is verified and some of the energy dependent terms of equation 4.11 (*e.g.* the coefficients A and B) will tend to cancel. Furthermore the effect of errors in the estimate of the mean free path from the TPP-2M or the Cumpson-Seah formulas will be minimized. It should be noted that the Gd $3d_{5/2}$ peak, with such low kinetic energies, represents an extreme case and it will only be employed in this section for the purpose of testing the range of applicability of the model.

Starting from the initial preparation, the Pt_5Gd sample was cleaned in UHV following the same sputter-cleaning procedure described in 2.3 and normally ap-

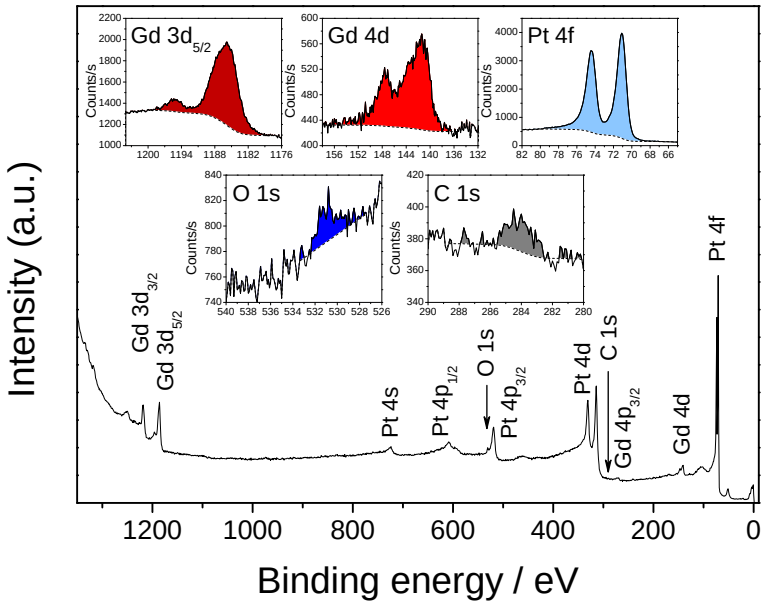

Figure 4.8: Overview XPS spectrum of the Pt_5Gd polycrystal after sputter-cleaning (as-prepared), with assignment of the main peaks. In the insets, the detailed spectra used for general quantification purposes are shown, with the typical choice of backgrounds and energy ranges.

plied before EC measurements. An overview XPS spectrum was acquired together with detailed AR-XPS spectra of the peaks Pt 4f, Gd 4d, Gd $3d_{5/2}$, O 1s and C 1s. Figure 4.8 shows the overview spectrum with details of the relevant peaks and the typical choices of energy ranges and backgrounds. Small signals from O and C raised during the time needed for the measurements, probably due to the high reactivity of the exposed Gd atoms: overall these signals still accounted for less than 2 %. The XPS intensities of the Pt 4f, Gd 4d (or Gd $3d_{5/2}$) will determine the quantities $I^{\infty}_{Pt,alloy}$ and $I^{\infty}_{Gd,alloy}$ when applying *method 2* to the solution of equation 4.11, as described in 4.5.2.

Following these measurements the sample was transferred to the electrochemical setup and normal ORR activity tests were carried out as described in Section 2.5.1. Soon after electrochemistry new detailed AR-XPS measurements were taken in the same energy regions: energy ranges and backgrounds were chosen consistently in order to determine the I_{Pt}/I_{Gd} ratio in equation 4.11. The overview spectrum did not show other contaminations apart from increased amounts of C and O.

The Pt to Gd atomic ratios were determined for the sample as-prepared and

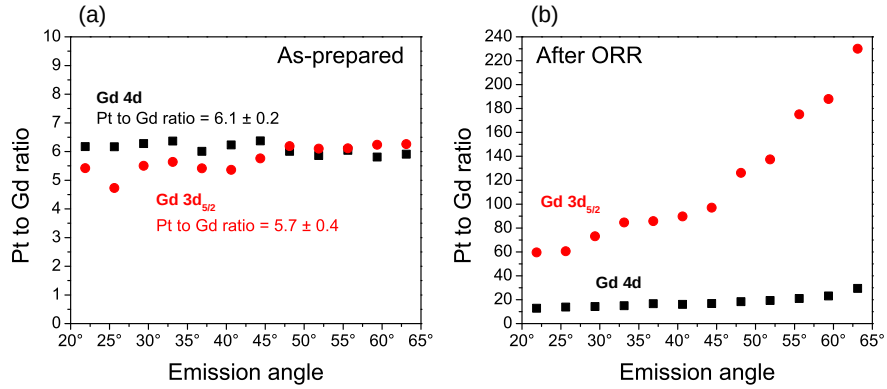

Figure 4.9: Pt to Gd XPS ratios obtained by application of *method 1* (*i.e.* Scofield cross sections) as a function of the electron emission angle. The ratios were measured choosing either the Gd 4d peak (black squares) or the Gd $3d_{5/2}$ peak (red circles). Data for the sputter-cleaned *as-prepared* Pt_5Gd alloy are shown on the left (a): on the right (b) ratios *after ORR* activity test.

after ORR activity test as a function of the emission angle by choosing Scofield cross sections (*method 1* in Section 2.2.2): the values are plotted in Figure 4.9 a. Both choosing the Gd 4d peak and the much more surface sensitive Gd $3d_{5/2}$ no clear angular dependence can be observed on the clean sample, suggesting that no preferential sputtering occurred. The homogeneity of the sample is also supported by the fact that Gd 4d and Gd $3d_{5/2}$ peaks predict a very similar composition despite their different surface sensitivity. It should be also noticed that the measured ratios are slightly higher than the nominal ratio of 5 expected for Pt_5Gd: about 6.1 in the case of Gd 4d and 5.7 in the case of Gd $3d_{5/2}$. As already mentioned similar or even bigger discrepancies were often noticed when applying Scofield cross sections. After electrochemistry in Figure 4.9 b the atomic ratios increased considerably as a consequence of the Pt overlayer formation. The particularly high ratios measured in the case of Gd $3d_{5/2}$ are also in agreement with the higher surface sensitivity at these low kinetic energies.

Definition of the C-O-H contamination layer

The solution of equation 4.11 still requires a choice of the parameter t representing the thickness of the contamination layer. In order to have the most precise estimate of the amount of C and O contaminations and determine t to be inserted in the attenuation coefficients A and B (equations 4.8a and 4.8b), two alternative approaches were used.

A very mild sputtering of the surface was performed by using He ions at low

energy of 300 eV at a total ion current of 400 nA rastered over a large area of 6 mm $\times$ 6 mm. The choice of light ions and low energies allows to preferentially lower the sputter yield of Pt with respect to those of lighter atoms as O and C [113], facilitating the removal of contaminations without drastically affecting the structure of the alloy. After 30 minutes of treatment the amount of surface contaminations was substantially reduced from about 43 % to 4%, while the Pt to Gd ratio did not exhibit significant changes indicating a negligible removal of Pt atoms from the overlayer. By considering the ratio of Pt 4f XPS intensities (or Gd 4d intensities) before and after this cleaning procedure, the level of attenuation of the Pt signal (or Gd signal) due to the C-O-H layer is measured for all the angles: equation 4.8a and 4.8b allow to estimate the thickness t independently for the attenuation of Pt and Gd. Since the C-O-H layer is mainly composed of adsorbed water and organic contaminations an average mass density of 1 mg cm^{-3} was chosen for the estimate of the electron mean free paths; with this assumption the TPP-2M formula gave $\lambda_{COH}\left(E_{Pt}\right) = 35.6$ Å for the Pt 4f electrons and $\lambda_{COH}\left(E_{Gd}\right) = 34.1$ Å for the Gd 4d electrons. The estimated thickness were $t = 6.7 \pm 0.5$ Å from the Pt 4f signal and $t = 6.2 \pm 3.0$ Å from the Gd 4d signal. As in the rest of this section the errors were estimated from the standard deviation of measurements at different angles, the higher uncertainty in the case of Gd is due to the much lower intensity of the Gd 4d signal. These values are consistent with a contamination layer consisting of a few adsorbed monolayers of water and organic impurities.

Although maybe more reliable the method described so far is not practical for a general estimate of the amount of contaminations and of the thickness t of the C-O-H layer which should be directly derived from the AR-XPS measurements without the addition of such particular cleaning procedure. The quantity t will in general be derived from the XPS intensities of C, O and Pt with the following

equations:

$$\frac{I_{Pt}}{I_C} = \frac{I_{Pt}^{\infty}\left(e^{\frac{-t}{\lambda_{COH}(E_{Pt})\cos(\theta)}}\right)}{I_C^{\infty}\left(1-e^{\frac{-t_C}{\lambda_{COH}(E_C)\cos(\theta)}}\right)} \tag{4.14a}$$

$$\frac{I_{Pt}}{I_O} = \frac{I_{Pt}^{\infty}\left(e^{\frac{-t}{\lambda_{COH}(E_{Pt})\cos(\theta)}}\right)}{I_O^{\infty}\left(1-e^{\frac{-t_O}{\lambda_{COH}(E_O)\cos(\theta)}}\right)}, \tag{4.14b}$$

where I_C and I_O are the XPS intensities from the C 1s and the O 1s XPS peaks. With the same considerations of Section 4.5.2 the exponential on top defines the attenuation of the Pt signal through the C-O-H layer while the one in the bottom is the C or O signal produced by a layer of C and O respectively: t_C and t_O are defined as the thicknesses of C and O under the simplifying assumption that they are spatially separated, hence $t = t_C + t_O$. Also in this case the mass density is taken as 1 mg cm^{-3} for both the C and the O parts, which means that in terms of attenuation of the Pt signal the two layers will have the same effect. The constants $I_{Pt,alloy}^{\infty}$, I_O^{∞} and I_C^{∞} are calculated from their definition (see equation 4.2) by using the Scofield cross sections of Pt, C and O. Once these parameters are known, equations 4.14a and 4.14a can be combined in order to determine t_C and t_O and consequently, t. For the particular case under study, this model predicted $t_C = 4.5$ Å and $t_O = 3.4$ Å so that $t = 7.9$ Å: a value which is reasonably close to the value of 6.7 Å measured with the previous approach. To summarize, equations 4.14a and 4.14b will be generally used to calculate the value of t, however in this particular case the value of $t = 6.7$ Å will be chosen for the following considerations.

Test of method 1.

Now that all the parameters have been determined, equation 4.11 allows to estimate the thickness of the Pt overlayer. Starting from *method 1* and the choice of Scofield cross sections for quantification, Figure 4.10 reports the calculated thicknesses d of the Pt overlayer for Pt_5Gd after ORR. All electron mean free paths were estimated from the TPP-2M formula. In order to check the influence of different levels of contaminations, different values of t have been chosen and are shown on

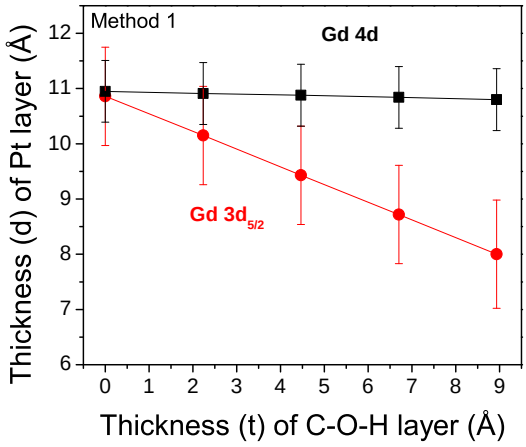

Figure 4.10: Thickness d of the Pt overlayer as calculated by *method 1* for different values of t (thickness of the C-O-H contamiantion layer). The calculation was made both choosing the Gd 4d (black squares) and the Gd $3d_{5/2}$ (red circles) XPS intensities. Error bars are taken as the standard deviation of the values calculated at 12 different emission angles between 21° and 65°.

the x axis: the estimated value of $t = 6.7$ Å in particular was also chosen. As in the rest of these calculations the error bars have been taken as the standard deviation of the thickness calculated at 12 different emission angles between 21° and 65° from the surface normal. All calculated thicknesses are between 8 and 11 Å which is in the same range as those predicted by the angle-resolved profiles reported before for Pt_5Gd [132]. As expected, different values of t have almost no influence on the Pt overlayer thickness when the Gd 4d peak is chosen for quantification: this is because $E_{Pt} \approx E_{Gd}$. However, in the case of Gd $3d_{5/2}$ an approximately linear dependence is observed and the values of d vary considerably, complicating a precise quantification. For this reason, XPS peaks with lower binding energies will be usually preferred. More importantly, when focusing on the relevant values of $t \approx 6.7$ Å, the choice of the two Gd peaks leads to quite different estimates: $d \approx 11.0$ Å for Gd 4d and $d \approx 8.7$ Å for Gd $3d_{5/2}$. This discrepancy could in principle be due to inaccuracies in the estimate of the electron mean free path at such different kinetic energies. In the present work a different interpretation is suggested.

As mentioned in Section 4.5.2 this first method assumes that the theoretical Scofield cross sections are correct and consistent with the experimental choice of XPS intensities. In other words, this would mean that in Figure 4.9 a the measured ratios (6.1 in the case of Gd 4d and 5.7 in the case of Gd $3d_{5/2}$) differ from the stoichiometric ratio of 5 due to a real Pt enrichment at the surface. Figure 4.11 shows

how the thickness d varies from the original values under a different assumption: the Scofield cross sections are now considered as inaccurate and they have been corrected in order to produce the stoichiometric ratio of 5 on the as-prepared sample.

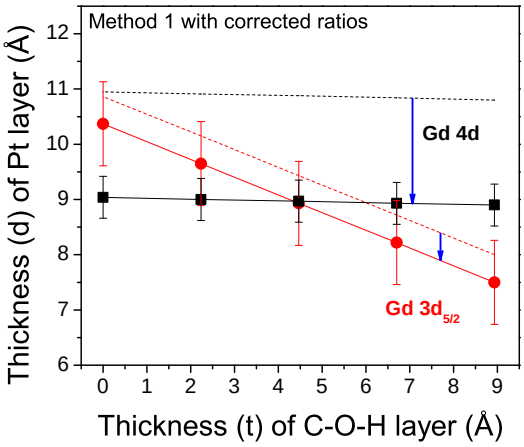

Figure 4.11: Thickness d of the Pt overlayer for different values of t (thickness of the C-O-H contamination layer). The originally calculated values (dotted lines) have been corrected by assuming that Scofield cross sections are inaccurate (full lines): Scofield cross sections have been modified in order to provide a Pt to Gd ratio of 5 in the measurements on a sputter-cleaned sample (see Figure 4.9 a).

With this correction, the two lines corresponding to the Gd 4d and the Gd $3d_{5/2}$ peaks move down and predict smaller thicknesses, particularly in the case of the Gd 4d peak which is less sensitive to the presence of contaminations but more sensitive to errors in the quantification of the Pt to Gd ratios. The two lines now cross each other at a value of $t \approx 4.5$ Å, reasonably close to the estimated value 6.7 Å. Most importantly at $t = 6.7$ Å the choice of the two peaks lead to a similar estimate of the Pt thickness, within the experimental uncertainty: $d \approx 9.1$ Å and $d \approx 8.2$ Å respectively. This is a further evidence of the fact that the measured discrepancies from the measured ratios on sputter-cleaned samples are mainly due to inaccuracies in the Scofield cross sections or in their association to the measured intensities. This also suggests that *method 1* does not provide the best estimate of the Pt overlayer thickness and that *method 2* should be preferred.

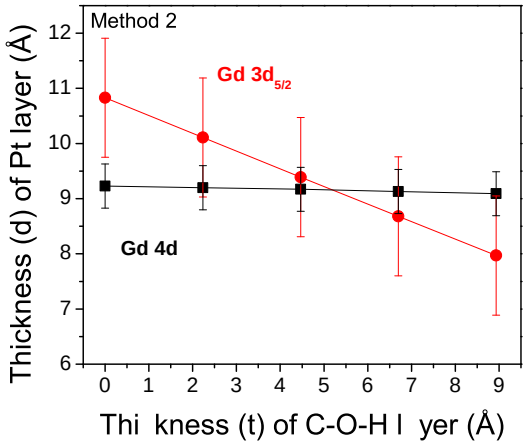

Figure 4.12: Thickness d of the Pt overlayer as calculated by *method 2* for different values of t (thickness of the C-O-H contamiantion layer). The calculation was made both choosing the Gd 4d (black squares) and the Gd $3d_{5/2}$ (red circles) XPS intensities. Error bars are taken as the standard deviation of the values calculated at 12 different emission angles between 21° and 65°.

Test of method 2.

The results of the application of *method 2* to equation 4.11 are shown in Figure 4.12. The assumption here is to have homogeneous stoichiometric alloys after the sputter-cleaning procedure so that the terms $I^{\infty}_{Pt,alloy}$ and $I^{\infty}_{M,alloy}$ can be directly measured. In this sense the correction applied to *method 1* is already included; therefore it is not surprising that the calculated thicknesses are similar to those of Figure 4.11. At the value of $t = 6.7$ Å the thickness of the Pt overlayer is similar for the choice of Gd 4d and Gd $3d_{5/2}$ peaks: $d \approx 9.0$ Å and $d \approx 8.7$ Å respectively. This indicates that the method can be applied over a wide range of kinetic energies: a property that will be particularly important when comparing the thicknesses of the Pt overlayer for different alloys with lanthanide XPS peaks in different energy positions. The estimated thickness of the C-O-H layer seems to be reasonable and the energy dependence of the TPP-2M electron mean free paths seem to provide consistent results. Compared to *method 1*, the error bars are slightly broader, probably due to the fact that experimental values are also used for the quantities $I^{\infty}_{Pt,alloy}$ and $I^{\infty}_{M,alloy}$, adding further experimental uncertainty to the estimate.

Since this method seem to give the best estimates of d, it will be also employed to verify two more conditions. In Figure 4.13 the TPP-2M formula, employed so

far, is compared to the Cumpson-Seah formula for the estimate of the electron mean free paths. A decrease in the estimated thicknesses can be easily observed in all cases. This is just a consequence of the fact that the Cumpson-Seah formula predicts in general lower electron mean free paths [112]. However the decrease is very similar in all cases, always leading to $\approx$ 15% lower values of d, indicating that the energy dependence of the formula is very similar for both TPP-2M and Cumpson-Seah expressions. Since the main interest of this work is to compare the thickness of the Pt overlayers for different alloys, the choice of the two formulas will basically be equivalent and only the TPP-2M formula will be used in the following.

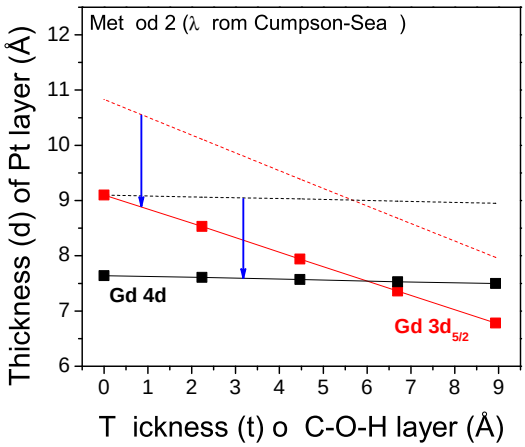

Figure 4.13: Thickness d of the Pt overlayer as calculated by *method 2* for different values of t (thickness of the C-O-H contamiantion layer). Results from the use of the TPP-2M formula (dotted lines) and of the Cumpson-Seah formula (full lines) are compared.

A final test of this method concerns the quality of the fit; in Section 4.5.2 it was shown how equation 4.11 can be simplified to equation 4.13 under the assumption of $E_{Pt} \approx E_{Gd}$. In Figure 4.14 the left side of equation 4.13 is plotted *vs.* $1/\left(\lambda_{Pt}\left(E_{Pt}\right)\cos(\theta)\right)$, which should give a linear relationship with a slope equal to thickness d of the Pt overlayer. Clearly, with the choice of the Gd $3d_{5/2}$ peak the assumption is not verified and a simple line does not fit well the experimental points. In particular, the intercept of the line lies far above the origin of the graph and the estimated value of $d = 14.9$ Å is far from the values presented above. Contrarily, the approximation works quite well in the case of the Gd 4d peak. The measured points lie on a line approximately crossing the origin of the axis and the estimated thickness of the Pt overlayer is $d = 9.8$ Å, which only slightly higher than the values of Figure 4.12. Figure 4.14 also shows that at very high emission angles the model fails. This is probably due to the presence of elastic scattering effects [112] and to the difficulties in achieving an accurate quantification of the XPS

intensities that become very low in these conditions, particularly for the strongly attenuated Gd peaks. This is also the reason why the angles over 65° have been omitted in the linear fit and for all the quantification purposes of this work.

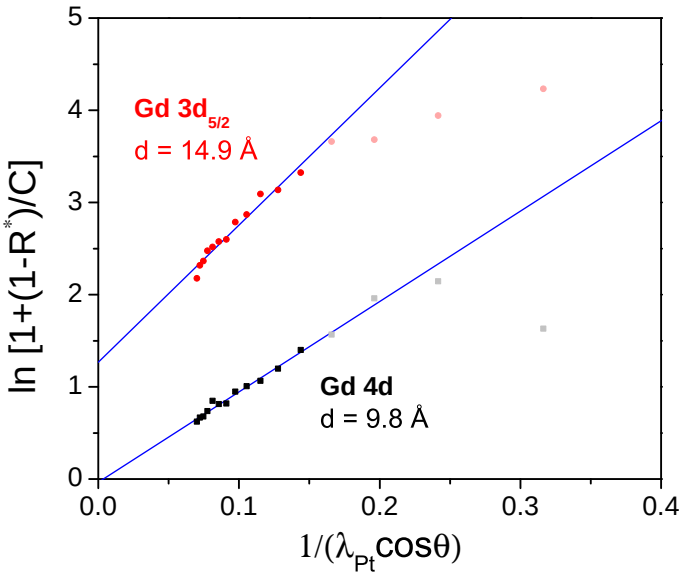

Figure 4.14: Plot of the results from *method 2*: if the approximation $E_{Pt} \approx E_{Gd}$ is verified a linear relationship should hold between the left term of equation 4.13 on the y axis and the quantity $1/\left(\lambda_{Pt}\left(E_{Pt}\right)\cos(\theta)\right)$ on the x axis. The experimental points for the Gd 4d (black squares) and for the Gd $3d_{5/2}$ (red circles) peaks are plotted with their linear fit represented by the blue lines. Grey and pink points represent electron emission angles higher than 65° which were not considered in the linear fit. The slope of the lines represents the estimated thickness of the Pt overlayer d.

4.6 Thickness of the Pt overlayers

In the previous section the application of *method 2* seemed to give the most reliable estimate of the Pt overlayer thickness for a particular AR-XPS measurement on Pt_5Gd after ORR, providing similar values for both the Gd 4d and Gd $3d_{5/2}$ peaks, despite their considerable distance in terms of energies. The fact that no strong preferential sputtering seem to occur on these alloys and that the intensity ratios obtained from Scofield cross sections do not seem accurate is also suggesting *method 2* as the most appropriate. Herein this method was applied to some

of the other alloys tested in this work in order to investigate possible trends in the thickness of these overlayers. The application to different alloys is not always straightforward due to the necessity of finding proper XPS peaks. These should be sufficiently intense and they should not overlap with other peaks from Pt, or O, C contaminations; preferably they should lie at sufficiently low binding energies (high kinetic energies) in order to minimize the influence of contaminations in the calculation. Proceeding in the order of atomic number the following XPS peaks were chosen for the correspondent alloys: La 3d, Ce 3d, Gd 4d, Tb 4d and Dy 4d. The La 4d and Ce 4d peaks unfortunately overlap with some of the Pt peaks. Indeed, the La 3d (binding energy ≈ 834 eV) and Ce 3d peaks (binding energy ≈ 884 eV) have rather low photoelectron kinetic energies, but still considerably higher than for the case of Gd $3d_{5/2}$ so that the applicability of the model should still hold.

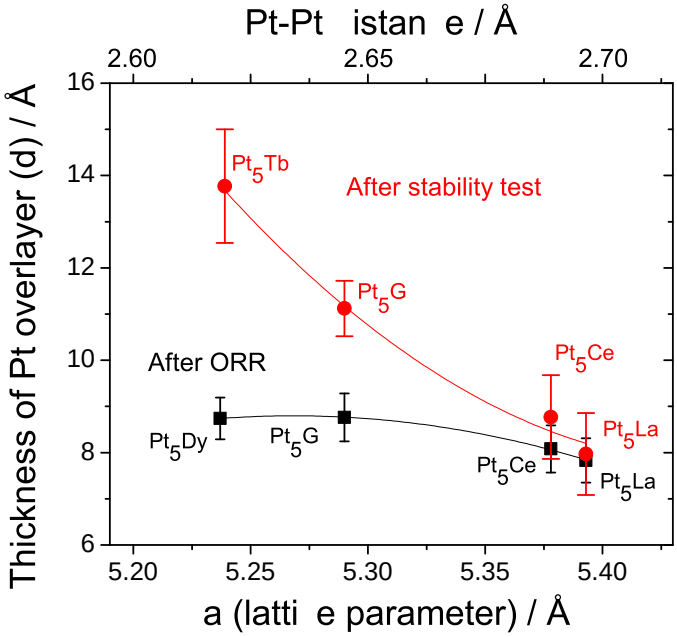

Figure 4.15: Estimated thicknesses (d) of the Pt overlayer for some Pt_5Ln alloys after ORR and after stability test. Values are plotted as a function of the lattice parameter (a) of the bulk (as measured by XRD) and on the top axis, of the Pt-Pt nearest neighbour distance in the bulk ($d_{Pt-Pt} = a/2$), which is expected to define the Pt-Pt distance in the overlayer. Error bars are taken as the standard deviation of the values calculated at 12 different emission angles between 21° and 65°, when possible, including results from more indipendent AR-XPS measurements.

Figure 4.15 shows the estimated thicknesses for some AR-XPS measurements

on these alloys after ORR activity testing and after stability tests. The thicknesses have been plotted as a function of the lattice parameter of the alloys, or alternatively, on the top axis, the correspondent nearest neighbour Pt-Pt distance in their bulk which is expected to define the strain in the Pt overlayer. Focusing on the measurements after ORR the measured thicknesses are similar for all alloys, possibly with a slight trend towards thicker overlayers in the samples with a higher level of compression. After stability tests this trend becomes very clear. For all samples the model predicts a thickening of the Pt overlayer which is a good indication of the reliability of the measurements and of the model. However, in the case of Pt_5La and Pt_5Ce the increase is very limited (lower than 1 Å) while for Pt_5Gd and Pt_5Tb it is in the order of 2 and 5 Å respectively. This trend is in agreement with the trends in stability measured for these alloys and an indication of the fact that the activity losses are primarily due to a slightly further level of dealloying in these materials. This corresponds to a thicker overlayer and probably to a higher level of strain relaxation. In other words, these measurements confirm the idea that a higher level of strain in the Pt overlayer with respect to pure Pt results in a lower intrinsic stability of the overlayer. Unfortunately this would also mean that for these kind of alloys the trend in activity and the trend in stability go in opposite directions. In the perspective of an application into a fuel cell, assuming that these catalytic performances could be reproduced in the more technologically relevant form of nanoparticles, it would probably be important to find the best compromise in terms of activity and stability, also depending on the particular requirements of the final product.

It should be noted that the results of Figure 4.15 are still preliminary: the measurements for the Pt_5Tb after ORR and for Pt_5Dy after stability test are missing and some of the points are taken from a single AR-XPS measurement. Furthermore, it would be highly interesting to include some of the other alloys of this chapter (*e.g.* Pt_5Tm, Pt_5Ca) in order to confirm the observed trends.

CHAPTER 5

Pt-Y nanoparticles

5.1 Introduction

So far, most of this thesis has focused on the search for new materials catalysing the ORR; for this kind of fundamental research most of the studies were performed on extended surfaces, typically on polycrystalline samples (see Chapter 3 and 4). However, any kind of application in PEMFCs requires a high catalyst dispersion, particularly for Pt based catalysts where it is essential to minimize the use of precious metals and the *mass activity* (defined as the ORR activity per mg of Pt) is the important parameter. In the case of Pt and alloys of Pt with late transition metals, such high dispersion is typically achieved through the synthesis of nanoparticles over a large surface area carbon support. Although various techniques for the chemical-electrochemical synthesis of Pt and Pt alloys nanoparticles are well established, in the case of alloys of Pt and rare earths new synthesis techniques have to be exploited. The reasons for this are once more related to the very high reactivity of rare earths and in particular to their high affinity to oxygen, which makes it very difficult to reduce these materials and to form an alloy. In this chapter a physical method relying on the gas aggregation technique (see Section 2.5.2) is used to fabricate size-selected Pt-Y nanoparticles. Once deposited onto a planar glassy carbon support physical and electrochemical characterizations were performed. This chapter presents the very high ORR activity of these particles together with their physical characterization and a discussion about the origins of the enhanced activity. These samples represent good model catalysts to shed light on the fundamental relationship between activity, particle size, shape and morphology, without the complica-

tions and artifacts that might be introduced by wet chemical syntheses. Although this preparation method is not suitable for a large scale production, this is a first evidence that alloys of Pt and early transition metals in the nanoparticulate form can exhibit such high activities and potentially be employed in low temperature fuel cells. This chapter is based on Paper 5 in the end of this thesis. Patricia Hernandez-Fernandez performed the electrochemical measurements. Federico Masini, David N. McCarthy, Christian E. Strebel and Anders Nierhoff have been in charge of the nanoparticle fabrication and part of the UHV characterization. Davide Deiana performed the microscopy studies. Daniel Friebel, Anders Bodin and Anna M. Wise have been in charge of the X-ray Absorption Spectroscopy (XAS) analysis.

5.1.1 Size distribution and morphology

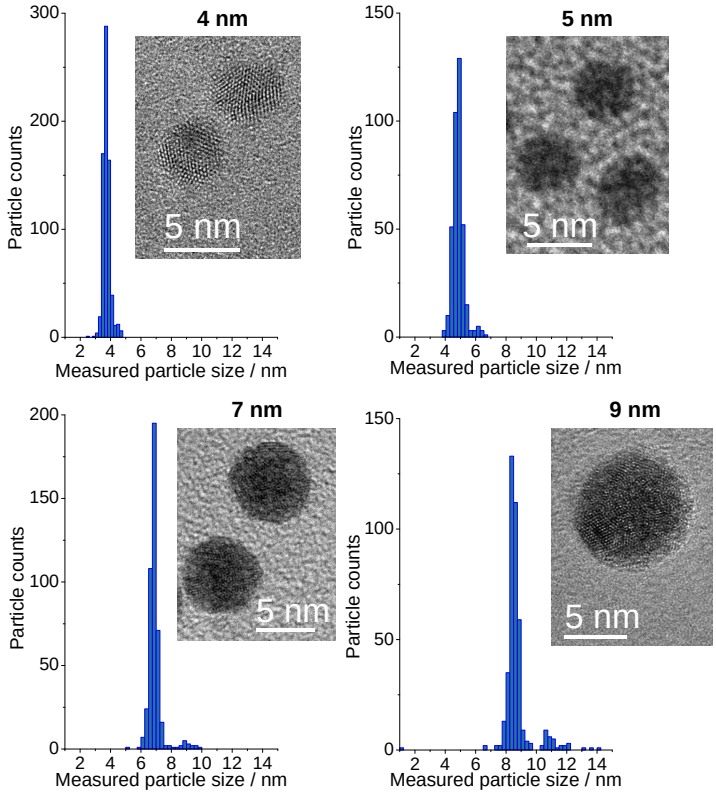

Figure 5.1: Particle size distributions of the as-prepared Pt-Y nanoparticles and correspondent typical TEM images for the four nominal sizes: 4 nm , 5 nm, 7 nm and 9 nm. Measurements performed by Davide Deiana.

In order to investigate the effective size selection, the nanoparticles were deposited under the same conditions (see Section 2.5.2) onto gold grids for Transmission Electron Microscopy (TEM) applications. The TEM measurements were performed in a separate setup: further details can be found in Paper 5 in the end of this thesis. Figure 5.1 shows the particle size distributions with correspondent selected TEM images for the four different sizes selected during this study. For nominal purposes the samples will be referred to with their originally intended sizes: 4 nm, 5 nm, 7 nm and 9 nm respectively. However, in the plots where the particle size appears as a numerical quantity on one of the axis the measured average size was used. As apparent from Figure 5.1 the measured average sizes turned out to resemble closely the intended sizes, with discrepancies considerably lower than 1 nm. A closer look at the histograms shows sharp narrow peaks around these mean values, demonstrating the high quality of the mass selection. Small satellite peaks can be noticed at higher sizes, particularly for the bigger particles. They are due to the presence of doubly charged nanoparticles during the mass selection, resulting in particles of double mass. Although the synthesis conditions were optimized to reduce these artifacts, the higher probability of having double charge in the largest particles could be reduced but not canceled. The TEM images show that the particles are spherical for all sizes. A close inspection of these images suggests that they are mainly polycrystalline nanoparticles as different crystalline orientations can be clearly observed.

5.2 Electrochemical characterization

After deposition onto the glassy carbon substrates and after an initial characterization by XPS, the alloy catalyst-loaded electrodes were transferred to the RRDE setup for the electrochemical characterization. This was preformed under similar conditions as for the other extended surfaces of this study (see Section 2.5.1). The samples were inserted into the electrochemical cell under potential control of 0.05 V *vs.* RHE in N_2 saturated 0.1 M $HClO_4$ electrolyte and cycled between 0.05 V and 1 V at a sweep rate of 50 mV/s until stable CVs were obtained. Later on the ORR activity tests were carried out in O_2 saturated 0.1 M $HClO_4$ electrolyte. Figure 5.2 summarizes the results for the four nominal particle sizes: the ORR activity is presented in terms of kinetic current density at 0.9 V *vs.* RHE, both in terms of specific and mass activity. For the determination of the specific activity the ECSA of the nanoparticles was measured by CO stripping as described in 2.5.1. Concerning the mass activity, the total amount of catalyst was determined from the particle beam current during deposition (see Section 2.5.2): the fraction of Pt mass was then deduced from the Pt to Y atomic ratios as measured by XPS just after deposition. The activity of size selected pure Pt nanoparticles was measured in a previous study and also reported for comparison in Figure 5.2 [64]. The specific activity of polycrystalline Pt and Pt_3Y extended surfaces is also plotted for the same purpose

[16].

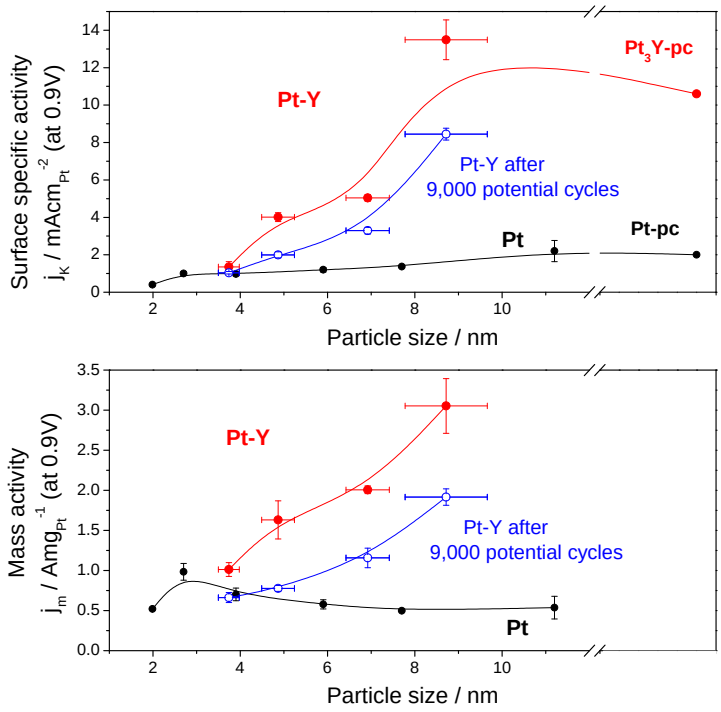

Figure 5.2: ORR specific activities and mass activities of the size-selected Pt-Y nanoparticles. Kinetic currents were recorded at 50 mVs^{-1}, 1600 rpm and 23 ± 1°C in O_2-saturated 0.1 M $HClO_4$ electrolyte. The previously published activities of pure Pt nanoparticles are also plotted for comparison [64]. Each data point represents an average of at least three independent measurements. The ORR activities were extracted from the anodic polarization scan and corrected for mass transport limitations. The activity of polycrystalline Pt_3Y was measured on a sputter-cleaned extended surface tested under the same conditions [16]. Measurements performed by Patricia Hernandez-Fernandez.

Apart from the smallest 4 nm nanoparticles, all the other Pt-Y samples exhibit a remarkable activity enhancement in specific activity. Similar to pure Pt, this activity increases while increasing the particle size and for the largest particles of 9 nm it resembles the value obtained for the extended surface of polycrystalline Pt_3Y. Focusing on the mass activity, the Pt-Y nanoparticles are also considerably more active than in the case of Pt. Interestingly, this mass activity increases monotonically with particle size, while for Pt nanoparticles it reaches a maximum at a size of approximately 3 nm: a particle size that is not optimal in terms of stability. The highest mass activity was measured on 9 nm Pt-Y nanoparticles, with a kinetic current of 3.05 A mg_{Pt}^{-1} at 0.9 V *vs.* RHE. This value corresponds to one of the highest mass

activities ever reported in literature, with more than a 5-fold enhancement with respect to state-of-the-art commercial Pt catalysts (0.55 A mg_{Pt}^{-1} [75]) and a 3-fold enhancement with respect to Pt nanoparticles prepared under the same conditions [64]. Higher mass activities were only measured on octahedral Pt-Ni nanoparticles, giving a similar value of 3.3 A mg_{Pt}^{-1} [92], and very recently on Pt_3Ni nanoframes with their record breaking activity of 5.7 A mg_{Pt}^{-1} [93].

In order to test the long-term stability of the nanoparticles, the catalysts were subjected to a total of 9 000 potential cycles between 0.6 V and 1 V *vs.* RHE. The conditions were the same as for the other stability tests of this thesis: details are given in 2.5.1. The results of the stability tests are also plotted in figure 5.2. Quite important activity losses can be observed for all particle sizes. These losses are quite similar in terms of specific activity and in terms of mass activity suggesting that the catalyst dispersion does not vary abruptly during cycling. In general the losses range between a 25 % and 50 %. Focusing for instance on the most active nanoparticles (nominal size of 9 nm), there is a 37 % loss of both specific and mass activity. Interestingly, the final mass activity of these 9 nm Pt-Y nanoparticles is still twice as high as the most active Pt nanoparticles of Figure 5.2 and more than three times more active than state-of-the-art commercial Pt catalysts (0.55 A mg_{Pt}^{-1} [75]). CO stripping experiments did not indicate a significant decrease of ECSA during cycling, suggesting the the main reason of deactivation is a decrease in specific activity: an example of CO stripping is found in Paper 5 in the end of this thesis, where Identical Location Transmission Electron Microscopy (IL-TEM) measurements confirm the same conclusion. It should be noticed that most of the activity losses occurred in the first 600 cycles; after this time a metastable condition is probably reached so that kinetic barriers hinder the further degradation of the catalyst. Under similar cycling conditions (5 000 cycles between 0.65 V and 1.0 V *vs.* RHE) the similarly active Pt-Ni octahedral nanoparticles reported by Choi *et al.* [92]) exhibited 40 % activity losses, very similar to these Pt-Y nanoparticles. A rigorous quantitative stability comparison would however require identical conditions and it should be ideally performed in a fuel cell. It should be also mentioned that, while ORR catalysts based on alloys of Pt and late transition metals have been studied for a couple of decades, this is the first reported attempt of fabricating Pt-Y nanoparticles for ORR; an extensive optimization might be required in order to find the best conditions for a high stability.

5.3 Physical characterization

5.3.1 X-ray photoelectron spectroscopy

Soon after deposition of the Pt-Y nanoparticles, XPS measurements were taken in-situ on the *as-prepared* samples with a setup similar to the one described in 2.2. In particular, the Pt to Y atomic ratios were measured in order to ensure a sim-

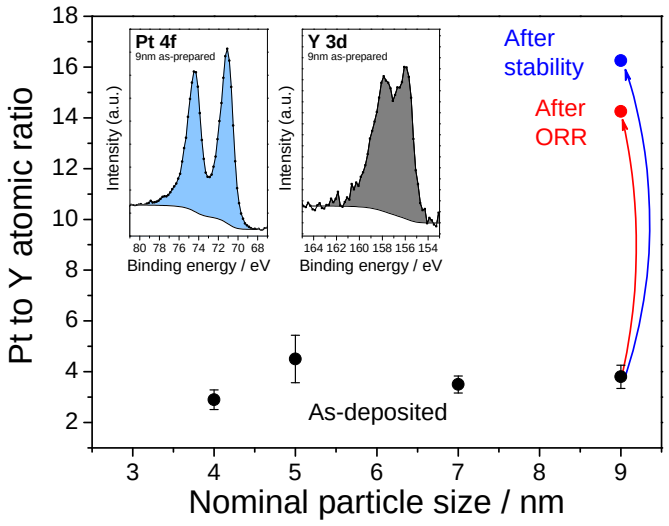

Figure 5.3: Pt to Y atomic ratios determined by XPS as a function of the nominal particle diameter. A clear increase of these ratios is observed after ORR and even more after stability tests for the 9 nm Pt-Y nanoparticles. In the inset, Pt 4f and Y 3d signals from the as-prepared 9 nm Pt-Y nanoparticles show the typical Shirley background subtraction and the areas used for quantification.

ilar composition for nanoparticles of different sizes. The results are reported in Figure 5.3 together with the Pt to Y ratios measured on a 9 nm Pt-Y sample *after ORR* and *after stability* test. In the inset, typical spectra of the Pt 4f and Y 3d core level regions can be also seen, with the typical choice of Shirley background and energy range. It can be noticed that the Pt to Y ratios of the as-prepared samples were quite similar for all sizes, although a certain variability between 3.1 and 4.3 was still observed. These ratios were obtained despite the nominal composition of the sputtered target (*i.e.* Pt_9Y) and were quite reproducible for the different sizes as can be deduced by the limited error bars of the measurements. Unfortunately the preparation technique does not allow a precise tuning of the final alloy composition. Similar to the extended surfaces a clear increase of the Pt to Y ratios was measured after ORR and after stability test, providing a first indication of the probable surface dealloying and leaching of surface Y.

More detailed information about the chemical state of these catalysts comes from the analysis of the Y 3d core level region. Figure 5.4 shows the Y 3d fitted spectra for 7 nm Pt-Y nanoparticles on glassy carbon, respectively *as-deposited*, *air-exposed* and *after ORR* testing. The 7 nm size is here selected as an indicative example: analogous measurements for the other sizes lead to totally similar ev-

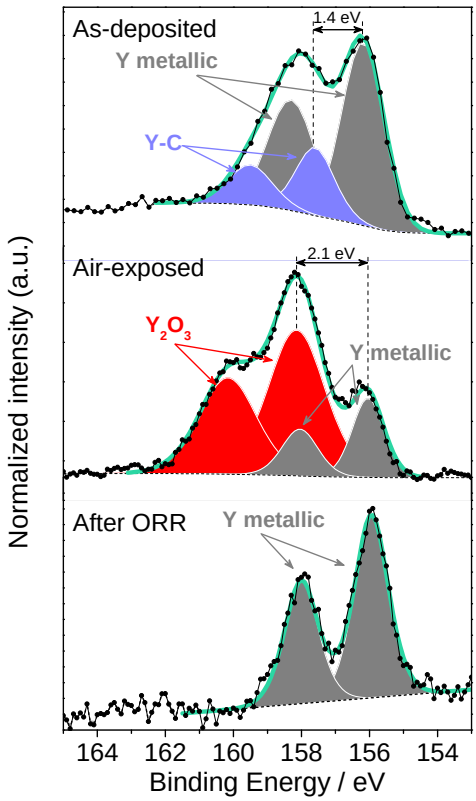

Figure 5.4: XPS spectra of the Y 3d core level region for Pt-Y 7 nm nanoparticles as-prepared (top), after air-exposure (middle) and after ORR testing (bottom). The low binding energy doublets (grey) represent the metallic components of Y (Y $3d_{5/2}$ peak at $\approx 156.0 \pm 0.2eV$). A secondary Y phase (blue) is present in the as-prepared sample and it is ascribed to the reaction of Y with the carbon support. After air-exposure the Y oxide phase (red) appears at even higher binding energies and becomes predominant. The energy shifts of these components are also indicated. Similar experimental evidences were observed for the other particle sizes.

idences. Focusing on the spectrum of the as-deposited sample, quite surprisingly, this could not be fitted by a single doublet, indicating that Y is present in more than a single chemical state. The most intense low binding energy species (Y $3d_{5/2}$ peak at $\approx 156.0 \pm 0.2eV$) is consistent with metallic Y as expected; the higher binding energy species is somewhat harder to identify. When compared to the Y peaks after air-exposure, clear differences can be observed; a clear Y oxidation occurred with the Y oxide peaks representing the majority of the XPS signal. These oxide peaks are shifted to very positive binding energies (Y $3d_{5/2}$ peak at $\approx 158.1 \pm 0.2eV$),

considerably more positive than the secondary Y phase of the as-deposited sample. This different position lead us ascribe this phase at intermediate binding energies to the reaction of the as-deposited Y with the C substrate; considering the high reactivity of metallic Y this would not be surprising. Another possibility could be related to the presence of some Y hydride [161] or hydroxide formed by the reaction with some residual water on the glassy carbon. It should be noticed that in literature no complete agreement on the position of the Y oxide peaks could be found [162, 163], but measurements acquired on an oxidized Y foil also registered very high binding energies (158.4eV for the Y $3d_{5/2}$ peak).

Remarkably, after ORR measurements only a single Y phase is observed at the typical binding energies of metallic Y. This indicates that the surface Y oxide is dissolved in the electrolyte, in a similar way as already demonstrated on extended surfaces of Pt_3Y and Pt_5Y [98]. Together with the increased Pt to Y ratios these XPS measurements suggest the formation of a core-shell structure, through a process of surface dealloying that resembles the one already described on extended surfaces for most of the probed alloys of Pt and rare earths. Although AR-XPS measurements cannot provide reliable depth profiles in this case due to the three dimentional morphology of the surface covered by nanoparticles, a Pt enriched shell should be expected.

5.3.2 Ion scattering spectroscopy

ISS measurements were performed after ORR in order to provide further information about the presence of a Pt shell. The ISS depth profile for a sample of 7 nm Pt-Y nanoparticles is depicted in Figure 5.5. Compared to the case of Pt and lanthanide metals, in this case He ions were able to distinguish the Pt and Y peaks. A ion energy of 1 keV was chosen so that the Pt peak appeared at kinetic energies $E_K \approx 890$ eV while the Y appeared at $E_K \approx 810$ eV, as can be observed from the fitted peaks of Figure 5.5 for some selected scans. The residual He pressure in the chamber was set to 1×10^{-7}mbar resulting in a ion current of about 300 nA. This value is considerably higher than those reported in Chapter 3 for ISS with Ne ions on a Pt_5Ce polycrystalline sample; however, the lighter He ions induce a much slower sputtering of the surface layers and higher currents could be used. Under these conditions the Pt ISS peak was already clearly visible from the very first scan, despite the presence of the typical background at lower kinetic energies originating from the C and O contaminations accumulated during the transfer of the sample and electrochemical measurements.

The ratio between the Pt and the Y ISS signals is very high (≈ 130) for this first scan since no Y peak can be seen and the small measured signal is on the level of the noise. In the following scans this ratio decreases quickly and it tends to stabilize after about 10-15 scans at a value ≈ 6. In Figure 5.5 the XPS ratios are also shown for comparison: these were calculated from the Pt 4f and Y 3d peaks

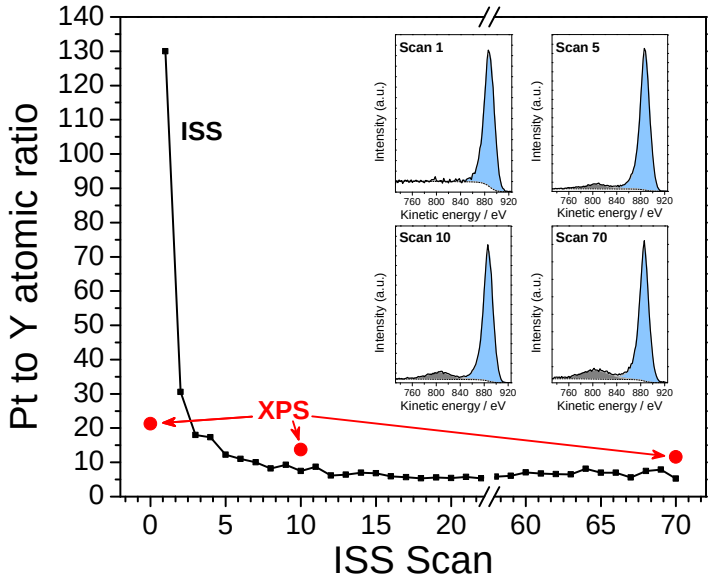

Figure 5.5: Pt to Y ratio derived from the fit of consecutive ISS scans on Pt-Y 7 nm nanoparticles after ORR. The XPS intensity ratios before ISS and after 20 and 70 cycles are also plotted for comparison. The inset shows a selection of ISS spectra corresponding to scans 1, 5, 10 and 70 with fitted Y (grey) and Pt (blue) peaks. Similar experimental evidences were observed for the other particle sizes.

acquired before ISS and after 10 and 70 ISS scans. Also in the case of XPS the Pt to Y ratios diminishes with time and further ISS sputtering, although the differences are much less pronounced, probably due to the lower surface sensitivity. This ISS measurement and in particular the first ISS scan of Figure 5.5 is in good agreement with the expected presence of a Pt shell surrounding an alloyed particle core.

5.3.3 Scanning transmission electron microscopy energy dispersive X-ray spectroscopy

To further investigate the structure and composition of the nanoparticles Scanning Transmission Electron Microscopy Energy Dispersive X-ray Spectroscopy (STEM-EDS) was performed on the most active catalysts (*i.e.* 9 nm Pt-Y nanoparticles) allowing to map the distribution of Pt and Y in the particles. Details of the employed experimental setup are found in Paper 5 in the end of this thesis. Figure 5.6 shows the acquired STEM images for the sample *as-prepared* and *after ORR*; the corresponding EDS elemental distributions are also plotted. In the case of the

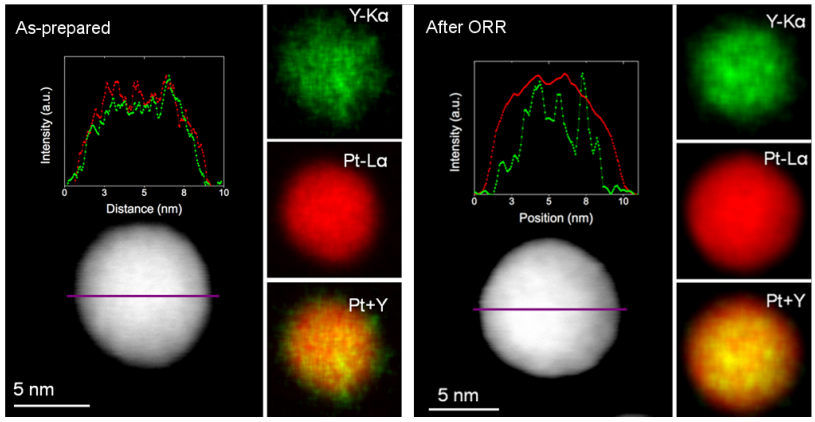

Figure 5.6: High Angle Annular Dark Field Scanning Transmission Electron Microscopy (HAADF-STEM) images and corresponding X-ray EDS elemental maps for Y, Pt and combined Pt+Y. Measurements were taken on Pt-Y 9 nm nanoparticles as-prepared (left) and after ORR (right). Linear profiles of the Pt and Y EDS intensity along the indicated purple lines are also plotted. The thickness of the Pt shell was estimated from ten line profiles, obtaining a value of 1.0 ± 0.3 nm. Measurements and figure made by Davide Deiana.

nanoparticles before electrochemical treatment, the concentration of Pt and Y is homogeneous over the entire particle as can be noticed for both the linear distribution along the indicated line and the overall particle distributions. Interestingly, the situation changes after ORR activity tests: as a consequence of Y dissolution, a Pt enriched shell can be clearly observed. The linear profile allows to estimate the thickness of such Pt overlayer, approximately 1 nm. This value is good agreement with those measured by AR-XPS on polycrystalline Pt_5Y in [98] and similar to those discussed in Chapter 4 for alloys of Pt and lanthanide metals.

5.3.4 Extended X-ray absorption fine structure

The presence of a thick Pt shell suggests that strain effects are the most probable mechanism enhancing the ORR activity over the one of pure Pt. In order to investigate the presence of strain in the Pt-Y catalysts and quantify it, synchrotron X-ray Absorption Spectroscopy (XAS) experiments were performed. In particular Extended X-ray Absorption Fine Structure measurements (EXAFS) allow to determine the average Pt-Pt distance in the nanoparticles, before and after electrochemical treatment. The results of such experiments are summarized in Figure 5.7, where the average nearest neighbour Pt-Pt distance is plotted for different sizes of Pt-Y nanoparticles: for comparison, similar measurements were also taken on pure Pt nanoparticles and on a reference Pt foil. Details of the fitting procedure and parameters can be found in Paper 5 in the end of this thesis. In the case of all

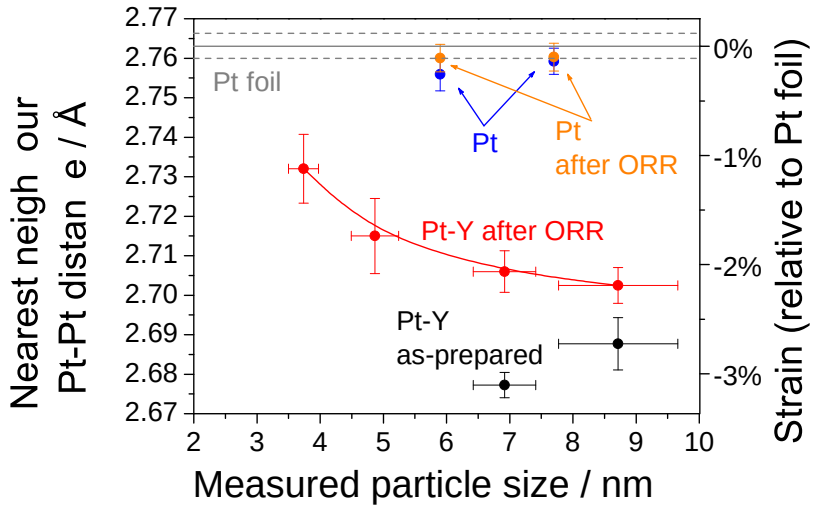

Figure 5.7: Average nearest neighbor Pt-Pt distance derived from the EXAFS analysis for Pt-Y nanoparticles of different sizes: as-prepared (black) and after ORR (red). The red line helps to guide the eye. For comparison, analogous measurements were taken on pure Pt nanoparticles: as-prepared (blue) and after ORR (orange). The measured nearest neighbor Pt-Pt distance in a Pt foil (grey) is also shown as reference. Measurements taken with Daniel Friebel, Anders Bodin and Anna M. Wise who also analyzed the data and prepared the figure.

Pt samples, the Pt-Pt average distance is approximately the same, both before and after ORR activity tests. On the other hand, the *as-prepared* Pt-Y nanoparticles (7 nm and 9 nm) exhibit a pronounced compressive strain ($\approx$ 3 %). *After ORR* clear differences can be noticed: the average Pt-Pt distance relaxes towards the one of pure Pt. However, some strain is still retained, with a clear dependence on the particle size. The residual compressive strain varies from 1.0 % for the smallest 4 nm nanoparticles, up to 2.1 % for the largest 9 nm nanoparticles.

5.4 Discussion on the activity enhancement

The similarities between the XPS-ISS results on these nanoparticles and those obtained on extended surfaces indicate that the surfaces of these catalysts are subjected to similar modifications during both air-exposure and electrochemical measurements. Namely, Y oxidizes under air-exposure and leaches out from the first atomic layers of the particles during potential cycling in 0.1 M $HClO_4$ electrolyte. The active chemical state and surface structure after ORR testing is also similar in both cases, suggesting that similar mechanisms might explain the enhanced ORR

activities. Since the surface consists of pure Pt either ligand or strain effects should explain the enhanced specific activities with respect to Pt nanoparticles. The remarkable increase of the XPS Pt to Y ratios and in particular the STEM-EDS elemental maps indicate the presence of a rather thick Pt overlayer, around 1 nm, over an alloyed Pt-Y core. These evidences are in rather good agreement with the AR-XPS measurements taken on polycrystalline samples. For such a structure ligand effects should vanish at the surface and strain effects would be the only explanation [52].

Although EXAFS measurements represent an average over the whole particle, they demonstrate the overall compression of the Pt-Pt distance in these catalysts, compared to pure Pt. The removal of surface Y during ORR testing causes a relaxation of such strain towards the Pt-Pt lattice parameter of pure Pt. However, low energy electron diffraction (LEED) studies on Pt/Cu(111) indicate that there would still be some residual compressive strain on the topmost layer, despite these relaxation effects [31]. Similar conclusions are suggested by X-ray surface scattering (XRS) experiments on the Pt overlayer of dealloyed $Cu_3Pt(111)$ [41]. Figure 5.8 shows the specific activity of the Pt-Y catalysts at various sizes as a function of the average Pt-Pt distance measured by EXAFS. A clear correlation can be observed. The specific activity increases monotonically with higher levels of compressive strain; a similar tendency was observed by Strasser *et al.* for dealloyed Pt-Cu nanoparticles [31].

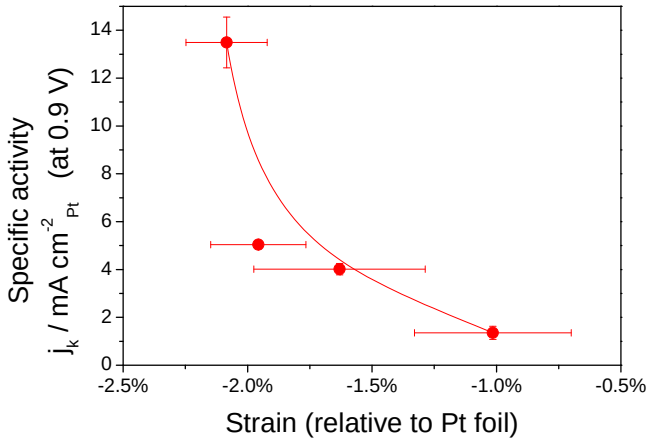

Figure 5.8: Specific activity of Pt-Y nanoparticles of different sizes, plotted as a function of the compressive strain relative to pure Pt, as determined from the EXAFS analysis (see Figure 5.7). The continuous line helps to guide the eye.

By assuming that the Pt-Y nanoparticles consist of $\approx$ 1 nm thick Pt shell over a Pt_5Y core, as estimated from the STEM-EDS measurements, the compression of the

Pt overlayers can be calculated. These would be slightly less compressed with values between 1.0 % and 1.8 %: these values are substantially relaxed with respect to the nearest neighbour Pt-Pt distance in bulk Pt_5Y, which is $\approx$ 4 % [98, 164]. In Chapter 4 the bulk structure of alloys of Pt and lanthanide metals (*e.g.* Pt_5La, Pt_5Ce, Pt_5Gd, ...), with analogous structure as Pt_5Y [164], was already related to the structure of the Pt overlayer. However, a direct measurement of the surface structure of the overlayer is challenging and it could not be performed yet due to the limited thickness of the overlayer and the polycrystalline nature of those samples: ongoing synchrotron measurements on alloyed Y/Pt(111) aim at resolving this surface structure.

CHAPTER 6

Towards *in-situ* XPS measurements

6.1 Introduction

In recent years there has been a general trend towards the development of *in-situ* techniques for the analyses of catalytic surfaces. Indeed, during reaction the catalyst conditions might vary considerably from its initial as-prepared status as well as from its final status after reaction and transfer to any *ex-situ* experimental setup [165]; surface composition, chemical states, morphology and surface structure of the catalysts can all be very sensitive to changes in the environmental conditions (*e.g.* exposure to air, to other reactive gases or to acidic/basic electrolytes). The electrochemical potential can also heavily affect these properties. A number of techniques have been developed in order to follow these changes under reaction conditions and possibly in a PEMFC: *in-situ* measurements based on X-ray diffraction (XRD), X-ray absorption (XAS), Fourier Transform Infrared Spectroscopy (FTIR), Transmission Electron Microscopy (TEM), electrochemical scanning tunneling microscopy (EC-STM) are well established. *In-situ* X-ray Photoelectron Spectroscopy (XPS) measurements would also be highly desirable as this technique can provide at the same time information about composition, chemical states and surface structure. The main challenge in the case of XPS is the very low electron mean free path of the photoemitted electrons in the range of pressures required for following a reaction. However, sophisticated multiple stages systems of differential pumping have been recently developed, allowing to acquire Ambient-Pressure X-

Ray Photoelectron Spectroscopy (AP-XPS) measurements up to pressures $\approx$ 100 mbar [166, 167].

For the interest of this study, AP-XPS measurements on ORR catalysts and in particular on Pt-alloys would be highly valuable. An *in-situ* study of the XPS signals of the alloyed rare earths, as for the alloys of the previous chapters of this work (Chapters 3 and 4), could provide, for instance, further information about the dealloying mechanism. Variations in the shape and position of the Pt 4f peak and of the d-band could be correlated to the level of strain in the Pt overlayer, enlightening how this evolves during the initial dealloying, or upon extended electrochemical cycling and how this strain is related to the enhanced ORR activity. Even more interestingly, AP-XPS could be employed to directly probe and distinguish the oxygenated species during ORR, which could extend our understanding of the catalytic steps of this reaction. In the introduction of this thesis (Chapter 1) it was shown how the binding energies of these oxygenated species (*i.e.* O^*, HO^*, HOO^*) are expected to influence the ORR activity according to DFT calculations. In particular, once the scaling relations have been taken into account, the O^* binding energy was used as a single descriptor of the ORR activity.

However, the direct observation of these species *in-situ* is particularly challenging. XAS measurements, for instance, allow to identify the Pt oxidation state but they cannot distinguish between OH and other oxygenated species adsorbed on the surface [168]. On the other hand FTIR measurements are hindered by the high level of absorbance of the electrolyte solution and of the electrolyte membrane making the detection of adsorbed HO^* virtually impossible [169]. Electrochemical studies have detected the presence of the HO^* intermediate on pure Pt surfaces under ORR conditions [22, 170]. XPS has already been employed in vacuum to study the presence of oxygenated intermediates on extended Pt single crystal surfaces [23, 171]. However, these *ex-situ* measurements always need to deal with the challenge of avoiding contaminations and of preserving the oxygenated species during the transfer: surface water species typically desorb above 200 K [172]. A good knowledge about the coverage of these species under reaction conditions would be fundamentally important. It could also help to explain the unusual ORR activities observed in presence of different ions [173, 174], in dehydrated environment [175] or on stepped surfaces [176] and at the same time facilitate the design of better catalysts.

Very recently Sanchez-Casalongue *et al.* have demonstrated the possibility of applying their AP-XPS experimental setup [166, 167] to the study of Pt nanoparticles in a specifically prepared fuel cell [24]. From the O 1s XPS peak they were able to directly identify the oxygenated species during ORR and to follow their relative concentrations for different cell voltages. In particular, they identified two different types of OH species: hydrated OH and non-hydrated OH. The second one being the main surface species covering the Pt surface under ORR conditions at high partial pressures of O_2. They also employed DFT calculations to show that the reduction of non-hydrated OH should occur at lower overpotentials, suggesting that tuning of

the OH hydration through a proper catalyst design could highly enhance the ORR activity.

In this chapter the same experimental setup of Sanchez-Casalongue *et al.* [24] is used on a specifically prepared Pt-Y nanoparticle cathode. Despite the remarkable differences from the typical operation conditions of PEMFC, this is the first attempt of employing nanoparticle catalysts based on alloys of Pt and rare earths in a fuel cell. The analysis of the Y 3d XPS region allows to follow the dealloying mechanism *in-situ* for the first time. Preliminary results on the evolution of the oxygenated species on these catalysts under ORR conditions are shown. These measurements were performed in collaboration with Hernan Sanchez-Casalongue and Ifan E. L. Stephens. In the end of the chapter the design and construction of a new experimental setup for combining the Theta-Probe analysis chamber with electrochemical measurements is also introduced. Such system will also contribute to bring us closer to *in-situ* XPS experiments.

6.2 Setup and sample preparation

6.2.1 Ambient pressure XPS setup

The experiments of this chapter have been carried out at the Stanford Synchrotron Radiation Lightsource (SSRL) and in particular at beamline 13-2. This is equipped with an Elliptically Polarized Undulator (EPU) beamline covering the photon energy regime between 150 and 1300 eV with resolving power of $E/\Delta E > 5\ 000$. The Kirkpatrick–Baez (KB) refocusing optics tightly focuses the X-ray beam onto the center of a high-pressure cell where the fuel cell apparatus is mounted; this is part of a larger UHV system where sample cleaning and preparation can be performed. The full width at half maximum (FWHM) of the focal spot of the X-ray beam is smaller than 10 μm (vertical) × 50 μm (horizontal). The fuel cell apparatus can be precisely positioned in the middle of the high-pressure cell by a number of piezoelectric positioners that allow to align the surface of the cathode with the X-ray beam and at the same time with the entrance aperture to the differentially pumped lens elements of the electron-energy analyzer. A total of five differentially pumped sections allow the electron spectrometer (VG Scienta, SES 100) to obtain XPS spectra at pressures up to ≈ 100 mbar. For all the spectra presented in this chapter a photon energy of ≈ 700 eV was chosen. The binding energies were referenced to the Fermi level by regularly acquiring XPS spectra of the valence band under the corresponding experimental conditions. The absence of beam damage effects was checked by acquiring consecutive spectra in the same position over the sample at different pressure conditions.

Figure 6.1 shows a schematic of the high-pressure cell with details about the geometry of the system. The choice of the X-ray incident angle and of the ac-

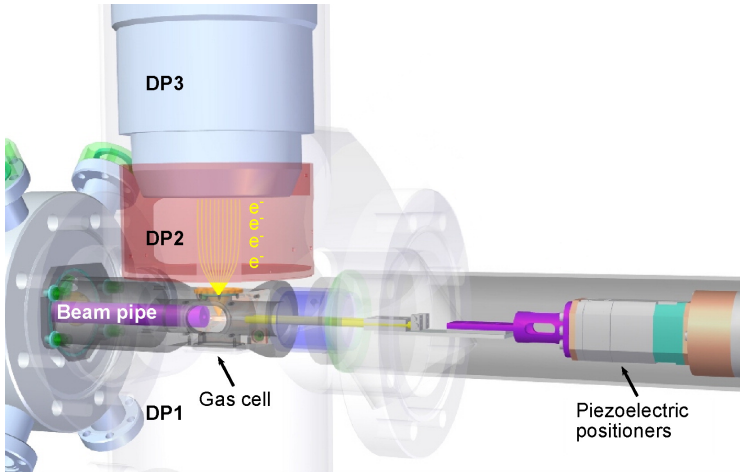

Figure 6.1: Schematic drawing of the high-pressure cell for AP-XPS measurements. The first three differential pumping sections (DP1, DP2, and DP3) are also visible. The first pumping section (DP1) is the UHV chamber hosting the high-pressure cell. A small aperture separates the high-pressure cell from the second pumping section (DP2). The first lens elements start focusing the photoelectrons between DP2 and DP3. The beam pipe on the left of the drawing (purple), separated from the high-pressure cell by a Si_3N_4 window, indicates the direction of the incoming X-ray beam. On the right, piezoelectric positioners allow to precisely align the sample with the beam. Figure adapted from [167].

ceptance angle of the emitted electrons is crucial. The sample is hit at grazing incidence in order to minimize the XPS signal originating from the gas molecules relative to that of the cathode and of its surface species. Furthermore the distance between the sample surface and the aperture to the stages of differential pumping and to the analyzer must be minimized being sure to maintain a good vertical alignment between the beam spot on the sample and the aperture itself. Further details about the AP-XPS experimental setup can be found in [24, 166, 167].

6.2.2 Fuel cell for ambient pressure XPS

Figure 6.2 shows a schematic drawing of the PEM fuel cell that was specifically designed for the high-pressure cell of this AP-XPS system. The two sides of the Membrane Electrode Assembly (MEA) are separated by an O-ring which is pressing on the anode side of the membrane itself. In this way the anode side (backside) can be filled through small tubes with humidified forming gas (95% N_2/ 5% H_2 saturated H_2O) providing both the fuel and the necessary humidification of the membrane. The cathode side (frontside) is directly exposed to the gases (typically O_2) of the high-pressure cell for the AP-XPS measurements.

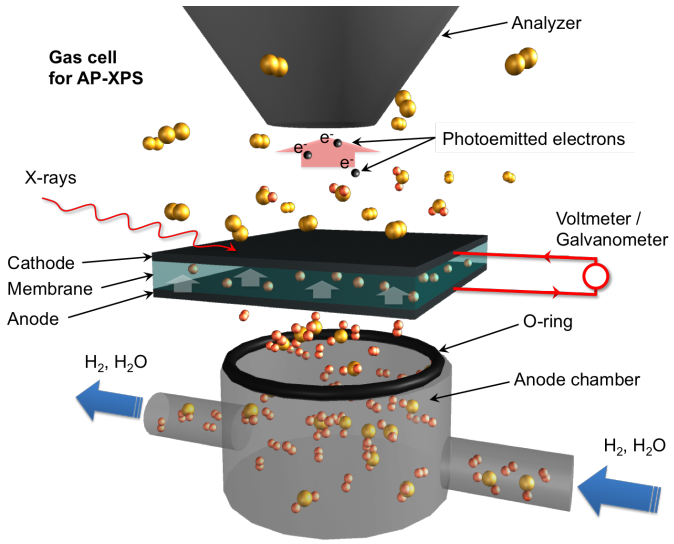

Figure 6.2: Schematic drawing of a PEMFC setup designed for APXPS investigations: the electrochemical cell has a Nafion membrane coated on the anode side with carbon-supported Pt nanoparticles and on the cathode side with 9 nm Pt-Y nanoparticles deposited on a Nafion/carbon-black mixture. The cathode side of the assembly is exposed to the AP-XPS gas cell, typically filled with O_2. The anode chamber is sealed to the backside of the membrane through an O-ring and is filled with humidified forming gas (95% N_2/5% H_2, saturated H_2O). A voltmeter and a galvanometer allow measurements of the cell potential or current while acquiring XPS measurements.

Concerning the MEA, the backside was prepared by coating a commercial Nafion 115 membrane with a mixture of Nafion and carbon-supported Pt nanoparticles (particle size 10-20 nm) with catalyst loading of 4 mg cm^{-2} (from the Fuel Cell Store, Inc (Boulder, CO)). On the frontside a Nafion/carbon-black mixture was first deposited onto the Nafion membrane. The membranes were then transferred to the cluster source (see Section 2.5.2) and degassed in vacuum for about 12 hours; subsequently, size-selected 9 nm Pt-Y nanoparticles, the most active presented in Chapter 5, were deposited onto the Nafion/carbon mixture using the same deposition procedure.

6.3 *In-situ* Y oxidation and dealloying

Once the MEA was assembled in the fuel cell apparatus and mounted in the high-pressure cell for AP-XPS preliminary measurements were acquired in vacuum. Figure 6.3 shows a typical overview spectrum with clear Pt and Y signals from the Pt-Y nanoparticles; signals from C, O and F can also be seen. F is expected from

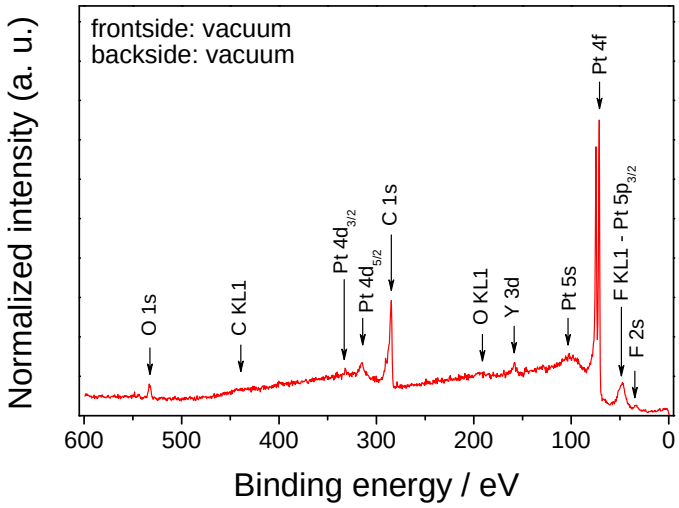

Figure 6.3: Initial XPS overview spectrum of Pt-Y nanoparticles acquired in vacuum on the cathode side of the MEA. The main XPS and Auger peaks have been assigned showing the presence of Pt and Y from the nanoparticles, C, O and F from the Nafion/carbon mixture.

the nafion and appears as an Auger KL1 peak at a binding energy of ≈ 48 eV. No S from the nafion could be observed suggesting that also the O 1s signal should not be affected by sulphur-containing oxygenated species. Similar measurements were taken on different spots over the sample area in order to investigate the homogeneity of the sample. The amount of Pt relative to the C signal from the support and to the F peak from the nafion was found to be quite variable. This variability is ascribed to the deposition of the high surface area carbon/nafion mixture, which might not be uniform over the all surface. However, the Pt to Y ratio was constant for different positions as expected. In the following measurements positions where the highest counts from the Pt 4f peak were generally chosen.

After these preliminary measurements the evolution of the main peaks (*i.e.* Y 3d, Pt 4f, C 1s, O 1s) was followed during pressurization of the anode/cathode side of the membrane and after applying potential cycles in order to induce the dealloying process. For this purpose the Y 3d peak provides the most interesting information. Figure 6.4 presents the comparison between the Y 3d peak measured in vacuum and the same peak after introduction of 5 Torr of H_2O vapor from the frontside and 40 potential cycles between -0.3 V and 1.4 V. The high quality of the X-ray beam provides a very good resolution and allows to easily distinguish two Y phases, a metallic phase (Y $3d_{5/2}$ peak at ≈ 156.0 eV in agreement with the measurements of Chapter 5) and a more intense oxidized phase (Y $3d_{5/2}$ peak at

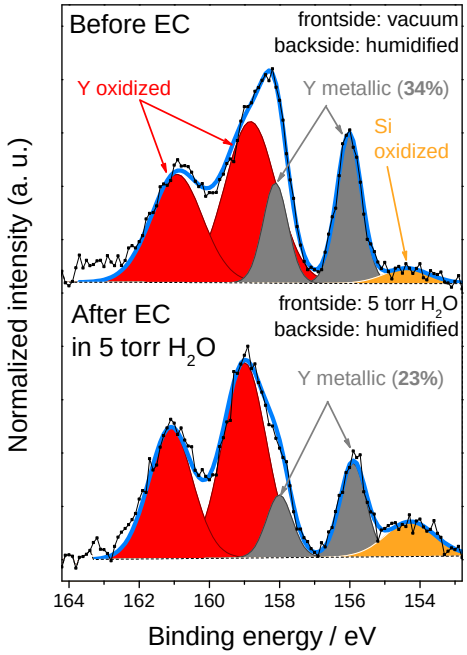

Figure 6.4: Comparison of the Y 3d XPS region between the initial as-prepared condition in vacuum (top) and the one after electrochemical cycling in 5 Torr H_2O pressure (bottom). A relative increase of the oxidized component is observed. The percentages of metallic Y with respect to the total Y, and the pressure conditions of anode and cathode side during acquisition of the XPS signals are indicated.

$\approx$ 158.6 eV probably corresponding to Y oxide or solvated Y ions [162]). Such high level of oxidation is expected from the long time air exposure that occurred between the deposition and the synchrotron measurements (*i.e.* about two weeks) and from the highly acidic conditions induced by the presence of Nafion. Figure 6.4 clearly shows an increase of the oxidized component compared to the metallic one after electrochemistry. This is the first *in-situ* XPS evidence of the dealloying process occurring on Pt alloy nanoparticles. It should be noted that the two spectra were acquired at the same position over the sample surface, as some variability in the percentage of metallic to oxidized Y was noticed at different spots: this might also be an effect of the inhomogeneous carbon/nafion film. Compared to the other XPS measurements reported in this thesis after electrochemistry, the absence of a

liquid electrolyte flow complicates the removal of the Y oxide or solvated Y ions from the surface. The presence of these oxidized species was already found to reduce the ORR performance of alloys of Pt and late transition metals [77, 177]. This suggests that, as in the case of Pt_3Co [3, 82], a proper acid leaching procedure should be optimized and performed prior to use of these particles in a fuel cell. This would prevent the accumulation of oxidized Y that could possibly poison the catalytic active sites or the membrane. Figure 6.4 also shows the presence of a small Si contamination; this was occasionally observed on some particular spots and found to increase during electrochemical measurements. This is expected to be a contamination from either the carbon substrate or the carbon/nafion mixture.

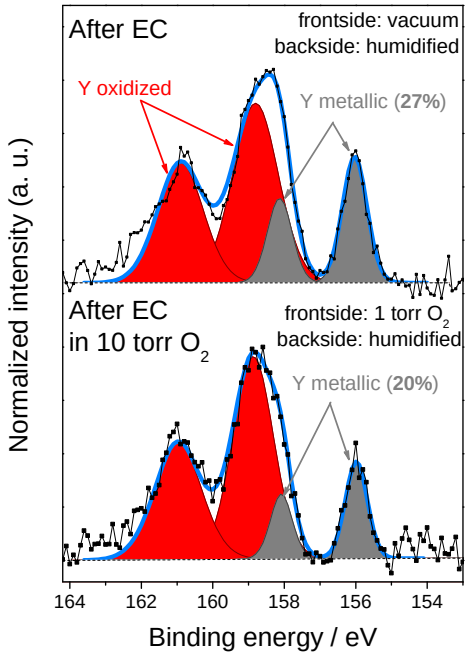

Figure 6.5: Comparison of the Y 3d XPS region after electrochemical cycling in ≈ 5 Torr H_2O pressure (top) and after electrochemical cycling reaching higher potentials in ≈ 10 Torr H_2O pressure (bottom). A further increase of the oxidized component is observed. The percentages of metallic Y with respect to the total Y, and the pressure conditions of anode and cathode side during acquisition of the XPS signals are indicated.

Figure 6.5 provides a further evidence of dealloying over a second spot of the

sample as a consequence of further electrochemical cycling in ≈ 10 Torr of O_2. This time the cathode was subjected to a total of 115 potential cycles between -0.4 V and 1.4 V. After this treatment the percentage of metallic Y decreased further from 27 % to only 20 %.

6.4 Acid leaching

After various combinations of electrochemical cycles under different H_2O and O_2 pressures, the membrane was extracted from the high-pressure cell. The cathode surface was exposed to a drop of 0.1 M H_2SO_4 electrolyte for 10 minutes followed by various drops of water for rinsing. This procedure was repeated two times in order to ensure a good acid leaching and the removal of the oxidized Y. The new measurements acquired in vacuum exhibited in average much lower levels of oxidized Y as apparent from Figure 6.6, where the metallic component represents 54 % of the total Y signal. It was still impossible to achieve a complete oxide removal with this procedure.

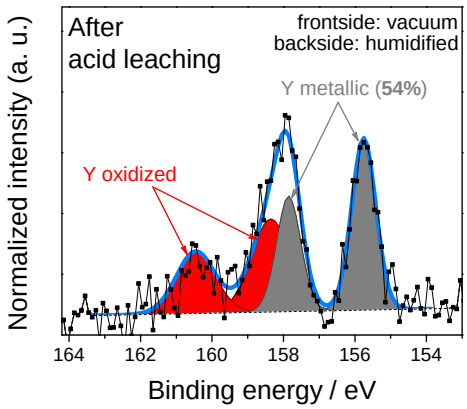

Figure 6.6: Typical Y 3d XPS spectrum after *ex-situ* acid leaching in 0.1 M H_2SO_4 electrolyte. The metallic component of Y increased to 54 % of the total Y area.

Figure 6.7 a shows a broad XPS spectrum including both the Pt 4f and Y 3d peaks and how their areas were calculated for estimating the Pt to Y ratios. The evolution of the Pt to Y XPS ratios is plotted in Figure 6.7 b for an average of at least three independent measurements in different spots for the membrane *as-prepared*, *after EC* mesurements and *after ex-situ acid leaching*. The ratios are expressed both in terms of Pt to total Y signal and in terms of Pt to metallic Y. In both cases the ratios are quite reproducible before electrochemical measurements confirming the

good compositional homogeneity of the particles over the surface. While the total quantity of Y after EC does not vary significantly, the Pt to metallic Y ratios increase as a consequence of dealloying. Some variability is due to the different level of dealloying for different cycling conditions (different H_2O or O_2 pressures and applied potentials). As anticipated from Figure 6.6, the acid leaching procedure raised all the ratios to higher values as a consequence of further dealloying and removal of the oxidized phase. The higher error bars are a sign of some spatial variability for different positions, particularly for the acid leached sample where different spots clearly exhibited different levels of oxide removal.

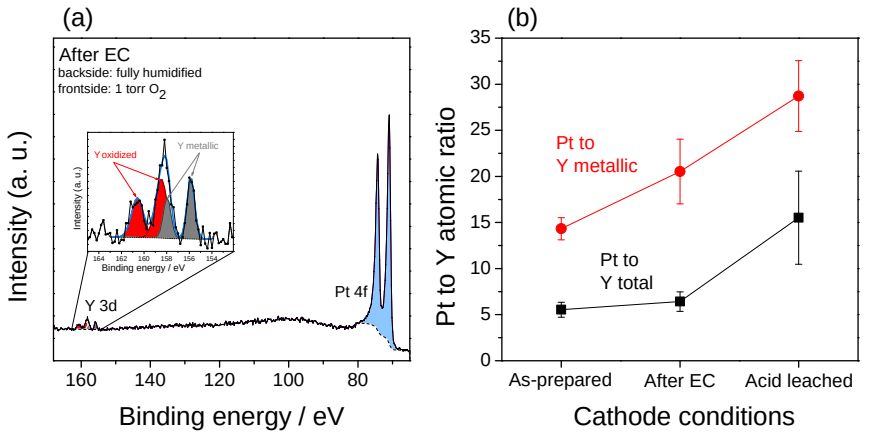

Figure 6.7: On the left (a) a typical broad spectrum including the Pt 4f and Y 3d regions illustrates the employed areas for quantifying the Pt to Y ratios. The inset is a zoom of the fitted Y 3d peaks. On the right (b) the Pt to total amount of Y (black) and Pt to metallic Y (red) ratios are plotted. Measurements were performed on the *as-prepared* membrane in vacuum, *after EC* cycling under different H_2O and O_2 frontside pressures and in vacuum *after ex-situ acid leaching*. Each point is calculated as an average of at least three independent measurements at different positions.

6.5 *In-situ* observation of oxygenated surface species

In the previous section AP-XPS measurements provided *in-situ* evidences of the dealloying process. Although that was the main focus of these measurements the direct observation and separation of the oxygenated species participating in the ORR process would be highly interesting. In particular, a comparison between the adsorbed species on these Pt-Y nanoparticles and those recently reported by Sanchez-Casalongue *et al.* on pure Pt nanoparticles [24], would be of great importance towards a better understanding of the ORR mechanisms and of the enhanced catalytic performance of this kind of alloys.

Preliminary results can be extrapolated from the spectra of Figure 6.8, where different O 1s spectra were acquired after introduction of 2.6 Torr of O_2 under open-circuit conditions and constant anodic hydrogen pressure ($\approx$ 600 Torr of humidified forming gas). The spectra were acquired on the Pt-Y nanoparticles before the acid leaching procedure of Section 6.4. Unfortunately, in the limited amount of time at the synchrotron it was not possible to reproduce the same measurements on the acid leached nanoparticles where the lower amount of oxidized Y would ensure a lower level of uncertainty on the deconvolution of the O 1s spectra. Ideally the fuel cell behaviour of these catalysts should be studied after an optimized procedure of acid leaching, removing the majority of the oxidized Y and leaving entirely metallic core-shell Pt-Y nanoparticles, with a Pt shell protecting the core Y from further oxidation and dissolution.

The XPS peak of gaseous oxygen, with the typical splitting due to the paramagnetic nature of O_2 molecules [166, 180], appears at high binding energies $\approx$ 536-540 eV. While the system evolves towards the equilibrium, a clear shift of these peaks towards lower binding energies is noticed. Previous works demonstrated that this shift of the gas phase relative to the probed Fermi level in proximity of the surface is the result of a variation of the work function [181, 182]. The same behaviour was observed on pure Pt nanoparticles [24] and it was correlated to a shift in the measured electrochemical potential at the cathode. Interestingly, the shifts of these two quantities, both describing how strongly the surface binds electrons, closely agreed. This also indicates that changes in the electrochemical potential can be deduced from XPS. In Figure 6.8 the measured shift of 0.9 eV corresponds to a 900 mV increase of the surface potential while the system approaches the equilibrium. This is approximately the maximum electrochemical potential expected at the cathode of this fuel cell: differences from the Nernst equilibirum potential ($U_0 = 1.195$ V) are ascribed to kinetic losses.

Focusing now on the low binding energy region of the O 1s spectra ($\approx$ 529-536 eV), clear modifications in the shape and position of the spectrum indicate a variation of the surface species at the cathode. Figure 6.8 also reports the positions of the main oxygenated species based on previously assigned XPS spectra of various oxygenated adsorbates on Pt(111) single crystals [178, 179]. Due to the large number of species involved and the complications due to the presence of oxygen from the oxidized component of Y, it was preferred to avoid a direct fit of these spectra. However, a clear qualitative trend can be observed. At low potentials water is the main component, both present as multilayer H_2O (purple peak at 533.1 eV) and adsorbed water $H_2O_{(ad)}$(orange peak at 532.2 eV). At higher potentials these signals are progressively substituted by those of hydroxide based species at lower binding energies: adsorbed water hydrogen bonded to hydroxide H_2O-OH (red peak at 531.6 eV), non-hydrated hydroxide OH-O (cyan peak at 531.0 eV) and a convolution of hydrated hydroxide H_2O-OH and atomic oxygen O_{ad} (blue peak at 530.1 eV). It should be noted that the O 1s components from oxidized Y are not expected to shift while the potential increases and they should not interfere with the

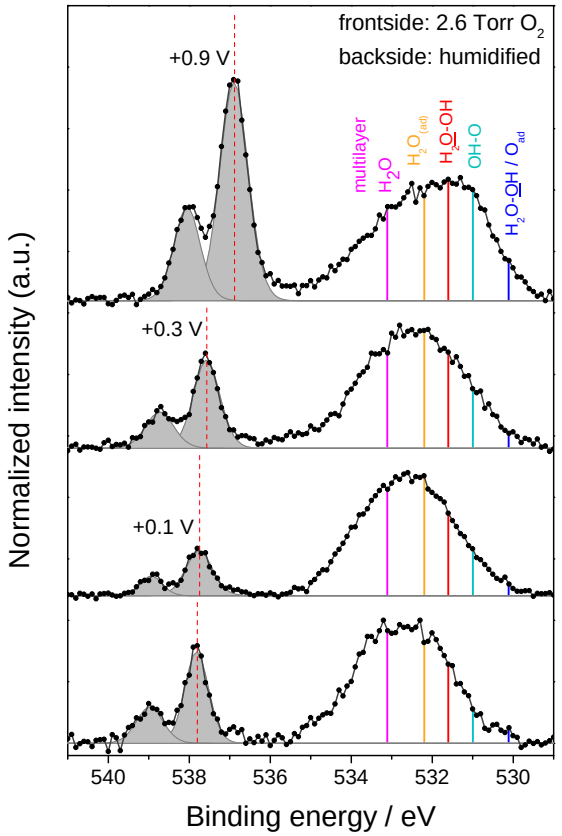

Figure 6.8: Open circuit potential evolution of O 1s XPS spectra under introduction of 2.6 Torr of O_2 gas in the cathode and constant hydrogen pressure in the anode. The shift of the double peak feature at high binding energies, corresponding to oxygen gas (red dotted line), is due to a change in the work function of the surface and can be used to determine the change in surface potential. At lower binding energies the positions of the main oxygenated species is shown [178, 179]: multilayer H_2O (purple); $H_2O_{(ad)}$ (orange); $H_2\underline{O}$-OH (red); OH-O (cyan); H_2O-$\underline{O}$H/O_{ad} (blue). For clarity the spectra have been normalized to the height of the low binding energy features. Analysis of the XPS spectra performed in collaboration with Hernan Sanchez-Casalongue.

observed trend. As in the case of pure Pt nanoparticles [24], the increase of non-hydrated OH can be identified as the most evident spectral change: from an almost negligible signal up to being one of the main components. A direct comparison with

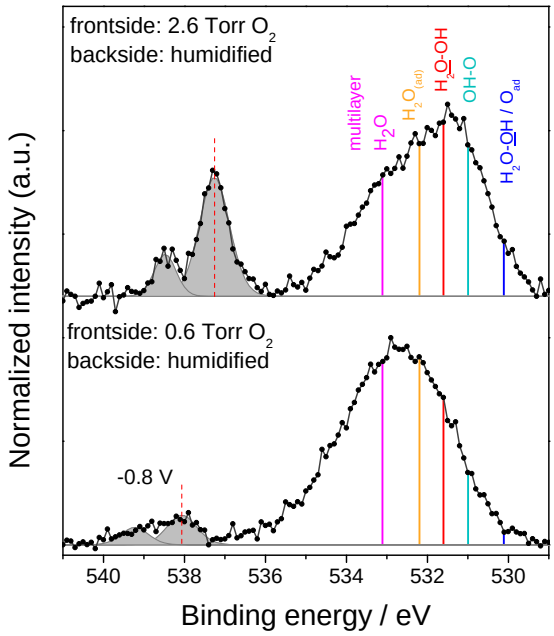

Figure 6.9: Closed circuit evolution of the O 1s XPS spectra under two different O_2 pressures at the cathode and constant anodic hydrogen pressure. The low oxygen condition (bottom) produced an electrochemical current of 5 μA, while the high oxygen condition (top) produced a current of 12 μA. The lower pressure of O_2 reduced the potential of 0.8 V. At lower binding energies the positions of the main oxygenated species is shown [178, 179]: multilayer H_2O (purple); $H_2O_{(ad)}$ (orange); $H_2\underline{O}$-OH (red); OH-O (cyan); H_2O-$\underline{O}H/O_{ad}$ (blue). For clarity the spectra have been normalized to the height of the low binding energy features. Analysis of the XPS spectra performed in collaboration with Hernan Sanchez-Casalongue.

their results is complicated by the possible presence of oxygen from oxidized Y and the difficulties of precisely compare the potential values [24]. Future experiments aim at investigating differences in the population of non-hydrated hyrdroxides on these Pt-Y nanoparticles with respect to pure Pt nanoparticles at different potentials. A higher level of non-hydrated hyrdroxides would support the theory that the stabilization of non-hydrated hydroxide can lead to higher catalytic performance.

Once the position of the peak from gaseous oxygen was stable indicating no more changes of the open circuit potential, the electrical circuit was closed simulating the operation of a fuel cell. Figure 6.9 shows two O 1s spectra of this closed circuit system at two different oxygen pressures while the pressure at the anode was maintained constant. At high pressures a current of 12 μA is measured and

the population of non-hydrated species is considerably high. Similar to pure Pt nanoparticles [24], at lower pressures (0.6 Torr) the current decreases to 5 μA is measured, the surface potential decreases of 0.8 V and the oxygen species are mainly constituted by water. These are the first experimental evidences of a successful application of Pt-Y nanoparticle catalysts in a fuel cell.

6.6 Combined Thetaprobe and EC-cell

The initial sections of this chapter have enlightened some of the potentialities of AP-XPS. The possibility of directly observing *in-situ* the dealloying mechanism and the evolution of the oxygenated species under reaction conditions are only some examples of a large number of experiments that could be extremely relevant, particularly in catalysis. Unfortunately not many facilities in the world allow to perform such kind of experiments. Synchrotron facilities are required and they are usually available for very limited amounts of time. Quite often it is not possible to prepare samples in the same laboratory and these need to be stored for a long time and transferred before carrying out the actual characterization. It would be highly desirable to perform these kind of experiments in the same laboratory where the samples (*e.g.* Pt-Y nanoparticles) are fabricated and where all the other characterization techniques shown in this work are also available. Herein, the design and preparation of an experimental setup combining spectroscopic techniques (*e.g.* XPS, UPS, ISS) with an electrochemical cell are introduced. The construction of the system took good part of this Ph.D. project, in particular the Theta-Probe chamber has been extended with three UHV-compatible extra chambers: respectively a *preparation chamber* allowing sputter-cleaning, annealing and thin film deposition, an *EC-compartment* for electrochemical measurements under controlled clean atmosphere and a *buffer chamber* for the clean transfer of samples from atmospheric pressure down to UHV conditions.

For this new combined EC-XPS system the idea is not to perform *in-situ* measurements but to facilitate the fastest and cleanest transfer between the experimental stages of preparation, characterization and testing, ideally avoiding all kind of contaminations. This would already represent a great improvement, for instance allowing to avoid the complications due to C and O in the model for the estimate of the Pt overlayer thickness of Chapter 4. The influence of different dealloying conditions, for instance of different electrochemical potentials, on the Pt overlayers could be easily studied. The fabrication of single crystal alloys would also allow to study the ORR activity of different facets as well as their differences in electrochemical and physical stability. Valuable information could be extrapolated from the analysis of the d-band of these alloys probed by UPS. The characterization of the active phases was so far hindered by the high sensitivity of this technique to contaminations.

Similar setups have been already developed in other laboratories. In particular,

Wakisaka *et al.* combined an UHV system with an electrochemical cell and were able to study the population of oxygenated species as function of potential on the surface of Pt single crystals [23, 171].

6.6.1 Design of the EC-XPS setup

In Figure 6.10 the extended Theta-Probe setup with the new chambers and a schematic of the main parts is shown. All chambers are separated by gate valves that are normally only opened when the transfer arms are extended in order to move the samples. Proceeding in order of positions the main analysis chamber of the Theta-Probe is connected to the *preparation chamber*. This is pumped by a 300 l/s turbopump providing a base pressure of 1×10^{-10} mbar. It has been equipped with an ion gun for sputter-cleaning, an evaporator for the deposition of thin films and a Quartz Crystal Microbalance (QCM) for quantification of the deposited amounts of material. The new gas system, also visible in Figure 6.10 has been connected to this chamber through a number of leak valves, so far ensuring the dosing of clean H_2, CO, Ar. An ion gauge monitors the pressure while a quadrupole mass spectrometer will be primarily intended for Temperature Programmed Desorption (TPD) experiments. A manipulator for the correct positioning of the sample is also visible in Figure 6.10. The central part of the chamber hosts a sample holder mounted on this manipulator. Its particular design allows to hold different kind of samples as can be seen in Figure 6.11 together with a schematic drawing showing the main components. The samples are insulated from the rest of the chamber so that electrical currents to ground can be measured. Heating is controlled by tuning the current of a filament which can be biased down to -1 250 V with respect to ground, it provides heating both through irradiation and electron beam to the backside of the sample. As a matter of fact, the Thetaprobe chamber has not been equipped with any heating system before. This new possibility might be particularly relevant in the perspective of studying Pt-skin structures on the polycrystalline alloys of this work or alternatively, on single crystal alloys. Two K-type thermocouples placed in different positions of the sample holder can measure the temperature independently. The metallic frame of the sample holder was made in molybdenum and all the other materials were selected so that temperatures around 1 200 °C can be reached. These might be required for the synthesis of some of the alloy phases described in this work [101, 156].

A second gate valve separates the preparation chamber from the *buffer chamber*, with the main function of ensuring a fast and clean transfer of samples between the EC-compartment and the preparation chamber. It can be pumped separately by a diaphragm pump for removal of the initial electrolyte residues and by an 80 l/s turbopump. Another manipulator on top of this chamber combined to a simpler version of the sample holder in Figure 6.11 allows to rotate the sample and align it with the transfer arms. A combined Pirani and cold cathode pressure gauge monitors the pressure in the wide range from 5×10^{-9} mbar up to atmospheric

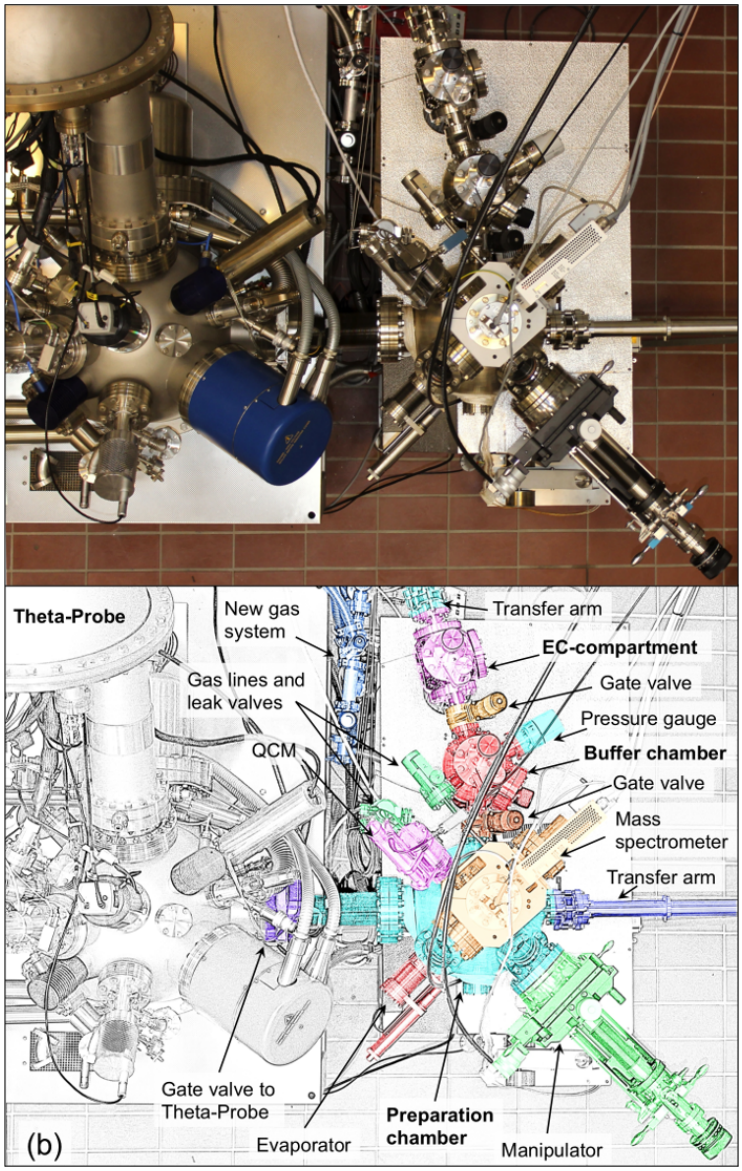

Figure 6.10: Top view of the Theta-Probe setup on the left and its extension chambers on the right (a). In the bottom the correspondent schematic representation with indications of the main components can be seen (b). In particular preparation chamber, buffer chamber and EC-compartment can be distinguished.

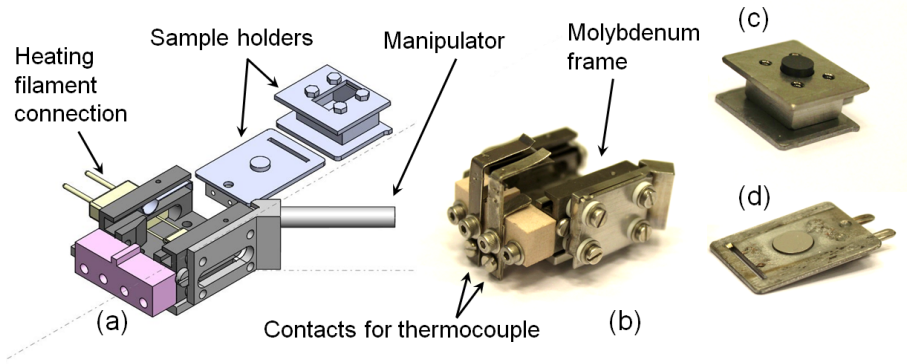

Figure 6.11: Schematic drawing of the sample holder of the preparation chamber (a) and corresponding photograph (b). The main components have been indicated. Typical molybdenum sample carriers for glassy carbon samples (c) and single crystals (d).

pressure.

Connected to the buffer chamber the *EC-compartment*, illustrated in Figure 6.12, is the crucial part of the Theta-Probe extension. It consists of a UHV compatible cubic chamber which will be constantly flushed with inert gases (*e.g.* Ar, N_2) in order to maintain a controlled atmosphere and avoid contaminations. In the middle of the cube a three electrode setup can be assembled for electrochemical measurements. The sample faces downwards and is kept in place by a manipulator mounted on the top flange of the chamber: it allows the rotation of the sample and it provides the necessary connections to the sample. In particular an electrical connection provides potential control of the sample (working electrode) which is insulated from the rest of the manipulator. The bottom flange of the EC-compartment is connected to a gate valve which is able to seal the chamber. However, during electrochemical measurements the gate valve is open so that an EC-cell can be moved upwards towards the sample. In this situation the EC-compartment is not sealed and the inert gases are free to flow out of the chamber through the bottom flange generating a constant gas flow. The EC-cell consists of a Kel-F (R) DuPont (PCTFE) cylinder whose central volume can be filled by the electrolyte. Three small channels in the bottom of the cell allow the insertion of the electrolyte and of the counter and reference electrode respectively. At the top of the EC-cell an O-ring (4 mm inner diameter) can be pressed upwards against the working electrode ensuring a good contact between its surface area and the electrolyte. A computer controlled syringe pump is used to introduce the electrolyte in the cell; thin channels allow to collect the excessive electrolyte in the surrounding reservoir. Electrochemical measurements are carried out with a Bio-Logic SP-200 Potentiostat, allowing floating operation.

Following the electrochemical experiments, the sample can be moved upwards

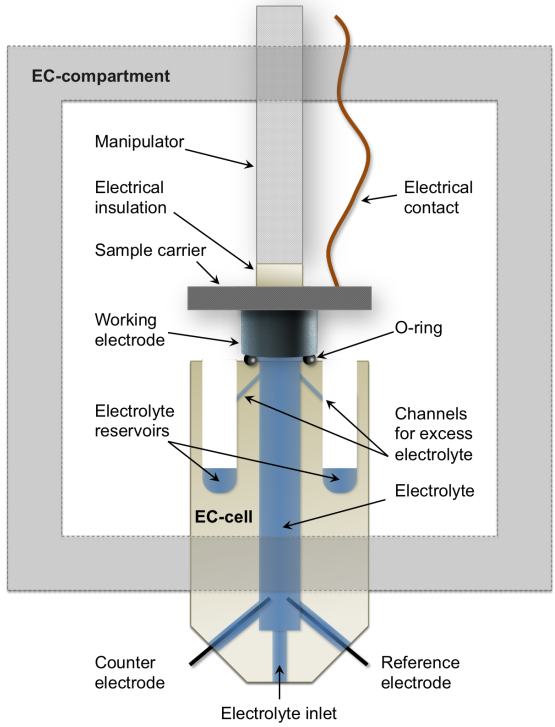

Figure 6.12: Schematic drawing of the EC-compartment hosting the EC-cell. The main components are indicated.

and extracted from the electrolyte under potential control in the inert atmosphere of the EC-cell. It is then readily moved to the buffer chamber while keeping it in Ar or N_2. Once the buffer chamber is sealed from the EC-cell, it is first pumped down by the membrane pump to remove possible electrolyte residues and just afterwards by the turbopump. As soon as good vacuum conditions are reached the sample can be moved to the preparation chamber, where for instance, it can be mildly annealed in order to remove residual adsorbed water from the surface, or transferred directly to the Theta-Probe setup for characterization.

Chapter 7

Conclusions and perspectives

The experimental studies of this thesis have given some examples of how spectroscopic techniques, in particular XPS with its more advanced versions of AR-XPS and AP-XPS, can be successfully applied to the study of electrocatalysts for PEMFCs. These techniques played an essential role in the development of a new class of bimetallic catalysts for the ORR. From the pioneering study on alloys of Pt and early transition metals such as Pt_3Y and Pt_3Sc [16] considerable advances towards the understanding of these catalysts were made [6, 98, 100, 101, 126, 132](Papers 1-6 in the end of this thesis). These allowed to extend the number of possible candidates for a future application at the cathode of PEMFCs: "alloys of Pt and rare earths" is now a more general classification, with solute metals consisting either of early transition metals or lanthanide metals. Some alloys of Pt and alkaline earths were also found to be promising ORR catalysts.

Polycrystalline alloys

The first part of this work focused on the physical and electrochemical characterization of various Pt-lanthanide polycrystalline alloys. Remarkably, they all consist of *intermetallic compounds*, not to confuse them with disordered solid solutions. This means that their structures are highly ordered, often radically different from the closed-packed structure of Pt; each phase has a peculiar heat of formation which turns out to be very negative for all the tested Pt_5Ln alloys and similar to that of

Pt_3Y and Pt_3Sc, indicating the high thermodynamic stability of these compounds. The example of Pt_3La, which was found to corrode in acid, stresses the importance of identifying and selecting the right intermetallic phase, as both ORR activity and stability of these catalysts might vary substantially from one to another.

XPS and ISS were applied extensively in order to clarify the active surface phase and surface structure of Pt-La and Pt-Ce alloys and, more generally, of all these Pt and rare earths alloys: as a matter of fact, from this point of view, they all behave similarly. Despite the stabilizing effect of the alloy, the high level of reactivity of the rare earths makes these elements highly susceptible to oxidation in air when they are present on the surface of these materials. As a result they are leached away from the first few superficial layers in acid, leaving a Pt-overlayer (Pt-skeleton) which is approximately 1 nm thick. This Pt overlayer provides kinetic stability against further dealloying of these intermetallic phases, which in some cases were found to be very stable upon potential cycling. Pt_5La and Pt_5Ce for instance, exhibiting an initial ORR activity 3-4 times higher than that of polycrystalline Pt, retained at least 90 % of this initial activity after 10 000 cycles between 0.6 and 1.0 V *vs.* RHE in 0.1 M $HClO_4$ electrolyte.

The presence of a thick Pt overlayer excluded bifunctional effects and ligand effects from the possible mechanisms of activity enhancement. These must be related to strain effects. On the basis of the similar bulk structures characterizing all the Pt_5Ln alloys, it was possible to establish a correlation between the bulk lattice parameter a of these materials and their ORR activities. In particular the lattice constant a is expected to define the Pt-Pt distance in the overlayer. When this assumption is taken into consideration a volcano trend appears. Initially, a compression of the Pt-Pt distance (relative to pure Pt) corresponds to an increase of ORR activity, as expected from theory since it should weaken the binding energy to the ORR intermediates. At higher levels of compression this trend is reversed and the ORR activity goes down. The maximum activity was reached by Pt_5Tb, with a specific activity of 11.2 mA cm^{-2}. This value is almost 6 times higher than that of state-of-the-art polycrystalline Pt. To the best of our knowledge this is the most active polycrystalline surface ever reported. It should be noted that strain relaxations are expected to occur in the Pt overlayer, this would result in effective Pt-Pt distances at the surface active sites which are closer to the one of pure Pt.

In terms of stability trends, the most active polycrystalline alloys were not found to be the most stable. On the contrary, there are some evidences that a higher level compression of the Pt-Pt distance in the overlayer corresponds to higher losses in activity during potential cycling. This would be in agreement with DFT calculations on the stability of the Pt overlayers. In order to further investigate this, a model for the analysis of the AR-XPS results was introduced with the purpose of quantitatively estimating the thickness of the Pt overlayers. While most of the alloys exhibit similar thicknesses after ORR, after stability tests the situation changes. Higher losses in activity relate well with the level of thickening of the overlayer indicating a direct relationship between chemical and physical stability. The dealloying

mechanism seems the main reason of deactivation, probably because a thicker Pt overlayer intensifies the effect of strain relaxations. The model also seems to confirm that more compressed overlayers have a lower resistance against dealloying.

It should be noted that, even after stability tests, most of the presented Pt_5Ln alloys are still 3 times more active than polycrystalline Pt: more than 4 times in the case of Pt_5Gd which seems to represent the best compromise of activity and stability. Similarly prepared alloys of Pt and late transition metals only exhibited a factor of activity enhancement around 2, before an analogous stability test. Alloys of Pt and rare earths can therefore be considered as promising catalysts for the application in PEMFCs, even though there is still no direct proof that their more negative heat of alloy formation would result in a higher long-term stability.

Pt-Y nanoparticles

The application of these materials in a fuel cell would require the fabrication of large surface area catalysts. The second part of this work focused on Pt-Y nanoparticles produced through a physical method. The combination of a gas aggregation technique and a time-of-flight mass spectrometer allowed the deposition of size-selected Pt-Y nanoparticles onto glassy carbon supports. The mass activity of the 9 nm Pt-Y nanoparticles (3.05 A mg_{Pt}^{-1}) is one of the highest ever reported, more than 5 times higher than the one of state-of-the-art Pt/C. Interestingly, the specific activity of these bimetallic nanoparticles increases monotonically with particle size (in the tested range of sizes), while pure Pt nanoparticles exhibit a maximum for a size of about 3 nm. This difference is probably due to the process of surface dealloying which originates a typical core-shell structure. Similar to the case of polycrystalline samples, a 1 nm thick Pt shell surrounds an alloyed core. Similarly, the activity enhancement is ascribed to strain effects. The presence of a bigger core in the large particles produces a higher level of compression of the nearest neighbour Pt-Pt distance leading to a higher specific activity. The activity losses after stability tests were 37 % in the case of the most active 9 nm Pt-Y nanoparticles. Similar or higher losses have been reported for most of the nanoparticles based on alloys of Pt and late transition metals, despite the high level of optimization achieved after two decades of studies.

The 9 nm Pt-Y nanoparticles were deposited on the cathode side of a Membrane Electrode Assembly (MEA), part of a specifically prepared fuel cell that allows AP-XPS measurements under operation conditions. By applying potential cycles under different pressures of H_2O or O_2 the oxidation of Y, due to the process of dealloying, was observed *in situ*. By focusing on the O 1s XPS signal the evolution of the adsorbed oxygenated species can be followed as a function of the electrochemical potential. At high potentials, close to the OCP as well as under operating conditions with high partial pressures of O_2, a shift of the O 1s XPS towards lower binding energies is measured. It corresponds to a higher population of

non-hydrated species, in particular non-hydrated OH, similar to what was reported for pure Pt nanoparticles.

Perspectives

The observed trends in activity and stability will need to be confirmed by a few more experiments on polycrystalline alloys. In all cases they already indicate various promising materials for application at the cathode of PEMFCs. The studies on polycrystalline alloys did not really allow to investigate the effect of composition on the catalytic performance of these alloys. However, we anticipate that it will probably be hard to overcome the stability of some ordered intermetallic phases and these will put strict requirements in terms of alloy stoichiometry. The comparison with polycrystalline alloys of Pt and late transition metals might elucidate the role of more negative heats of alloy formation on stability, since this was the original reason motivating our search of new materials for catalyzing the ORR. However, definitive conclusions will probably require a stability comparison between similarly prepared nanoparticles.

At the current level of knowledge, a better understanding of the catalytic properties of these new materials will most probably require the study of single crystals. Studies that were already initiated in the case of the Pt-Y system [101] (Paper 4 in the end of this thesis). Single crystals of these intermetallic compounds would allow, not only to achieve a more precise characterization, but most importantly to select single ordered facets and distinguish their behaviour in terms of activity and stability. Some of them might exhibit outstanding activities, similar or higher than that of $Pt_3Ni(111)$ [39]. In this perspective the realization of Pt-skin structures and their stabilization in acidic electrolytes will probably be the main challenge. The completion of the EC-XPS setup will help to characterize these single crystal alloys and to investigate their electronic structures by XPS and UPS.

Similar challenges will also concern the Pt-Y (or Pt-rare earth) nanoparticles. Also in this case the improvement of their catalytic activity and stability will probably require an enhanced level of ordering. On the basis of the progresses achieved on large surface area catalysts of Pt and late transition metals, the optimization of acid leaching and annealing procedures is expected to stabilize more ordered structures, with advantages both in terms of activity and stability. Tuning the morphology of the particles in order to select particular facets and active sites of these ordered structures might bring further advances.

Finally, the biggest challenge will probably be the development of an economically viable and scalable process for the production of nanoparticles based on these new alloys. Various synthesis methods are currently under investigation. The production of thin films in perspective of an application onto nanostructured substrates might represent another promising alternative towards the fabrication of large surface area catalysts.

Appendix A

Components of La 3d and Ce 3d XPS spectra

Pt_5La	Binding Energy La3d 5/2 (eV)				Binding Energy La3d 3/2 (eV)				Relative intensity (%)			
	La		La^{3+}		La		La^{3+}		La		La^{3+}	
	f_0	f_1	f_0	f_1	f_0	f_1	f_0	f_1	f_0	f_1	f_0	f_1
As-prepared	836.3	832.7	-	-	853.0	849.4	-	-	71	29	-	-
After air-exposure	836.3	832.7	838.4	835.0	853.0	849.3	855.2	851.7	49	14	18	19
After ORR	836.1	832.5	-	-	852.8	849.2	-	-	66	34	-	-
After stability	836.1	832.5	-	-	852.8	849.2	-	-	66	34	-	-

Pt_5Ce	Binding Energy La3d 5/2 (eV)						Binding Energy La3d 3/2 (eV)						Relative intensity (%)					
	Ce			Ce^{4+}			Ce			Ce^{4+}			Ce			Ce^{4+}		
	f_0	f_1	f_2	f_0	f_1	f_2	f_0	f_1	f_2	f_0	f_1	f_2	f_0	f_1	f_2	f_0	f_1	f_2
As-prepared	896.6	884.4	880.1	-	-	-	914.9	903.1	898.7	-	-	-	5	66	28	-	-	-
After air-exposure	896.5	884.4	880.1	897.9	887.0	881.8	914.9	903.1	898.7	916.2	906.0	900.4	3	35	15	15	16	16
After ORR	896.8	884.2	879.8	-	-	-	914.9	902.6	898.3	-	-	-	10	75	15	-	-	-
After stability	896.8	884.4	879.8	-	-	-	914.9	903.0	898.6	-	-	-	9	73	18	-	-	-

Pt_3La	Binding Energy La3d 5/2 (eV)				Binding Energy La3d 3/2 (eV)				Relative intensity (%)			
	La		La^{3+}		La		La^{3+}		La		La^{3+}	
	f_0	f_1	f_0	f_1	f_0	f_1	f_0	f_1	f_0	f_1	f_0	f_1
As-prepared	836.4	832.8	-	-	853.1	849.5	-	-	69	31	-	-
After air-exposure	836.4	832.8	838.2	834.6	853.0	849.4	855.0	851.3	42	19	18	21
After ORR	836.1	832.5	-	-	852.8	849.2	-	-	66	34	-	-
After stability	-	-	-	-	-	-	-	-	-	-	-	-

Table A.1: Binding energies and relative intensities of the XPS peaks for Pt_5La, Pt_5Ce and Pt_3La [126]. The f_n components of the La 3d and Ce 3d spectra have been divided into metallic species (La and Ce) and oxidized species (La^{3+} and Ce^{4+}).

Bibliography

[1] W. Reitz. 'Handbook of fuel cells: fundamentals, technology, and applications, (volume 2) W. Vielstich, A. Lamm, and Hubert A. Gasteiger (editors).' *Materials and Manufacturing Processes* **22**(6):789–789 (2007).

[2] H. A. Gasteiger & J. Garche. 'Fuel cells.' In *Handbook of Heterogeneous Catalysis*. Wiley-VCH Verlag GmbH & Co. KGaA (2008).

[3] H. A. Gasteiger, S. S. Kocha, B. Sompalli, & F. T. Wagner. 'Activity benchmarks and requirements for Pt, Pt-alloy, and non-Pt oxygen reduction catalysts for PEMFCs.' *Applied Catalysis B: Environmental* **56**(1–2):9–35 (2005).

[4] U. Eberle, B. Müller, & R. v. Helmolt. 'Fuel cell electric vehicles and hydrogen infrastructure: status 2012.' *Energy & Environmental Science* **5**(10):8780–8798 (2012).

[5] P. C. K. Vesborg & T. F. Jaramillo. 'Addressing the terawatt challenge: scalability in the supply of chemical elements for renewable energy.' *RSC Advances* **2**(21):7933–7947 (2012).

[6] I. E. L. Stephens, A. S. Bondarenko, U. Grønbjerg, J. Rossmeisl, & I. Chorkendorff. 'Understanding the electrocatalysis of oxygen reduction on platinum and its alloys.' *Energy & Environmental Science* **5**(5):6744–6762 (2012).

[7] M. K. Debe. 'Electrocatalyst approaches and challenges for automotive fuel cells.' *Nature* **486**(7401):43–51 (2012).

[8] M. Pourbaix. *Atlas of electrochemical equilibria in aqueous solutions*. National Association Of Corrosion (1974).

[9] Y. Shao-Horn, W. C. Sheng, S. Chen, P. J. Ferreira, E. F. Holby, & D. Morgan. 'Instability of supported platinum nanoparticles in low-temperature fuel cells.' *Topics in Catalysis* **46**(3-4):285–305 (2007).

[10] K. J. J. Mayrhofer, K. Hartl, V. Juhart, & M. Arenz. 'Degradation of carbon-supported Pt bimetallic nanoparticles by surface segregation.' *Journal of the American Chemical Society* **131**(45):16348–16349 (2009).

[11] A. A. Topalov, I. Katsounaros, M. Auinger, S. Cherevko, J. C. Meier, S. O. Klemm, & K. J. J. Mayrhofer. 'Dissolution of platinum: Limits for the deployment of electrochemical energy conversion?' *Angewandte Chemie International Edition* **51**(50):12613–12615 (2012).

[12] C. W. B. Bezerra, L. Zhang, K. Lee, H. Liu, A. L. B. Marques, E. P. Marques, H. Wang, & J. Zhang. 'A review of Fe–N/C and Co–N/C catalysts for the oxygen reduction reaction.' *Electrochimica Acta* **53**(15):4937–4951 (2008).

[13] Z. Chen, D. Higgins, A. Yu, L. Zhang, & J. Zhang. 'A review on non-precious metal electrocatalysts for PEM fuel cells.' *Energy & Environmental Science* **4**(9):3167–3192 (2011).

[14] P. Sabatier. 'Hydrogénations et déshydrogénations par catalyse.' *Berichte der deutschen chemischen Gesellschaft* **44**(3):1984–2001 (1911).

[15] I. Chorkendorff & J. W. Niemantsverdriet. *Concepts of modern catalysis and kinetics*. Wiley-VCH, Weinheim (2007).

[16] J. Greeley, I. E. L. Stephens, A. S. Bondarenko, T. P. Johansson, H. A. Hansen, T. F. Jaramillo, J. Rossmeisl, I. Chorkendorff, & J. K. Nørskov. 'Alloys of platinum and early transition metals as oxygen reduction electrocatalysts.' *Nature Chemistry* **1**(7):552–556 (2009).

[17] J. Rossmeisl, G. S. Karlberg, T. Jaramillo, & J. K. Nørskov. 'Steady state oxygen reduction and cyclic voltammetry.' *Faraday Discussions* **140**:337 (2009).

[18] G. S. Karlberg, J. Rossmeisl, & J. K. Nørskov. 'Estimations of electric field effects on the oxygen reduction reaction based on the density functional theory.' *Physical Chemistry Chemical Physics* **9**(37):5158–5161 (2007).

[19] J. K. Nørskov, J. Rossmeisl, A. Logadottir, L. Lindqvist, J. R. Kitchin, T. Bligaard, & H. Jónsson. 'Origin of the overpotential for oxygen reduction at a fuel-cell cathode.' *The Journal of Physical Chemistry B* **108**(46):17886–17892 (2004).

[20] A. Damjanovic & V. Brusic. 'Electrode kinetics of oxygen reduction on oxide-free platinum electrodes.' *Electrochimica Acta* **12**(6):615–628 (1967).

[21] A. A. Gewirth & M. S. Thorum. 'Electroreduction of dioxygen for fuel-cell applications: materials and challenges.' *Inorganic Chemistry* **49**(8):3557–3566 (2010).

[22] A. S. Bondarenko, I. E. L. Stephens, H. A. Hansen, F. J. Pérez-Alonso, V. Tripkovic, T. P. Johansson, J. Rossmeisl, J. K. Nørskov, & I. Chorkendorff. 'The Pt(111)/electrolyte interface under oxygen reduction reaction conditions: an electrochemical impedance spectroscopy study.' *Langmuir* **27**(5):2058–2066 (2011).

[23] M. Wakisaka, H. Suzuki, S. Mitsui, H. Uchida, & M. Watanabe. 'Identification and quantification of oxygen species adsorbed on Pt(111) single-crystal and polycrystalline Pt electrodes by photoelectron spectroscopy.' *Langmuir* **25**(4):1897–1900 (2009).

[24] H. S. Casalongue, S. Kaya, V. Viswanathan, D. J. Miller, D. Friebel, H. A. Hansen, J. K. Nørskov, A. Nilsson, & H. Ogasawara. 'Direct observation of the oxygenated species during oxygen reduction on a platinum fuel cell cathode.' *Nature Communications* **4** (2013).

[25] A. B. Anderson & T. V. Albu. 'Ab initio determination of reversible potentials and activation energies for outer-sphere oxygen reduction to water and the reverse oxidation reaction.' *Journal of the American Chemical Society* **121**(50):11855–11863 (1999).

[26] C. D. Taylor, S. A. Wasileski, J.-S. Filhol, & M. Neurock. 'First principles reaction modeling of the electrochemical interface: consideration and calculation of a tunable surface potential from atomic and electronic structure.' *Physical Review B* **73**(16):165402 (2006).

[27] J. Rossmeisl, E. Skúlason, M. E. Björketun, V. Tripkovic, & J. K. Nørskov. 'Modeling the electrified solid-liquid interface.' *Chemical Physics Letters* **466**(1-3):68–71 (2008).

[28] E. Skúlason, V. Tripkovic, M. E. Björketun, S. Gudmundsdóttir, G. Karlberg, J. Rossmeisl, T. Bligaard, H. Jónsson, & J. K. Nørskov. 'Modeling the electrochemical hydrogen oxidation and evolution reactions on the basis of density functional theory calculations.' *Journal of Physical Chemistry C* **114**(42):18182–18197 (2010).

[29] J. K. Nørskov, T. Bligaard, A. Logadottir, S. Bahn, L. B. Hansen, M. Bollinger, H. Bengaard, B. Hammer, Z. Sljivancanin, M. Mavrikakis, Y. Xu, S. Dahl, & C. J. H. Jacobsen. 'Universality in heterogeneous catalysis.' *Journal of Catalysis* **209**(2):275–278 (2002).

[30] P. Nieto, E. Pijper, D. Barredo, G. Laurent, R. A. Olsen, E.-J. Baerends, G.-J. Kroes, & D. Farías. 'Reactive and nonreactive scattering of H_2 from a metal surface is electronically adiabatic.' *Science* **312**(5770):86–89 (2006).

[31] P. Strasser, S. Koh, T. Anniyev, J. Greeley, K. More, C. Yu, Z. Liu, S. Kaya, D. Nordlund, H. Ogasawara, M. F. Toney, & A. Nilsson. 'Lattice-strain control of the activity in dealloyed core-shell fuel cell catalysts.' *Nature Chemistry* **2**(6):454–460 (2010).

[32] V. Tripković, E. Skúlason, S. Siahrostami, J. K. Nørskov, & J. Rossmeisl. 'The oxygen reduction reaction mechanism on Pt(111) from density functional theory calculations.' *Electrochimica Acta* **55**(27):7975–7981 (2010).

[33] M. J. Janik, C. D. Taylor, & M. Neurock. 'First-principles analysis of the initial electroreduction steps of oxygen over Pt(111).' *Journal of the Electrochemical Society* **156**(1):B126–B135 (2009).

[34] J. Rossmeisl, A. Logadottir, & J. K. Nørskov. 'Electrolysis of water on (oxidized) metal surfaces.' *Chemical Physics* **319**(1–3):178–184 (2005).

[35] T. Toda, H. Igarashi, H. Uchida, & M. Watanabe. 'Enhancement of the electroreduction of oxygen on Pt alloys with Fe, Ni, and Co.' *Journal of the Electrochemical Society* **146**(10):3750–3756 (1999).

[36] V. Stamenković, T. J. Schmidt, P. N. Ross, & N. M. Marković. 'Surface composition effects in electrocatalysis: Kinetics of oxygen reduction on well-defined Pt_3Ni and Pt_3Co alloy surfaces.' *The Journal of Physical Chemistry B* **106**(46):11970–11979 (2002).

[37] V. R. Stamenkovic, B. S. Mun, K. J. J. Mayrhofer, P. N. Ross, & N. M. Markovic. 'Effect of surface composition on electronic structure, stability, and electrocatalytic properties of Pt-transition metal alloys: Pt-skin versus Pt-skeleton surfaces.' *Journal of the American Chemical Society* **128**(27):8813–8819 (2006).

[38] V. Stamenkovic, B. S. Mun, K. J. J. Mayrhofer, P. N. Ross, N. M. Markovic, J. Rossmeisl, J. Greeley, & J. K. Nørskov. 'Changing the activity of electrocatalysts for oxygen reduction by tuning the surface electronic structure.' *Angewandte Chemie* **118**(18):2963–2967 (2006).

[39] V. R. Stamenkovic, B. Fowler, B. S. Mun, G. Wang, P. N. Ross, C. A. Lucas, & N. M. Marković. 'Improved oxygen reduction activity on $Pt_3Ni(111)$ via increased surface site availability.' *Science* **315**(5811):493–497 (2007).

[40] R. Yang, J. Leisch, P. Strasser, & M. F. Toney. 'Structure of dealloyed $PtCu_3$ thin films and catalytic activity for oxygen reduction.' *Chemistry of Materials* **22**(16):4712–4720 (2010).

[41] R. Yang, P. Strasser, & M. F. Toney. 'Dealloying of $Cu_3Pt(111)$ studied by surface X-ray scattering.' *The Journal of Physical Chemistry C* **115**(18):9074–9080 (2011).

[42] N. Wakabayashi, M. Takeichi, H. Uchida, & M. Watanabe. 'Temperature dependence of oxygen reduction activity at Pt-Fe, Pt-Co, and Pt-Ni alloy electrodes.' *Journal of Physical Chemistry B* **109**(12):5836–5841 (2005).

[43] S. Koh & P. Strasser. 'Electrocatalysis on bimetallic surfaces: modifying catalytic reactivity for oxygen reduction by voltammetric surface dealloying.' *Journal of the American Chemical Society* **129**(42):12624–12625 (2007).

[44] V. R. Stamenkovic, B. S. Mun, M. Arenz, K. J. J. Mayrhofer, C. A. Lucas, G. Wang, P. N. Ross, & N. M. Markovic. 'Trends in electrocatalysis on extended and nanoscale Pt-bimetallic alloy surfaces.' *Nature Materials* **6**(3):241–247 (2007).

[45] L.-J. Wan, T. Moriyama, M. Ito, H. Uchida, & M. Watanabe. 'In situ STM imaging of surface dissolution and rearrangement of a Pt–Fe alloy electrocatalyst in electrolyte solution.' *Chemical Communications* **1**(1):58–59 (2002).

[46] Y. Gauthier, Y. Joly, R. Baudoing, & J. Rundgren. 'Surface-sandwich segregation on nondilute bimetallic alloys: $Pt_{50}Ni_{50}$ and $Pt_{78}Ni_{22}$ probed by low-energy electron diffraction.' *Physical Review B* **31**(10):6216–6218 (1985).

[47] J. Zhang, M. B. Vukmirovic, Y. Xu, M. Mavrikakis, & R. R. Adzic. 'Controlling the catalytic activity of platinum-monolayer electrocatalysts for oxygen reduction with different substrates.' *Angewandte Chemie International Edition* **44**(14):2132–2135 (2005).

[48] N. Todoroki, Y. Iijima, R. Takahashi, Y. Asakimori, & T. Wadayama. 'Structure and electrochemical stability of Pt-enriched Ni/Pt(111) topmost surface prepared by molecular beam epitaxy.' *Journal of The Electrochemical Society* **160**(6):F591–F596 (2013).

[49] P. B. Balbuena, D. Altomare, N. Vadlamani, S. Bingi, L. A. Agapito, & J. M. Seminario. 'Adsorption of O, OH, and H_2O on Pt-based bimetallic clusters alloyed with Co, Cr, and Ni.' *The Journal of Physical Chemistry A* **108**(30):6378–6384 (2004).

[50] Y. Xu, A. V. Ruban, & M. Mavrikakis. 'Adsorption and dissociation of O_2 on Pt-Co and Pt-Fe alloys.' *Journal of the American Chemical Society* **126**(14):4717–4725 (2004).

[51] M. Teliska, V. S. Murthi, S. Mukerjee, & D. E. Ramaker. 'Correlation of water activation, surface properties, and oxygen reduction reactivity of supported Pt–M/C bimetallic electrocatalysts using XAS.' *Journal of The Electrochemical Society* **152**(11):A2159–A2169 (2005).

[52] J. R. Kitchin, J. K. Nørskov, M. A. Barteau, & J. G. Chen. 'Modification of the surface electronic and chemical properties of Pt(111) by subsurface 3d

transition metals.' *The Journal of Chemical Physics* **120**(21):10240–10246 (2004).

[53] B. Hammer & J. K. Nørskov. 'Theoretical surface science and catalysis-calculations and concepts.' In H. K. Bruce C. Gates, ed., *Advances in Catalysis*, vol. Volume 45 of *Impact of Surface Science on Catalysis*, pp. 71–129. Academic Press (2000).

[54] M. Mavrikakis, B. Hammer, & J. K. Nørskov. 'Effect of strain on the reactivity of metal surfaces.' *Physical Review Letters* **81**(13):2819–2822 (1998).

[55] J. R. Kitchin, J. K. Nørskov, M. A. Barteau, & J. G. Chen. 'Role of strain and ligand effects in the modification of the electronic and chemical properties of bimetallic surfaces.' *Physical Review Letters* **93**(15):156801 (2004).

[56] I. E. L. Stephens, A. S. Bondarenko, F. J. Perez-Alonso, F. Calle-Vallejo, L. Bech, T. P. Johansson, A. K. Jepsen, R. Frydendal, B. P. Knudsen, J. Rossmeisl, & I. Chorkendorff. 'Tuning the activity of Pt(111) for oxygen electroreduction by subsurface alloying.' *Journal of the American Chemical Society* **133**(14):5485–5491 (2011).

[57] B. Cordero, V. Gómez, A. E. Platero-Prats, M. Revés, J. Echeverría, E. Cremades, F. Barragán, & S. Alvarez. 'Covalent radii revisited.' *Dalton Transactions* **1**(21):2832–2838 (2008).

[58] A. Bonakdarpour, J. Wenzel, D. A. Stevens, S. Sheng, T. L. Monchesky, R. Löbel, R. T. Atanasoski, A. K. Schmoeckel, G. D. Vernstrom, M. K. Debe, & J. R. Dahn. 'Studies of transition metal dissolution from combinatorially sputtered, nanostructured Pt_{1-x} M_x (M = Fe, Ni; $0 < x < 1$) electrocatalysts for PEM fuel cells.' *Journal of The Electrochemical Society* **152**(1):A61–A72 (2005).

[59] M. K. Debe, A. K. Schmoeckel, G. D. Vernstrom, & R. Atanasoski. 'High voltage stability of nanostructured thin film catalysts for PEM fuel cells.' *Journal of Power Sources* **161**(2):1002–1011 (2006).

[60] D. van der Vliet, C. Wang, M. Debe, R. Atanasoski, N. M. Markovic, & V. R. Stamenkovic. 'Platinum-alloy nanostructured thin film catalysts for the oxygen reduction reaction.' *Electrochimica Acta* **56**(24):8695–8699 (2011).

[61] D. F. v. d. Vliet, C. Wang, D. Tripkovic, D. Strmcnik, X. F. Zhang, M. K. Debe, R. T. Atanasoski, N. M. Markovic, & V. R. Stamenkovic. 'Mesostructured thin films as electrocatalysts with tunable composition and surface morphology.' *Nature Materials* **11**(12):1051–1058 (2012).

[62] J. Kibsgaard, Y. Gorlin, Z. Chen, & T. F. Jaramillo. 'Meso-structured platinum thin films: Active and stable electrocatalysts for the oxygen reduction reaction.' *Journal of the American Chemical Society* **134**(18):7758–7765 (2012).

[63] G. A. Tritsaris, J. Greeley, J. Rossmeisl, & J. K. Nørskov. 'Atomic-scale modeling of particle size effects for the oxygen reduction reaction on Pt.' *Catalysis Letters* **141**(7):909–913 (2011).

[64] F. J. Perez-Alonso, D. N. McCarthy, A. Nierhoff, P. Hernandez-Fernandez, C. Strebel, I. E. L. Stephens, J. H. Nielsen, & I. Chorkendorff. 'The effect of size on the oxygen electroreduction activity of mass-selected platinum nanoparticles.' *Angewandte Chemie International Edition* **51**(19):4641–4643 (2012).

[65] F. Maillard, S. Pronkin, & E. R. Savinova. 'Influence of size on the electrocatalytic activities of supported metal nanoparticles in fuel cells related reactions.' In *Handbook of Fuel Cells*. John Wiley & Sons, Ltd (2010).

[66] C. Wang, H. Daimon, T. Onodera, T. Koda, & S. Sun. 'A general approach to the size- and shape-controlled synthesis of platinum nanoparticles and their catalytic reduction of oxygen.' *Angewandte Chemie International Edition* **47**(19):3588–3591 (2008).

[67] V. Komanicky, H. Iddir, K.-C. Chang, A. Menzel, G. Karapetrov, D. Hennessy, P. Zapol, & H. You. 'Shape-dependent activity of platinum array catalyst.' *Journal of the American Chemical Society* **131**(16):5732–5733 (2009).

[68] S. Mostafa, F. Behafarid, J. R. Croy, L. K. Ono, L. Li, J. C. Yang, A. I. Frenkel, & B. R. Cuenya. 'Shape-dependent catalytic properties of Pt nanoparticles.' *Journal of the American Chemical Society* **132**(44):15714–15719 (2010).

[69] B. Roldan Cuenya. 'Metal nanoparticle catalysts beginning to shape-up.' *Accounts of Chemical Research* **46**(8):1682–1691 (2013).

[70] M. Nesselberger, M. Roefzaad, R. Fayçal Hamou, P. Ulrich Biedermann, F. F. Schweinberger, S. Kunz, K. Schloegl, G. K. H. Wiberg, S. Ashton, U. Heiz, K. J. J. Mayrhofer, & M. Arenz. 'The effect of particle proximity on the oxygen reduction rate of size-selected platinum clusters.' *Nature Materials* **12**(10):919–924 (2013).

[71] S. Mukerjee & S. Srinivasan. 'Enhanced electrocatalysis of oxygen reduction on platinum alloys in proton exchange membrane fuel cells.' *Journal of Electroanalytical Chemistry* **357**(1–2):201–224 (1993).

[72] S. Mukerjee, S. Srinivasan, M. P. Soriaga, & J. McBreen. 'Role of structural and electronic properties of Pt and Pt alloys on electrocatalysis of oxygen reduction an in situ XANES and EXAFS investigation.' *Journal of The Electrochemical Society* **142**(5):1409–1422 (1995).

[73] U. Paulus, A. Wokaun, G. Scherer, T. Schmidt, V. Stamenkovic, N. Markovic, & P. Ross. 'Oxygen reduction on high surface area Pt-based alloy catalysts

in comparison to well defined smooth bulk alloy electrodes.' *Electrochimica Acta* **47**(22–23):3787–3798 (2002).

[74] P. Yu, M. Pemberton, & P. Plasse. 'PtCo/C cathode catalyst for improved durability in PEMFCs.' *Journal of Power Sources* **144**(1):11–20 (2005).

[75] M. Nesselberger, S. Ashton, J. C. Meier, I. Katsounaros, K. J. J. Mayrhofer, & M. Arenz. 'The particle size effect on the oxygen reduction reaction activity of Pt catalysts: Influence of electrolyte and relation to single crystal models.' *Journal of the American Chemical Society* **133**(43):17428–17433 (2011).

[76] S. Chen, H. A. Gasteiger, K. Hayakawa, T. Tada, & Y. Shao-Horn. 'Platinum-alloy cathode catalyst degradation in proton exchange membrane fuel cells: nanometer-scale compositional and morphological changes.' *Journal of The Electrochemical Society* **157**(1):A82–A97 (2010).

[77] F. Maillard, L. Dubau, J. Durst, M. Chatenet, J. André, & E. Rossinot. 'Durability of Pt_3Co/C nanoparticles in a proton-exchange membrane fuel cell: direct evidence of bulk Co segregation to the surface.' *Electrochemistry Communications* **12**(9):1161–1164 (2010).

[78] A. Zana, J. Speder, M. Roefzaad, L. Altmann, M. Bäumer, & M. Arenz. 'Probing degradation by IL-TEM: the influence of stress test conditions on the degradation mechanism.' *Journal of The Electrochemical Society* **160**(6):F608–F615 (2013).

[79] K. C. Neyerlin, R. Srivastava, C. Yu, & P. Strasser. 'Electrochemical activity and stability of dealloyed Pt–Cu and Pt–Cu–Co electrocatalysts for the oxygen reduction reaction (ORR).' *Journal of Power Sources* **186**(2):261–267 (2009).

[80] C. Wang, M. Chi, D. Li, D. Strmcnik, D. van der Vliet, G. Wang, V. Komanicky, K.-C. Chang, A. P. Paulikas, D. Tripkovic, J. Pearson, K. L. More, N. M. Markovic, & V. R. Stamenkovic. 'Design and synthesis of bimetallic electrocatalyst with multilayered Pt-skin surfaces.' *Journal of the American Chemical Society* **133**(36):14396–14403 (2011).

[81] L. Gan, M. Heggen, R. O'Malley, B. Theobald, & P. Strasser. 'Understanding and controlling nanoporosity formation for improving the stability of bimetallic fuel cell catalysts.' *Nano Letters* **13**(3):1131–1138 (2013).

[82] D. Wang, H. L. Xin, R. Hovden, H. Wang, Y. Yu, D. A. Muller, F. J. DiSalvo, & H. D. Abruña. 'Structurally ordered intermetallic platinum–cobalt core–shell nanoparticles with enhanced activity and stability as oxygen reduction electrocatalysts.' *Nature Materials* **12**(1):81–87 (2013).

[83] K. Mayrhofer, V. Juhart, K. Hartl, M. Hanzlik, & M. Arenz. 'Adsorbate-induced surface segregation for core-shell nanocatalysts.' *Angewandte Chemie International Edition* **48**(19):3529–3531 (2009).

[84] M.-H. Shao, K. Sasaki, & R. R. Adzic. 'Pd-Fe nanoparticles as electrocatalysts for oxygen reduction.' *Journal of the American Chemical Society* **128**(11):3526–3527 (2006).

[85] K. A. Kuttiyiel, K. Sasaki, Y. Choi, D. Su, P. Liu, & R. R. Adzic. 'Bimetallic IrNi core platinum monolayer shell electrocatalysts for the oxygen reduction reaction.' *Energy & Environmental Science* **5**(1):5297–5304 (2012).

[86] K. Sasaki, H. Naohara, Y. Choi, Y. Cai, W.-F. Chen, P. Liu, & R. R. Adzic. 'Highly stable Pt monolayer on PdAu nanoparticle electrocatalysts for the oxygen reduction reaction.' *Nature Communications* **3**:1115 (2012).

[87] J. Wu, J. Zhang, Z. Peng, S. Yang, F. T. Wagner, & H. Yang. 'Truncated octahedral Pt_3Ni oxygen reduction reaction electrocatalysts.' *Journal of the American Chemical Society* **132**(14):4984–4985 (2010).

[88] J. Zhang, H. Yang, J. Fang, & S. Zou. 'Synthesis and oxygen reduction activity of shape-controlled Pt_3Ni nanopolyhedra.' *Nano Letters* **10**(2):638–644 (2010).

[89] M. Ahmadi, F. Behafarid, C. Cui, P. Strasser, & B. R. Cuenya. 'Long-range segregation phenomena in shape-selected bimetallic nanoparticles: chemical state effects.' *ACS Nano* **7**(10):9195–9204 (2013).

[90] C. Cui, M. Ahmadi, F. Behafarid, L. Gan, M. Neumann, M. Heggen, B. R. Cuenya, & P. Strasser. 'Shape-selected bimetallic nanoparticle electrocatalysts: evolution of their atomic-scale structure, chemical composition, and electrochemical reactivity under various chemical environments.' *Faraday Discussions* **162**:91 (2013).

[91] C. Cui, L. Gan, M. Heggen, S. Rudi, & P. Strasser. 'Compositional segregation in shaped Pt alloy nanoparticles and their structural behaviour during electrocatalysis.' *Nature Materials* **12**(8):765–771 (2013).

[92] S.-I. Choi, S. Xie, M. Shao, J. H. Odell, N. Lu, H.-C. Peng, L. Protsailo, S. Guerrero, J. Park, X. Xia, J. Wang, M. J. Kim, & Y. Xia. 'Synthesis and characterization of 9 nm Pt–Ni octahedra with a record high activity of 3.3 A/mgPt for the oxygen reduction reaction.' *Nano Letters* **13**(7):3420–3425 (2013).

[93] C. Chen, Y. Kang, Z. Huo, Z. Zhu, W. Huang, H. L. Xin, J. D. Snyder, D. Li, J. A. Herron, M. Mavrikakis, M. Chi, K. L. More, Y. Li, N. M. Markovic,

G. A. Somorjai, P. Yang, & V. R. Stamenkovic. 'Highly crystalline multimetallic nanoframes with three-dimensional electrocatalytic surfaces.' *Science* **343**(6177):1339–1343 (2014).

[94] G. H. Jóhannesson, T. Bligaard, A. V. Ruban, H. L. Skriver, K. W. Jacobsen, & J. K. Nørskov. 'Combined electronic structure and evolutionary search approach to materials design.' *Physical Review Letters* **88**(25):255506 (2002).

[95] T. Bligaard, G. H. Jóhannesson, A. V. Ruban, H. L. Skriver, K. W. Jacobsen, & J. K. Nørskov. 'Pareto-optimal alloys.' *Applied Physics Letters* **83**(22):4527–4529 (2003).

[96] S. J. Yoo, S.-K. Kim, T.-Y. Jeon, S. J. Hwang, J.-G. Lee, S.-C. Lee, K.-S. Lee, Y.-H. Cho, Y.-E. Sung, & T.-H. Lim. 'Enhanced stability and activity of Pt–Y alloy catalysts for electrocatalytic oxygen reduction.' *Chemical Communications* **47**(41):11414–11416 (2011).

[97] S. J. Yoo, K.-S. Lee, S. J. Hwang, Y.-H. Cho, S.-K. Kim, J. W. Yun, Y.-E. Sung, & T.-H. Lim. 'Pt_3Y electrocatalyst for oxygen reduction reaction in proton exchange membrane fuel cells.' *International Journal of Hydrogen Energy* **37**(12):9758–9765 (2012).

[98] I. E. L. Stephens, A. S. Bondarenko, L. Bech, & I. Chorkendorff. 'Oxygen electroreduction activity and X-ray photoelectron spectroscopy of platinum and early transition metal alloys.' *ChemCatChem* **4**(3):341–349 (2012).

[99] S. J. Yoo, S. J. Hwang, J.-G. Lee, S.-C. Lee, T.-H. Lim, Y.-E. Sung, A. Wieckowski, & S.-K. Kim. 'Promoting effects of la for improved oxygen reduction activity and high stability of Pt on Pt–La alloy electrodes.' *Energy & Environmental Science* **5**(6):7521–7525 (2012).

[100] T. P. Johansson, E. T. Ulrikkeholm, P. Hernandez-Fernandez, P. Malacrida, H. Hansen, A. S. Bandarenka, J. K. Nørskov, J. Rossmeisl, I. E. L. Stephens, & I. Chorkendorff. 'Pt skin vs. Pt skeleton structures of Pt_3Sc as electrocatalysts for oxygen reduction.' *Topics in Catalysis* **57**(1-4):245–254 (2014).

[101] T. P. Johansson, E. T. Ulrikkeholm, P. Hernandez-Fernandez, M. Escudero-Escribano, P. Malacrida, I. E. L. Stephens, & I. Chorkendorff. 'Towards the elucidation of the high oxygen electroreduction activity of Pt_xY: surface science and electrochemical studies of Y/Pt(111).' *Physical Chemistry Chemical Physics* (2014).

[102] K. G. Nishanth, P. Sridhar, & S. Pitchumani. 'Enhanced oxygen reduction reaction activity through spillover effect by Pt–$Y(OH)_3$/C catalyst in direct methanol fuel cells.' *Electrochemistry Communications* **13**(12):1465–1468 (2011).

[103] M. K. Jeon & P. J. McGinn. 'Carbon supported Pt–Y electrocatalysts for the oxygen reduction reaction.' *Journal of Power Sources* **196**(3):1127–1131 (2011).

[104] M. P. Seah. 'The quantitative analysis of surfaces by XPS: a review.' *Surface and Interface Analysis* **2**(6):222–239 (1980).

[105] D. Briggs & M. P. Seah, eds. *Practical Surface Analysis, Auger and X-ray Photoelectron Spectroscopy*. John Wiley & Sons (1996).

[106] J. Scofield. 'Hartree-Slater subshell photoionization cross-sections at 1254 and 1487 eV.' *Journal of Electron Spectroscopy and Related Phenomena* **8**(2):129–137 (1976).

[107] M. P. Seah. 'Data compilations: their use to improve measurement certainty in surface analysis by AES and XPS.' *Surface and Interface Analysis* **9**(2):85–98 (1986).

[108] M. Seah, I. Gilmore, & S. Spencer. 'Quantitative XPS: I. Analysis of X-ray photoelectron intensities from elemental data in a digital photoelectron database.' *Journal of Electron Spectroscopy and Related Phenomena* **120**(1–3):93–111 (2001).

[109] C. D. Wagner, L. E. Davis, M. V. Zeller, J. A. Taylor, R. H. Raymond, & L. H. Gale. 'Empirical atomic sensitivity factors for quantitative analysis by electron spectroscopy for chemical analysis.' *Surface and Interface Analysis* **3**(5):211–225 (1981).

[110] M. P. Seah & W. A. Dench. 'Quantitative electron spectroscopy of surfaces: a standard data base for electron inelastic mean free paths in solids.' *Surface and Interface Analysis* **1**(1):2–11 (1979).

[111] S. Tanuma, C. J. Powell, & D. R. Penn. 'Calculations of electorn inelastic mean free paths. II. Data for 27 elements over the 50–2000 eV range.' *Surface and Interface Analysis* **17**(13):911–926 (1991).

[112] P. J. Cumpson & M. P. Seah. 'Elastic scattering corrections in AES and XPS. II. Estimating attenuation lengths and conditions required for their valid use in overlayer/substrate experiments.' *Surface and Interface Analysis* **25**(6):430–446 (1997).

[113] M. P. Seah, C. A. Clifford, F. M. Green, & I. S. Gilmore. 'An accurate semi-empirical equation for sputtering yields I: for argon ions.' *Surface and Interface Analysis* **37**(5):444–458 (2005).

[114] *Energy Efficiency and Renewable Energy http://www.eere.energy.gov/ hydrogenandfuelcells/mypp/pdfs/fuel_cells.pdf and the US DRIVE Fuel Cell Technical Team Technology Roadmap www.uscar.org/guest/teams/17/Fuel-Cell-Tech-Team*. U. S. Department of Energy (DOE) (2013).

[115] A. Ohma, K. Shinohara, A. Iiyama, T. Yoshida, & A. Daimaru. 'Membrane and catalyst performance targets for automotive fuel cells by FCCJ membrane, catalyst, MEA WG.' *ECS Transactions* **41**(1):775–784 (2011).

[116] K. Mayrhofer, D. Strmcnik, B. Blizanac, V. Stamenkovic, M. Arenz, & N. Markovic. 'Measurement of oxygen reduction activities via the rotating disc electrode method: from Pt model surfaces to carbon-supported high surface area catalysts.' *Electrochimica Acta* **53**(7):3181–3188 (2008).

[117] M. Watanabe, Y. Zhu, & H. Uchida. 'Oxidation of CO on a Pt-Fe alloy electrode studied by surface enhanced infrared reflection-absorption spectroscopy.' *The Journal of Physical Chemistry B* **104**(8):1762–1768 (2000).

[118] A. S. Bandarenka, A. S. Varela, M. Karamad, F. Calle-Vallejo, L. Bech, F. J. Perez-Alonso, J. Rossmeisl, I. E. L. Stephens, & I. Chorkendorff. 'Design of an active site towards optimal electrocatalysis: Overlayers, surface alloys and near-surface alloys of Cu/Pt(111).' *Angewandte Chemie International Edition* **51**(47):11845–11848 (2012).

[119] D. F. van der Vliet, C. Wang, D. Li, A. P. Paulikas, J. Greeley, R. B. Rankin, D. Strmcnik, D. Tripkovic, N. M. Markovic, & V. R. Stamenkovic. 'Unique electrochemical adsorption properties of Pt-skin surfaces.' *Angewandte Chemie* **124**(13):3193–3196 (2012).

[120] R. Walker & J. Darby Jr. 'Thermodynamic properties of solid nickel-platinum alloys.' *Acta Metallurgica* **18**(12):1261–1266 (1970).

[121] R. Pretorius, T. Marais, & C. Theron. 'Thin film compound phase formation sequence: an effective heat of formation model.' *Materials Science Reports* **10**(1–2):1–83 (1993).

[122] R. Hultgren, P. D. Desai, D. T. Hawkins, M. Gleiser, & K. K. Kelley. *Selected Values of the Thermodynamic Properties of Binary Alloys*. Metals Park, Ohio : American Society for Metals (1973).

[123] H. Kleykamp. 'Thermodynamics of the systems of the platinum metals with other transition metals: I. Integral data.' *Journal of Nuclear Materials* **201**:193–217 (1993).

[124] K. T. Jacob & Y. Waseda. 'Thermodynamic properties of Pt_5La, Pt_5Ce, Pt_5Pr, Pt_5Tb and Pt_5Tm intermetallics.' *Bulletin of Materials Science* **13**(4):235–244 (1990).

[125] H. L. Xin, J. A. Mundy, Z. Liu, R. Cabezas, R. Hovden, L. F. Kourkoutis, J. Zhang, N. P. Subramanian, R. Makharia, F. T. Wagner, & D. A. Muller. 'Atomic-resolution spectroscopic imaging of ensembles of nanocatalyst particles across the life of a fuel cell.' *Nano Letters* **12**(1):490–497 (2012).

[126] P. Malacrida, M. Escudero-Escribano, A. Verdaguer-Casadevall, I. Stephens, & I. Chorkendorff. 'Enhanced activity and stability of Pt-La and Pt-Ce alloys for oxygen electroreduction: the elucidation of the active surface phase.' *Journal of Materials Chemistry A* (2014).

[127] W. Bronger. 'Preparation and X-ray investigation of platinum alloys with the rare-earth metals (Pt_5Ln and Pt_3Ln phases).' *Journal of the Less Common Metals* **12**(1):63–68 (1967).

[128] T. B. Massalski, J. L. Murray, L. Bennett, & H. Baker. *Binary alloy phase diagrams*. American Society for Metals (1986).

[129] S. Reimann & H.-J. Schaller. 'Constitution and thermodynamics of Pt-La alloys.' *Journal of Alloys and Compounds* **419**(1–2):133–139 (2006).

[130] A. de Asha & R. Nix. 'Oxidation of lanthanum overlayers on Cu(111).' *Surface Science* **322**(1–3):41–50 (1995).

[131] J. Knudsen, A. U. Nilekar, R. T. Vang, J. Schnadt, E. L. Kunkes, J. A. Dumesic, M. Mavrikakis, & F. Besenbacher. 'A Cu-Pt near-surface alloy for water-gas shift catalysis.' *Journal of the American Chemical Society* **129**(20):6485–6490 (2007).

[132] M. Escudero-Escribano, A. Verdaguer-Casadevall, P. Malacrida, U. Grønbjerg, B. P. Knudsen, A. K. Jepsen, J. Rossmeisl, I. E. L. Stephens, & I. Chorkendorff. 'Pt_5Gd as a highly active and stable catalyst for oxygen electroreduction.' *Journal of the American Chemical Society* **134**(40):16476–16479 (2012).

[133] J. C. Fuggle, M. Campagna, Z. Zolnierek, R. Lässer, & A. Platau. 'Observation of a relationship between core-level line shapes in photoelectron spectroscopy and the localization of screening orbitals.' *Physical Review Letters* **45**(19):1597–1600 (1980).

[134] J. Allen, S. Oh, O. Gunnarsson, K. Schönhammer, M. Maple, M. Torikachvili, & I. Lindau. 'Electronic structure of cerium and light rare-earth intermetallics.' *Advances in Physics* **35**(3):275–316 (1986).

[135] J. Fuggle. 'X-ray and photoelectron spectroscopy of light rare earths.' *Journal of the Less Common Metals* **93**(1):159–169 (1983).

[136] F. Zhang, P. Wang, J. Koberstein, S. Khalid, & S.-W. Chan. 'Cerium oxidation state in ceria nanoparticles studied with X-ray photoelectron spectroscopy and absorPtion near edge spectroscopy.' *Surface Science* **563**(1–3):74–82 (2004).

[137] M. Juel, S. Martinsen, & S. Raaen. 'Oxidation of thin Ce layers on Rh(110).' *Thin Solid Films* **517**(2):805–810 (2008).

[138] L. Schlapbach. 'XPS/UPS study of the oxidation of La and $LaNi_5$ and of the electronic structure of $LaNi_5$.' *Solid State Communications* **38**(2):117–123 (1981).

[139] J. C. Fuggle, F. U. Hillebrecht, Z. Zołnierek, R. Lässer, C. Freiburg, O. Gunnarsson, & K. Schönhammer. 'Electronic structure of Ce and its intermetallic compounds.' *Physical Review B* **27**(12):7330–7341 (1983).

[140] F. U. Hillebrecht & J. C. Fuggle. 'Invalidity of 4f count determination and possibilities for determination of 4f hybridization in intermetallics of the light rare earths by core-level spectroscopy.' *Physical Review B* **25**(6):3550–3556 (1982).

[141] W.-D. Schneider, B. Delley, E. Wuilloud, J.-M. Imer, & Y. Baer. 'Electron-spectroscopic manifestations of the 4f states in light rare-earth solids.' *Physical Review B* **32**(10):6819–6831 (1985).

[142] A. Pfau & K. Schierbaum. 'The electronic structure of stoichiometric and reduced CeO_2 surfaces: an XPS, UPS and HREELS study.' *Surface Science* **321**(1–2):71–80 (1994).

[143] M. Watanabe, K. Tsurumi, T. Mizukami, T. Nakamura, & P. Stonehart. 'Activity and stability of ordered and disordered Co-Pt alloys for phosphoric acid fuel cells.' *Journal of The Electrochemical Society* **141**(10):2659–2668 (1994).

[144] G. Praline, B. Koel, R. Hance, H.-I. Lee, & J. White. 'X-ray photoelectron study of the reaction of oxygen with cerium.' *Journal of Electron Spectroscopy and Related Phenomena* **21**(1):17–30 (1980).

[145] T. L. Barr. 'An ESCA study of the termination of the passivation of elemental metals.' *The Journal of Physical Chemistry* **82**(16):1801–1810 (1978).

[146] D. D. Sarma, M. S. Hegde, & C. N. R. Rao. 'Study of surface oxidation of rare-earth metals by photoelectron spectroscopy.' *Journal of the Chemical Society, Faraday Transactions 2: Molecular and Chemical Physics* **77**(9):1509–1520 (1981).

[147] B. C. Beard & P. N. Ross. 'The structure and activity of Pt-Co alloys as oxygen reduction electrocatalysts.' *Journal of The Electrochemical Society* **137**(11):3368–3374 (1990).

[148] H. Abe, F. Matsumoto, L. R. Alden, S. C. Warren, H. D. Abruña, & F. J. DiSalvo. 'Electrocatalytic performance of fuel oxidation by Pt_3Ti nanoparticles.' *Journal of the American Chemical Society* **130**(16):5452–5458 (2008).

[149] W. M. Haynes, ed. *CRC Handbook of Chemistry and Physics, 93rd Edition*. CRC Press (2012).

[150] C. Wang, M. Chi, G. Wang, D. van der Vliet, D. Li, K. More, H.-H. Wang, J. A. Schlueter, N. M. Markovic, & V. R. Stamenkovic. 'Correlation between surface chemistry and electrocatalytic properties of monodisperse Pt_xNi_{1-x} nanoparticles.' *Advanced Functional Materials* **21**(1):147–152 (2011).

[151] S. J. Hwang, S.-K. Kim, J.-G. Lee, S.-C. Lee, J. H. Jang, P. Kim, T.-H. Lim, Y.-E. Sung, & S. J. Yoo. 'Role of electronic perturbation in stability and activity of Pt-based alloy nanocatalysts for oxygen reduction.' *Journal of the American Chemical Society* **134**(48):19508–19511 (2012).

[152] T. H. Yu, T. Hofmann, Y. Sha, B. V. Merinov, D. J. Myers, C. Heske, & W. A. Goddard. 'Finding correlations of the oxygen reduction reaction activity of transition metal catalysts with parameters obtained from quantum mechanics.' *The Journal of Physical Chemistry C* **117**(50):26598–26607 (2013).

[153] H. Nowotny. 'Die kristallstrukturen von Ni_5Ce, Ni_5La, Ni_5Ca, Cu_5La, Cu_5Ca, Zn_5La, Zn_5Ca, Ni_2Ce, MgCe, MgLa und MgSr.' *Zeitschrift für Metallkunde* (1942).

[154] C. J. Baddeley, A. W. Stephenson, C. Hardacre, M. Tikhov, & R. M. Lambert. 'Structural and electronic properties of Ce overlayers and low-dimensional Pt-Ce alloys on Pt(111).' *Physical Review B* **56**(19):12589–12598 (1997).

[155] V. Ohm, S. Raetz, M. Sauer, M. Merkens, H. Schilder, & H. Lueken. 'Formation of lanthanide-platinum alloys by reaction of platinum with lanthanide iodides part II. Structural and magnetochemical investigations into the systems with Ln = Nd, Gd, Tb, Dy, Tm.' *Journal of Alloys and Compounds* **238**(1–2):95–101 (1996).

[156] T. P. Johansson. *New Materials for Oxygen Reduction Electrodes*. Ph.D. thesis, Technical University of Denmark (2012).

[157] U. Grønbjerg. *Modelling of structure and reactivity of Platinum alloys as catalysts for the Oxygen Reduction Reaction*. Ph.D. thesis, Technical University of Denmark (2012).

[158] M. Notin, J. Mejbar, A. Bouhajib, J. Charles, & J. Hertz. 'The thermodynamic properties of calcium intermetallic compounds.' *Journal of Alloys and Compounds* **220**(1–2):62–75 (1995).

[159] T. Heumann & M. Kniepmeyer. 'A_5B-Phasen vom typ Cu_5Ca und lavesphasen in den systemen des strontiums mit palladium, platin, rhodium und iridium.' *Zeitschrift für anorganische und allgemeine Chemie* **290**(3-4):191–204 (1957).

[160] W. Bronger & W. Klemm. 'Darstellung von legierungen des platins mit unedlen metallen.' *Zeitschrift für anorganische und allgemeine Chemie* **319**(1-2):58–81 (1962).

[161] A. Fujimori & L. Schlapbach. 'Electronic structure of yttrium hydride studied by X-ray photoemission spectroscopy.' *Journal of Physics C: Solid State Physics* **17**(2):341 (1984).

[162] R. Reichl & K. H. Gaukler. 'An investigation of air-grown yttrium oxide and experimental determination of the sputtering yield and the inelastic mean free path.' *Applied Surface Science* **26**(2):196–210 (1986).

[163] R. P. Vasquez, M. C. Foote, & B. D. Hunt. 'Reaction of nonaqueous halogen solutions with $YBa_4Cu_3O_7$-x.' *Journal of Applied Physics* **66**(10):4866–4877 (1989).

[164] N. Krikorian. 'The reaction of selected lanthanide carbides with platinum and iridium.' *Journal of the Less Common Metals* **23**(3):271–279 (1971).

[165] A. S. Varela, C. Schlaup, Z. P. Jovanov, P. Malacrida, S. Horch, I. E. L. Stephens, & I. Chorkendorff. 'CO_2 electroreduction on well-defined bimetallic surfaces: Cu overlayers on Pt(111) and Pt(211).' *The Journal of Physical Chemistry C* **117**(40):20500–20508 (2013).

[166] M. Salmeron & R. Schlögl. 'Ambient pressure photoelectron spectroscopy: a new tool for surface science and nanotechnology.' *Surface Science Reports* **63**(4):169–199 (2008).

[167] S. Kaya, H. Ogasawara, L.-A. Naslund, J.-O. Forsell, H. S. Casalongue, D. J. Miller, & A. Nilsson. 'Ambient-pressure photoelectron spectroscopy for heterogeneous catalysis and electrochemistry.' *Catalysis Today* **205**(7):101–105 (2013).

[168] A. E. Russell & A. Rose. 'X-ray absorption spectroscopy of low temperature fuel cell catalysts.' *Chemical reviews* **104**(10):4613–4635 (2004).

[169] Y. Ayato, K. Kunimatsu, M. Osawa, & T. Okada. 'Study of Pt electrode/nafion ionomer interface in $HClO_4$ by in situ surface-enhanced FTIR spectroscopy.' *Journal of The Electrochemical Society* **153**(2):A203–A209 (2006).

[170] N. M. Marković & P. N. Ross Jr. 'Surface science studies of model fuel cell electrocatalysts.' *Surface Science Reports* **45**(4–6):117–229 (2002).

[171] M. Wakisaka, Y. Udagawa, H. Suzuki, H. Uchida, & M. Watanabe. 'Structural effects on the surface oxidation processes at Pt single-crystal electrodes studied by X-ray photoelectron spectroscopy.' *Energy & Environmental Science* **4**(5):1662–1666 (2011).

[172] G. Zimbitas, M. E. Gallagher, G. R. Darling, & A. Hodgson. 'Wetting of mixed OH-H_2O layers on Pt(111).' *The Journal of Chemical Physics* **128**(7):074701 (2008).

[173] D. Strmcnik, K. Kodama, D. v. d. Vliet, J. Greeley, V. R. Stamenkovic, & N. M. Marković. 'The role of non-covalent interactions in electrocatalytic fuel-cell reactions on platinum.' *Nature Chemistry* **1**(6):466–472 (2009).

[174] D. Strmcnik, M. Escudero-Escribano, K. Kodama, V. R. Stamenkovic, A. Cuesta, & N. M. Markovic. 'Enhanced electrocatalysis of the oxygen reduction reaction based on patterning of platinum surfaces with cyanide.' *Nature Chemistry* **2**(10):880–885 (2010).

[175] J. Snyder, T. Fujita, M. W. Chen, & J. Erlebacher. 'Oxygen reduction in nanoporous metal–ionic liquid composite electrocatalysts.' *Nature Materials* **9**(11):904–907 (2010).

[176] M. D. Maciá, J. M. Campiña, E. Herrero, & J. M. Feliu. 'On the kinetics of oxygen reduction on platinum stepped surfaces in acidic media.' *Journal of Electroanalytical Chemistry* **564**:141–150 (2004).

[177] J. Durst, M. Chatenet, & F. Maillard. 'Impact of metal cations on the electrocatalytic properties of Pt/C nanoparticles at multiple phase interfaces.' *Physical Chemistry Chemical Physics: PCCP* **14**(37):13000–13009 (2012).

[178] T. Schiros, L. Näslund, K. Andersson, J. Gyllenpalm, G. S. Karlberg, M. Odelius, H. Ogasawara, L. G. M. Pettersson, & A. Nilsson. 'Structure and bonding of the water-hydroxyl mixed phase on Pt(111).' *Journal of Physical Chemistry C* **111**(41):15003–15012 (2007).

[179] T. Schiros, O. Takahashi, K. J. Andersson, H. Öström, L. G. M. Pettersson, A. Nilsson, & H. Ogasawara. 'The role of substrate electrons in the wetting of a metal surface.' *The Journal of Chemical Physics* **132**(9):094701 (2010).

[180] M. Larsson, P. Baltzer, S. Svensson, B. Wannberg, N. Martensson, A. N. d. Brito, N. Correia, M. P. Keane, M. Carlsson-Gothe, & L. Karlsson. 'X-ray photoelectron, auger electron and ion fragment spectra of O_2 and potential curves of O_2^{2+}.' *Journal of Physics B: Atomic, Molecular and Optical Physics* **23**(7):1175 (1990).

[181] H. Bluhm, M. Hävecker, A. Knop-Gericke, E. Kleimenov, R. Schlögl, D. Teschner, V. I. Bukhtiyarov, D. F. Ogletree, & M. Salmeron. 'Methanol oxidation on a copper catalyst investigated using in situ X-ray photoelectron spectroscopy.' *Journal of Physical Chemistry B* **108**(38):14340–14347 (2004).

[182] C. Zhang, M. E. Grass, A. H. McDaniel, S. C. DeCaluwe, F. E. Gabaly, Z. Liu, K. F. McCarty, R. L. Farrow, M. A. Linne, Z. Hussain, G. S. Jackson, H. Bluhm, & B. W. Eichhorn. 'Measuring fundamental properties in operating solid oxide electrochemical cells by using in situ X-ray photoelectron spectroscopy.' *Nature Materials* **9**(11):944–949 (2010).

Included papers

JACS
JOURNAL OF THE AMERICAN CHEMICAL SOCIETY

Communication

pubs.acs.org/JACS

Pt_5Gd as a Highly Active and Stable Catalyst for Oxygen Electroreduction

María Escudero-Escribano,[†] Arnau Verdaguer-Casadevall,[†] Paolo Malacrida,[†] Ulrik Grønbjerg,[†,‡] Brian P. Knudsen,[†] Anders K. Jepsen,[†] Jan Rossmeisl,[‡] Ifan E. L. Stephens,[†] and Ib Chorkendorff*[,†]

[†]Center for Individual Nanoparticle Functionality, Department of Physics, Building 312, Technical University of Denmark (DTU), DK-2800 Lyngby, Denmark

[‡]Center for Atomic-Scale Materials Design, Department of Physics, Building 307, Technical University of Denmark (DTU), DK-2800 Lyngby, Denmark

Supporting Information

ABSTRACT: The activity and stability of Pt_5Gd for the oxygen reduction reaction (ORR) have been studied, using a combination of electrochemical measurements, angle-resolved X-ray photoelectron spectroscopy (AR-XPS), and density functional theory calculations. Sputter-cleaned, polycrystalline Pt_5Gd shows a 5-fold increase in ORR activity, relative to pure Pt at 0.9 V, approaching the most active in the literature for catalysts prepared in this way. AR-XPS profiles after electrochemical measurements in 0.1 M $HClO_4$ show the formation of a thick Pt overlayer on the bulk Pt_5Gd, and the enhanced ORR activity can be explained by means of compressive strain effects. Furthermore, these novel bimetallic electrocatalysts are highly stable, which, in combination with their enhanced activity, makes them very promising for the development of new cathode catalysts for fuel cells.

Proton exchange membrane fuel cells (PEMFCs) are a potentially zero emission source of power, which are expected to play a key role in a future society based on sustainable energy. The main obstacle to the development of PEMFCs as a commercially competitive reality is the high overpotential required for the oxygen reduction reaction (ORR) to proceed at an adequate rate. Due to this fact, the ORR has been the most intensively studied fuel-cell reaction over the past decade.[1−7] The most active electrocatalysts known for the ORR are based upon Pt. However, high loadings of Pt are necessary at the cathode in order to achieve acceptable power densities.[1] In order to reduce the Pt loading, there is a need to develop novel catalysts with enhanced activity and long-term stability under operating conditions.[1,2]

The activity of Pt toward the ORR can be improved by slightly weakening its binding to the O-containing reaction intermediates, O, OH, and OOH. The optimal catalyst should have an OH binding energy ≈0.1 eV weaker than pure Pt.[4a] The most widely used approach to achieve this goal is to alloy Pt with other metals, such as Co, Ni, Fe, Cu, hence improving its ORR activity.[1,3−5,8] The more reactive solute metal, e.g. Co, Ni, Fe, Cu, will tend to dissolve in the acidic electrolyte of a PEMFC, leaving behind a Pt overlayer. Unless the catalyst has been pre-annealed,[3b,c,5b] this overlayer is typically several monolayers thick.[5a,8] On the acid leached catalysts, the weakening of the binding to OH occurs as a result of the compressive strain imposed onto the Pt-overlayer by the alloy bulk.

It is crucial to improve not only the fuel-cell cathode catalyst activity but also its durability. Alloys of Pt and late transition metals generally degrade by dealloying.[1b,4a,9] This involves the segregation of the solute metal to the surface[9a,c] and its subsequent dissolution. The susceptibility of Pt alloys with late transition metals, such as Fe, Co, Ni and Cu toward dealloying can be understood on the basis of their negligible heat of formation.

Recently, Pt_3Y was identified on the basis of density functional theory (DFT) calculations as being a catalyst that should be both active and stable for the ORR.[4a] Experiments confirmed that the catalyst exhibited the highest ORR activity ever measured for a polycrystalline surface.[1b,4] Alloys of Pt with early transition metals or rare earths, such as Y, Gd, or La, have exceptionally negative heats of formation;[1b,10,11] this should provide them with the kinetic stability to prevent dealloying under fuel cell reaction conditions, unlike alloys of Pt and late transition metals. This is because the kinetic barrier for solute metal diffusion through the alloy core and the thick Pt overlayer should be at least partially determined by the heat of formation. Moreover, despite their denomination, rare earths are more abundant, produced on a larger scale, and less expensive than Pt.[12] Very recent studies on Pt_xLa[1b,13] have demonstrated that these alloys present enhanced activity compared to pure Pt[1b] as well as high stability.[13] To the best of our knowledge, no other studies concerning the activity and/or the stability of Pt and rare earth metal alloys have been reported so far. Pt_5Gd is a very stable alloy, with a formation energy of −3.9 eV/formula unit,[11] similar to that of Pt_3Y[4a] and Pt_5La.[1b]

In this communication, we present, for the first time, experimental and theoretical studies concerning the activity and stability of Pt_5Gd for the ORR. The bulk, polycrystalline electrode was sputter cleaned in an ultrahigh-vacuum chamber, before being transferred to a rotating ring disk electrode (RRDE) assembly to conduct electrochemical measurements in 0.1 M $HClO_4$. Full experimental details can be found in the Supporting Information (SI).

Received: June 29, 2012
Published: September 21, 2012

   dx.doi.org/10.1021/ja306348d | J. Am. Chem. Soc. 2012, 134, 16476−16479

The activity of the catalyst toward the ORR was evaluated in an O_2-saturated 0.1 M $HClO_4$ solution, using cyclic voltammetry. Typical cyclic voltammograms (CVs) on sputter-cleaned Pt_5Gd and Pt polycrystalline electrodes in oxygen-saturated perchloric acid solutions are shown in Figure 1a. The ORR was measured once a stable CV was obtained in a

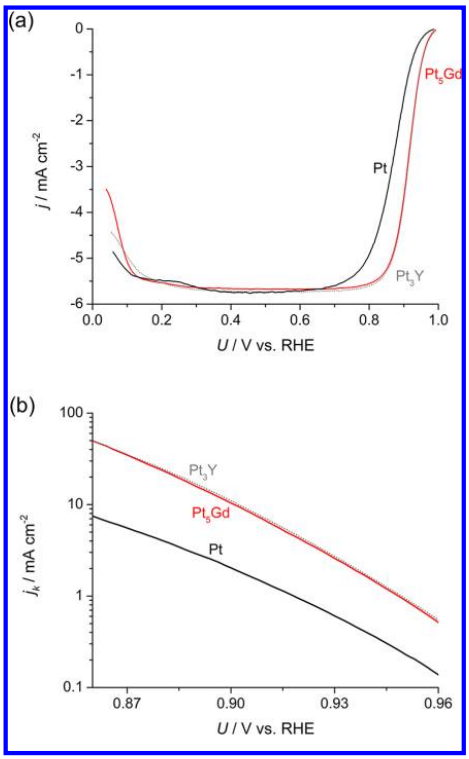

Figure 1. (a) RRDE polarization curves at 1600 rpm and 50 mV s^{-1} for the ORR on Pt_5Gd (red curve), Pt (black curve), and Pt_3Y (dotted gray curve) polycrystalline electrodes in O_2-saturated 0.1 M $HClO_4$. (b) Tafel plots showing the kinetic current density (j_k) of Pt_5Gd, Pt, and Pt_3Y as a function of the potential (U), based on data from (a).

nitrogen-saturated electrolyte (typically after ca. 100 cycles). On both electrodes, the onset for the ORR starts at ≈1 V, and the current increases exponentially with decreasing potential, characteristic of kinetic control. At more negative potentials, the current becomes increasingly controlled by mass transport, until it is completely transport limited, reaching the value of 5.7 mA cm^{-2}. We assume that the roughness factor was 1 cm^2/cm^2, as found for other Pt alloys tested for the ORR.[4] In the potential region of mixed kinetic transport, there is a considerable positive shift for Pt_5Gd, relative to Pt. This represents a substantial decrease in the overpotential for the alloy surface. Moreover, Figure 1 also shows that the ORR activity on Pt_5Gd is essentially the same as that of polycrystalline Pt_3Y (see gray dotted curve).[4] In the Tafel plot shown in Figure 1b, the kinetic current density, j_k, i.e., the current density in the absence of any mass-transfer effects, is represented as a function of the potential, U. Pt_5Gd exhibits a kinetic current density, at 0.90 V, $j_k = (10.4 \pm 0.2)$ mA cm^{-2}, which means that Pt_5Gd exhibits a 5-fold improvement over Pt. A similar enhancement was obtained on polycrystalline Pt_3Y (see gray dotted curve in Figure 1b).[4] Previous results on sputter-cleaned polycrystalline Pt_3M (M = Ni, Co, Fe) alloys by Stamenkovic et al.[3] showed up to 2-fold improvements in activity over pure Pt. However, our results show that Pt_5Gd and Pt_3Y[1b,4] present the highest activities for sputter-cleaned (Pt-skeleton)[3b] structures reported in the literature so far. According to these results, the ranking of ORR activity for the most active polycrystalline Pt alloys is in ascending order: Pt ≪ Pt_5La ≈ Pt_5Y < Pt_3Y ≈ Pt_5Gd.[1b]

In order to investigate the chemical composition of the active phase of the Pt_5Gd electrocatalyst, angle-resolved XPS (AR-XPS) experiments were carried out before and after the electrochemical measurements. After sputter cleaning the sample (before electrochemistry, see Figure 2a), the Pt to Gd

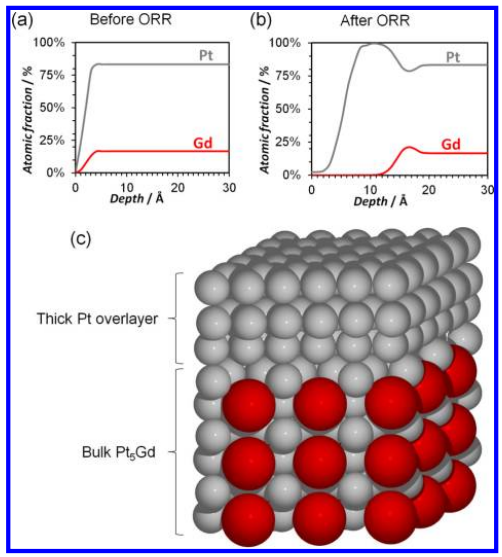

Figure 2. Nondestructive AR-XPS profiles of polycrystalline, sputter cleaned, Pt_5Gd before (a) and after (b) the ORR measurements. The adventitious C and O traces have been omitted for clarity; these are presumably accumulated during the transfer. The sputter cleaned sample exhibited a small submonolayer coverage of C and O, associated with the high sticking coefficient of any residual molecules on Gd, which is very reactive. (c) Schematic three-dimensional view of the structure shown in (b), consisting of a Pt (gray balls) overlayer, covering a bulk Pt_5Gd alloy (the large red balls are Gd atoms). In this case, the thickness of the Pt overlayer, at three monolayers, is arbitrary.

ratio was 5.0 ± 0.2, as estimated from three different measurements at 21° emission angle from the normal to the surface. At this angle, the surface sensitivity is lower, and the effects of possible differential sputtering are minimized. However, these do not seem to play an important role on the surface composition, as the Pt to Gd ratio does not change significantly with the emission angle (see Figure S8). Following the ORR experiments, the sample was transferred to the UHV chamber, and Pt to Gd ratio of 9.1 ± 0.9 was measured. This suggests that Gd is partially dissolved in the acidic electrolyte. Figure 2 shows the typical depth profiles of Pt_5Gd before (a) and after (b) ORR. Evidently a Pt overlayer with a thickness of

dx.doi.org/10.1021/ja306348d | J. Am. Chem. Soc. 2012, 134, 16476−16479

few Pt layers was formed. This is consistent with other acid leached Pt-skeleton alloys, including Pt_5La, Pt_5Y, and Pt_3Y.[1,4,14] Further investigations are underway to quantify the exact thickness of the Pt overlayer. Accordingly, the effect of alloying Pt is to impose strain onto the Pt overlayer. In the absence of Gd in the first three atomic layers, there would be no "ligand effect".[1b,15]

It must be noted that under the acidic and oxidizing operating conditions of a PEMFC, there would be a strong thermodynamic force toward the dissolution of Gd from Pt_5Gd: the standard dissolution potential, U_0, for Gd to Gd^{3+} is −2.40 V vs the normal hydrogen electrode (NHE)[16] (which means that the standard Gibbs free energy for the dissolution of Gd to Gd^{3+} is −7.20 eV), and the alloying energy of Pt_5Gd stabilizes each Gd atom by 3.9 eV.[11] Then, the standard Gibbs free energy for the dissolution of Gd to Gd^{3+} will be −3.30 eV, and the corresponding standard reduction potential is −1.10 V vs NHE. Hence, despite the stabilization of Gd atoms in the Pt_5Gd alloy by 3.9 eV, at 1 V vs NHE we are 2.1 V above the standard reduction potential, i.e., there is a driving force of −6.3 eV for the dissolution of each Gd atom. A similar driving force exists for the dissolution of other rare earths or early transition metals when alloyed with Pt, including Pt_3Y and Pt_5La, explaining why the solute metal will dissolve from these surfaces.[1b] However, this is inconsistent with reports that metallic La or Y could be present at the surface Pt_3La or Pt_3Y electrodes under ORR conditions.[13,17] Despite the thermodynamic driving force, the Pt overlayer provides kinetic stability against Gd dissolution from the alloy bulk.

DFT calculations were performed in order to understand the high ORR activity of Pt_5Gd. The Pt_5Gd structure was modeled following the same procedure as for Pt_5La,[1b] as a strained close-packed pure Pt overlayer. The surface strain was estimated on the basis that the Pt−Pt interatomic distance would be set by the bulk lattice parameter of Pt_5Gd, a = 0.522 nm (based on XRD measurements described in the SI). A schematic representation of the structure is shown in Figure 2c. This would lead to a Pt overlayer that is compressed by 6% relative to Pt(111). Our DFT calculations suggest that this strain would result in an excessive weakening of the OH binding energy, relative to Pt(111), of ≈0.3 eV. The compressive strain that would provide the optimal OH binding energy ≈0.1 eV weaker than Pt(111) would be 2%.[5a] On the basis of the DFT model, we would expect the perfect, defect-free surface to have a lower activity than pure Pt, in contradiction to our experiments.[7,18] However, we expect that on the experimentally tested phase of Pt_5Gd, the strain at the surface would be significantly lower than the 6% we estimate for a "perfect" overlayer on Pt_5Gd, due to relaxation effects.[5a,19]

In order to study the stability of polycrystalline Pt_5Gd electrodes in acidic solutions, we first performed an accelerated stability test (test I) consisting of continuous cycles from 0.6 to 1.0 V vs RHE in an oxygen-saturated 0.1 M $HClO_4$ electrolyte at 100 mV s^{-1} and 23 °C. The CVs in an O_2-saturated 0.1 M $HClO_4$ solution before and after 10 000 cycles (after around 20 h of experiments) between 0.6 and 1.0 V are shown in Figure S4. Figure 3a shows the Tafel plots for the ORR on Pt_5Gd before (red curve) and after (orange dotted curve) 10 000 cycles in the conditions described above. Interestingly, these results show that the percentage of activity loss after 10 000 cycles is 14%, most of this loss occurring in the first 2000 cycles. For comparison, when subject to the same treatment, polycrystalline Pt loses 5% of its initial activity after 10 000

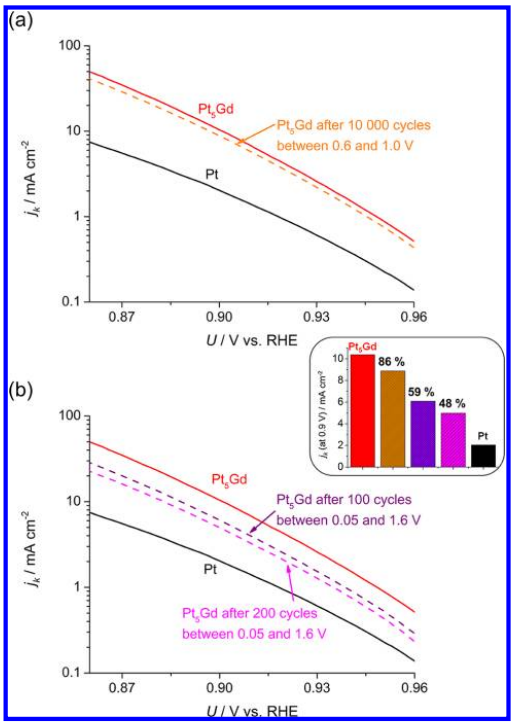

Figure 3. Tafel plots showing the stability of Pt_5Gd after: (a) 10 000 cycles between 0.6 and 1.0 V vs RHE at 100 mV s^{-1} (test I) and (b) 100 (purple curve) and 200 (magenta curve) cycles between 0.05 and 1.6 V vs RHE at 50 mV s^{-1} in O_2-saturated 0.1 M $HClO_4$ (test II). The inset shows the kinetic current density at 0.9 V of Pt_5Gd: sputter cleaned (red), after test I (orange), and after 100 (purple) and 200 (magenta) cycles of test II. For comparison, the kinetic current density of Pt is represented in black.

cycles. Presumably, this loss in activity can be explained by residual contamination from the electrolyte. The CV in N_2-saturated 0.1 M $HClO_4$ taken immediately before the ORR measurements was completely recovered after stability test I (not shown). This <15% deactivation seems to be related to a slight decrease in Gd from the near-surface region: the Pt:Gd XPS ratio at 21° to the sample normal increased from 9.1 (after ORR) to 12.3 (after stability test I, see Figure S5).

Following stability test I, we exposed it to a more aggressive experiment, by cycling it between 0.05 and 1.6 V (i.e., very strong corrosive conditions) at 50 mV s^{-1} in O_2-saturated solutions (test II). After 10 cycles, we did not observe any additional loss in activity in the ORR. However, after 50 cycles between 0.05 and 1.6 V the ORR polarization curve (after stability test I) could not be recovered. As shown in Figure 3b, the sample retains 59% of its initial activity after 100 cycles and 48% after 200 cycles (after ca. 30 h of experiments). Despite these very promising results, the stability of the catalyst will ultimately need to be tested in nanoparticulate form in a PEMFC.

In summary, we present a novel highly active and stable electrocatalyst for the ORR. The activity of Pt_5Gd is similar to that obtained on Pt_3Y in previous studies, which was identified as the most active Pt-based polycrystalline alloy for the ORR.

Moreover, polycrystalline Pt_5Gd electrodes are extremely stable, resistant to cycling to potentials as positive as 1.6 V. For all these reasons, we expect that alloying Pt with Gd and other rare earths will be a fruitful strategy toward the development of highly active and durable cathodes for PEMFCs.

■ ASSOCIATED CONTENT

Supporting Information

Experimental procedures, computational details, and additional figures. This material is available free of charge via the Internet at http://pubs.acs.org.

■ AUTHOR INFORMATION

Corresponding Author

ibchork@fysik.dtu.dk

Notes

The authors declare no competing financial interests.

■ ACKNOWLEDGMENTS

Financial support is gratefully acknowledged from Energinet.dk through the R&D program ForskEL (CATBOOSTER project) and the Danish Ministry of Science through the UNIK program: Catalysis for Sustainable Energy (CASE). The Center for Individual Nanoparticle Functionality is supported by the Danish National Research Foundation. The Center for Atomic-scale Materials Design is supported by the Lundbeck Foundation.

■ REFERENCES

(1) (a) Gasteiger, H. A.; Kocha, S. S.; Sompalli, B.; Wagner, F. T. *Appl. Catal., B* **2005**, *56*, 9. (b) Stephens, I. E.L.; Bondarenko, A. S.; Grønbjerg, U.; Rossmeisl, J.; Chorkendorff, I. *Energy Environ. Sci.* **2012**, *5*, 6744.

(2) (a) Adzic, R. R.; Zhang, J.; Sasaki, K.; Vukmirovic, J. X.; Shao, M.; Wang, J. X.; Nikelar, A. U.; Mavrikakis, M.; Valerio, J. A.; Uribe, F. *Top. Catal.* **2007**, *46*, 249. (b) Bing, Y.; Liu, H.; Zhang, L.; Ghosh., D.; Zhang, J. *Chem. Soc. Rev.* **2010**, *39*, 2184. (c) Wang, C.; van der Vliet, D.; More, K. L.; Zaluzec, N. J.; Peng, S.; Sun, S.; Daimon, H.; Wang, G.; Greeley, J.; Pearson, J.; Paulikas, A. P.; Karapetrov, G.; Strmcnik, D.; Markovic, N. M.; Stamenkovic, V. R. *Nano Lett.* **2011**, *11*, 919. (d) Rabis, A; Rodriguez, P.; Schmidt, T. J. *ACS Catal.* **2012**, *2*, 864.

(3) (a) Stamenkovic, V.; Mun, B. S.; Mayrhofer, K. J. J.; Ross, P. N.; Markovic, N. M.; Rossmeisl, J.; Greeley, J.; Nørskov, J. K. *Angew. Chem., Int. Ed.* **2006**, *45*, 2897. (b) Stamenkovic, V. R.; Mun, B. S.; Mayrhofer, K. J.J.; Ross, P. N.; Markovic, N. M. *J. Am. Chem. Soc.* **2006**, *128*, 8813. (c) Stamenkovic, V. R.; Fowler, B.; Mun, B. S.; Wang, G. F.; Ross, P. N.; Lucas, C. A.; Markovic, N. M. *Science* **2007**, *315*, 493. (d) Stamenkovic, V. R.; Mun, B. S.; Arenz, M.; Mayrhofer, K. J. J.; Lucas, C. A.; Wang, G. F.; Ross, P. N.; Markovic, N. M. *Nat. Mater.* **2007**, *6*, 241.

(4) (a) Greeley, J.; Stephens, I. E.L.; Bondarenko, A. S.; Johansson, T. P.; Hansen, H. A.; Jaramillo, T. F.; Rossmeisl, J.; Chorkendorff, I.; Nørskov, J. K. *Nat. Chem.* **2009**, *1*, 552. (b) Stephens, I. E.L.; Bondarenko, A. S.; Bech, L.; Chorkendorff, I. *ChemCatChem* **2012**, *4*, 341.

(5) (a) Strasser, P.; Koh, S.; Anniyev, T.; Greeley, J.; More, K.; Yu, C.; Liu, Z.; Kaya, S.; Nordlund, D.; Ogasawara, H.; Toney, M. F.; Nilsson, A. *Nat. Chem.* **2010**, *2*, 454. (b) Stephens, I. E.L.; Bondarenko, A. S.; Perez-Alonso, F. J.; Calle-Vallejo, F.; Jepsen, A. K.; Frydendal, R.; Knudsen, B. P.; Rossmeisl, J.; Chorkendorff, I. *J. Am. Chem. Soc.* **2011**, *133*, 5485.

(6) Strmcnik, D.; Escudero-Escribano, M.; Kodama, K.; Stamenkovic, V. R.; Cuesta, A.; Markovic, N. M. *Nat. Chem.* **2010**, *2*, 880.

(7) Nørskov, J. K.; Rossmeisl, J; Logadottir, A.; Lindqvist, L.; Kitchin, J. R.; Bligaard, T.; Jónsson, H. *J. Phys. Chem. B* **2004**, *108*, 17886.

(8) Toda, T.; Igarashi, H.; Uchida, H.; Watanabe, M. *J. Electrochem. Soc.* **1999**, *146*, 3750.

(9) (a) Mayrhofer, K. J. J.; Hartl, K.; Juhart, V.; Arenz, M. *J. Am. Chem. Soc.* **2009**, *131*, 16348. (b) Chen, S.; Gasteiger, H. A.; Hayakawa, K.; Tada, T.; Shao-Horn, Y. *J. Electrochem. Soc.* **2010**, *157*, A82. (c) Xin, H. L. L.; Mundy, J. A.; Liu, Z.; Cabezas, R.; Hovden, R.; Kourkoutis, L. F.; Zhang, J.; Subramanian, N. P.; Makharia, R.; Wagner, F. T.; Muller, D. A. *Nano Lett.* **2012**, *12*, 490.

(10) (a) Johannesson, G. H.; Bligaard, T.; Ruban, A. V.; Skriver, H. L.; Jacobsen, W.; Nørskov, J. K. *Phys. Rev. Lett.* **2002**, *88*, 255506. (b) Bligaard, T.; Johannesson, G. H.; Ruban, A. V.; Skriver, H. L.; Jacobsen, W.; Nørskov, J. K. *Appl. Phys. Lett.* **2003**, *83*, 4527.

(11) Jakob, K. T.; Waseda, Y. *Mater. Trans., JIM* **1990**, *31*, 135.

(12) Vesborg, P. C.K.; Jaramillo, T. F. *RSC Adv.* **2012**, *2*, 7933.

(13) Yoo, S. J.; Hwang, S. J.; Lee, J.-G.; Lee, S.-C.; Lim, T.-H.; Sung, Y.-E.; Wieckowski, A.; Kim, S.-K. *Energy Environ. Sci.* **2012**, *5*, 7521.

(14) Johansson, T. P. Ph.D. Thesis, Technical University of Denmark: Lyngby, Denmark, 2012.

(15) Kitchin, J. R.; Nørskov, J. K.; Barteau, M. A.; Chen, J. G. *J. Chem. Phys.* **2004**, *120*, 10240.

(16) Pourbaix, M. *Atlas of Electrochemical Equilibria in Aqueous Solutions*; National Association of Corrosion Engineers: Houston, TX, 1974.

(17) Yoo, S. J.; Kim, S.-K.; Jeon, T.-Y.; Hwang, S. J.; Lee, J.-G.; Lee, K.-S.; Cho, Y.-H.; Sung, Y.-E.; Lim, T.-H. *J Chem. Commun.* **2011**, *47*, 11414.

(18) Rossmeisl, J.; Karlberg, G. S.; Jaramillo, T. F.; Nørskov, J. K. *Faraday Discuss.* **2008**, *140*, 337.

(19) Yang, R.; Strasser, P.; Toney, M. F. *J. Phys. Chem. C* **2011**, *115*, 9074.

Top Catal
DOI 10.1007/s11244-013-0179-y

ORIGINAL PAPER

Pt Skin Versus Pt Skeleton Structures of Pt_3Sc as Electrocatalysts for Oxygen Reduction

T. P. Johansson · E. T. Ulrikkeholm · P. Hernandez-Fernandez · P. Malacrida · H. A. Hansen · A. S. Bandarenka · J. K. Nørskov · J. Rossmeisl · I. E. L. Stephens · I. Chorkendorff

Abstract In order for low temperature polymer electrolyte membrane fuel cells to become economically viable Pt catalyst loading must be significantly reduced. The cathode of the polymer electrolyte membrane fuel cell, where oxygen reduction takes place, is responsible for the main activity loss. The development of new materials for this reaction is essential in order to increase the overall effeciency of the fuel cell. Herein, we study the effect of ultra high vacuum annealing on the structure and activity of polycrystalline Pt_3Sc. Upon annealing in ultra high vacuum a Pt overlayer is formed on the polycrystalline Pt_3Sc. The reactivity of the overlayer is probed by temperature programmed desorption of CO. The onset of CO desorption is around 130 K lower on UHV annealed Pt_3Sc than on Pt(111) and the temperature of the desorption peak maximum at saturation was ~50 K lower on UHV annealed Pt_3Sc, relative to Pt(111), consistent with the CO adsorption energies calculated using density functional theory calculations. Exposing the annealed Pt_3Sc sample to 200 mbar O_2 at room temperature results in ~14 % Sc oxide as measured by X-ray photoelectron spectroscopy. Electrochemical testing of the oxygen reduction reaction shows the same activity as sputter cleaned Pt_3Sc.

Keywords Carbon monoxide · Temperature programmed desorption · Platinum · Scandium · Oxygen reduction reaction · Ion scattering spectroscopy · Angle resolved X-ray photoelectron spectroscopy

1 Introduction

The main loss in a low temperature polymer electrolyte membrane fuel cell (PEMFC) is due to the slow kinetics of the oxygen reduction reaction (ORR), even when Pt is used as a catalyst [1]. The high overpotential (or potential losses) required to drive this reaction can be understood on the basis of the reaction mechanism. The reaction is complex: there are four coupled electron and proton transfers as well as at least two intermediates, HO* and HOO*, and possibly O*. It turns out that the adsorption energies of these intermediates scale linearly with each other [2–4]. Consequently, the binding of one intermediate can describe the overall trends in activity for the reaction. There is a volcano relationship between the ORR activity and the binding energy of one intermediate, e.g. HO*. On the left side of the volcano HO* is bound too strong and on the right side of the volcano HO* is bound too weak. Pt lies close to the tip of the volcano, however, it binds oxygen slightly too strong. In order to reach the tip of the volcano, a catalyst should be found which binds HO* around 0.1 eV weaker than the binding of HO* on pure Pt [5].

T. P. Johansson · E. T. Ulrikkeholm · P. Hernandez-Fernandez · P. Malacrida · I. E. L. Stephens · I. Chorkendorff (✉)
Department of Physics, Center for Individual Nanoparticle Functionality, Building 312, Technical University of Denmark, 2800 Lyngby, Denmark
e-mail: ibchork@fysik.dtu.dk

H. A. Hansen · J. K. Nørskov
Department of Chemical Engineering, SUNCAT Center for Interface Science and Catalysis, Stanford University, Stanford, CA, USA

A. S. Bandarenka
Center for Electrochemical Sciences, Ruhr-Universität Bochum, Universitätsstrasse 150 NC 4/73, 44780 Bochum, Germany

J. Rossmeisl
Department of Physics, Center for Atomic-scale Materials Design, Building 311, Technical University of Denmark, 2800 Lyngby, Denmark

Published online: 26 October 2013

In recent years, most research activities on the development of new ORR catalysts have been focused on improving the activity of Pt by alloying with other transition metals [1, 6–9]. By having an overlayer of Pt on top of a core of a different composition, it is possible to alter the electronic structure of the Pt overlayer, making it more active for the ORR. The core typically consists of Pt alloyed with a transition metal or rare earth such as La, Ni, Co, Fe, Cu or Gd [10–14]. All of these Pt alloys are thermodynamically unstable under the reaction conditions of a cathode in a PEMFC and therefore improving the stability during ORR is an important issue [15, 16].

For platinum overlayer structures the binding of O*, HO* and HOO*, is influenced by two different effects, namely the ligand effect and the strain effect [17–20]. The strain effect occurs when the Pt overlayer is laterally strained, e.g. by placing it on top of a core with a different lattice parameter. Compressive lattice strain causes a downshift in the d-band centre leading to a weakening in the binding of adsorbed intermediates to the Pt surface atoms. Tensile lattice strain will cause the opposite effect [8, 18]. The ligand effect originates from subsurface alloying: The electronic structure of Pt is altered by nearby subsurface atoms with a different atomic number. If the solute atoms are in the third atomic layer the ligand effect is much less pronounced [10, 17, 19, 21, 22]. It is challenging to separate the ligand effect from the strain effect in Pt overlayers on bulk Pt bimetallic alloys.

We recently discovered Pt_3Y and Pt_3Sc as very promising catalysts for the ORR [5]. The alloys were identified by a theoretical screening study as being the most stable Pt-based binary Pt_3M alloys and were predicted to bind oxygen species slightly weaker than pure Pt, making them likely to show a high ORR activity. The high stability of these alloys can be explained in terms of the filling degree of the d-band. Y and Sc are both early transition metals and have one d electron, whereas Pt is a late transition metal and has nine d electrons. When combining the two the metal–metal d-bonds are therefore approximately half filled corresponding to the bonding states being filled and the antibonding states being empty [23]. The ORR activity of sputter cleaned polycrystalline Pt_3Sc and Pt_3Y was measured to be enhanced relative to pure Pt by a factor of 1.5–1.8 and 6–10, respectively, in the range 0.9–0.87 V [5].

Ultra high vacuum (UHV) studies of Pt alloys can help to understand the increased ORR activity and by annealing the alloys in vacuum new structures can be observed. Markovic and coworkers [24–26] have comprehensively studied bulk polycrystalline platinum bimetallic alloys, Pt_3M (M = Ni, Co, Fe, Ti, V) . They reported two different ways of producing the active Pt overlayer on these alloys. When the surface of the bulk polycrystalline platinum alloy is prepared by sputter cleaning, followed by immersion into acidic electrolyte, a so called “platinum skeleton” structure is obtained. This structure was first observed by Watanabe and coworkers [27, 28], but first denoted as Pt skeleton by Markovic and coworkers.

The platinum skeleton surfaces are not very well defined, but are reported to have 100 % platinum in the first layer and a minimum of 75 % platinum from the second layer and down [13]. In the case of UHV annealing, the platinum overlayer is formed by Pt diffusion to the surface. Markovic and coworkers [13, 29] reports that for Pt alloyed with late transition metals, Pt_3M (M = Ni, Co, Fe) the platinum overlayer formation occurs by platinum atoms from the second layer exchanging place with the solute atoms in the surface layer leading to a structure with 100 % platinum in the first layer, 50 % platinum in the second layer and (roughly) 75 % platinum in the following layers. Experiments by Chen et al. [30] and modelling studies from Duan et al. [31] on $Pt_3Ti(111)$ suggest that the platinum overlayer on $Pt_3Ti(111)$ forms by the diffusion of a slight Pt excess in the bulk, producing a structure consisting of an overlayer of Pt on top of the bulk Pt_3Ti alloy, i.e. with 25 % Ti in the second atomic layer. Notably, for alloys of Pt and late transition metals such as Ni, Co and Cu, the Pt skin structure is stable, both under reaction conditions, and upon exposure to air under ambient conditions [10, 13, 25].

Ross and coworkers have studied the CO TPD spectra of vacuum annealed Pt alloys [32]. The $Pt_3Co(111)$ single crystal formed a Pt overlayer upon UHV annealing [33], whereas $Pt_3Ti(111)$ [34] and $Pt_3Sn(111)$ [35] were found to be bulk terminated. For all three crystals a downshift in the CO desorption temperature on the order of 50 K compared to Pt(111) was found.

The ORR activity of the recently discovered Pt_3Sc and Pt_3Y alloys was measured after sputter cleaning, corresponding to a Pt skeleton overlayer [5]. The high ORR activity combined with the possible high stability of these alloys strongly motivates further investigations on the nature of the active site for the ORR. Moreover the much higher increase in ORR activity for Pt_3Y than for Pt_3Sc is thus far not well understood.

Nilsson and coworkers recently studied nanostructured Pt monolayer electrocatalysts on Rh(111) and found that the ORR activity is very sensitive to the exact structure of the surface and near surface region [36]. In order to understand the origin of the increased ORR activity for Pt_3Sc and Pt_3Y knowledge of the structure of the surface and near surface region is essential.

In this article we present results from UHV annealed polycrystalline Pt_3Sc and compare both the near surface composition and the activity to that of sputter cleaned Pt_3Sc. In particular, we would like to determine whether it

is possible to form Pt skin structures of Pt_3Sc and whether they are stable and active under ORR conditions.

2 Methods

2.1 Experimental Details

The main instrument used during this study is an UHV chamber with a base pressure of 1×10^{-10} torr, as described earlier [37]. A high pressure cell (HPC) is attached to the main chamber and can be isolated from it by a lock which utilises a Cu gasket. In the main chamber ion scattering spectroscopy (ISS) and X-ray photoelectron spectroscopy (XPS) can be performed. A dual anode X-ray gun is used for the XPS. All XPS spectra are acquired using the Al Kα anode (1486.7 eV). The chamber is also equipped with a quadropole mass spectrometer (QMS). The Pt_3Sc polycrystalline sample is 5-mm in diameter and 3-mm thick and was supplied by MaTecK, GmbH, Germany. The sample is mounted by hanging it in a hairpin shaped 0.38 mm diameter tungsten wire and the temperature of the sample is measured by a thermocouple (type K). The sample is resistively heated by passing DC current through the tungsten wire from which it hangs. Cooling of the sample is achieved by pumping pressurised air or liquid nitrogen into the hollow manipulator.

Angle resolved X-ray photoelectron spectroscopy (AR-XPS) depth profiles are obtained from a Theta Probe UHV chamber described elsewhere [12]. By acquiring XPS spectra from electrons emitted from different angles and fitting the spectra using the simulation tool ARProcess software (Thermo Avantage), non destructive ARXPS depth profiles are obtained. A restriction on the fit is that from 12 Å and deeper the Pt:Sc ratio is set to 3, corresponding to Pt_3Sc. Using ARXPS it is possible to obtain the near surface region concentration profiles of different elements. Due to uncertainty in the fit, the ARXPS depth profile should mainly be considered qualitatively. It has, however, for near surface alloys of Cu on Pt been shown to be in excellent agreement with previous surface science studies [10].

The XPS cross section for Sc reported in the literature is not known accurately [38]. The XPS cross section for Sc used in this article was found by comparing the measured Sc 2p peak from a sputter cleaned Sc foil with that of the Pt 4f line from clean sputtered Pt(111) and following the procedure from Seah et al. [39]. The obtained Sc 2p cross section (referenced to C 1s) was 2.8, whereas the Scofield cross section for Sc 2p is 6.4 [40].

The electrochemical experiments were performed with Bio-Logic Instruments' VMP2 potentiostat, controlled by a computer. A standard three-compartment glass cell was used for all the experiments, equipped with an external jacket attached to a water bath with temperature control. All glassware was cleaned in 96 % H_2SO_4 and 30 % H_2O_2 (3:1 v/v). The glassware was subsequently rinsed several times in hot Millipore water (358 K, $> 18.2\,M\Omega\,cm^{-1}$, TOC <5 ppb). The electrolyte, 0.1 M $HClO_4$ (Merck, Suprapur) was prepared using Millipore water. The counter electrode was a platinum wire and the reference electrode was a Hg/Hg_2SO_4 electrode separated from the working electrode compartment using a ceramic frit. All potentials in the manuscript are quoted with respect to the reversible hydrogen electrode (RHE) and corrected for Ohmic losses. The catalysts were inserted into the arbor of a rotating ring disk electrode (RRDE) and were immersed into the electrochemical cell under potential control at 0.05 V in N_2 (N5, Air Products) saturated 0.1 M $HClO_4$ electrolyte. All electrochemical measurements were performed at 296 K using a scan rate of 20 mV/s and each catalyst was measured at least 3 times.

The polycrystalline Pt_3Sc sample is cleaned by performing cycles of Ar^+ sputtering at room temperature and annealing to 1273 K.

2.2 Computational Details

Density functional theory (DFT) calculations have been performed on the (111) facets of Pt in the fcc structure and Pt_3Sc in the $L1_2$ crystal structure using the DACAPO and ASE codes [41]. The ionic cores are described with Vanderbilt ultrasoft pseudopotentials [42] and the one-electron states are expanded in planewaves with kinetic energies below 340 eV. The density is expanded in planewaves with kinetic energies below 500 eV. The one-electron states are populated according to a Fermi–Dirac distribution with $k_BT = 0.1$ eV and the total energy is extrapolated to $k_BT = 0$ eV. The effects of exchange and correlation are approximated by the RPBE functional [43]. The surfaces are modeled using 4 layer slabs with approximately 16 Å of vacuum separating the periodic images of the slab. The energy and density have been corrected for the electrostatic dipole interaction between vacuum separated slab [44]. A 2×2 surface unit cell has been employed in the present calculations of adsorption energies and surface segregation energies. The first Brilluin zone is sampled using an $8 \times 8 \times 1$ Monkhorst-Pack grid of k-points [45]. Adsorbates and the two topmost layers of the slab are relaxed until all force components are below 0.02 eV/Å.

The free energy diagram (Fig. 7) for Pt and Pt_3Sc with 50 and 25 % in the second layer are adapted from Ref. [5], where a $2\sqrt{3} \times 2\sqrt{3}$ unit cell was used to obtain commensurate structures for the 2×2 alloy lattice and the $\sqrt{3} \times \sqrt{3}$ H_2O–OH lattice. For Pt_3Sc with 0 % Sc in the

second layer, we have found that the binding energies of the ORR intermediates considered vary by less than 0.02 eV depending on the adsorption site. In this case, the free energy diagram has been constructed from the average stabilisation of these ORR intermediates relative to Pt in a 2 × 2 unit cell.

3 Results

3.1 UHV Measurements

Figure 1 shows the ISS spectrum of polycrystalline Pt_3Sc sputter cleaned before and after annealing. Before annealing, two peaks are present in the ISS spectrum: one at around 900 eV, which corresponds to Sc and one at around 1120 eV, which corresponds to Pt. No other peaks are seen, indicating a clean surface containing only Pt and Sc. After annealing, the Sc peak at around 900 eV disappears and only the Pt peak remains. This suggests the formation of a Pt overlayer upon annealing, in line with the results of Markovic and coworkers [13] for polycrystalline Pt_3M (M = Ni, Co, Fe, Ti, V) samples. We have used ISS only qualitatively, in order to determine which elements are present at the surface. Calculating atomic percentages from ISS is challenging due to ISS equipment not being standardised and therefore reference samples (measured in the same setup) are needed [46, 47].

Table 1 shows the concentration of different elements from XPS, before and after annealing. After annealing, the carbon content on the surface increases slightly. Even when the surface was subjected to a large number of sputtering-annealing cycles, no change was observed in the intensity of the C peak. The Pt:Sc ratio is close to 3. It is worth noting that even though carbon was not observed using ISS, carbon could be present on the surface of the sample. This is due to graphitic carbon not being detectable by ISS unless a high beam voltage is used (above 3.5 keV, whereas we use 1.2 keV) [48, 49].

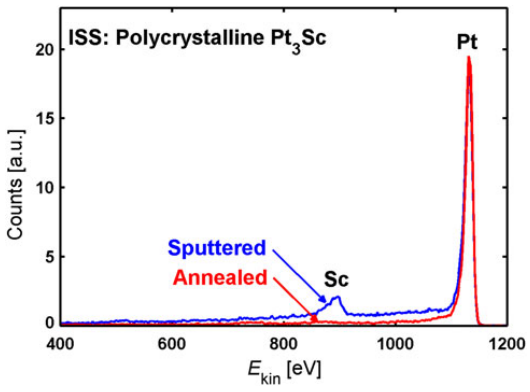

Fig. 1 ISS spectrum of polycrystalline Pt_3Sc before (*blue curve*) and after (*red curve*) annealing to T = 1273 K. A Pt overlayer appears upon annealing in UHV

Table 1 Relative concentration (%) as obtained by XPS, of the different elements in the polycrystalline Pt_3Sc sample before UHV annealing, after UHV annealing and after UHV annealing and exposure to 200 mbar O_2

	Pt	Sc	C	O	Pt:Sc ratio
Pt_3Sc sputter cleaned (no Pt overlayer)	70	27	1	2	2.6
Pt_3Sc annealed (Pt overlayer)	70	25	4	1	2.8
Pt_3Sc annealed and exposed to 200 mbar O_2	56	23	7	14	2.4

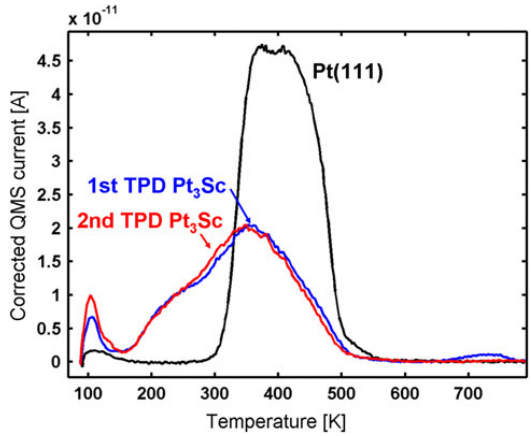

Fig. 2 First (*blue curve*) and second (*red curve*) CO TPD of Pt_3Sc after annealing at T = 1273 K. The CO TPD of Pt(111) (*black curve*) is shown for comparison. The ramp rate of each TPD was 2 K/s

The reactivity of the Pt overlayer was probed in vacuo, by the temperature programmed desorption of CO (CO TPD). CO was background dosed at a pressure of 2.0×10^{-7} torr for 500 s during which the sample was cooled from 550 to 88 K using liquid nitrogen. The blue curve in Fig. 2 shows the CO TPD of the freshly annealed Pt_3Sc. The red curve is the second TPD, carried out following the first TPD measurement. Both CO TPD's look similar except for the small peak around 740 K, indicating that the surface does not irreversibly reconstruct during the course of the experiment. The black curve in Fig. 2 is the CO TPD for Pt(111). The onset of CO desorption is around 130 K lower on UHV annealed Pt_3Sc than on Pt(111) and the main desorption peak is around 50 K lower on UHV annealed Pt_3Sc than on Pt(111). This clearly demonstrates

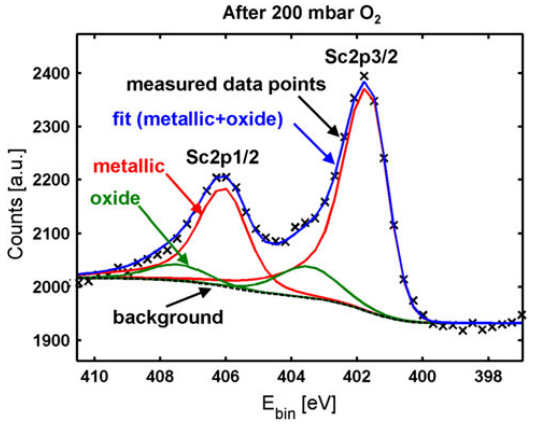

Fig. 3 Sc 2p core level region of annealed Pt_3Sc after exposure to 200 mbar O_2. Fitting the recorded data to metallic (*red curve*) and oxidised (*green curve*) Sc gives 14 % of Sc oxide. Before exposure to 200 mbar O_2 only metallic Sc was seen (data not shown)

that CO is bound weaker on Pt_3Sc than on Pt(111). The large shift in the onset of CO desorption could be due to differences in the CO–CO adsorbate interactions on Pt(111) and UHV annealed Pt_3Sc [50, 51]. In a CO TPD the area under the peak is proportional to the amount of CO desorbed from the surface. The area under the Pt_3Sc curve is 56 % of the area under the Pt(111) curve. This difference could be due to a lower saturation coverage of CO on Pt_3Sc compared to Pt(111). Bardi et al. [33] found a 60–70 % lower saturation coverage by CO on $Pt_3Co(111)$ compared to Pt(111), determined by CO TPD. Bandarenka et al. [52] found that the coverage of CO on the Cu/Pt(111) near surface alloy, determined voltammetrically was 1/3 monolayer (ML), whereas for Pt(111) it was around 2/3 ML. The difference in saturation coverage of CO on Pt_3Sc compared to Pt(111) could however also be due to some of the sites on Pt_3Sc being blocked by carbon (see XPS data, Table 1).

In order to investigate the effect of exposure to oxygen during the unavoidable transfer of the Pt_3Sc sample from the UHV system to the electrochemical testing, the surface was exposed to 200 mbar oxygen in a HPC adhered to the UHV system [37]. Figure 3 shows the XPS of the annealed Pt_3Sc after exposure to 200 mbar oxygen. By deconvoluting the spectrum into two components, we estimated that 14 % of the Sc is in the oxidised state, indicating that the Pt overlayer is not completely hindering the Sc from oxidising when exposed to air.

Having established that UHV annealing of Pt_3Sc to 1273 K gives a Pt overlayer structure the sample was sputtered, annealed and taken out for electrochemical testing. Before measuring the ORR activity of the sample, an angle resolved XPS (ARXPS) analysis was carried out in a second UHV chamber [10] in order to check the stability of the catalyst before and after electrochemical testing. The ARXPS depth profile before electrochemistry is depicted in Fig. 4a. The depth profile shows that air exposure resulted in some Sc oxide, in agreement with the 200 mbar O_2 exposure experiment shown in Fig. 3. The Sc oxide layer covers a layer of pure Pt, followed by a layer with increased Sc content, below which lies the bulk Pt_3Sc surface. As mentioned in Sect. 2, the ARXPS depth profile should mainly be considered qualitatively and it is therefore challenging to determine the exact thickness of the Pt overlayer. It is also worth noting that uncertainty in the determined sensitivity factor of Sc 2p might effect the ARXPS profiles.

Figure 4b shows the ARXPS depth profile of UHV annealed Pt_3Sc after electrochemical testing. The Sc oxide which was at the surface before electrochemistry has disappeared and furthermore the subsurface Sc content is lower. The removal of Sc oxide from the surface is expected since Sc is soluble under acidic conditions [53].

ARXPS depth profiles of a sputter cleaned Pt_3Sc sample before and after electrochemical testing have also been recorded (Fig. 4c, d). The depth profile before electrochemistry (Fig. 4c) was measured without exposing the sample to air and corresponds to a bulk terminated Pt_3Sc sample and is clearly different from that of the UHV annealed sample. After electrochemical testing the profile of the sputter cleaned and UHV annealed samples are very similar, indicating that the UHV annealing has a negligible effect on the structure of the actual ORR catalyst (i.e. the catalyst after exposure to 0.1 M $HClO_4$).

3.2 Electrochemical Measurements

After measuring the ARXPS depth profile the sample was mounted in a RRDE setup for electrochemical testing. Figure 5 shows the measured oxygen reduction activity on a Tafel plot. The UHV annealed Pt_3Sc sample has an increased activity compared to polycrystalline Pt. The increase in activity is similar to that of sputter cleaned Pt_3Sc. The similar ORR activity of sputter cleaned and UHV annealed Pt_3Sc is in agreement with the similar ARXPS depth profiles obtained after electrochemical testing. The ORR activity of both sputter cleaned and UHV annealed Pt_3Sc is lower than that of sputter cleaned polycrystalline Pt_3Y, which has the highest ORR activity ever measured for a sputter cleaned, Pt-skeleton surface [5].

Summarising the experimental observations: When annealing the polycrystalline Pt_3Sc sample in vacuo a Pt overlayer is formed. The onset of CO desorption is around 130 K lower on the UHV annealed Pt_3Sc than on Pt(111) and the main desorption peak is around 50 K lower on the

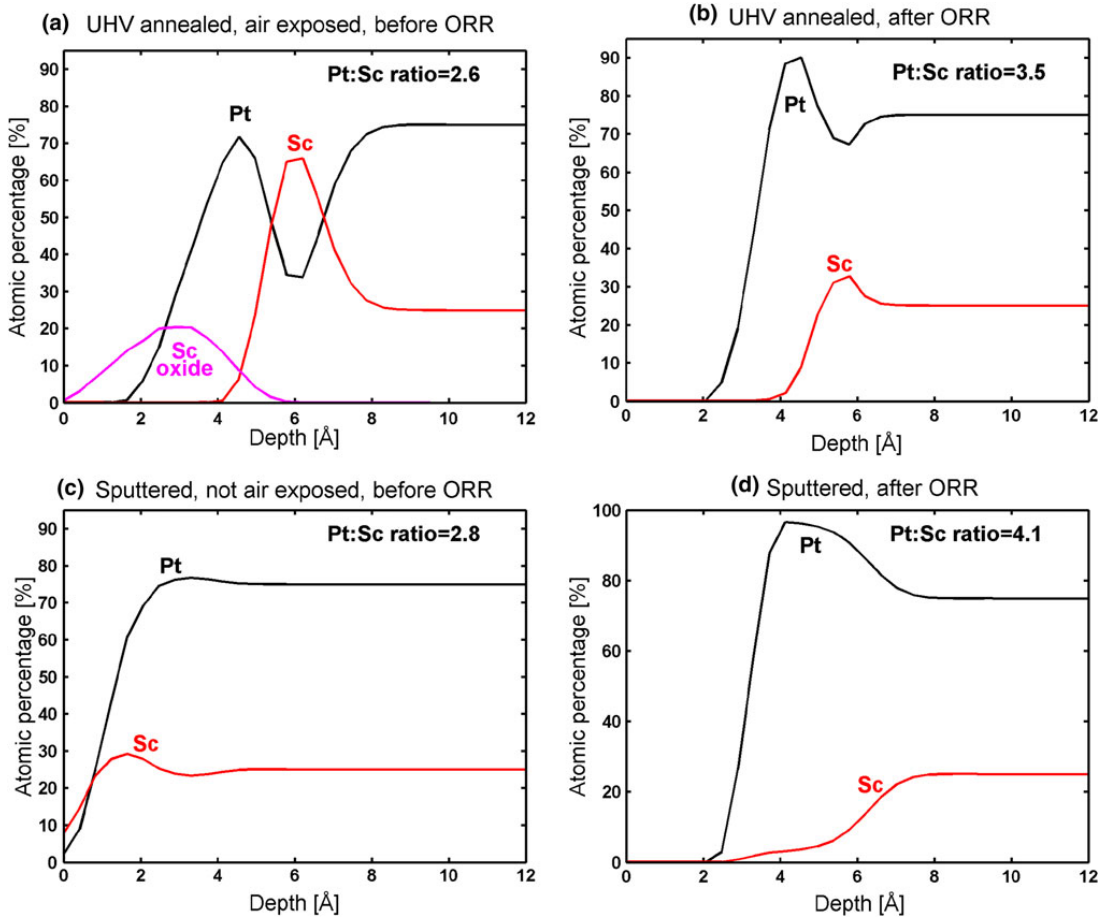

Fig. 4 ARXPS depth profiles of both sputter cleaned and UHV annealed Pt_3Sc before and after measuring the oxygen reduction activity. **a**, **b** and **d** are exposed to air before the ARXPS depth profile is measured, whereas **c** is not. The C and O traces have been omitted for clarity. The average Pt:Sc ratio for all angles is stated on each figure

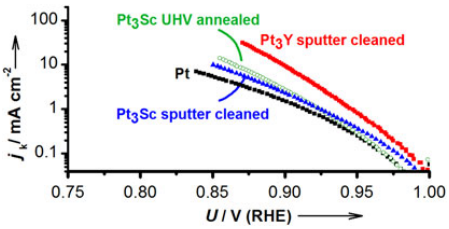

Fig. 5 Specific activity as a function of the electrode potential for the vacuum annealed polycrystalline Pt_3Sc sample compared with sputter cleaned polycrystalline samples of Pt_3Sc, Pt_3Y and Pt. The data corresponds to the anodic cycle. The temperature was kept at 296 ± 1 K and the scan rate was 20 mV/s. The kinetic current has been corrected for mass transport limitations

UHV annealed Pt_3Sc than on Pt(111). The alloy stability, is insufficient to prevent Sc from segregating to the surface upon 200 mbar O_2 exposure. The ARXPS depth profiles obtained after electrochemical measurements are similar for UHV annealed and sputter cleaned Pt_3Sc. The depth profiles show that very little Sc is left in the second layer, although some might be left in the third layer. The ORR activity of UHV annealed Pt_3Sc is similar to that of sputter cleaned Pt_3Sc.

4 DFT Calculations

In order to provide microscopic understanding of the reaction, DFT calculations were performed. The first issue

Table 2 Energy in eV required to move 1 X atom from the sub surface layer to the surface layer of a Pt_3X alloy with a 1 ML thick Pt skin

Concentration (%)	Pt_3Y	Pt_3Sc	Pt_3Ni	Pt_3Ti
50	−2.27	−1.24	0.36	−0.74
25	0.41	0.90	0.75	1.16

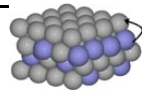

Calculations are made for both 50 and 25 % initial X concentrations in the second layer

considered was the formation of the Pt overlayer upon annealing in vacuo.

Table 2 shows the calculated energy required to move an X atom from the second layer to the surface layer of a Pt_3X alloy with a 1 ML thick Pt skin. The calculation is made for initial X concentrations of 50 and 25 % in the second layer. If the energy is negative the Pt overlayer is not stable. For Pt_3Ni the Pt overlayer is stable both for 50 and 25 % Ni in the second layer which is in agreement with experiments made by Stamenkovic et al. [25]. The system with 50 % concentration of the solute metal in the second layer is not stable for either Pt_3Ti, Pt_3Sc or Pt_3Y, but the system with 25 % concentration of the solute metal in the second layer is. This is consistent with experiments and theoretical investigations on $Pt_3Ti(111)$, where the most stable configuration is with 25 % Ti in the second atomic layer [30, 31, 34]. The difference between Pt_3Ni and the other alloys in the table is related to the strength of the interaction between the alloy components. In Pt_3Ti, Pt_3Y and Pt_3Sc there are very strong bonds between the Pt and the solute metal. This provides a strong driving force towards maximising the number of Pt nearest neighbours surrounding the early transition metal atom. For Pt_3Sc this is in agreement with our ISS data, showing that a Pt overlayer is formed upon annealing in UHV.

The surface reactivity of the different polycrystalline alloys was tested in UHV by CO TPD. The main interest of these alloys is, however, for the oxygen reduction reaction, which has oxygenated species as intermediates (O*, HO* and HOO*) [54]. A relevant question is therefore if it is possible to relate the binding energy of OC* to that of the oxygen species in the oxygen reduction reaction. When considering different pure metals their OC* and HO* binding energies do not scale [55]. For the Pt overlayers on top of Pt_3M alloys such a relation could, however, still be possible. Figure 6 shows the calculated OC*, HO* and HOO* binding energies on three different atop sites ("0", "1" and "2") of Pt overlayer structures on Pt_3Sc and Pt_3Y with subsurface solute metal concentrations of 25 and 50 %. Although not perfectly linear, a clear trend is observed. A surface which binds OC* weaker will also bind HO* and HOO* weaker. Two datapoints ("Pt_3Y 50 % 2" and "Pt_3Sc 50 % 2") on the HO* versus OC* binding energy graph are outliers and it is noted that they are also outliers when comparing the HO* and HOO* binding energies which should scale linearly. A linear fit is made to the data (except the two outliers) giving the following relations:

$$\Delta E_{\mathrm{bin,OH}} = (0.42 \pm 0.04) \times \Delta E_{\mathrm{bin,CO}} \quad (1)$$

$$\Delta E_{\mathrm{bin,OOH}} = (0.48 \pm 0.05) \times \Delta E_{\mathrm{bin,CO}} \quad (2)$$

The ideal ORR catalyst should bind oxygen around 0.2 eV weaker than Pt [5]. From the scaling relations between O* and HO* this corresponds to binding HO* 0.1 eV weaker. From Eq. 1 this is seen to correspond to a weaker binding of OC* by $\frac{0.1\,\mathrm{eV}}{0.42} = 0.24\,\mathrm{eV}$. Ruff et al. [56] have plotted the

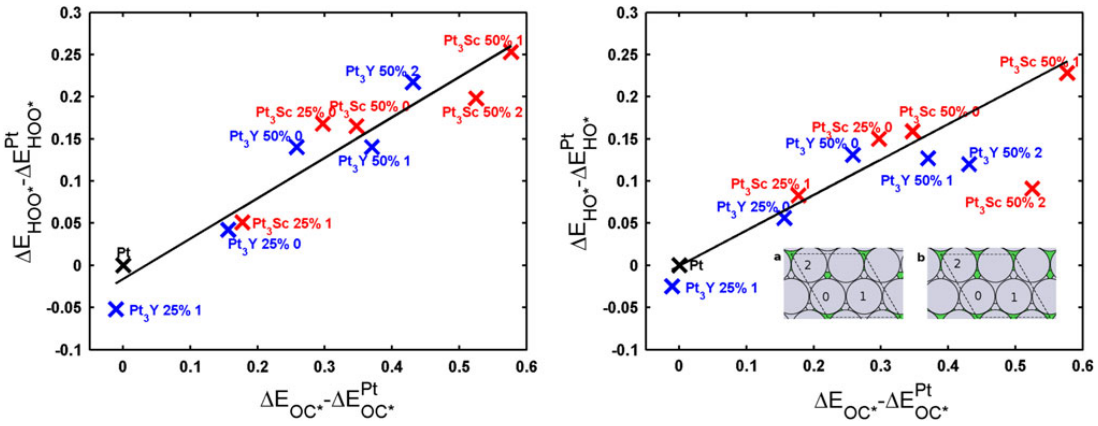

Fig. 6 Calculated OC*, HO* and HOO* binding energies on various Pt overlayer structures. "Pt_3Sc 50% X" refers to the on top site X on the *inset* figure for a Pt_3Sc sample with 50 % Sc in the *second layer*

calculated CO adsorption energies and activation energies for desorption on different Pd nanostructures versus the corresponding desorption temperatures. They found that there is a linear relation between the two, which can be expressed as:

$$\Delta E_{\mathrm{bin,CO}} \approx 0.0028 \frac{\mathrm{eV}}{\mathrm{K}} \times \Delta T_{\mathrm{des,CO}} \quad (3)$$

From Eq. (3) we get that a weaker binding of OC* by 0.24 eV corresponds to a lowering in desorption temperature of CO by $\frac{0.24\,\mathrm{eV}}{0.0028\frac{\mathrm{eV}}{\mathrm{K}}} = 85\,\mathrm{K}$. There is clearly some uncertainty on this value, but the important point is that a Pt overlayer catalyst should bind CO weaker (on the order of 85 K) in order for it to have an optimal bonding of the O species relevant for the oxygen reduction reaction.

The ARXPS depth profiles shown in Fig. 4 indicate that some subsurface scandium leaches out upon electrochemical testing. In the following we consider the calculated effect of different amounts of scandium in the second layer on the binding of ORR intermediates.

Figure 7 shows the calculated free energy diagram for the oxygen reduction reaction considering 1 ML Pt skins on Pt_3Sc with 50, 25 and 0 % Sc in the second layer. For 25 and 50 % Sc in the second layer oxygen intermediates are bound weaker than for pure Pt and the free energy change for the formation of HOO* is increased whereas the free energy change for the removal of HO* is decreased. For 0 % Sc in the second layer (i.e. 2 layers of Pt on top of Pt_3Sc) the oxygen intermediates are bound stronger than for pure Pt, resulting in an increase in the free energy change for the removal of HO*. By comparing the free energy changes for the different catalysts the theoretical volcano shown in Fig. 8 is obtained.

The solid line marks the Sabatier volcano [4, 54] based on the observed scaling relation between the free energies

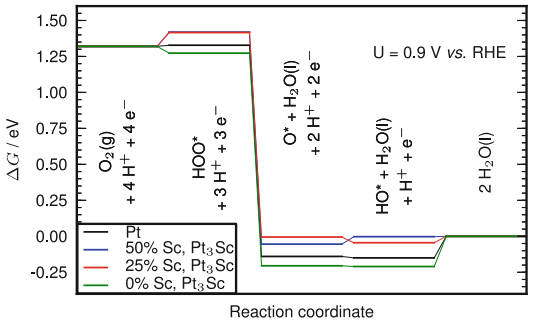

Fig. 7 Calculated free energy diagram for the oxygen reduction reaction at 0.9 V versus RHE under standard conditions for Pt(111) (*black curve*) and for Pt overlayers on Pt_3Sc (*green, red and blue*). The Pt_3Sc data are calculated for Pt overlayers with Pt_3Sc in the bulk and different Sc content in the *second layer* indicated on the figure

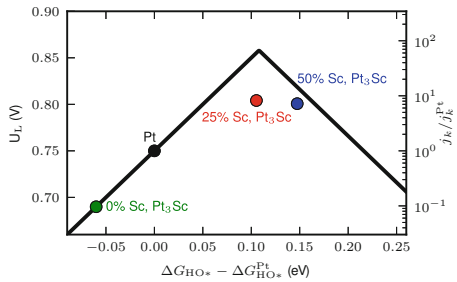

Fig. 8 DFT calculated volcano plot for Pt overlayers on Pt_3Sc: calculated potential, U_L, required for all reaction steps to be negative in free energy as a function of hydroxyl binding energy, ΔG_{HO^*}, relative to pure Pt. Also shown is the calculated activity enhancement relative to Pt at $U = 0.9$ V (RHE). The Pt_3Sc data are calculated for Pt overlayers with Pt_3Sc in the bulk and different Sc content in the *second layer* indicated on the figure. The *lines* are theoretical predictions, based on a simple Sabatier analysis [4, 54]

of HO* and HOO* : $\Delta G_{\mathrm{HOO}^*} \approx \Delta G_{\mathrm{HO}^*} + 3.2$ eV [11, 57]. For Pt_3Sc with 25 % Sc in the second layer the free energy of HOO* is higher than predicted from the free energy of HO* resulting in a decrease of the rate predicted by the Sabatier volcano. For 50 and 25 % Sc in the second layer the calculated activity is increased compared to pure Pt (cf. Greeley et al. [5]) whereas for 0 % Sc in the second layer the calculated activity is decreased. We do not anticipate the Pt_3Sc structures with 0 and 50 % Sc in the second layer to be stable structures. In the structure with two Pt layers, we would expect the Pt–Pt interatomic distance to relax towards that of unstrained pure Pt [58]. The structure with 50 % Sc in the second layer will likely reconstruct in order to minimise Sc–Sc neighbours (cf. Table 2 and the accompanying discussion).

5 Discussion

For vacuum annealed polycrystalline Pt_3Sc, the onset of CO desorption is around 130 K lower than on Pt(111) and the main desorption peak is around 50 K lower than on Pt(111). According to the above relation between the CO desorption temperature and the HO* binding energy, the vacuum annealed surface would be situated close to the tip of the ORR volcano, if it were stable under reaction conditions. However, despite the very negative enthalpy of formation of Pt_3Sc, at 200 mbar O_2, the Sc segregated to the surface to form scandium oxide. This shows that more generally, Pt-skin structures do not seem to be stable for alloys of Pt and early transition metals, unlike alloys such as Pt_3Ni, Pt_3Co or Cu/Pt. It is worth perusing upon why this is the case. The segregation of the solute metal from the subsurface layer to the surface layer is possibly

initiated by direct interactions between oxygen containing adsorbates and the solute metal in the subsurface layer. For instance, monoatomic O tends to adsorb in the threefold hollow site of Pt overlayers with the (111) termination [59]; in the case of Pt_3Sc, adsorbed O would have Sc as a nearest neighbour. Menning and Chen found this to be the case for the Ni/Pt and Co/Pt systems at temperatures above 630 K [60]. Moreover, Sc and O would form a much stronger bond than Ni–O or Co–O [53]. Consequently, the barrier for Sc segregation in the presence of adsorbed oxygen would be low, allowing it to take place at room temperature. Nonetheless, we anticipate that the strong interaction between Sc (or Y, La or Gd for that matter) would provide a large barrier for its diffusion through a thicker Pt overlayer, in comparison to the small barrier for the diffusion of a late transition metal in a Pt matrix [5, 11, 14].

It is interesting to note that the thickness of the Pt overlayer that is formed under reaction conditions on polycrystalline Pt_3Sc (cf. Fig. 4), at 1 or 2 monolayers, is much lower than that on Pt_3Y or Pt_5Y, typically greater than 3 monolayers [12]. The standard reduction potential and affinity towards oxygen are similar for Sc and Y [53, 61]. Furthermore, the heat of formation per formula unit of Pt_3Sc, Pt_3Y and Pt_5Y are also roughly equal [5, 62]. Comparing Pt_3Sc, Pt_3Y and Pt_5Y, the most striking difference is the difference in strain of a pure Pt overlayer on top of the alloy (0.9 % tensile strain for Pt_3Sc, 3.8 % tensile strain for Pt_3Y and 5% compressive strain for Pt_5Y [5, 63]). The difference in strain could therefore be the reason for the difference observed in the Pt overlayer thickness between Pt_3Sc, Pt_3Y and Pt_5Y after electrochemical measurements. Moreover, the significant compressive strain imposed on Pt_5Y by the bulk is presumably the reason why it is significantly more active than Pt_3Sc [63].

The relatively small amount of strain induced by Sc means that the binding energy of oxygen containing species will be affected little by the presence of Sc in the bulk. Moreover a tensile strained Pt overlayer would bind oxygen containing species stronger, moving further away from the tip of the ORR volcano. On this basis, an increased oxygen reduction activity would require some Sc in the second layer. In summary, we cannot rule out a strain effect; nonetheless, to the best of our current understanding the increase in ORR activity should be due to the ligand effect.

The ARXPS depth profile of vacuum annealed Pt_3Sc from Fig. 4a would suggest that the second atomic layer would be enriched in Sc, similar to that observed previously for Pt_3Ni [25]. Even so, this is inconsistent with our understanding of this type of compound, based on experiments on similar alloys, e.g. Pt_3Ti and our DFT calculations. As discussed earlier, the negative enthalpy of formation of Pt_3Sc [5] would imply that forming Sc–Sc neighbours (which would be the case for 50% Sc in the second layer) is not likely. Consequently, the enrichment of subsurface Sc is likely an artefact from the fitting procedure used for the ARXPS depth profiles. Such artefacts are related to the uncertainties in the absolute XPS sensitivity factors. Even so, the relative differences in ARXPS depth profile between Pt_3Sc prepared in various ways is more likely to be significant. After oxygen reduction measurements the overall Pt:Sc ratio increases and correspondingly the amount of Sc in the second layer clearly decreases due to Sc dissolution. Therefore, we propose that the reason for the slight increase in activity observed on sputter cleaned and vacuum annealed Pt_3Sc, relative to Pt, is due to some residual amount of Sc in the subsurface layer.

According to the free energy diagram and the volcano in Figs. 7 and 8, the oxygen reduction activity is extremely sensitive to the subsurface concentration of Pt. For 50 and 25% Sc in the second layer, oxygen containing species are bound weaker that on Pt and the calculated ORR activity is higher than for Pt. However, for 0% Sc in the second layer a stronger binding of oxygen containing species is observed and the calculated ORR activity is lower than for Pt. The origin of the increased ORR activity should then mainly be due to a modification of the electronic structure of the Pt surface atoms by Sc atoms in the underlying layers, cf. the ligand effect [17].

6 Conclusions

We studied the effect of sputter cleaning and vacuum annealing on the structure of Pt_3Sc, (a) under vacuum (b) following exposure to 200 mbar O_2 and (c) following exposure to oxygen reduction reaction conditions. It turns out that the vacuum annealed structure is slightly unstable in air and under reaction conditions. Although we predict that the vacuum annealed structure would be very active for oxygen reduction, the loss of Sc under reaction conditions results in a surface with somewhat lower activity.

We anticipate that the phenomena observed here are more general: Pt alloys with rare earths and early transition metals are unlikely to be stable as Pt-skin structures, with significant subsurface concentrations of the solute metal. Nonetheless, the negative enthalpy of formation of these compounds could stabilise them against dealloying under the harsh conditions of a fuel cell cathode as Pt skeleton structures. Consequently, it seems that a promising strategy towards obtaining highly active and stable catalyts for oxygen reduction would be to find alloys of Pt and early transition metals or lanthanides which impose compressive strain on the Pt surface layer [11, 14].

Acknowledgements Funding by the Danish Council for Technology and Innovations FTP program and by the Danish Strategic Research Councils HyCycle program is gratefully acknowledged. P.H.F. acknowledges funding from the Danish Council for Strategic Research in Sustainable Energy and Environment-project "MEDLYS". I.E.L.S. gratefully acknowledges financial support from Energinet.dk through the R&D program ForskEL (CATBOOSTER project). The Center for Atomic-scale Materials Design is supported by the Lundbeck Foundation. The Center for Individual Nanoparticle Functionality is supported by the Danish National Research Foundation.

References

1. Gasteiger HA, Kocha SS, Sompalli B, Wagner FT (2005) Appl Catal B 56:9
2. Rossmeisl J, Logadottir J, Nørskov JK (2005) Chem Phys 319:178
3. Abild-Pedersen F, Greeley J, Studt F, Rossmeisl J, Munter TR, Moses PG, Skulason E, Bligaard T, Nørskov JK (2007) Phys Rev Lett 99:016105
4. Nørskov JK, Rossmeisl J, Logadottir A, Lindqvist L, Kitchin JR, Bligaard T, Jonsson H (2004) J Phys Chem B 108:17886
5. Greeley J, Stephens IEL, Bondarenko AS, Johansson TP, Hansen HA, Jaramillo TF, Rossmeisl J, Chorkendorff I, Nørskov JK (2009) Nat Chem 1:552
6. Gasteiger HA, Markovic NM (2009) Science 324:48
7. Adzic RR, Zhang J, Sasaki K, Vukmirovic MB, Shao M, Wang JX, Nilekar AU, Mavrikakis M, Valerio JA, Uribe F (2007) Top Catal 46:249
8. Strasser P, Koh S, Anniyev T, Greeley J, More K, Yu CF, Liu ZC, Kaya S, Nordlund D, Ogasawara H, Toney MF, Nilsson A (2010) Nat Chem 2:454
9. Mukerjee S, Srinivasan S, Soriaga MP, McBreen J (1995) J Electrochem Soc 142:409
10. Stephens IEL, Bondarenko AS, Perez-Alonso FJ, Calle-Vallejo F, Bech L, Johansson TP, Jepsen AK, Frydendal R, Knudsen BP, Rossmeisl J, Chorkendorff I (2011) J Am Chem Soc 133:5485
11. Stephens IEL, Bondarenko AS, Grønbjerg U, Rossmeisl J, Chorkendorff I (2012) Energy Environ Sci 5:6744
12. Stephens IEL, Bondarenko AS, Bech L, Chorkendorff I (2012) ChemCatChem 4:341
13. Stamenkovic VR, Mun BS, Arenz M, Mayrhofer KJJ, Lucas CA, Wang GF, Ross PN, Markovic NM (2007) Nat Mater 6:241
14. Escudero-Escribano M, Verdaguer-Casadevall A, Malacrida P, Grønbjerg U, Knudsen BP, Jepsen AK, Rossmeisl J, Stephens IEL, Chorkendorff I (2012) J Am Chem Soc 134:16476
15. Dubau L, Maillard F, Chatenet M, Andre J, Rossinot E (2010) Electrochim Acta 56:776
16. Maillard F, Dubau L, Durst J, Chatenet M, Andre J, Rossinot E (2010) Electrochem Commun 12:1161
17. Kitchin J, Nørskov JK, Barteau M, Chen J (2004) J Chem Phys 120:10240
18. Mavrikakis M, Hammer B, Nørskov JK (1998) Phys Rev Lett 81:2819
19. Lischka M, Mosch C, Gross A (2007) Electrochim Acta 52:2219
20. Hoster HE, Alves OB, Koper MTM (2010) ChemPhysChem 11:1518
21. Schlapka A, Lischka M, Gross A, Kasberger U, Jakob P (2003) Phys Rev Lett 91:016101
22. Calle-Vallejo F, Martinez JI, Garcia-Lastra JM, Rossmeisl J, Koper MTM (2012) Phys Rev Lett 108:116103
23. Ruban AV, Skriver HL, Nørskov JK (1998) Phys Rev Lett 80:1240
24. Stamenkovic V, Schmidt TJ, Ross PN, Markovic NM (2002) J Phys Chem B 106:11970
25. Stamenkovic VR, Fowler B, Mun BS, Wang GF, Ross PN, Lucas CA, Markovic NM (2007) Science 315:493
26. Stamenkovic V, Mun BS, Mayrhofer KJJ, Ross PN, Markovic NM, Rossmeisl J, Greeley J, Nørskov JK (2006) Angew Chem Int Ed Engl 45:2897
27. Watanabe M, Tsurumi K, Mizukami T, Nakamura T, Stonehart P (1994) J Electrochem Soc 141:2659
28. Toda T, Igarashi H, Uchida H, Watanabe M (1999) J Electrochem Soc 146:3750
29. Mun BS, Watanabe M, Rossi M, Stamenkovic V, Markovic NM, Ross PN (2005) J Chem Phys 123:204717
30. Chen W, Paul JAK, Barbieri A, Van Hove MA, Cameron S, Dwyer DJ (1993) J Phys Condens Matter 5:4585
31. Duan Z, Zhong J, Wang G (2010) J Chem Phys 133:114701
32. Ross PN (1992) J Vac Sci Technol A 10:2546
33. Bardi U, Beard BC, Ross PN (1990) J Catal 124:22
34. Bardi U, Dahlgren D, Ross PN (1986) J Catal 100:196
35. Haner AH, Ross PN, Bardi U, Atrei A (1992) J Vac Sci Technol A 10:2718
36. Friebel D, Viswanathan V, Miller DJ, Anniyev T, Ogasawara H, Larsen AH, O'Grady CP, Nørskov JK, Nilsson A (2012) J Am Chem Soc 134:9664
37. Andersson KJ, Calle-Vallejo F, Rossmeisl J, Chorkendorff I (2009) J Am Chem Soc 131:2404
38. Wagner CD, Davis LE, Zeller MV, Taylor JA, Raymond RH, Gale LH (1981) Surf Interface Anal 3:211
39. Seah M, Gilmore I, Spencer S (2001) J Elec Spect Relat Phenom 120:93
40. Scofield J (1976) J Elec Spect Relat Phenom 8:129
41. ASE and DACAPO are open source codes available at http://wiki.fysik.dtu.dk
42. Vanderbilt D (1990) Phys Rev B 41:7892
43. Hammer B, Hansen LB, Nørskov JK (1999) Phys Rev B 59:7413
44. Bengtsson L (1999) Phys Rev B 59:12301
45. Monkhorst HJ, Pack JD (1976) Phys Rev B 13:5188
46. Niehus H, Heiland W, Taglauer E (1993) Surf Sci Rep 17:213
47. Brongersmaa HH, Draxler M, de Ridder M, Bauer P (2007) Surf Sci Rep 62:63
48. Fiordaliso EM, Dahl S, Chorkendorff I (2012) J Phys Chem C 116:5773
49. Mikhailov SN, van den Oetelaar LCA, Brongersma HH (1994) Nucl Instrum Method Phys Res B 93:210
50. Petrova NV, Yakovkin IN (2002) Surf Sci 519:90
51. Nieskens DLS, van Bavel AP, Niemantsverdriet JW (2003) Surf Sci 546:159
52. Bandarenka AS, Varela AS, Karamad MR, Calle-Vallejo F, Bech L, Perez-Alonso FJ, Rossmeisl J, Stephens IEL, Chorkendorff I (2012) Angew Chem Int Ed 51:11845
53. Pourbaix M (1974) Atlas of electrochemical equilibria in aqueous solutions. National Association of Corrosion Engineers, Houston
54. Rossmeisl J, Karlberg GS, Jaramillo T, Nørskov JK (2008) Faraday Discuss 140:337
55. Ferrin P, Nilekar A, Greeley J, Mavrikakis M, Rossmeisl J (2008) Surf Sci 602:3424
56. Ruff M, Takehiro N, Liu P, Nørskov JK, Behm RJ (2007) Chem Phys Chem 8:2068
57. Koper MTM (2011) J Electroanal Chem 660:254
58. Yang RZ, Strasser P, Toney MF (2011) J Phys Chem C 115:9074
59. Viswanathan V, Hansen HA, Rossmeisl J, Jaramillo TF, Pitsch H, Nørskov JK (2012) J Phys Chem C 116:4698
60. Menning CA, Chen JG (2010) J Power Source 195:3140
61. Haynes WM (Ed) (2012) CRC handbook of chemistry and physics, Taylor and Francis, Boca Raton (Internet version)
62. Palenzona A, Cirafici S (1990) J Phase Equilib 11:493
63. Johansson TP (2012) New materials for oxygen reduction electrodes. PhD thesis, Technical University of Denmark, Lyngby

Journal of Materials Chemistry A

PAPER

View Article Online
View Journal

Enhanced activity and stability of Pt–La and Pt–Ce alloys for oxygen electroreduction: the elucidation of the active surface phase†

Cite this: DOI: 10.1039/c3ta14574c

Paolo Malacrida, María Escudero-Escribano, Arnau Verdaguer-Casadevall, Ifan E. L. Stephens and Ib Chorkendorff*

Received 7th November 2013
Accepted 7th January 2014

DOI: 10.1039/c3ta14574c

www.rsc.org/MaterialsA

Three different Pt–lanthanide metal alloys (Pt_5La, Pt_5Ce and Pt_3La) have been studied as oxygen reduction reaction (ORR) electrocatalysts. Sputter-cleaned polycrystalline Pt_5La and Pt_5Ce exhibit more than a 3-fold activity enhancement compared to polycrystalline Pt at 0.9 V, while Pt_3La heavily corrodes in 0.1 M $HClO_4$ electrolyte. Angle Resolved X-ray Photoelectron Spectroscopy (AR-XPS) and Low Energy Ion Scattering (LEIS) have been extensively combined with electrochemical techniques to follow the chemical and structural changes at the surface. The highly reactive lanthanide atoms are not stable in the presence of oxygen and readily oxidize. The surface oxides are completely dissolved in the electrolyte. In Pt_5La and Pt_5Ce the so formed Pt overlayer provides kinetic stability against the further oxidation and dissolution. At the same time, it ensures a very high stability during ORR potential cycling, suggesting that these alloys hold promise as cathode catalysts in Proton Exchange Membrane Fuel Cells (PEMFCs).

1. Introduction

Proton Exchange Membrane Fuel Cells (PEMFCs) represent one of the most promising alternatives to traditional power sources in a future sustainable society, especially for transportation applications. Using hydrogen as a fuel, they could provide an efficient and clean alternative to engines based on fossil fuels.[1,2] However, the commercialisation of PEMFCs is still inhibited by their relatively low performances and high production costs. This is, to a large part, due to the slow kinetics of the oxygen reduction reaction (ORR) at the cathode and the copious amounts of Pt used to catalyse this reaction.[2,3] Although Pt-based materials are the most active ORR catalysts, they still exhibit rather high overpotentials. For this reason, in order to ensure high power densities, for instance in automotive vehicles, high Pt loadings are needed. Consequently, there has been much interest during the past few decades in developing new ORR catalysts. They should both be highly active and stable under the acidic oxidising conditions of a PEMFC cathode.[2–7] Since Pt is both expensive and scarce, it is necessary to decrease the amount of Pt required to catalyse the ORR, in favour of cheaper and more abundant materials. To date, the most successful catalysts which reach this aim are alloys of Pt and other transition metals.

Alloys of Pt and late transition metals such as Fe, Co, Ni, and Cu have been studied extensively, leading to strongly enhanced ORR activities.[2,3,7–12] Nonetheless, these alloys are thermodynamically unstable under fuel-cell conditions; the transition metal tends to dissolve into the electrolyte *via* a process known as dealloying.[5,11,13] The resulting surface composition is Pt enriched. However, a precise description of the structure is challenging, the level of enrichment and the thickness of the dealloyed region varying for different alloys, preparation techniques and electrochemical treatments. Generally the dissolution proceeds until a several layer-thick Pt overlayer is formed,[14] denoted by Stamenkovic *et al.* as a "Pt skeleton" structure.[7,8,10] Although this Pt overlayer might provide temporary kinetic stability against further dissolution, further dealloying is considered as the main cause of deactivation for these catalysts.[15]

A single Pt monolayer on the surface of the alloy can be stabilised by vacuum annealing. This structure was denoted by Stamenkovic *et al.* as a "Pt-skin" structure.[8,10] Such surfaces have exhibited the highest ORR activities ever reported.[9,16–18] However, it may be challenging to synthesise a supported Pt-skin catalyst in large amounts and stabilise it over the long time periods and many potential cycles required for a PEMFC cathode.[19]

The above considerations led to the search for new Pt-alloy catalysts. A theoretical screening based on Density Functional Theory (DFT) calculations was set out to identify alloys that were both active and stable.[20] The activity of the catalyst was predicted on the notion that the optimal metal catalyst for the ORR should bind O (or OH) slightly more weakly than pure Pt.[21,22]

Center for Individual Nanoparticle Functionality, Department of Physics, Technical University of Denmark (DTU), Building 312, 2800 Lyngby, Denmark. E-mail: ibchork@fysik.dtu.dk

† Electronic supplementary information (ESI) available. See DOI: 10.1039/c3ta14574c

The key descriptor for stability was that the catalysts have as negative an alloying energy, or heat of formation, as possible. The calculations predicted that Pt_3Y and Pt_3Sc fulfilled these criteria. Indeed experiments confirmed an activity enhancement relative to polycrystalline Pt for both Pt_3Y and Pt_3Sc:[20,23] Pt_3Y in particular exhibiting the highest activity ever reported for a Pt-skeleton structure.

A negative heat of formation may stabilise a Pt alloy catalyst against degradation *via* dealloying. This is because the kinetic barrier for metal diffusion through the alloy should, to a large part, be dictated by the alloying energy. The exceptionally negative heat of formation of Pt_3Y, $\Delta H_{f(alloy)} \sim -4$ eV, is characteristic of several other alloys of Pt with early transition metals or lanthanides, such as Pt_5Gd, Pt_5La and Pt_5Ce as shown in Fig. 1.[24–29] This is because the d-band of these alloys is half filled, meaning that all the bonding states are full, and antibonding states are empty.[3,20,30,31] On the other hand, Fig. 1 also shows that alloys of Pt and late transition metals, such as Pt_3Co and Pt_3Ni, have much less negative alloying energies. Very recently, we also discovered that alloys of Pt_5La and Pt_5Gd are very promising catalysts for the ORR,[3,32,33] with Pt_5Gd, together with Pt_3Y, being the most active catalyst amongst polycrystalline Pt-skeleton structures. In addition to its high activity, the percentage of activity loss after 10 000 cycles between 0.6 and 1 V for Pt_5Gd is less than 15%. We note that despite their denomination as "rare earths", they are much more inexpensive and much more abundant than Pt.[34]

In order to elucidate the active phase of Pt_5Y, Pt_3Y, Pt_5Gd and Pt_5La, we employed angle resolved X-ray photoelectron spectroscopy. Our measurements suggested that in each case, the surface comprised of a thick Pt overlayer, to the order of 1 nm in depth. This is easily understood on the basis that there is a strong driving force for the dissolution of the metal from the surface layer. Moreover, oxides of Y, La and Gd are all unstable in acid solution.[35] In the absence of any solute metal in the near-surface region, we proposed that the activity of these catalysts was due to a compressive strain induced by the alloy bulk on the Pt overlayer, weakening the binding of surface adsorbates such as OH or O.

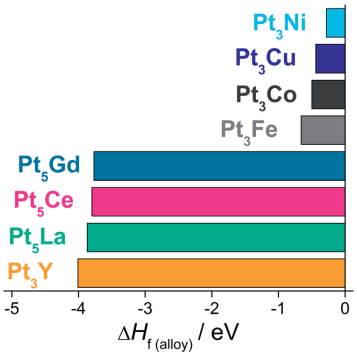

Fig. 1 Experimental enthalpies of formation specified per formula unit. Values for the different Pt alloys are respectively taken from: Pt_3Ni,[24] Pt_3Cu,[25] Pt_3Co,[26] Pt_3Fe,[26] Pt_5Gd,[27] Pt_5Ce,[27,28] Pt_5La[27,28] and Pt_3Y.[27]

Recent studies by Kim and coworkers have also focused on alloys of Pt and early transition metals and lanthanides as ORR catalysts.[36–38] Their Pt_3La sample exhibited a similar activity to that of the Pt_5La we reported,[3,32] although their interpretation of its activity was somewhat different. On the basis of their AR-XPS measurements, they report that the surface composition is essentially unchanged before and after the reaction. Using DFT calculations on a closely packed structure of Pt_3La, they show that La will have a tendency to segregate towards the surface, in vacuum. They also suggest that the negative alloying energy is sufficient to ensure that the alloy is *thermodynamically* stable against oxidation or dissolution. This discrepancy between their interpretation and our own led us to revisit the issue of the surface composition of alloys of Pt and La. Moreover, there is a broader debate about the possible stabilisation of more reactive metals at the surface of Pt and Pd alloys, even for more extensively studied alloys, such as Pt–Ni and Pt–Co.[8,13,39,40] This possibility would be of fundamental relevance, since their enhanced activity could be also explained in terms of bifunctional effects: with both metals providing active sites during ORR, the more reactive atoms facilitating the O_2 dissociation or the removal of OH radicals from the more noble Pt sites.[41,42]

This article, for the first time, investigates the electrochemical behaviour of Pt_5Ce, demonstrating its very high activity and stability towards the ORR. Ce, together with La, is the most abundant, most largely produced and cheapest element among the rare earths.[34] Moreover, by comparing Pt_5Ce with Pt_5La and Pt_3La, we can elucidate the origin of the enhancement of the activity and stability for these alloys, which is still controversial. Furthermore, we use these catalysts to provide evidence for the intrinsic instability of Ce and La on the surface.

2. Experimental

Polycrystalline alloys (5 mm in diameter disks) of Pt_5La, Pt_3La and Pt_5Ce were supplied by Mateck GmbH, Germany. The crystal structures of the alloys were investigated by X-ray diffraction (XRD) and are in agreement with that reported in the literature. XRD measurements and full experimental details are described in the ESI.† The surface stoichiometry and the absence of impurities were checked by X-ray photoelectron spectroscopy (XPS). Before all electrochemical measurements the samples were cleaned under Ultra High Vacuum (UHV) conditions by Ar sputtering, until no C contaminations were observed. The ion energy was set to 0.5 keV and a beam current of 1 μA over a 7×7 mm^2 area was used to homogenously sputter the active surface.

2.1 Electrochemical characterization

The electrochemical experiments were performed with a VMP2 potentiostat (Bio-Logic Instruments), controlled by a computer. The rotating ring-disk electrode (RRDE) assemblies were provided by Pine Instruments Corporation. A standard two-compartment glass cell was used, which was equipped with a water jacket attached to a hot water bath to control the

temperature. All the electrochemical experiments were carried out at 23 °C. The electrolyte, 0.1 M $HClO_4$ (Merck Suprapur), was prepared with Millipore (Milli-Q, 18.2 MΩ cm^{-1}) water. The counter electrode was a Pt wire and the reference was an Hg/Hg_2SO_4 electrode, separated from the working electrode compartment using ceramic frits. All the potentials in the text are referred to the reversible hydrogen electrode (RHE), and are corrected for ohmic losses. The polycrystalline alloys, inserted into the arbor of a RRDE, were immersed into the electrochemical cell under potential control of 0.1 V *vs.* RHE into a N_2 (N5, Air Products) saturated electrolyte. The electrodes were cycled until stable cyclic voltammograms (CVs) were obtained. The ORR activity measurements were conducted in an electrolyte saturated with O_2 (N55, Air Products).

2.2 Physical characterization

Angle Resolved X-ray Photoelectron Spectroscopy (AR-XPS) was used as a non-destructive technique to investigate the chemical state of the alloys and their surface morphology. Measurements were performed on a Thermo Scientific Theta Probe instrument with a base pressure of 5×10^{-10} mbar. The X-ray source is monochromatised Al Kα (1486.7 eV), giving a resolution better than 1.0 eV at the employed pass energy of 100 eV. The analyser has an acceptance angle of 60°, between 20° and 80° to the surface normal; for the angle resolved profiles, 16 different channels were analysed in parallel corresponding to 3.75° wide angle intervals. Angle resolved data were processed using the simulation tool, ARProcess (Thermo Avantage software), which uses a maximum entropy method combined with a genetic algorithm to define the depth profiles: angles over 65° were omitted to minimize the effects of elastic scattering. Further technical details are provided in the ESI.†

AR-XPS was initially carried out during sputter-cleaning starting 20 minutes after the beginning of the cleaning procedure. Sputtering was not stopped during these measurements in order to avoid sub-monolayer amounts of O to be adsorbed on the sample due to the expected high reactivity and high sticking coefficients of O on La and Ce (see ESI†).[43,44] This procedure did not induce any significant changes in the Ce 3d, La 3d and Pt 4f peak shape but prevented the presence of C and O contaminations: lower than 1% in all cases. Subsequently, samples were transferred to a fast-entry air lock, vented in dry nitrogen up to atmospheric pressure and readily protected by a drop of H_2-saturated Milli-Q water for transfer to a rotating ring disk electrode assembly. AR-XPS measurements were repeated after ORR testing and after stability tests in order to evaluate the active structure of the alloy and its stability. In order to investigate the stability of the alloys in the presence of oxygen, identical measurements were also taken after exposure of the sputtered-cleaned surfaces to air for 1 hour.

Low Energy Ion Scattering (LEIS) was used to probe the composition of the outmost layer of Pt_5Ce after electrochemical measurements. LEIS spectra were acquired with Ne^+ ions at 1 keV energy. A residual Ne pressure of 5×10^{-9} mbar gave sample currents between 10 and 16 nA. The beam was rastered over a large sample area, approximately 4 mm × 4 mm, in order to minimize the destructive effects induced by ion sputtering. The average scattering angle was 125°, and the incidence angle was 45°. Initially, a few scans were repeated in order to clean the tested alloys from the organic impurities collected during the transfer and the electrochemical measurements. Each scan took approximately 2 minutes. This cleaning phase took 10 to 15 minutes, until the Pt signal started appearing. For comparison, LEIS spectra were also taken using the same parameters on the sputter-cleaned alloy.

3. Results

3.1 Crystal structure

The structure of the alloys was investigated by XRD as reported in the ESI.† No closed-packed structure is observed for either Pt_5La or Pt_5Ce, they instead exhibited a hexagonal structure with a lattice parameter of $a = 5.39$ Å and $a = 5.38$ Å respectively, in good agreement with the values reported previously.[45] The polycrystalline sample with nominal composition of Pt_3La was, as a matter of fact, composed of a mixture of two phases: Pt_2La and Pt_5La. This is consistent with the Pt–La phase diagrams in the literature, which do not show the existence of a stable Pt_3La phase.[46–48]

3.2 Electrochemical characterisation and ORR activity

Fig. S2† shows the stable CVs in N_2-saturated 0.1 M $HClO_4$ solutions on sputter-cleaned Pt_5Ce and Pt_5La, as compared to the base CV on polycrystalline Pt. The ORR activities of the electrocatalysts were evaluated in oxygen-saturated solutions after stable CVs in N_2 were obtained (typically after *ca.* 100 cycles). Fig. S6† shows typical CVs on sputter-cleaned Pt_5Ce, Pt_5La and Pt polycrystalline electrodes in O_2-saturated perchloric acid solutions. We assume that the roughness factor was 1 cm^2/cm^2, as we found to be the case for other Pt alloys, prepared in the same manner.[20,49] We have also performed CO-stripping measurements on Pt_5La and Pt_5Ce (all the results are explained and discussed in the ESI†). As the CO-stripping charges were similar or slightly lower for Pt_5La and Pt_5Ce alloys than for pure Pt, all currents were normalised by the geometric surface area, consistent with our previous studies.[3,20,23,33,49] Given that the electrodes consist of planar surfaces, with a surface composition of pure Pt, we consider the geometric surface area to be a more reliable and more conservative estimate of the microscopic surface area (single crystal studies have shown that the saturation coverages of CO and H on Pt overlayers can be highly sensitive to alloying).[50] The kinetic current density, j_k, *i.e.* the current density in the absence of any mass-transfer effects, was calculated by the equation $[(j_d j)/(j_d - j)]$, where j_d is the limited current density and j the measured current density. Fig. 2 shows the Tafel plot (j_k as a function of the potential, U) for sputter-cleaned Pt_5Ce, Pt_5La, Pt_3La and Pt polycrystalline electrodes in O_2-saturated 0.1 M $HClO_4$. It must be noted that the reported activity for the Pt polycrystalline sample agrees well, or is slightly higher, than recent experiments conducted by reputable groups under nominally the same conditions.[10,51,52] Pt_5Gd (which is, together with P_3Y, the

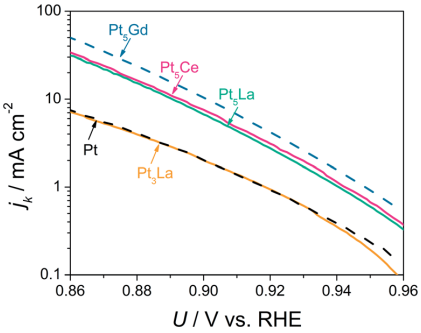

Fig. 2 Tafel plots showing the kinetic current density (j_k) normalized per geometric surface area of Pt_5Ce, Pt_5La, Pt_3La, Pt and Pt_5Gd[33] as a function of the potential (U).

most active polycrystalline Pt-alloy reported in the literature so far)[20,33] is also represented for comparison. As can be observed in Fig. 2, the kinetic current densities for Pt_5Ce and Pt_5La, at 0.90 V *vs.* RHE, are (7.4 ± 0.4) mA cm^{-2} and (6.8 ± 0.3) mA cm^{-2}, respectively. This means that the ORR activity enhancements for Pt_5Ce and Pt_5La are 3.7 and 3.4, respectively. This enhancement in activity is considerably higher than that exhibited by Pt_3Fe, Pt_3Co and Pt_3Ni catalysts prepared under similar conditions, which revealed about a factor of 2 enhancement compared to polycrystalline Pt.[8,53] According to our previous results, Pt_5Ce is the most active polycrystalline catalyst for the ORR after Pt_3Y[20] and Pt_5Gd.[33]

In contrast, the ORR activity on Pt_3La is very similar to that on pure Pt. It must be noted that, as discussed in the ESI and shown in Fig. S5,† CVs in N_2-saturated solutions present remarkable changes during cycling, indicating that the polycrystalline Pt_3La sample is corroded. This was confirmed by Inductively Coupled Plasma Mass Spectrometry (ICP-MS) measurements of equal volumes of electrolyte taken after measurements of the Pt_5La and Pt_3La ORR activity (Fig. S7†) and compared to a clean as-prepared electrolyte. In the case of Pt_3La, a substantial increase of the La signal was found indicating a strong La dissolution and a possible reason for such low activity, similar to Pt. In contrast, Yoo *et al.*[37] reported an appreciable enhancement in activity for the Pt_3La alloy over that of pure Pt, as well as high stability. Pt_3La results, together with a comparison between the behaviour of Pt_3La and the Pt_5La samples, and a discussion about the stability of these catalytic surfaces will be assessed below.

3.3 Active chemical state and surface stability

In order to follow the chemical state of the catalytic surfaces, AR-XPS was performed before and after all the preparation and testing steps of this study. The shapes of the La 3d and Ce 3d peaks in particular provide useful diagnostic information, despite the high level of complexity which is typical of the lanthanide metals. The presence of localized electrons in the 5d or 4f shells generates intense shake-up satellites in the 3d region of the La and Ce spectrum; their relative intensity and energy position are strongly dependent on the chemical state.[54] The origin of such behaviour has been addressed by various studies and can be well described by the Schönhammer–Gunnarsson treatment.[55] The La and Ce initial state as well as the final state, excited by photoelectron emission, cannot be described with a single electron approximation and a many-body description is required. Both systems are described as the linear combination of different f^n states, where n is the electron occupancy of the 4f shell. These valence orbitals and in particular the 4f orbitals affect the level of screening of the core-hole and, as a result, the observed energy position of the 3d lines. A higher number of electrons in this 4f shell better screens the photoemitted electron from the core hole, resulting in a higher kinetic energy. In the spectra shown in Fig. 3 the La 3d and Ce 3d signals were fitted according to the assignment of f^n states reported in the literature.[44,56,57] Defining f^n as the predominant component of each lanthanide in the ground state, elemental La (valence electron configuration $5d_16s_2$) is predominantly composed of the $n = 0$ state, while for Ce ($4f_15d_16s_2$) the one electron occupancy of the 4f shell gives $n = 1$. For the interest of this study, it should be noted that these main peaks are the most intense in the metallic state and in intermetallic compounds; weaker satellites arise from the f^1 state in the case of La and from the f^0 and f^2 states in the case of Ce.[57] The charge transfer occurring during oxidation shifts the position of these states and, remarkably, results in a strong intensification of the f^0 satellite for La, and of the f^1 and f^2 satellites for Ce providing a clear diagnostic tool.[43,44,54]

Fig. 3a and b shows the La 3d and Ce 3d XPS peaks measured during sputtering of Pt_5La and Pt_5Ce respectively. Analogous results were obtained for Pt_3La and are presented in Fig. S11† together with the details of the fitting parameters (see ESI†). The shape of the 3d peaks is metallic; the f^n peak accounts for most of the intensity with distinctive visible f^{n+1} satellites at lower binding energies. The overall spectra resemble those measured on similar compounds, such as Pd_3La, Ni_5La, Pd_3Ce, Pd_5Ce and Ni_5Ce.[57–60] The well screened f^{n+1} satellites are strengthened compared to pure La or pure Ce as typical for such alloys.

It turns out that the chemical state of such reactive metals cannot be maintained while transferring the electrodes from UHV to air and to the acidic electrolyte for the electrochemical measurements. As shown in Fig. 3c and d, the La 3d and Ce 3d peaks drastically vary as a consequence of one hour long air exposure. Despite the very negative heat of alloy formation, there is an even stronger driving force towards the surface oxidation.[3] As described in the literature,[44,61] all peaks shift to higher binding energies and the satellite peaks grow in intensity: in some cases becoming even more intense than the principal ones. Similar effects were also measured after few seconds of air exposure, indicating that the surface is always oxidized before introduction into the electrolyte, even if protected by a drop of Milli-Q water.

Concerning Pt_5Ce, the fit of the Ce oxide phase is in general complicated by the presence of trivalent Ce from Ce_2O_3 and tetravalent Ce from CeO_2 overlapping to the metallic peaks. The intense f^0 components, which is absent for trivalent Ce,[44,62] suggest CeO_2 as the main oxidized phase. Therefore, for

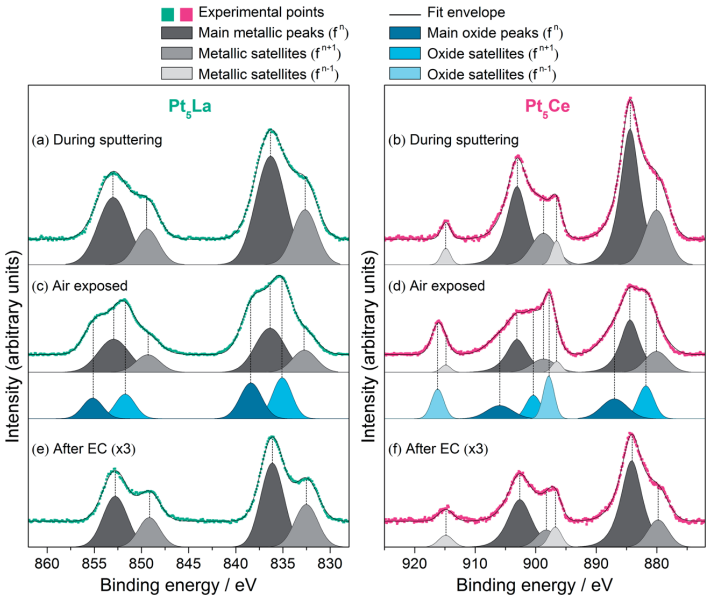

Fig. 3 XPS spectra of Pt_5La (left) and Pt_5Ce (right) at an average emission angle of 45°. For each alloy the spectra were acquired under three different conditions: during sputter-cleaning (a and b), after one hour long air exposure (c and d), and after electrochemical measurements (e and f). The measurements after electrochemical measurements were magnified three times due to the lower signal intensity. Fitted spectra of the metallic peaks (grey) and of the oxidized peaks (blue) appear under the experimental points. Details of the peak positions and relative intensities are found in Table S2.†

simplicity, in the fit of Fig. 3d only the CeO_2 phase was considered. This gave an oxide spectrum similar to the one of previously reported fits[44,56] and a sufficiently good agreement with the experimental data. A full quantification of the oxide components is complicated by the possible presence of sub-oxides and is beyond the interest of this study. Table S2† summarizes the intensity ratios of the main peaks and satellites. Remarkably the amount of oxidized La relative to the total La signal is similar for both Pt_3La and Pt_5La, indicating a similar level of surface oxidation.

AR-XPS spectra were taken after electrochemical measurements. Due to the mentioned surface instability of the alloyed lanthanides, only the spectra of Fig. 3e and f can provide direct information on the chemical state and structure of the active catalysts. In this case the La 3d and Ce 3d spectra are completely metallic, similar to those measured during sputtering. The disappearance of the oxide peaks suggests that any oxide phase is unstable under ORR conditions and dissolves in the acidic electrolyte. At the same time, the conservation of the metallic peaks during the air-exposure between the EC cell and the XPS setup indicates the presence of a protective layer, preventing the lanthanides from air contact and oxidation. The Pt enriched surface resulting from the dissolution of the oxides is expected to provide this kind of protection. A careful comparison with the XPS on sputter cleaned samples provides further information; despite the overall similarities the intensity ratios between the main peaks and the satellites show a slight intensification of the f^{n+1} satellites for La and of the f^{n-1} satellites for Ce (see Fig. 3e and f and S11†); since this intensification is typical of La and Ce alloys,[57,59] it could be associated with the removal of surface La (or Ce) atoms which would be under-coordinated to Pt atoms. For all these considerations no metallic La or Ce should be expected on the surface of these electrochemically tested alloys.

By discerning the XPS spectra at different emission angles, AR-XPS is a powerful technique for reconstructing the surface structure of these catalysts. Fig. 4a and b shows how the catalyst composition changes as a function of the analyser acceptance angle. The presence of a Pt overlayer explains the increase in the Pt to La and Pt to Ce ratios, from the initial values measured during sputtering. This is particularly evident for higher angles due to the higher surface sensitivity. Fig. 4c and d represents the correspondent calculated depth profiles of Pt_5La and Pt_5Ce after electrochemistry. Both catalysts exhibit the formation of a thick Pt overlayer, which has been already described for other de-alloyed surfaces,[7,8,14,33,49] including Pt_3Co, Pt_3Ni, Pt_3Y, Pt_5Y and Pt_5Gd. The formation of this structure from the initial sputter-cleaned surface is illustrated in Fig. 4e for Pt_5Ce.

It should be noted that AR-XPS profiles represent an average over a 400 μm wide region of the crystals and over a depth of a few electron mean free paths ($\lambda \approx 10$ Å).[63] Therefore the presence of surface La or Ce atoms on some parts of the samples, which might be inhomogeneous due to their polycrystalline nature, cannot be excluded. In contrast LEIS only probes the outmost layer composition, hence allowing us to rule out this

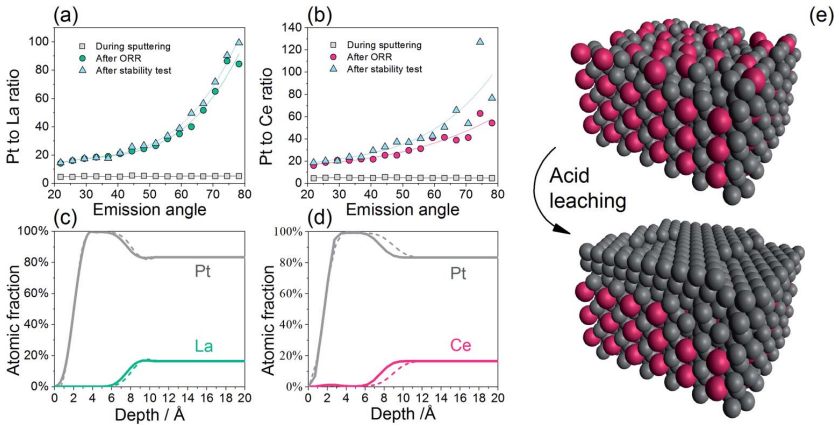

Fig. 4 Pt to lanthanide atomic ratios in Pt_5La (a) and Pt_5Ce (b) from AR-XPS under three different conditions: during sputter-cleaning (□), after electrochemical ORR testing (○) and after stability test (△). Corresponding AR-XPS depth profiles of Pt_5La (c) and Pt_5Ce (d), after the ORR activity test (solid line) and after the stability test (dashed line). An illustrative three-dimensional view of the Pt_5Ce structure after sputter-cleaning (e) and after ORR activity test with the formation of a Pt overlayer on top of the Pt_5Ce bulk alloy (f). Grey and red spheres represent Pt and Ce atoms respectively.

possibility. Fig. 5 shows the LEIS spectra acquired on Pt_5Ce after electrochemical ORR testing at different times. The spectrum of the sputter-cleaned surface is also reported for comparison, showing the typical energy positions of the ions backscattered from Pt ($E_K \approx 680$ eV) or from Ce ($E_K \approx 580$ eV). The very first scans (not shown) are dominated by the background originating from adventitious O and C surface contamination accumulated between the electrochemical measurements and the transfer to UHV. The progressive cleaning of the surface induced by the Ne^+ ions allows to clearly see the Pt peak after 18 minutes. At this time no Ce peaks can be seen. At increasing times and higher levels of ion sputtering on the surface, weak peaks from Ce start arising and the ratio of the peak areas progressively approaches the one measured on sputter-cleaned samples which is similar to the stoichiometric ratio. A plot of the estimated areas as a function of the sputtering time is shown in Fig. S12.† These observations prove the existence of a complete Pt overlayer, for which bifunctional effects are unlikely.

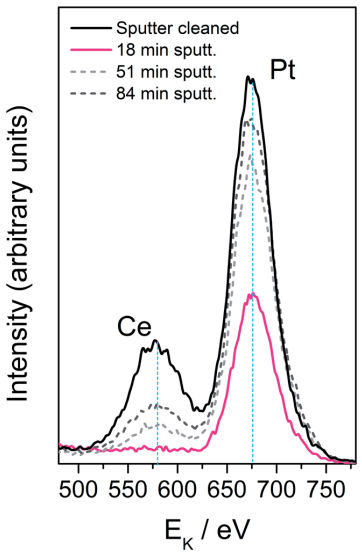

Fig. 5 LEIS spectra of Pt_5Ce after ORR testing for different sputtering times and comparison with the sputter-cleaned reference surface.

3.4 Stability

The stability of the alloys under ORR conditions was tested by applying 10 000 consecutive cycles from 0.6 to 1.0 V *vs.* RHE in an O_2-saturated 0.1 M $HClO_4$ electrolyte at 100 mV s^{-1} and 23 °C. The choice of this standard accelerated stability test was based on the protocols of the U.S. Department Of Energy[64] and of the Fuel Cell Commercialization Conference of Japan.[19] CVs from 0.6 to 1.0 V *vs.* RHE in an O_2-saturated 0.1 M $HClO_4$ electrolyte at 50 mV s^{-1} were taken before and after this procedure in order to compare the ORR activity (not shown). Both for Pt_5La and Pt_5Ce the losses in kinetic activities are remarkably low: around 8% for Pt_5La and 10% for Pt_5Ce, respectively. This is a further proof of the long-term stability of alloys of Pt with lanthanide metals, as shown recently for Pt_5Gd.[33] Fig. 6 shows the total activity enhancement for Pt_5La and Pt_5Ce, as compared to polycrystalline Pt and Pt_5Gd,[33] before and after the stability test, measured under the same conditions. As can be seen, after 10 000 potential cycles under the above described conditions, for both catalysts the final specific activity is still more than 3 times higher than for pure Pt. Very recently, Todoroki *et al.* studied the stability of Pt-enriched Ni/Pt(111) catalysts. Interestingly, although their ORR activity was 8 times higher than that of pure Pt(111), after only

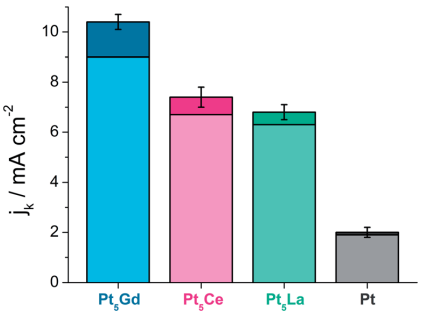

Fig. 6 Kinetic current density (per geometric surface area) measured at 0.9 V of Pt_5Gd,[33] Pt_5Ce, Pt_5La and Pt before and after a stability test consisting of 10 000 cycles between 0.6 and 1.0 V *vs.* RHE in an O_2-saturated 0.1 M $HClO_4$ electrolyte at 100 mV s^{-1}.

1000 potential cycles between 0.6 and 1.0 V they lost the 75% of their initial activity.[65] Previous studies on state-of-the-art Pt_3Co cathode catalysts for PEMFCs also show a substantial degradation of these catalysts under fuel-cell reaction conditions, mainly due to the dealloying of the Pt_3Co particles at the cathode.[15,66] The enhancement in activity and stability for both Pt_5Ce and Pt_5La as compared to pure Pt show that these alloys are very promising as cathode catalysts for PEMFCs. However, it should be anticipated that the chemical synthesis of Pt–La or Pt–Ce alloys in the nanoparticulate form, more suitable for their application in PEMFCs, will be technologically challenging, due to the high reactivity of lanthanide metals and the difficulties of reducing them by chemical-electrochemical techniques.

New AR-XPS measurements were acquired after the stability test. The comparison with the spectra achieved just after the ORR measurements provides useful information regarding the changes in the structure and composition which might occur during cycling. The aspect of the La 3d and Ce 3d peaks is very similar to the one observed in Fig. 3 after EC measurements. This indicates that no big changes in the chemical state of these reactive metals occur, as shown in Table S2.† The Pt overlayer still provides kinetic stability against their dissolution. Fig. 4a and b shows further changes on the catalyst composition after stability tests. By comparing the concentration ratios after ORR testing and after the stability test it is possible to notice a further increase, indicating a slight thickening of the Pt overlayer. AR-XPS depth profiles of Pt_5La and Pt_5Ce (Fig. 4c and d) accordingly exhibit small increments in the Pt overlayer thicknesses. For both alloys, and in particular for Pt_5La, these changes are very modest, demonstrating the high structural stability of these alloys.

4. Discussion

4.1 Surface stability and active chemical state

The XPS spectra of Fig. 3 have clearly demonstrated the inherent surface instability of Pt–La and Pt–Ce alloys under air exposure. The tendency towards the surface oxidation of La and Ce prevails; this is despite the very negative heat of formation of such compounds stabilised by the high alloying temperatures. The metallic components of the La 3d and Ce 3d still account for most of the XPS signal (see Table S2†) indicating that the presence of the alloy introduces kinetic barriers against deep oxidation, while pure La or Ce would quickly form a thick oxide layer.[67,68]

Our evidence clearly differs from the recent results and conclusions of Yoo *et al.* on Pt_3La.[37] They claim that La atoms are stable on the surface of Pt_3La under reaction conditions. However, the peak shape and position of their La 3d peaks resemble those of the La oxide peaks shown in Fig. 3c and S11,† with absent or negligible metallic components. It turns out that these spectra are characteristic of compounds where La is in an oxidized state, with f^{n+1} satellite components almost as intense as the main La 3d peaks.[43,61,69] This consideration, as well as the fact that no explicit details about the purity of the synthesized alloys or any surface cleaning procedures are given in their work[37] suggest the presence of oxygen on the surface and the formation of a rather thick La oxide layer. It is also worth noting that the XRD trace that Yoo *et al.* report suggests that their Pt_3La phase is a solid solution with the same crystal structure as Pt, albeit with some lattice strain.[70,71] In a Pt_3La solid solution, although the bulk composition may be constant, there would be random substitution of Pt and La at any given atomic coordinate. A stable solid solution typically forms in metal compounds where there are weak interactions between the different constituent atoms. However, the strong interaction between Pt and La would provide a significant driving force to form an ordered intermetallic compound; in such a compound the number of La–La nearest neighbours would be minimised and the number of Pt–La nearest neighbours would be maximised. Notably, the phase diagrams of Pt–La intermetallic compounds found in the literature do not report the existence of a stable Pt_3La phase.[46–48] This is in agreement with our XRD measurements on Pt_3La (Fig. S1†), composed of a mixture of two phases: Pt_2La and Pt_5La. In our view, the reason for which a meta-stable solid solution was formed under Yoo *et al.*'s experimental conditions is that they prepared their compounds by magnetron sputtering at room temperature, without any additional heat treatment. On this basis, the low stability of Yoo *et al.*'s Pt_3La solid solution towards air oxidation is unsurprising.

According to the XPS data (Fig. 3e and f, 4c and d and S11†), both the La oxide and metallic La are dissolved from the near-surface region under ORR conditions. Simple thermodynamic considerations provide an intuitive explanation for this phenomenon. First focusing on Pt_5La, the instability of the oxide layer is trivial to explain: La_2O_3 is thermodynamically unstable against dissolution to La^{3+} at pH 0.[35] Moreover, metallic La is also unstable under these conditions. The standard dissolution potential of a La atom to La^{3+} is −2.38 V *vs.* the standard hydrogen electrode (SHE).[72] Accounting for the three electrons involved in the reaction, the resulting standard Gibbs free energy of dissolution of a La atom would be around −7.1 eV at 0 V SHE. The standard Gibbs free energy of formation ($\Delta G_{Pt5La} = -3.8$ eV)[28] partially stabilizes the La atoms, lowering the standard Gibbs free energy of dissolution to −3.3 eV. The

corresponding standard reduction potential is still −1.1 V *vs.* SHE. For Pt_5Ce a similar analysis results in a standard reduction potential of Ce^{3+} to Ce of −1.1 V, essentially the same as for Pt_5La. These values are 2.1 V lower than the potential a fuel cell cathode may reach during shut down. At that potential, there is a strong driving force of about −6.3 eV for the dissolution of La and Ce, despite the very negative heat of alloy formation. Hence no La and Ce atoms should be present on the surface of these catalysts. Despite the different preparation technique described by Yoo *et al.*[37] for Pt_3La, it is very unlikely that any kind of pure Pt–La phase could overcome this huge driving force towards dissolution of the La atoms from the surface; a tendency that seems to be independent of the bulk structure. This is even more unlikely in the absence of any stabilising heat treatment.

On the other hand, the Pt overlayer, formed by the dissolution of the lanthanide metals from the first few monolayers of the alloy, provides kinetic stability to the catalyst. The diffusion of La or Ce would be very slow through the overlayer, due to the strong Pt–La and Pt–Ce interactions. On the other hand, Pt_3La continuously corrodes. We ascribe this difference to the presence of multiple phases in the XRD pattern of Pt_3La. We previously demonstrated the influence of stoichiometry on the stability of Pt_xY phases:[49] Pt_2Y and PtY, in particular, heavily corroded. We anticipate a similar behaviour for the Pt_2La phase. Others have made similar observations for alloys of Pt and late transition metals, when the concentration of the less noble metal is relatively high.[73,74] The high activity and stability of Pt_5La and Pt_5Ce, in comparison to Pt_3La, outlines the importance of comprehensive physical characterization to identify the most active and stable phases.

4.2 Mechanism of activity enhancement

An approximate thickness of the Pt overlayer of around 6–7 Å can be gauged from the angle-resolved depth profiles of Fig. 4c and d, on both Pt_5La and Pt_5Ce, respectively. This would correspond to approximately 3 Pt monolayers. Assuming that the overlayer thickness is uniform, ligand effects would be neglibible.[75] It should be noted, however, that the XPS technique averages over a large area, whose homogeneity is not certain. Furthermore, the algorithms analysing the AR-XPS data are rather sensitive to uncertainties on the sensitivity factors of the peaks used for quantification. Therefore, our data cannot provide a more precise estimation of the Pt overlayer thickness.

The thick Pt overlayers shown in Fig. 4c and d suggest that the high ORR activity is due to strain effects. This notion is supported by the data shown in Fig. 7, which shows that the ORR activity of Pt_5La, Pt_5Ce and Pt_5Gd is correlated with the lattice parameter *a*. We recently proposed that the structure of the overlayer would resemble closely packed Pt, as suggested by our DFT calculations on Pt_5La.[3] A similar behaviour has been experimentally observed on single crystal Pt_5Y that, in a vacuum, forms a compressed Pt overlayer on top of the alloy.[76] In acid electrolyte, *in situ* STM studies on Pt–Fe alloys have also shown the formation of a closely packed Pt overlayer, resembling Pt(111).[77] For this kind of structure the Pt–Pt distance in the overlayer would be correlated with the distance of the closest Pt nearest neighbours in the bulk, d_{Pt-Pt}.[3,33] In the case of Pt_5La, Pt_5Ce and Pt_5Gd it turns out that $d_{Pt-Pt} = a/2$. Consequently, a lower value of *a* suggests increased compressive strain to the surface and higher ORR activity. We note that in a thick Pt overlayer, the strain may relax somewhat, relative to the bulk.[13,78] In the future, we will aim to more accurately quantify the actual strain in the surface overlayer.

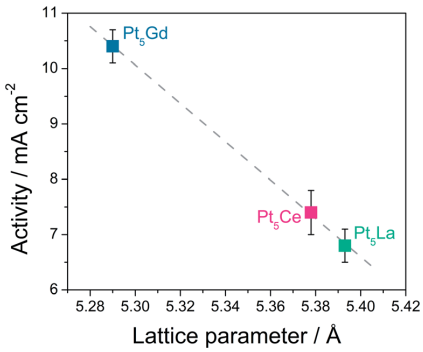

Fig. 7 Experimental ORR activity (kinetic current density per geometric surface area at 0.9 V *vs.* RHE) of polycrystalline Pt_5La, Pt_5Ce, Pt_5Gd[33] *versus* the lattice parameter *a* of the alloys as determined from XRD measurements. The dotted line is a linear fit of the points.

5. Conclusions

This study addresses the electrochemical properties of three ORR catalysts: Pt_5La, Pt_3La and Pt_5Ce, the latter being reported here, for the first time, as a highly active ORR catalyst. Both Pt_5La and Pt_5Ce exhibited a more than 3-fold activity improvement, relative to Pt, with only minor losses after accelerated stability tests. This suggests that they are promising materials for future implementation in PEMFCs. In contrast, we found that the catalyst with a nominal composition of Pt_3La tended to corrode.

Despite the strong tendency towards the oxidation of lanthanide metals, AR-XPS shows that in the active phase of the catalyst, La and Ce exist in the metallic form. This powerful technique also showed the formation of a ~3 monolayer thick Pt overlayer, which stabilizes Pt_5La and Pt_5Ce and prevents the further oxidation and dissolution in an electrochemical environment. This evidence is inconsistent with the recent reports by Yoo *et al.* for Pt–La compounds, where La appears in an oxidized state and is also present on the surface of the catalyst.[37] AR-XPS and LEIS experiments, as well as simple thermodynamic considerations rationalise our own results. In the presence of the thick Pt overlayer reported here, only strain effects can explain the enhanced activity of Pt_5La and Pt_5Ce.

Acknowledgements

For funding of this work we gratefully acknowledge the EU PF7's initiative Fuel Cell and Hydrogen Joint Undertaking's project

CathCat (GA 303492), the Danish National Research Foundation's Center for Individual Nanoparticle Functionality (DNRF54) and the Danish Ministry of Science's UNIK initiative CAtalysis for Sustainable Energy (CASE). Particular thanks to associate professor Jens E. T. Andersen for his help in the ICP measurements.

References

1 U. Eberle, B. Müller and R. von Helmolt, *Energy Environ. Sci.*, 2012, **5**, 8780–8798.
2 H. A. Gasteiger, S. S. Kocha, B. Sompalli and F. T. Wagner, *Appl. Catal., B*, 2005, **56**, 9–35.
3 I. E. L. Stephens, A. S. Bondarenko, U. Grønbjerg, J. Rossmeisl and I. Chorkendorff, *Energy Environ. Sci.*, 2012, **5**, 6744–6762.
4 R. R. Adzic, J. Zhang, K. Sasaki, M. B. Vukmirovic, M. Shao, J. X. Wang, A. U. Nilekar, M. Mavrikakis, J. A. Valerio and F. Uribe, *Top. Catal.*, 2007, **46**, 249–262.
5 J. Zhang, M. B. Vukmirovic, Y. Xu, M. Mavrikakis and R. R. Adzic, *Angew. Chem., Int. Ed.*, 2005, **44**, 2132–2135.
6 F. T. Wagner, B. Lakshmanan and M. F. Mathias, *J. Phys. Chem. Lett.*, 2010, **1**, 2204–2219.
7 V. Stamenkovic, B. S. Mun, K. J. J. Mayrhofer, P. N. Ross, N. M. Markovic, J. Rossmeisl, J. Greeley and J. K. Nørskov, *Angew. Chem.*, 2006, **118**, 2963–2967.
8 V. R. Stamenkovic, B. S. Mun, K. J. J. Mayrhofer, P. N. Ross and N. M. Markovic, *J. Am. Chem. Soc.*, 2006, **128**, 8813–8819.
9 V. R. Stamenkovic, B. Fowler, B. S. Mun, G. Wang, P. N. Ross, C. A. Lucas and N. M. Marković, *Science*, 2007, **315**, 493–497.
10 V. R. Stamenkovic, B. S. Mun, M. Arenz, K. J. J. Mayrhofer, C. A. Lucas, G. Wang, P. N. Ross and N. M. Markovic, *Nat. Mater.*, 2007, **6**, 241–247.
11 K. J. J. Mayrhofer, K. Hartl, V. Juhart and M. Arenz, *J. Am. Chem. Soc.*, 2009, **131**, 16348–16349.
12 L. Gan, R. Yu, J. Luo, Z. Cheng and J. Zhu, *J. Phys. Chem. Lett.*, 2012, **3**, 934–938.
13 H. L. Xin, J. A. Mundy, Z. Liu, R. Cabezas, R. Hovden, L. F. Kourkoutis, J. Zhang, N. P. Subramanian, R. Makharia, F. T. Wagner and D. A. Muller, *Nano Lett.*, 2012, **12**, 490–497.
14 M. Watanabe, K. Tsurumi, T. Mizukami, T. Nakamura and P. Stonehart, *J. Electrochem. Soc.*, 1994, **141**, 2659–2668.
15 S. Chen, H. A. Gasteiger, K. Hayakawa, T. Tada and Y. Shao-Horn, *J. Electrochem. Soc.*, 2010, **157**, A82–A97.
16 D. F. van der Vliet, C. Wang, D. Tripkovic, D. Strmcnik, X. F. Zhang, M. K. Debe, R. T. Atanasoski, N. M. Markovic and V. R. Stamenkovic, *Nat. Mater.*, 2012, **11**, 1051–1058.
17 I. E. L. Stephens, A. S. Bondarenko, F. J. Perez-Alonso, F. Calle-Vallejo, L. Bech, T. P. Johansson, A. K. Jepsen, R. Frydendal, B. P. Knudsen, J. Rossmeisl and I. Chorkendorff, *J. Am. Chem. Soc.*, 2011, **133**, 5485–5491.
18 C. Wang, M. Chi, D. Li, D. Strmcnik, D. van der Vliet, G. Wang, V. Komanicky, K.-C. Chang, A. P. Paulikas, D. Tripkovic, J. Pearson, K. L. More, N. M. Markovic and V. R. Stamenkovic, *J. Am. Chem. Soc.*, 2011, **133**, 14396–14403.
19 A. Ohma, K. Shinohara, A. Iiyama, T. Yoshida and A. Daimaru, *ECS Trans.*, 2011, **41**, 775–784.
20 J. Greeley, I. E. L. Stephens, A. S. Bondarenko, T. P. Johansson, H. A. Hansen, T. F. Jaramillo, J. Rossmeisl, I. Chorkendorff and J. K. Nørskov, *Nat. Chem.*, 2009, **1**, 552–556.
21 J. K. Nørskov, J. Rossmeisl, A. Logadottir, L. Lindqvist, J. R. Kitchin, T. Bligaard and H. Jónsson, *J. Phys. Chem. B*, 2004, **108**, 17886–17892.
22 J. Rossmeisl, G. S. Karlberg, T. Jaramillo and J. K. Nørskov, *Faraday Discuss.*, 2009, **140**, 337.
23 T. P. Johansson, E. T. Ulrikkeholm, P. Hernandez-Fernandez, P. Malacrida, H. A. Hansen, A. S. Bandarenka, J. K. Nørskov, J. Rossmeisl, I. E. L. Stephens and I. Chorkendorff, *Top. Catal.*, 2013, 1–10.
24 R. A. Walker and J. B. Darby Jr, *Acta Metall.*, 1970, **18**, 1261–1266.
25 R. Pretorius, T. K. Marais and C. C. Theron, *Mater. Sci. Rep.*, 1993, **10**, 1–83.
26 R. Hultgren, P. D. Desai, D. T. Hawkins, M. Gleiser and K. K. Kelley, *Selected Values of the Thermodynamic Properties of Binary Alloys*, 1973.
27 H. Kleykamp, *J. Nucl. Mater.*, 1993, **201**, 193–217.
28 K. T. Jacob and Y. Waseda, *Thermochim. Acta*, 1990, **165**, 223–233.
29 K. T. Jacob and Y. Waseda, *Bull. Mater. Sci.*, 1990, **13**, 235–244.
30 G. H. Jóhannesson, T. Bligaard, A. V. Ruban, H. L. Skriver, K. W. Jacobsen and J. K. Nørskov, *Phys. Rev. Lett.*, 2002, **88**, 255506.
31 T. Bligaard, G. H. Jóhannesson, A. V. Ruban, H. L. Skriver, K. W. Jacobsen and J. K. Nørskov, *Appl. Phys. Lett.*, 2003, **83**, 4527–4529.
32 J. Nørskov, J. Greeley, I. Stephens, A. S. Bondarenko, T. Johansson, H. A. Hansen, T. Jaramillo, J. Rossmeisl and I. Chorkendorff, Platinum and Palladium Alloys Suitable as Fuel Cell Electrodes, *U.S. Patent* No. 20,120,214,083, 2012.
33 M. Escudero-Escribano, A. Verdaguer-Casadevall, P. Malacrida, U. Grønbjerg, B. P. Knudsen, A. K. Jepsen, J. Rossmeisl, I. E. L. Stephens and I. Chorkendorff, *J. Am. Chem. Soc.*, 2012, **134**, 16476–16479.
34 P. C. K. Vesborg and T. F. Jaramillo, *RSC Adv.*, 2012, **2**, 7933–7947.
35 M. Pourbaix, *Atlas of electrochemical equilibria in aqueous solutions*, Nat'L Assoc. Of Corrosion, [S.l.], 1974.
36 S. J. Yoo, K.-S. Lee, S. J. Hwang, Y.-H. Cho, S.-K. Kim, J. W. Yun, Y.-E. Sung and T.-H. Lim, *Int. J. Hydrogen Energy*, 2012, **37**, 9758–9765.
37 S. J. Yoo, S. J. Hwang, J.-G. Lee, S.-C. Lee, T.-H. Lim, Y.-E. Sung, A. Wieckowski and S.-K. Kim, *Energy Environ. Sci.*, 2012, **5**, 7521–7525.
38 S. J. Hwang, S.-K. Kim, J.-G. Lee, S.-C. Lee, J. H. Jang, P. Kim, T.-H. Lim, Y.-E. Sung and S. J. Yoo, *J. Am. Chem. Soc.*, 2012, **134**, 19508–19511.
39 A. S. Bandarenka, A. S. Varela, M. Karamad, F. Calle-Vallejo, L. Bech, F. J. Perez-Alonso, J. Rossmeisl, I. E. L. Stephens and I. Chorkendorff, *Angew. Chem., Int. Ed.*, 2012, **51**, 11845–11848.

40 M. Teliska, V. S. Murthi, S. Mukerjee and D. E. Ramaker, *J. Electrochem. Soc.*, 2005, **152**, A2159–A2169.
41 P. B. Balbuena, D. Altomare, N. Vadlamani, S. Bingi, L. A. Agapito and J. M. Seminario, *J. Phys. Chem. A*, 2004, **108**, 6378–6384.
42 Y. Xu, A. V. Ruban and M. Mavrikakis, *J. Am. Chem. Soc.*, 2004, **126**, 4717–4725.
43 A. M. de Asha and R. M. Nix, *Surf. Sci.*, 1995, **322**, 41–50.
44 M. Juel, S. Martinsen and S. Raaen, *Thin Solid Films*, 2008, **517**, 805–810.
45 W. Bronger, *J. Less-Common Met.*, 1967, **12**, 63–68.
46 T. B. Massalski, J. L. Murray, L. H. Bennett and H. Baker, *Binary alloy phase diagrams*, American Society for Metals, 1986.
47 S. Reimann and H.-J. Schaller, *J. Alloys Compd.*, 2006, **419**, 133–139.
48 H. Okamoto, *J. Phase Equilib. Diffus.*, 2008, **29**, 122.
49 I. E. L. Stephens, A. S. Bondarenko, L. Bech and I. Chorkendorff, *ChemCatChem*, 2012, **4**, 341–349.
50 D. F. van der Vliet, C. Wang, D. Li, A. P. Paulikas, J. Greeley, R. B. Rankin, D. Strmcnik, D. Tripkovic, N. M. Markovic and V. R. Stamenkovic, *Angew. Chem.*, 2012, **124**, 3193–3196.
51 K. J. J. Mayrhofer, D. Strmcnik, B. B. Blizanac, V. Stamenkovic, M. Arenz and N. M. Markovic, *Electrochim. Acta*, 2008, **53**, 3181–3188.
52 M. Nesselberger, S. Ashton, J. C. Meier, I. Katsounaros, K. J. J. Mayrhofer and M. Arenz, *J. Am. Chem. Soc.*, 2011, **133**, 17428–17433.
53 U. A. Paulus, A. Wokaun, G. G. Scherer, T. J. Schmidt, V. Stamenkovic, N. M. Markovic and P. N. Ross, *Electrochim. Acta*, 2002, **47**, 3787–3798.
54 J. C. Fuggle, M. Campagna, Z. Zolnierek, R. Lässer and A. Platau, *Phys. Rev. Lett.*, 1980, **45**, 1597–1600.
55 J. W. Allen, S. J. Oh, O. Gunnarsson, K. Schönhammer, M. B. Maple, M. S. Torikachvili and I. Lindau, *Adv. Phys.*, 1986, **35**, 275–316.
56 F. Zhang, P. Wang, J. Koberstein, S. Khalid and S.-W. Chan, *Surf. Sci.*, 2004, **563**, 74–82.
57 J. C. Fuggle, *J. Less-Common Met.*, 1983, **93**, 159–169.
58 L. Schlapbach, *Solid State Commun.*, 1981, **38**, 117–123.
59 J. C. Fuggle, F. U. Hillebrecht, Z. Zołnierek, R. Lässer, C. Freiburg, O. Gunnarsson and K. Schönhammer, *Phys. Rev. B: Condens. Matter Mater. Phys.*, 1983, **27**, 7330–7341.
60 F. U. Hillebrecht and J. C. Fuggle, *Phys. Rev. B: Condens. Matter Mater. Phys.*, 1982, **25**, 3550–3556.
61 W.-D. Schneider, B. Delley, E. Wuilloud, J.-M. Imer and Y. Baer, *Phys. Rev. B: Condens. Matter Mater. Phys.*, 1985, **32**, 6819–6831.
62 A. Pfau and K. D. Schierbaum, *Surf. Sci.*, 1994, **321**, 71–80.
63 S. Tanuma, C. J. Powell and D. R. Penn, *Surf. Interface Anal.*, 1991, **17**, 911–926.
64 The US Department of Energy (DOE), *Energy Efficiency and Renewable Energy* http://www.eere.energy.gov/hydrogenandfuelcells/mypp/pdfs/fuel_cells.pdf *and the US DRIVE Fuel Cell Technical Team Technology Roadmap* http://www.uscar.org/guest/teams/17/Fuel-Cell-Tech-Team, 2013.
65 N. Todoroki, Y. Iijima, R. Takahashi, Y. Asakimori and T. Wadayama, *J. Electrochem. Soc.*, 2013, **160**, F591–F596.
66 F. Maillard, L. Dubau, J. Durst, M. Chatenet, J. André and E. Rossinot, *Electrochem. Commun.*, 2010, **12**, 1161–1164.
67 G. Praline, B. E. Koel, R. L. Hance, H.-I. Lee and J. M. White, *J. Electron Spectrosc. Relat. Phenom.*, 1980, **21**, 17–30.
68 T. L. Barr, *J. Phys. Chem.*, 1978, **82**, 1801–1810.
69 D. D. Sarma, M. S. Hegde and C. N. R. Rao, *J. Chem. Soc., Faraday Trans. 2*, 1981, **77**, 1509–1520.
70 B. C. Beard and P. N. Ross, *J. Electrochem. Soc.*, 1990, **137**, 3368–3374.
71 H. Abe, F. Matsumoto, L. R. Alden, S. C. Warren, H. D. Abruña and F. J. DiSalvo, *J. Am. Chem. Soc.*, 2008, **130**, 5452–5458.
72 *CRC Handbook of Chemistry and Physics*, ed. W. M. Haynes, CRC Press, 93rd edn, 2012.
73 A. Bonakdarpour, J. Wenzel, D. A. Stevens, S. Sheng, T. L. Monchesky, R. Löbel, R. T. Atanasoski, A. K. Schmoeckel, G. D. Vernstrom, M. K. Debe and J. R. Dahn, *J. Electrochem. Soc.*, 2005, **152**, A61–A72.
74 C. Wang, M. Chi, G. Wang, D. van der Vliet, D. Li, K. More, H.-H. Wang, J. A. Schlueter, N. M. Markovic and V. R. Stamenkovic, *Adv. Funct. Mater.*, 2011, **21**, 147–152.
75 J. R. Kitchin, J. K. Nørskov, M. A. Barteau and J. G. Chen, *J. Chem. Phys.*, 2004, **120**, 10240–10246.
76 T. P. Johansson, New Materials for Oxygen Reduction Electrodes, PhD thesis, Department of Physics, Technical University of Denmark, 2012.
77 L.-J. Wan, T. Moriyama, M. Ito, H. Uchida and M. Watanabe, *Chem. Commun.*, 2002, 58–59.
78 P. Strasser, S. Koh, T. Anniyev, J. Greeley, K. More, C. Yu, Z. Liu, S. Kaya, D. Nordlund, H. Ogasawara, M. F. Toney and A. Nilsson, *Nat. Chem.*, 2010, **2**, 454–460.

PCCP

PAPER

View Article Online
View Journal

Towards the elucidation of the high oxygen electroreduction activity of Pt_xY: surface science and electrochemical studies of Y/Pt(111)

Cite this: DOI: 10.1039/c4cp00319e

T. P. Johansson, E. T. Ulrikkeholm, P. Hernandez-Fernandez, M. Escudero-Escribano, P. Malacrida, I. E. L. Stephens* and I. Chorkendorff*

Received 21st January 2014,
Accepted 3rd April 2014

DOI: 10.1039/c4cp00319e

www.rsc.org/pccp

We have prepared an yttrium modified Pt(111) single crystal under ultra-high vacuum conditions, simulating a bulk alloy. A Pt overlayer is formed upon annealing the crystal above 800 K. The annealed structure binds CO weaker than Pt(111), with a pronounced peak at 295 K in the temperature programmed desorption of CO. When depositing a large amount of yttrium at 1173 K, a $(1.88 \times 1.88)R30^\circ$ structure relative to Pt(111) was observed by low energy electron diffraction. Such an electron diffraction pattern could correspond to a $(2 \times 2)R30^\circ$ structure under 6% compressive strain. This structure is in agreement with the structure of the vacancies in a Pt Kagomé layer in Pt_5Y rotated 30° with respect to the bulk of the Pt(111). The Pt overlayer is relatively stable in air; however, after performing oxygen reduction activity measurements in an electrochemical cell, a thick Pt overlayer was measured by the angle resolved X-ray photoelectron spectroscopy depth profile. The activity of the annealed Y/Pt(111) for the oxygen reduction reaction was similar to that of polycrystalline Pt_3Y.

Introduction

Global energy demand is continuously increasing.[1] With limited oil and gas supplies it is desirable to establish an energy economy based on renewable energy.[2] For energy storage much focus has lately been on storing energy in the form of fuels. This could *e.g.* be in the form of alcohols produced from reduction of CO_2,[3,4] ammonia from the reduction of nitrogen[5] or hydrogen from the electrolysis of water.[6] Much attention has recently been put on hydrogen.[7] One of the most promising technologies for utilising the energy stored in hydrogen is the low temperature polymer electrolyte membrane fuel cell (PEMFC). The commercialization of such devices is still hampered by their high cost, which is in part due to the expensive catalysts. In a PEMFC, catalysts are needed for both the hydrogen oxidation (HOR) and the oxygen reduction reactions (ORR). Expensive Pt-based catalysts are typically used for both reactions. However, due to the slow kinetics of oxygen reduction almost ten times more Pt is required on the cathode compared to the anode of the PEMFC.[8] In order for PEMFCs to become viable, improvements in the catalytic activity of the ORR catalyst are still needed.[9–17]

The conditions at the cathode in a PEMFC are extremely corrosive and, therefore, stability issues limit the choice of catalyst materials. The ORR is a complex reaction involving the transfer of 4 protons and 4 electrons.[18] Although pure Pt nanoparticles are typically used for the ORR, the most active catalysts are those formed by a Pt overlayer on Pt bimetallic alloys.[10,19] The oxygen reduction activity of Pt alloys has been studied extensively both on model catalysts (*e.g.* bulk polycrystalline and single crystal surfaces) and on the industrially more relevant nanoparticles, nanostructured thin films and nanoparticle networks.[14,20–24] The increased ORR activity measured on some Pt alloy catalysts is caused by the alloy modifying the Pt overlayer in such a way that ORR intermediates are bound slightly weaker than on pure Pt. The optimal ORR catalyst should bind the ORR intermediates HO* and HOO* ~0.1 eV weaker than pure Pt.[10,25–27] This decrease in binding energy of ORR intermediates can be influenced by two effects, strain effects and ligand effects.[26,28–32] Strain effects are related to the lateral strain of the Pt overlayer, *e.g.* originating from the Pt overlayer being supported on a material with a different lattice parameter. The binding energy of the intermediates on the Pt overlayer is decreased for compressive strain and increased for tensile strain. The ligand effect is related to the modification of the electronic structure of the Pt surface atoms by subsurface atoms of different atomic numbers. Solute atoms must be present in close proximity of the Pt surface atoms in order for the ligand effect to be noticed.[10]

The surface of Pt_3M (M = Ni, Co, Fe, Ti, V) alloys will, under ORR reaction conditions, be terminated by a Pt overlayer.[21]

Center for Individual Nanoparticle Functionality, Department of Physics, Technical University of Denmark, Building 312, DK-2800 Lyngby, Denmark. E-mail: ifan.stephens@fysik.dtu.dk, ibchork@fysik.dtu.dk

When the overlayer is produced by acid leaching the so-called Pt skeleton structure is produced.[21] The skeleton surface on Pt_3M (M = Ni, Co, Fe, Ti, V) alloys is not very well defined, but is reported to consist of 100% Pt in the first layer and a minimum of 75% Pt in the consecutive layers.[21] Markovic and coworkers[20,21,33] found that when annealing bulk Pt_3M (M = Ni, Co, Fe) alloys under ultra-high vacuum (UHV) conditions, platinum atoms from the second layer exchange place with the solute atoms in the surface layer. This leads to a structure with 100% platinum in the first layer, 50% platinum in the second layer and (roughly) 75% platinum in the following layers. Such a structure is denoted as a Pt skin structure.[21]

The above mentioned alloys are not particularly stable during oxygen reduction[14–16] and we therefore made an investigation to find alloys which have a high heat of formation for alloying while at the same time potentially being active for the ORR. In this manner we recently reported Pt_3Y and Pt_3Sc as promising ORR catalyst materials, based on measurements performed on acid leached polycrystalline bulk alloys.[27] The Pt overlayer was formed by acid leaching and found to be similar to the Pt skeleton surfaces reported by Markovic and coworkers.[21,27,34] Notably, on Pt_3Y it was much thicker than we originally anticipated, suggesting that the origin of the activity was somewhat different to our original expectations.

In a recent paper we investigated the possible Pt skin formation on a bulk polycrystalline alloy of Pt_3Sc when annealing it under UHV.[35] An overlayer was demonstrated to be formed, but after testing the ORR activity in an acid electrolyte, a 1–2 monolayer Pt overlayer developed. For both polycrystalline Pt_3Y and polycrystalline Pt_5Y no overlayer formation was observed when annealing under UHV conditions.[36]

In the literature, deposition of some rare earth metals under UHV on Pt(111) has been studied, namely La, Ce and Tm.[37–43] Tang *et al.*,[37] Baddeley *et al.*[38] and Essen *et al.*[43] all studied the growth of thin Ce films on Pt(111) and found that after heat treatment to 770 K, ordered Ce–Pt compounds were formed. Depending on the initial Ce coverage, the following structures, with respect to Pt(111), were observed: (1.96×1.96), (1.94×1.94) with small satellites around the main spots and $(1.96 \times 1.96)R30^{\circ}$. The satellites had a real space periodicity of 10.2 compared to Pt(111). All of these structures were found to be based on the growth of crystalline Pt_5Ce, which is a hexagonal layer structure consisting of alternating layers of Pt_2Ce and the so called Kagomé nets of Pt atoms. The Kagomé net is formed from corner sharing hexagons of close-packed Pt atoms with a missing atom in the center of each set of six Pt atoms.[38,43] Raaen and coworkers measured the desorption temperature of CO for both Ce, La and Tm on Pt(111).[39–42] For all these three systems a downshift on the order of 120 K in desorption temperature of CO was observed, in comparison to Pt(111).

In this paper we use a similar approach to the above mentioned for preparing a Pt overlayer on a Pt–Y sample. We study the structure, reactivity and ORR activity of Y deposited on a Pt(111) single crystal. By investigating a single crystal alloy surface, with a well-defined structure and composition, we gain fundamental insight into the reactivity of Pt_xY.[20,26,44–48]

Experimental

UHV setup

The main part of the experiments in this paper was performed in a UHV chamber with a base pressure of 1×10^{-10} mbar, as described earlier.[35,49] The sample, a Pt(111) single crystal 5 mm in diameter and 3 mm thick, was supplied by MaTecK, GmbH, Germany. The sample is held by a "U shaped" 0.38 mm tungsten wire and the temperature is measured using a type K thermocouple which is placed in a hole of the crystal (parallel to the crystal surface). The sample is heated by applying a DC voltage over the tungsten wire and cooled by either pressurised air or liquid nitrogen.

For evaporation of yttrium a thermal yttrium evaporator was constructed and mounted on the chamber. The yttrium evaporator was made by cutting yttrium flakes from a 0.15 mm 99.9% yttrium foil (supplied by Goodfellow) and attaching them to a coil shaped 0.25 mm 99.95% tungsten wire. By applying a voltage on the tungsten wire it was possible to thermally evaporate yttrium. A quartz crystal microbalance (QCM) is mounted in the chamber, enabling deposition rates to be monitored before and after deposition on the sample. The QCM is positioned in the line of sight of the Y evaporator.[36]

The chamber is equipped with different surface science techniques to investigate the properties of the sample surface. Ion scattering spectroscopy (ISS) is performed using He^+ ions, and an acceleration voltage of 1.2 kV. X-ray photoelectron spectroscopy (XPS) utilizes the Al K_α anode (1486.7 eV) of a dual anode X-ray gun. A quadrupole mass spectrometer is used for temperature programmed desorption (TPD) measurements of CO. Saturating the sample is done by dosing 100 Langmuir CO and the heat ramp used is 2 K s^{-1}. The ordering of the surface region can be investigated using low energy electron diffraction (LEED). A high pressure cell (HPC) is attached to the main chamber, enabling high pressure dosing of gases.

Depth profile measurements are performed in a separate UHV chamber by angle resolved X-ray photoelectron spectroscopy (ARXPS). The ARXPS setup is described elsewhere.[34,35]

Electrochemical setup

The electrochemical experiments were performed using a Bio-Logic Instruments' VMP2 potentiostat, controlled by a computer. A standard three-compartment glass cell equipped with an external jacket attached to a water bath with temperature control was used for the experiments. All glassware was cleaned in 96% H_2SO_4 and 30% H_2O_2 (3 : 1 v/v). This was subsequently rinsed several times in hot Millipore water (358 K, >18.2 MΩ cm^{-1}, TOC < 5 ppb). The electrolyte, 0.1 M $HClO_4$ (Merck, Suprapur), was prepared using Millipore water. The counter electrode was a platinum wire and the reference electrode was a Hg/Hg_2SO_4 electrode separated from the working electrode compartment using a ceramic frit. The measurements were conducted at 333 ± 1 K. All potentials in the manuscript are quoted with respect to the RHE and corrected for Ohmic losses. Following each measurement, 0 V *vs.* RHE was established by carrying out the hydrogen oxidation and hydrogen evolution reaction in the

same electrolyte. The Ohmic resistance was evaluated by performing an impedance spectrum with a peak-to-peak amplitude of 10 mV, at frequencies from 1 kHz to 500 kHz; its value was typically *ca.* 20 Ω.

The annealed Y/Pt(111) catalysts prepared under UHV conditions were inserted into the arbor of a rotating ring disk electrode (RRDE) and were immersed into the electrochemical cell under potential control at 0.05 V in a N_2 (N5, Air Products) saturated 0.1 M $HClO_4$ electrolyte. The potential was then constantly cycled between 0.05 V and 1.0 V at 50 mV s^{-1} and 20 mV s^{-1} until a stable cyclic voltammogram was recorded. Afterwards, the ORR activity was measured by cycling the potential between 0 V and 1 V at 50 and 20 mV s^{-1} and 1600 rpm in an O_2 (N55, AGA) saturated electrolyte. The kinetic current density for the oxygen reduction, j_k, has been calculated using the following equation, $1/j = 1/j_k + 1/j_d$, where j is the measured current density and j_d is the diffusion limited current density.

Results

We first investigated whether it is at all possible to make a Pt overlayer on a Pt–Y alloy by deposition of Y on Pt(111). 3 Å of yttrium is deposited on the Pt(111) crystal and the surface segregation is studied as a function of temperature.

The Pt(111) crystal was sputter cleaned, annealed and then kept at 317 K while evaporating 3 Å of Y on to the crystal. Fig. 1 shows the ISS spectrum before and after Y evaporation. Both an Y and a Pt peak are observed in the ISS spectrum after Y deposition. Table 1 shows the concentrations obtained from XPS. The near surface region mainly consists of Pt and Y, while small amounts of C and O were also observed.

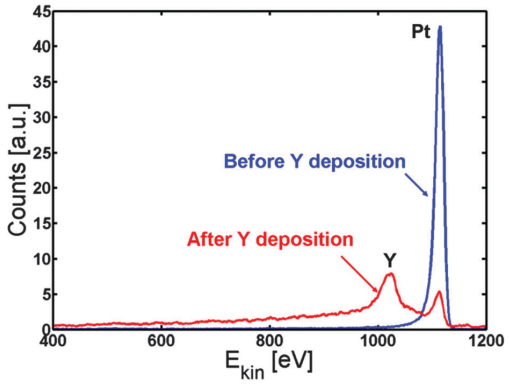

Fig. 1 ISS spectrum of Pt(111) before (blue) and after (red) deposition of Y. According to the QCM measurements, around 3 Å of Y was deposited.

Table 1 Relative concentration of the different elements as obtained by XPS for the 3 Å Y/Pt(111) crystal

	Pt	Y	C	O
After Y dep.	81	11	4	4
After Y dep. and annealing	92	6	1	1

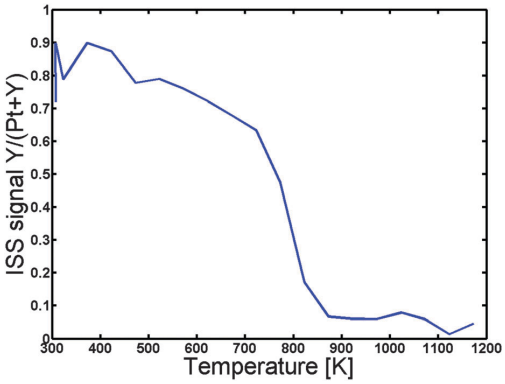

Fig. 2 Y to "Pt + Y" ratio in the surface as a function of temperature. The ratio is obtained by integrating the Pt and Y peaks in ISS for every 50 K using a linear background. No sensitivity factors are used and the ratio should therefore only be considered qualitatively. The ratio decreases significantly at 800 K corresponding to the formation of a Pt overlayer.

In order to establish at what temperature we can achieve inter-diffusion the sample was then heated under UHV at a rate of 2 K s^{-1} in steps of 50 K, and ISS spectra were acquired for each 50 K. Fig. 2 depicts the Y to "Pt + Y" ratio as a function of the temperature. Evidently, the Y to "Pt + Y" ratio exhibits a rapid decrease, corresponding to the formation of a Pt overlayer, at a temperature of around 800 K. The sample was annealed to a maximum temperature of 1173 K and then cooled down to 673 K, where detailed XPS spectra were obtained. The near surface concentration as measured by XPS is given in Table 1.

We have now established that a Pt overlayer is formed upon annealing Y/Pt(111) above 800 K. However, in order to simulate a bulk Pt_xY alloy, we will prepare a much thicker alloy layer.

The Pt(111) sample was cleaned by argon sputtering and annealed to 1273 K. The temperature of the sample was then kept at 1173 K while 90 ± 10 Å (measured on the QCM) of Y was deposited on top of the sample. Evaporating at this elevated temperature ensures that the Y immediately goes to the subsurface and is protected from oxidation by the Pt overlayer. Fig. 3 shows the ISS spectrum before (blue line) and after (red line) Y evaporation. Only Pt was observed in both spectra.

Table 2 shows the relative concentrations obtained by XPS after Y evaporation. A Pt : Y ratio of 4.8 was found, proving that Y is present in the near surface region. Furthermore, the relative concentration of C and O was at the limit of detection. Therefore, the deposition at a higher temperature hinders the formation of yttrium oxide. Combining the results from ISS and XPS gives that the sample consists of a Pt overlayer on top of some Pt–Y system. Assuming the structure to be a single monolayer of Pt on top of a Pt_xY alloy, x was calculated to be 3.7.[36,50]

Images of the LEED patterns obtained before (left image) and after (right image) Y deposition and annealing are shown in Fig. 4. The LEED pattern after deposition at 1173 K consists

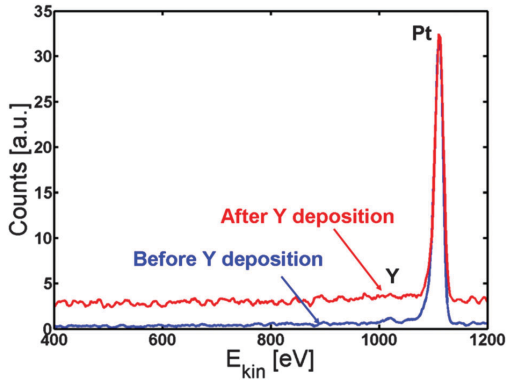

Fig. 3 ISS spectrum before (blue) and after (red) Y deposition. Only Pt is observed, indicating the formation of a Pt skin.

Table 2 Relative concentration of the different elements as obtained by XPS for the 90 Å Y/Pt(111) annealed at 1173 K and 1348 K. Pt/Pt_xY refers to a Pt overlayer on top of Pt_xY

	Annealed at 1173 K	Annealed at 1348 K
Pt	81%	87%
Y	17%	12%
C	1%	0%
O	1%	1%
Pt : Y ratio	4.8	7.3
X assuming Pt/Pt_xY	3.7	5.7

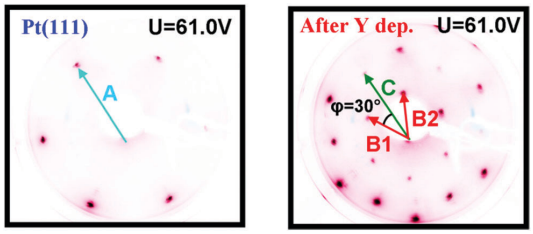

Fig. 4 Images of the LEED patterns of Pt(111) (left, T = 316 K) and of Y/Pt(111) annealed to 1173 K (right, T = 373 K).

of a large hexagon together with a smaller one. Some of the LEED images displayed weak superspots, too low in intensity to enable the analysis of them. The ratio $B1/C$ was measured to be 1.72 ± 0.02, which is close to $\sqrt{3}$, and the angle between $B1$ and C was 30°. Combining vectors $B1$ and $B2$ therefore gives vector C, meaning that the larger hexagon can be constructed from the smaller hexagon. The ratio $A/B1$ was 1.88 ± 0.02 and the angle between A and $B1$ was 30°. Therefore, the annealed Y/Pt(111) showed a $(1.88 \times 1.88)R30°$ structure relative to pure Pt(111). Such a structure could correspond to a $(2 \times 2)R30°$ structure where the lattice is under 6% compressive strain, or a $(\sqrt{3} \times \sqrt{3})R30°$ structure where the lattice is under 9% tensile strain. These possibilities will be considered further in the Discussion section.

100 Langmuir CO was now dosed in order to saturate the surface of the annealed Y/Pt(111). The blue line in Fig. 5 shows

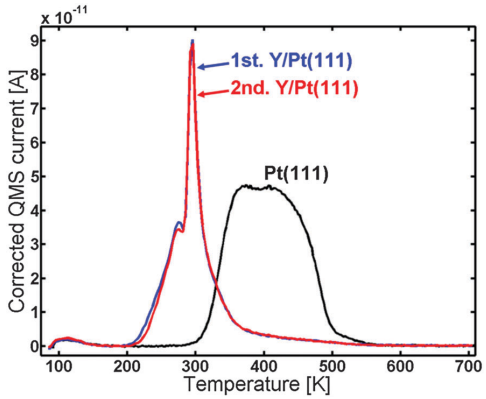

Fig. 5 CO TPD of the Y/Pt(111) sample annealed at 1173 K. The first TPD (blue) and second TPD (red) are compared to the annealed Pt(111) (black). Areas: 1st TPD compared to Pt(111): 0.63, 2nd TPD compared to Pt(111): 0.62.

the CO TPD spectrum of the sample. It is observed that the CO is bound weaker than for Pt(111), with a pronounced sharp peak at around 295 K and a smaller peak at around 275 K. The red line corresponds to the second (repeated) CO TPD of the same sample which was made in order to check the reproducibility. The first and the second TPDs are almost identical.

After the CO TPD experiments, XPS measurements were again carried out, showing the same relative concentrations of Pt, Y, C and O as before, indicating that the surface was stable to the CO TPD.

Since the samples will later be exposed to air it is interesting to evaluate their performance in an oxygen atmosphere. This was tested by dosing 200 mbar O_2 in the HPC for 10 min at 300 K. After oxygen exposure, XPS showed 11% of oxygen on the surface; however, the yttrium 3d peak did not show any oxide feature. A TPD was consequently performed to test if the oxygen would preferably desorb or form yttrium oxide. The temperature was ramped linearly at 2 K s^{-1} from 304 K to 1173 K. Hardly any oxygen was observed in the TPD, which could indicate the formation of yttrium oxide during the temperature ramp. XPS measurements (not shown here) were performed at 1173 K after the CO TPD and showed 5% oxygen. Furthermore, the yttrium 3d region displayed some oxidised feature indicating that yttrium oxide was formed. A CO TPD was also performed and it showed roughly the same features as before oxygen exposure; however, the area under the TPD was 35% smaller. Thus the exposure to air did not cause any oxidation of the yttrium unless it is heated to high temperatures.

The sample was then slightly sputtered in order to remove the formed yttrium oxide, and then annealed to 1348 K. The higher annealing temperature was used in order to obtain a higher degree of ordering on the surface and possibly intensify the weak superspots in the LEED pattern. Fig. 6 shows the LEED image after annealing to 1348 K. The higher annealing temperature enlightened two sets of hexagonal superspots, corresponding to long range ordered structures. The distances B and C,

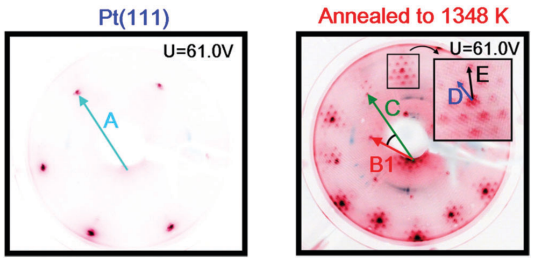

Fig. 6 Images of the LEED patterns of Pt(111) (left, T = 316 K) and of Y/Pt(111) annealed to 1348 K (right, T = 312 K). The increased annealing temperature causes superspots, indicated on the inset zoom by D and E, to appear.

indicated in the LEED pattern, were measured to be the same as in Fig. 4. The ratios A/D and A/E in the two superspot patterns were 10.4 ± 0.5 and 6.4 ± 0.3, respectively. The angle between A and D was 0° and the angle between A and E was 30°. Therefore, the superspots correspond to $(6.4 \times 6.4)R30^\circ$ and (10.4×10.4) structures, referring to the original Pt(111) spots. Since $6.4 \cdot \sqrt{3} \approx 11.1$, combining vectors from the smaller superspots roughly gives the larger superspots, meaning that the E hexagon could be interpreted as a higher order diffraction of D.

The blue line in Fig. 7 shows the CO TPD of the sample after annealing to 1348 K. The TPD displayed the same features as the one annealed to 1173 K; however, the very distinct peak at 295 K was lower in intensity and possessed a bit broader shoulder to the right of it. The CO TPD was repeated two times and showed very good reproducibility.

Table 2 lists the concentrations of Pt, Y, C and O obtained by XPS after annealing to 1348 K. The higher annealing temperature caused an increase in the Pt : Y ratio. Assuming a Pt overlayer on a Pt_xY structure gives x = 5.7.

Afterwards, the sample was taken out of the chamber to measure its oxygen reduction activity. Angle resolved X-ray photoelectron spectroscopy (ARXPS) experiments were carried out *ex situ*

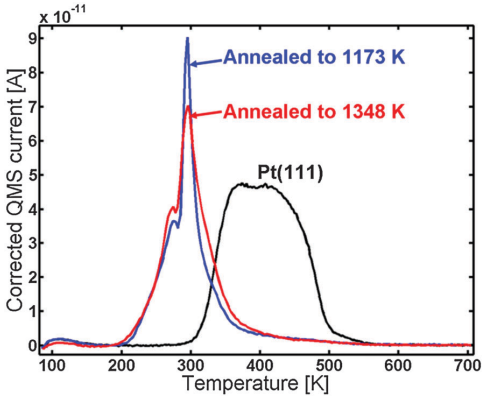

Fig. 7 CO TPD of the Y/Pt(111) after annealing to 1348 K (red) compared to the sample annealed to 1173 K (blue) and to pure Pt(111) (black).

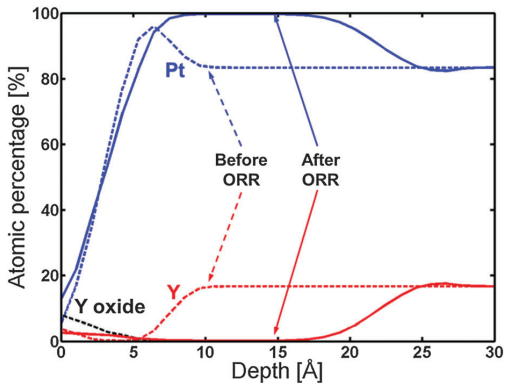

Fig. 8 ARXPS depth profile of the 1348 K UHV annealed Y/Pt(111) before (dashed lines) and after (solid lines) ORR activity measurements. The C and O traces have been omitted for clarity.

in order to produce non-destructive depth profiles of the crystal and follow any changes in the surface composition (the same procedure as we previously used for different Pt alloys[26,34,35,51,52]).

Fig. 8 displays the ARXPS depth profile before electrochemical measurements. Apart from the formation of a small amount of Y oxide on the surface, the presence of a Pt overlayer on top of a Pt_5Y bulk alloy can be observed. This ratio of Pt : Y was chosen on the basis of the XPS measurements shown in Table 2, together with the fact that Pt_5Y is the stable Pt–Y phase with the highest Pt content.[53]

Afterwards, the oxygen reduction activity was measured. Fig. 9 shows the measured activity on a Tafel plot. The activity of the annealed Y/Pt(111) sample is significantly higher than polycrystalline platinum and close to that of the clean sputtered Pt_3Y. Fig. 8 also shows the ARXPS depth profile after ORR activity measurements. The platinum overlayer has substantially grown in thickness. This evidence, together with the disappearance of any Y oxide phase, suggests that yttrium leached out from the surface layers. Therefore, the Pt skin structure prepared under UHV results in a Pt skeleton structure upon ORR activity measurements in an acid electrolyte. This also means that the surface studied

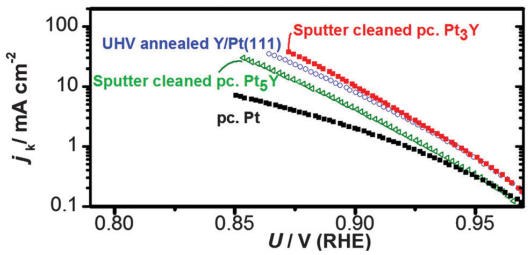

Fig. 9 Tafel plot of the 1348 K UHV annealed Y/Pt(111) sample compared with the sputter cleaned polycrystalline samples of Pt_3Y, Pt_5Y and Pt. Measurements were carried out in O_2-saturated 0.1 M $HClO_4$ at 1600 RPM, T = 333 K and at a scan rate of 50 mV s^{-1}. The current was corrected for mass transport limitations, and normalised according to the geometric surface area.

under UHV conditions is different from the one relevant for the electrochemical experiments. In order to directly correlate measurements done under UHV with electrochemical experiments it would be necessary to have a surface which is stable under reaction conditions.[20,26,54]

Discussion

The ISS data showed that the annealed Y/Pt(111) only has Pt atoms in the surface layer. XPS indicated that Y is present in the near surface region and, if the near surface region is assumed to be composed of a Pt overlayer covering a Pt_xY bulk alloy, x would be roughly 4–6 depending on the annealing temperature.

Fig. 5 shows the CO TPD for the annealed Y/Pt(111) compared to Pt(111). The desorption temperature was clearly shifted down on the annealed Y/Pt(111) compared to Pt(111). The CO TPD of the annealed Y/Pt(111) consisted of a pronounced peak at around 295 K and a smaller peak at around 275 K. The origin of the sharp peak at around 295 K could be due to strong CO–CO interactions on an ordered CO layer on the surface.[55] At around 295 K some of the CO from this ordered structure desorbs, which causes the ordered CO structure to collapse and immediately desorb from the surface.

Since XPS and ISS data indicated the presence of an overlayer consisting of pure Pt on top of a Pt_xY alloy, the decrease in CO desorption temperature can be either related to ligand or strain effects.

In our recent article about UHV annealed polycrystalline Pt_3Sc, the change in desorption temperature of CO was correlated with a change in binding energy of the ORR intermediates, O*, HO* and HOO*.[35] The optimal ORR catalyst should bind HO* ~0.1 eV weaker than pure Pt, which would correspond to a decrease in CO desorption temperature of ~85 K.[56] For the annealed Y/Pt(111) sample, the onset of the CO desorption was shifted down ~100 K compared to Pt(111). The sharp desorption feature at ~295 K is also ~100 K lower than the center of the peak for Pt(111). This places the expected ORR activity for the annealed Y/Pt(111) close to optimal.

The LEED pattern from Fig. 4 indicates that the annealed Y/Pt(111) has a $(1.88 \times 1.88)R30^\circ$ structure relative to Pt(111), which corresponds to a strained surface. The structure could correspond to a $(2 \times 2)R30^\circ$ structure where the lattice is under 6% compressive strain, or a $(\sqrt{3} \times \sqrt{3})R30^\circ$ structure where the lattice is under 9% tensile strain.

Presumably a surface under 6% strain would be more stable than a surface under 9% strain. Furthermore, a surface under tensile strain would increase the binding of intermediates. The weaker binding of CO in the TPD of Fig. 5 is consistent with a surface under compressive, rather than tensile strain. Consequently, it appears that the structure under compressive strain is more likely.

The observed LEED pattern and CO TPD for annealed Y/Pt(111) bare many similarities to those reported in the literature for the deposition of rare earth metals on Pt(111).[37–43] The superspots on Fig. 6 correspond to a long range ordering on the crystal. The appearance of the superspots could be induced by the higher annealing temperature leading to a more ordered surface. However, since the sample was also slightly sputtered between experiments, the superspots could also originate from the border between the bulk Pt(111) and the Pt–Y alloy layer. Tang *et al.* observed similar superspots and attributed this superstructure to the lattice mismatch between the alloy and the Pt(111) substrate.[37]

Considering all of the experiments performed on the annealed Y/Pt(111) under UHV, the most probable structure seems to be a Pt overlayer on top of a Pt_5Y alloy. X-ray diffraction measurements performed by Stephens *et al.*[34] on a bulk polycrystalline Pt_5Y sample show that the bulk structure is not a closely packed structure. The Pt_5Y alloy consists of alternating layers of Pt_2Y and Kagomé nets of Pt atoms, similar to the structure reported for Pt_5Ce.[38,43] However, the structure of the annealed Y/Pt(111) after electrochemical testing is different.

The ARXPS depth profile in Fig. 8 shows that the thickness of the Pt overlayer changed from a few angstroms to around 15 angstroms after electrochemistry. Due to both uncertainties in the sensitivity factor for Y and general uncertainty in the ARXPS measurements, the absolute value for the thickness of the Pt overlayer is indicative. However, the ARXPS clearly showed a dramatic change in the overlayer thickness by a factor of around 5. The Pt overlayer does therefore not provide sufficient protection against dissolution of the yttrium atoms from the subsurface layers. This was also observed for the Pt overlayer on polycrystalline Pt_3Sc, although in that case the post-ORR Pt overlayer thickness was much lower.[35] This indicates that Pt-skin structures do not seem to be stable for alloys of Pt and early transition metals. As a consequence of the observed thick Pt overlayer on the annealed Y/Pt(111) after ORR testing, the measured increase in the ORR activity cannot be explained by the ligand effect and could be attributed to the strain effect.

The fact that yttrium is not stable in the second layer could be due to different effects. One is the high driving force for Y dissolution due to the very negative standard reduction potential of Y ($E_0 = -2.372$ V for $Y \Rightarrow Y^{3+}$).[57] Another is the high affinity of yttrium for oxygen ($\Delta H = -1905$ kJ mol^{-1} or corresponding to a gain of 9.9 eV per yttrium atom for $2Y + 1.5O_2 = Y_2O_3$),[58] which could favour the formation of subsurface oxygen or segregation of Y, leading to a depletion of yttrium.[59–61]

It is interesting to compare the UHV annealed Y/Pt(111) crystal with the UHV annealed Pt_3Sc polycrystalline sample from our earlier work. For scandium the standard reduction potential ($E_0 = -2.077$ V for $Sc \Rightarrow Sc^{3+}$)[57] and affinity for oxygen ($\Delta H = -1908$ kJ mol^{-1} for $2Sc + 1.5O_2 = Sc_2O_3$)[58] are approximately as high as for yttrium. The heat of formation of Pt_3Sc, Pt_3Y and Pt_5Y is also about the same.[27,62] Nevertheless, UHV annealed Pt_3Sc showed little change in the Pt overlayer thickness after ORR measurements, whereas for UHV annealed Y/Pt(111) a thick Pt overlayer was formed. The most striking difference between UHV annealed Pt_3Sc and UHV annealed Y/Pt(111) is the degree of strain. Pt_3Sc is under 0.9% tensile strain whereas UHV annealed Y/Pt(111) is under 3.8% tensile strain, assuming a Pt_3Y structure, or 5% compressive strain,

assuming a Pt_5Y structure. We hypothesise that this difference in the degree of strain is the reason for the difference in stability of the Pt overlayer.

It seems to be quite plausible that the high activity of polycrystalline Pt_3Y could also be due to the formation of a compressed Pt overlayer. Although the bulk Pt–Pt interatomic distance would be greater than that of pure Pt, presumably upon dealloying the surface would more closely resemble Pt_5Y. Our present work shows that a Pt overlayer covering Pt_5Y would likely be under compression. Evidently, this thick, compressed Pt overlayer differs significantly from our original assumptions.

Conclusion

We have studied the structure and activity of annealed Y/Pt(111). Under UHV conditions the structure was a Pt overlayer on top of what appears to be a Pt_5Y alloy. The structure exhibited a clear decrease in the desorption temperature of CO. This structure is, however, not preserved under electrochemical conditions as a thick Pt overlayer is formed. The Pt overlayer does not supply sufficient kinetic stability against yttrium dissolution from the first few atomic layers under ORR conditions. Even so, we anticipate that the strong interaction between Pt and Y would hinder continued dissolution from deeper layers. It seems likely that the Pt overlayer formed is under compressive strain, similar to other alloys of Pt and rare earths.[10,34,51,52] Our future investigations will focus on the elucidation of the Pt overlayer formed under ORR conditions.

Acknowledgements

Funding by the Danish Council for Technology and Innovations FTP program and by the Danish Strategic Research Councils HyCycle program is gratefully acknowledged. P.H.F. acknowledges funding from the Danish Council for Strategic Research in Sustainable Energy and Environment-project "MEDLYS". M.E.E. gratefully acknowledges funding from the EU PF7's initiative Fuel Cell and Hydrogen Joint Undertaking's project CathCat (GA 303492). The Danish National Research Foundation's Center for Individual Nanoparticle Functionality is supported by the Danish National Research Foundation (DNRF54).

Notes and references

1 BP Statistical Review of World Energy June 2013. http://www.bp.com.
2 N. Armaroli and V. Balzani, *Angew. Chem., Int. Ed.*, 2007, **46**, 52–66.
3 E. E. Benson, C. P. Kubiak, A. J. Sathrum and J. M. Smieja, *Chem. Soc. Rev.*, 2008, **38**, 89–99.
4 Y. Hori, K. Kikuchi and S. Suzuki, *Chem. Lett.*, 1985, 1695–1698.
5 B. Hinnemann and J. K. Nørskov, *Top. Catal.*, 2006, **37**, 55–70.
6 J. Rossmeisl, Z.-W. Qu, H. Zhu, G.-J. Kroes and J. K. Norskov, *J. Electroanal. Chem.*, 2007, **607**, 83–89.
7 G. W. Crabtree, M. S. Dresselhaus and M. V. Buchanan, *Phys. Today*, 2004, **57**, 39–44.
8 H. A. Gasteiger, D. R. Baker and R. N. Carter, *Hydrogen Fuel Cells: Fundamentals and Applications.*, Wiley-CPH, 2010.
9 H. A. Gasteiger, S. S. Kocha, B. Sompalli and F. T. Wagner, *Appl. Catal., B*, 2005, **56**, 9–35.
10 I. E. L. Stephens, A. S. Bondarenko, U. Grønbjerg, J. Rossmeisl and I. Chorkendorff, *Energy Environ. Sci.*, 2012, **5**, 6744–6762.
11 A. Rabis, P. Rodriguez and T. J. Schmidt, *ACS Catal.*, 2012, **2**, 864–890.
12 F. T. Wagner, B. Lakshmanan and M. F. Mathias, *J. Phys. Chem. Lett.*, 2010, **1**, 2204–2219.
13 T. Toda, H. Igarashi, H. Uchida and M. Watanabe, *J. Electrochem. Soc.*, 1999, **146**, 3750–3756.
14 L. Dubau, J. Durst, F. Maillard, L. Guétaz, M. Chatenet, J. André and E. Rossinot, *Electrochim. Acta*, 2011, **56**, 10658–10667.
15 L. Dubau, F. Maillard, M. Chatenet, J. André and E. Rossinot, *Electrochim. Acta*, 2010, **56**, 776–783.
16 F. Maillard, L. Dubau, J. Durst, M. Chatenet, J. Andre and E. Rossinot, *Electrochem. Commun.*, 2010, **12**, 1161–1164.
17 S. Chen, H. A. Gasteiger, K. Hayakawa, T. Tada and Y. Shao-Horn, *J. Electrochem. Soc.*, 2010, **157**, A82–A97.
18 J. Rossmeisl, G. S. Karlberg, T. Jaramillo and J. K. Nørskov, *Faraday Discuss.*, 2008, **140**, 337–346.
19 I. Katsounaros, S. Cherevko, A. R. Zeradjanin and K. J. J. Mayrhofer, *Angew. Chem., Int. Ed.*, 2014, **53**, 102–121.
20 V. R. Stamenkovic, B. Fowler, B. S. Mun, G. F. Wang, P. N. Ross, C. A. Lucas and N. M. Markovic, *Science*, 2007, **315**, 493–497.
21 V. R. Stamenkovic, B. S. Mun, M. Arenz, K. J. J. Mayrhofer, C. A. Lucas, G. F. Wang, P. N. Ross and N. M. Markovic, *Nat. Mater.*, 2007, **6**, 241–247.
22 A. Bonakdarpour, K. Stevens, G. D. Vernstrom, R. Atanasoski, A. K. Schmoeckel, M. K. Debe and J. R. Dahn, *Electrochim. Acta*, 2007, **53**, 688–694.
23 Y. Xu, S. Hou, Y. Liu, Y. Zhang, H. Wang and B. Zhang, *Chem. Commun.*, 2012, **48**, 2665–2667.
24 Y. Xu and B. Zhang, *Chem. Soc. Rev.*, 2014, **43**, 2439–2450.
25 J. K. Nørskov, J. Rossmeisl, A. Logadottir, L. Lindqvist, J. R. Kitchin, T. Bligaard and H. Jónsson, *J. Phys. Chem. B*, 2004, **108**, 17886–17892.
26 I. E. L. Stephens, A. S. Bondarenko, F. J. Perez-Alonso, F. Calle-Vallejo, L. Bech, T. P. Johansson, A. K. Jepsen, R. Frydendal, B. P. Knudsen, J. Rossmeisl and I. Chorkendorff, *J. Am. Chem. Soc.*, 2011, **133**, 5485–5491.
27 J. Greeley, I. E. L. Stephens, A. S. Bondarenko, T. P. Johansson, H. A. Hansen, T. F. Jaramillo, J. Rossmeisl, I. Chorkendorff and J. K. Nørskov, *Nat. Chem.*, 2009, **1**, 552–556.
28 M. Mavrikakis, B. Hammer and J. K. Nørskov, *Phys. Rev. Lett.*, 1998, **81**, 2819–2822.
29 J. R. Kitchin, J. K. Nørskov, M. A. Barteau and J. G. Chen, *J. Chem. Phys.*, 2004, **120**, 10240–10246.
30 P. Strasser, S. Koh, T. Anniyev, J. Greeley, K. More, C. F. Yu, Z. C. Liu, S. Kaya, D. Nordlund, H. Ogasawara, M. F. Toney and A. Nilsson, *Nat. Chem.*, 2010, **2**, 454–460.

31 F. Calle-Vallejo, J. I. Martínez, J. M. García-Lastra, J. Rossmeisl and M. T. M. Koper, *Phys. Rev. Lett.*, 2012, **108**, 116103.
32 H. E. Hoster, O. B. Alves and M. T. M. Koper, *ChemPhysChem*, 2010, **11**, 1518–1524.
33 B. S. Mun, M. Watanabe, M. Rossi, V. Stamenkovic, N. M. Markovic and P. N. Ross, *J. Chem. Phys.*, 2005, **123**, 204717.
34 I. E. L. Stephens, A. S. Bondarenko, L. Bech and I. Chorkendorff, *ChemCatChem*, 2012, **4**, 341–349.
35 T. P. Johansson, E. T. Ulrikkeholm, P. Hernandez-Fernandez, P. Malacrida, H. A. Hansen, A. S. Bandarenka, J. K. Nørskov, J. Rossmeisl, I. E. L. Stephens and I. Chorkendorff, *Top. Catal.*, 2014, **57**, 245–254.
36 T. P. Johansson, *New Materials for Oxygen Reduction Electrodes*, PhD thesis, DTU, 2012.
37 J. Tang, J. M. Lawrence and J. C. Hemminger, *Phys. Rev. B: Condens. Matter Mater. Phys.*, 1993, **48**, 15342–15352.
38 C. J. Baddeley, A. W. Stephenson, C. Hardacre, M. Tikhov and R. M. Lambert, *Phys. Rev. B: Condens. Matter Mater. Phys.*, 1997, **56**, 12589–12598.
39 B. Vermang, M. Juel and S. Raaen, *Phys. Rev. B: Condens. Matter Mater. Phys.*, 2006, **73**, 033407.
40 A. Kildemo, A. Juel and S. Raaen, *Surf. Sci.*, 2005, **581**, 133–141.
41 A. Ramstad and S. Raaen, *Phys. Rev. B: Condens. Matter Mater. Phys.*, 1999, **59**, 15935–15941.
42 A. Ramstad, S. Raaen and N. Barrett, *Surf. Sci.*, 2000, **448**, 179–186.
43 J. M. Essen, C. Becker and K. Wandelt, *e–J. Surf. Sci. Nanotechnol.*, 2009, **7**, 421–428.
44 W.-P. Zhou, X. Yang, M. B. Vukmirovic, B. E. Koel, J. Jiao, G. Peng, M. Mavrikakis and R. R. Adzic, *J. Am. Chem. Soc.*, 2009, **131**, 12755–12762.
45 A. S. Bandarenka, A. S. Varela, M. Karamad, F. Calle-Vallejo, L. Bech, F. J. Perez-Alonso, J. Rossmeisl, I. E. L. Stephens and I. Chorkendorff, *Angew. Chem., Int. Ed.*, 2012, **51**, 11845–11848.
46 N. Todoroki, Y. Iijima, R. Takahashi, Y. Asakimori and T. Wadayama, *J. Electrochem. Soc.*, 2013, **160**, F591–F596.
47 S. Brimaud, A. K. Engstfeld, O. B. Alves and R. J. Behm, *J. Electroanal. Chem.*, 2014, **716**, 71–79.
48 R. Yang, P. Strasser and M. F. Toney, *J. Phys. Chem. C*, 2011, **115**, 9074–9080.
49 K. J. Andersson, F. Calle-Vallejo, J. Rossmeisl and I. Chorkendorff, *J. Am. Chem. Soc.*, 2009, **131**, 2404–2407.
50 D. Briggs and M. P. Seah, *Practical Surface Analysis*, John Wiley & Sons Ltd., 1992, vol. 1 Auger and X-ray Photoelectron Spectroscopy.
51 M. Escudero-Escribano, A. Verdaguer-Casadevall, P. Malacrida, U. Grønbjerg, B. P. Knudsen, A. K. Jepsen, J. Rossmeisl, I. E. L. Stephens and I. Chorkendorff, *J. Am. Chem. Soc.*, 2012, **134**, 16476–16479.
52 P. Malacrida, M. Escudero-Escribano, A. Verdaguer-Casadevall, I. E. L. Stephens and I. Chorkendorff, *J. Mater. Chem. A*, 2014, **2**, 4234–4243.
53 B. Predel, Pt-Y (Platinum-Yttrium), in *SpringerMaterials - The Landolt-Börnstein Database*, ed. O. Madelung, 1998, vol. 5I, DOI: 10.1007/10542753_2539.
54 V. R. Stamenkovic, B. S. Mun, K. J. J. Mayrhofer, P. N. Ross and N. M. Markovic, *J. Am. Chem. Soc.*, 2006, **128**, 8813–8819.
55 S. Raaen and A. Ramstad, *Energy*, 2005, **30**, 821–830.
56 M. Ruff, N. Takehiro, P. Liu, J. K. Nørskov and R. J. Behm, *ChemPhysChem*, 2007, **8**, 2068–2071.
57 M. Pourbaix, *Atlas of Electrochemical Equilibria in Aqueous Solutions*, National Association of Corrosion Engineers, Houston, Texas, 1974.
58 Standard thermodynamic properties of chemical substances, in *CRC Handbook of Chemistry and Physics*, ed. W. M. Haynes, CRC Press, Boca Raton, FL, 94th edn, 2013, section 5, pp. 5–17.
59 C. A. Menning and J. G. Chen, *J. Power Sources*, 2010, **195**, 3140–3144.
60 C. A. Menning and J. G. Chen, *Top. Catal.*, 2010, **53**, 338–347.
61 C. A. Menning and J. G. Chen, *J. Chem. Phys.*, 2008, **128**, 164703.
62 A. Palenzona and S. Cirafici, *J. Phase Equilib.*, 1990, **11**, 493–497.

Mass-selected nanoalloys as model catalysts: Pt_xY nanoparticles for oxygen electroreduction

Patricia Hernandez-Fernandez[a], Federico Masini[a], David N. McCarthy[a], Christian E. Strebel[a], Daniel Friebel[c], Davide Deiana[b], Paolo Malacrida[a], Anders Nierhoff[a], Anders Bodin[a], Anna M. Wise,[c] Jane H. Nielsen[a], Thomas W. Hansen[b], Anders Nilsson[c], Ifan E.L. Stephens[a],* Ib Chorkendorff[a*]

[a] Center for Individual Nanoparticle Functionality (CINF), Department of Physics, Technical University of Denmark, Kgs Lyngby DK-2800, Denmark

[b] Center for Electron Nanoscopy (CEN), Technical University of Denmark, Kgs Lyngby DK-2800, Denmark

[c] SLAC National Accelerator Laboratory, 2575 Sand Hill Road, MS31, Menlo Park CA 94025, USA

[*] Corresponding authors

Abstract

Low temperature fuel cells are limited by the oxygen reduction reaction, occurring at the cathode. Their widespread implementation in automotive vehicles requires a decrease in the loading of Pt necessary to catalyse oxygen reduction by alloying Pt with other metals. Pt_xY nanocatalysts should, in principle, exhibit the hitherto unreachable combination of high activity and stability. Herein, we demonstrate the synthesis, characterisation and catalyst testing of Pt_xY nanoparticles prepared through the gas aggregation technique. The catalysts reported here are highly active, with a mass activity of 3.05 Amg_{Pt}^{-1} at 0.9 V versus a reversible hydrogen electrode. State-of-the-art commercial Pt/C exhibits up to ~0.55 Amg_{Pt}^{-1} under similar conditions. Using a variety of characterization techniques, we show that the high activity of Pt_xY is exclusively due to a compressive strain exerted onto the Pt surface atoms by the alloy core.

Introduction

Polymer electrolyte membrane fuel cells (PEMFC's) hold the potential to provide a zero-emission power source for future automotive applications. However, their widespread commercialisation is hindered by the high loadings of Pt required to catalyse the oxygen reduction reaction (ORR) at the cathode. [1-4] An order of magnitude increase in ORR mass activity, i.e. current density per unit mass Pt, over state-of-the art commercial pure Pt catalysts would bring the precious metal loading in fuel cells to a similar level to that used for emission control in internal combustion engines.[3,5] Some alloys of PtX (X =Co, Ni, Cu) show higher ORR

activity in comparison to pure Pt,[1-4] but their long term performance is typically compromised by their poor stability against dealloying.[6,7] New Pt based alloys are required that meet the criteria of both high activity and stability.

In collaboration with Nørskov, Rossmeisl and coworkers, we discovered a new catalyst that could bring us one step closer to this goal.[8] Pt_3Y exhibited the highest ORR activity ever measured on an extended, polycrystalline surface, to the best of our knowledge only surpassed by single crystal $Pt_3Ni(111)$.[9] Subsequent studies from our laboratory show that extended surfaces of polycrystalline Pt_5Y, Pt_5Gd and Pt_5La also exhibited high ORR activity.[3,10,11] The uniquely negative heat of formation of Pt-rare earth alloys should provide them with greater kinetic stability than the more commonly tested alloys of Pt and late transition metals.[8,11,12] This notion is supported by our own stability tests on extended surfaces [11] as well as those of Lim and coworkers on sputtered thin films.[13,14]

To understand the effect of alloying on the ORR activity of Pt, we invoke the theoretical model developed by Nørksov, Rossmeisl and coworkers.[14] The potential losses, or overpotential, for the ORR on pure Pt catalysts originate from the final step in the reaction;[14] the electroreduction of HO* to H_2O (where HO* is an adsorbed hydroxyl intermediate[15]). Pt alloy ORR catalysts are typically encased by an overlayer of pure Pt; the less noble metal will dissolve from the surface.[10,16-22] Alloying Pt decreases the overpotential for the electroreduction of HO* to H_2O by weakening the binding to HO*. The optimal catalyst should have an HO* binding that is ~0.1 eV weaker than Pt(111).[3,23] DFT calculations originally suggested that the activity of Pt_3Y should be contingent upon a substantial concentration of Y in the second surface layer,[8] i.e. ligand effects.[19,24,25] Nonetheless, subsequent experiments showed that the active phases of polycrystalline Pt_3Y and Pt_5Y are encased by a 3-4 monolayer thick overlayer of pure Pt.[10] The considerable thickness of these overlayers excludes the possibility that the enhanced ORR activity of Pt_xY is due to ligand effects.. Consequently, the underlying mechanism for the enhanced activity of Pt_xY alloys is still an open question.

One hypothesis that we propose to be test is that the activity is due to strain effects,[26] which can be exerted over at least 10 atomic layers.[20] A compressive surface strain is the most probable cause of the enhanced activity for many Pt alloys for the ORR, as demonstrated to be the case on dealloyed $PtCu_x$.[20] Given that Y has a larger covalent radius than Pt,[27] one would intuitively expect a Pt overlayer on a Pt-Y alloy core to impose tensile strain on the Pt surface atoms. Even

so, this notion is inconsistent with the ORR activity data, as a tensile strain would strengthen,[20] rather than weaken the binding of Pt to HO*, which should lead to a higher overpotential for the ORR.

Thus far, the ORR activity of Pt_xY has only been demonstrated on extended polycrystalline surfaces and thin films.[8,10,13,14] In order for Pt_xY to make an impact to PEMFC's, the catalyst needs to be synthesised in the nanoparticulate form. In the case of Pt_xY and other alloys of Pt and rare earths, such a task is not trivial, given the high affinity of rare earth elements to oxygen.[28] There are reports in the literature where researchers have attempted to produce nanoparticles of this or similar catalysts.[29,30] Nevertheless, there is no firm evidence that metallic Pt_xY can be synthesised in the nanoparticulate form and that it shows superior catalytic performance for the ORR. In contrast, alloys of Pt and late transition metals such as Ni, Co, Cu, Pd and Fe are less challenging to synthesise; the *solute* metal element will typically have a much less negative reduction potential than rare earths such as Y, Gd or La.[28] However, alloys or core shell structures of Pt and late transition metals have been investigated for more than 25 years.[31,32] Despite recent advances in the ORR on Pt-late transition metal alloys,[21,33-38] we envision that the relatively uncharted territory offered by alloys of Pt and rare earths should provide much room for improvement, should their synthesis be possible in nanoparticulate form.

Thus, in order to further the development of Pt_xY as a catalyst for the ORR, two critical questions should be addressed: (a) *what is the origin of the enhanced catalytic activity?* and (b) *can it be prepared in nanoparticulate form?* Herein, we address the above challenges by preparing model size selected nanoparticles of Pt_xY by gas aggregation. Furthermore, we characterise the structure and composition of the nanoparticles before and after ORR conditions using X-ray photoelectron spectroscopy (XPS), ion scattering spectroscopy (ISS), transmission electron microscopy (TEM) and X-ray absorption spectroscopy (XAS) measurements.

Experimental results

The mass-selected Pt_xY particles were prepared through the gas aggregation of a Pt_9Y target and time of flight separation as shown in Fig. 1a. The charged nanoparticles were subsequently deposited directly onto a planar glassy carbon substrate under ultra-high vacuum conditions. By resorting to a physical method, we can elucidate fundamental relationships between reactivity, particle size, shape and morphology,[39-43] without the inherent artefacts introduced by wet

chemical synthesis from the precursors or surfactants. [44-46] Moreover, it allows for the production of well-defined nanoparticles of materials which are otherwise challenging to synthesise by conventional chemical methods.

The results of the physical characterisation are summarised on Fig. 1b-k, and described in detail in the supplementary information. We first attempted to produce the catalysts from a Pt_3Y (rather than a Pt_9Y) target. However, this resulted in the formation of nanoparticles with a very high Y content; the particles corroded excessively, analogous to our earlier results on extended surfaces of PtY and Pt_2Y[10].

The surface composition of the as-prepared catalysts was characterized by ISS and XPS, as seen in Fig. 1b-1d. Fig. 1 c, d show the XPS spectra of the Pt 4f and Y 3d core level regions acquired after deposition, respectively. The Pt:Y ratios of the as-prepared samples are all ~4, as shown in Fig. S1 of the supporting information. The XPS spectrum of the Y 3d core level region for the as-prepared nanoparticles could not be fitted by a single set of peaks, suggesting that the Y is in more than one chemical state. The position of the most intense, low binding energy peak is consistent with metallic Y. However, the shift between the metallic Y species and the second, less intense Y species is inconsistent with the notion that this latter species is Y_2O_3 see also Fig. S3 for air exposed samples.[47] The unidentified species may be formed from the reaction of Y with the carbon substrate although the presence of Y hydrate or Y hydroxide cannot be excluded. The presence of both Pt and Y in the ISS spectrum shown in Fig. 1b, confirms that the surface layer is composed of both elements.

The particle size distribution (PSD) histograms of the different particles, determined using TEM are plotted on Fig. 1h-k. In the text and figure captions we refer to the particle according to the intended size, rather than the measured size. However, when plotting data on numerical axes we use the measured size, from the mean value in the PSD's. The sharp narrow peaks on the PSDs clearly demonstrate the high quality of the mass selection. The presence of satellite peaks at higher diameters is due to the formation of doubly charged nanoparticles, i.e. with a mass which is twice the intended mass. This artefact was minimised by optimising the synthesis conditions. The particles preserve the spherical shape, independent of diameter. Close inspection of the TEM images suggest that the nanoparticles mostly consist of several crystallites (see supplementary information).

Once deposited and characterised, the alloy catalyst-loaded electrode was transferred from the vacuum chamber to the arbour of a rotating ring disk electrode assembly, where the oxygen reduction reaction activity was evaluated in a liquid half-cell containing 0.1 M $HClO_4$. The electrochemical surface area was measured by CO stripping, see Fig. S4 and supplementary information for details. The activity of the alloy catalysts, expressed as a kinetic current density at 0.9 V, is summarised in Fig. 2, both in terms of specific activity (i.e. $mAcm^{-2}$ microscopic surface area), and mass activity (i.e. Amg_{Pt}^{-1}). For the purpose of comparison, the plots also include the activity of extended surfaces of sputter-cleaned, polycrystalline Pt_3Y, as well as our previously reported data for pure Pt surfaces.[8,10,11,40] Each of the Pt_xY catalysts exhibits a marked enhancement in specific activity over pure Pt of the same size, with the exception of the smallest, 4 nm nanoparticles. Similar to pure Pt, the specific activity of Pt_xY increases with particle size, with the activity of the larger nanoparticles converging towards that of extended polycrystalline surfaces. Most notably, the mass activity of Pt_xY is not only significantly higher than that of pure Pt, but within the range of particle sizes studied here it increases monotonically with particle size. This trend is of great advantage; larger particles are inherently more stable against dissolution, sintering and Ostwald ripening.[3,48] In contrast, pure Pt exhibits a peak in mass activity at ~3 nm, a suboptimal particle size in terms of stability. The highest mass activity is found at 9 nm diameter, 3.05 Amg_{Pt}^{-1} at 0.9 V. This is close to the highest activity reported in the literature (3.3 Amg_{Pt}^{-1} for Pt_xNi nanoparticles[49]), over 5.5 times higher than the most active commercial pure Pt catalyst (0.55 A mg_{Pt}^{-1}),[50] and 3 times higher than the peak mass activity for Pt nanoparticles measured in the same manner.[40]

Upon extended cycling for 9,000 times between 0.6 V and 1 V, the catalyst retained 63 % of its initial activity, as shown in Fig. S5. Fig. S6 highlights the most of the activity losses occur during the first 600 cycles. The surface coverage of Pt, measured on the basis of CO-stripping, is constant with time. This suggests that the losses in activity are due to a decrease in specific activity, rather than the loss of surface area. Consequently, following some initial performance losses, it seems that the catalyst reaches a metastable state that is kinetically hindered from degrading further. Moreover, the specific activity, even after cycling, is still ca. 2-4 times higher than pure Pt nanoparticles of the same size, as shown in Fig. S5. We note that the activity and stability of the Pt_xY nanoparticles compares closely to to the aforementioned Pt_xNi nanoparticles which exhibited a record high activity.[49] The Pt_xY nanoparticles retain 63% of their activity after

9,000 cycles while for the Pt_xNi 60% was retained after 5,000 cycles between 0.65 V and 1 V. Nonetheless, a quantitative comparison of the catalyst stability we report here with other Pt alloys is challenging. Ideally the stability of the Pt_xY nanoparticles should be compared with other Pt-alloy catalysts prepared and tested under identical conditions.

To understand the cause of the high activity of our nanoparticulate alloy catalysts, we performed a series of *ex situ* examinations of the active phase. We used scanning transmission electron microscopy energy dispersive X-ray spectroscopy (STEM-EDS) to map the distribution of Pt and Y. The STEM images and the corresponding EDS elemental maps of Pt_xY 9 nm particles before electrochemical treatment and after ORR activity measurements are shown in Fig. 3. The combined Pt and Y EDS maps of the as-prepared particles show a homogeneous distribution of the two elements over the entire particle (Fig. 3a). However, the EDS maps on Fig. 3b reveal that a Pt-rich shell is formed around the Pt-Y core of the sample that was exposed to the ORR conditions, due to dissolution of Y. This overlayer can be clearly seen on the EDS line profile on the inset of Fig. 3b. On the basis of the line profile data, we estimate that the Pt-shell is ~1 nm thick. These microscopic data are confirmed macroscopically by the ISS and XPS spectra shown in Fig. 1 b-d to e-g. The total Y intensity is diminished in magnitude on the acid treated sample, with a Pt:Y XPS ratio of 14.3 for the 9 nm particles. Moreover, only a single set of Y peaks appears, representing a metallic phase. The presence of the Pt peak and absence of the Y peak on the ISS spectrum on Fig. 1e confirms that there is no Y at the surface of the catalyst. Further evidence for the formation of a core-shell structure is described in the supplementary information.

The identical location-TEM measurements in Fig. S7 show that there is no significant change in catalyst morphology or size distribution, before and after reaction conditions. Fig. S8 shows the STEM-EDX mapping of the 9 nm nanoparticles after 9,000 cycles, further confirming the Pt overlayer formation. To summarise our STEM, XPS and ISS data, thus far, exposure to ORR conditions results in a significant increase of the Pt:Y ratio in the near-surface region, due to Y dissolution. This is consistent with our earlier measurements on extended surfaces of Pt_3Y and Pt_5Y, which have a 3-4 monolayer thick overlayer.[10] On this basis, we can conclude that enhanced activity of the Pt_xY nanoparticles cannot be traced back to ligand effects, which leads us to investigate strain effects.

To quantify the strain in the Pt_xY catalysts, we employed extended X-ray absorption fine structure measurements (EXAFS), before and after the ORR treatment, in comparison to a bulk Pt foil and pure Pt nanoparticles. The main output of the EXAFS experiments is summarised in Fig. 4, where the average nearest neighbour Pt-Pt distance of the different Pt_xY and Pt catalysts is plotted as a function of the particle size. For details see Fig. S10 and supplementary information. All the pure Pt samples exhibit the same Pt-Pt distance, , before and after electrochemical testing, independent of the particle size. On the contrary, the Pt_xY catalysts not only exhibit a lower Pt-Pt distance, relative to pure Pt, but also maintain this compressive strain after the electrochemical testing. The lowest Pt-Pt distance was displayed by the as-prepared Pt_xY samples, with up to 3 % decrease in Pt-Pt distance, i.e. compressive strain versus pure Pt. After ORR testing, the compression of the Pt_xY structure diminishes and is clearly dependent on the particle size, varying from a strain of to -1.0 % for the 4 nm Pt_xY particles and -2.1 % for the 9 nm Pt_xY particles.

Our results conclusively show that alloying Pt with Y brings about an overall compression to the Pt-Pt distance in Pt_xY. Exposure to ORR conditions removes the Y from the first atomic layers. In the absence of Y in the near-surface region, there will be a driving force for the interatomic distance in the Pt overlayers to expand towards that of pure Pt. Nonetheless, experiments on Pt/Cu(111) and Cu_3Pt(111) single crystals suggest that there would still be some degree of compressive strain within the overlayer, despite the relaxation.[18,20] Assuming that the Pt-Pt distance determined with EXAFS represents the average over Pt_xY core and Pt shell, and that a ~1 nm thick overlayer is formed, consistent with the TEM measurements, the Pt overlayer is compressed by ~ 1.8%.

It is somewhat counterintuitive that alloying Pt with Y reduces the Pt-Pt distance in the alloy, given that Y is larger than Pt.[27] However, in bulk Pt_5Y, the nearest neighbour Pt-Pt distance is 2.65 Å, which is compressed by 4 % relative to pure Pt.[10] Pt_5La and Pt_5Gd have bulk structures to Pt_5Y, albeit with different stacking.[3,11] The bulk structure of these compounds consists of alternating rows of pure Pt and Pt-rare earth atoms. According to earlier DFT calculations, a Pt overlayer covering an extended surface of Pt_5La would resemble a compressed closely-packed Pt

layer.[3] Essentially, the larger rare earth atoms deform the closely packed structure of Pt, allowing a larger number of Pt atoms to fit onto the Pt overlayer than on bulk Pt.

In Fig. 5 we demonstrate that the activity of Pt_xY catalysts is strongly correlated to the Pt-Pt distance in the particles, similar to dealloyed $PtCu_x$.[20] An increase in compression brings about an increased ORR activity, relative to Pt, via slightly weakened OH binding to the surface. On the other hand, Pt_xY nanoparticles should be inherently more stable than $PtCu_x$ and other Pt-late transition metal alloys against continued dealloying under reaction conditions.[3,8,11,49] Dealloying via diffusion of Y through the bulk and the Pt overlayer will be hindered by the strong interaction between Y and Pt.[8] The moderate stability we report here could be improved even further through optimisation of the catalyst composition and by suitable annealing.[38] This will be a subject of future studies.

In conclusion, the mass activity of the catalyst, at 3.05 Amg_{Pt}^{-1} at 0.9 V is, within the range of experimental error, as high as the best reported in the literature. By using mass selected nanoparticles, not only do we provide a proof-of-concept that nanoparticles of Pt-Y alloys are highly active, but we also shed scientific insight into the underlying mechanism of their enhanced activity. It turns out that their superior performance is due to a compressive strain exerted by the catalyst core onto the surface. Our work provides a strong impetus for the implementation of Pt_xY in fuel cells. Nevertheless, the methods used here do not allow for mass production. The next step is to develop the chemical synthesis of this catalyst in bulk quantities, where the Y content may also be optimised.

Author Contributions

I.C. and I.S. conceived the experiments. P.H-F. performed the electrochemical experiments. F.M., D.N.M., C.E.S., P.M. and A.N. performed the UHV-based experiments. D.F., A.B. and A.M.W performed the XAS measurements. D.D. performed the microscopy. P.H.F. designed the figures. P.H-F. wrote the first draft of the paper. All authors discussed the results and commented on the manuscript.

Acknowledgements

The authors gratefully acknowledge financial support from the Danish Ministry of Science's UNIK initiative, Catalysis for Sustainable Energy. The Danish National Research Foundation's Center for Individual Nanoparticle Functionality is supported by the Danish National Research Foundation (DNRF54). The A.P. Møller and Chastine Mc-Kinney Møller Foundation is gratefully acknowledged for its contribution towards the establishment of the Centre for Electron Nanoscopy in the Technical University of Denmark. The Interdisciplinary Centre for Electron Microscopy (CIME) at EPFL is gratefully acknowledged for the use of the FEI Tecnai Osiris TEM. P.A.H.F. gratefully acknowledges support from the Danish Council for Strategic Research's project MEDLYS (10-093906). I.E.L.S. was supported by the ForskEL programme's project CATBOOSTER (2001-1-10669). D.N.M. is the recipient of a HC Ørsted postdoctoral fellowship. Part of this work is supported by the Department of Energy, Office of Basic Energy Sciences, US Department of Energy, Basic Energy Science through the SUNCAT Center for Interface Science and Catalysis. This research was partly carried out at the Stanford Synchrotron Radiation Lightsource, a National User Facility operated by Stanford University on behalf of the U.S. Department of Energy, Office of Basic Energy Sciences. We thank John Bargar, Apurva Mehta, Ryan Davis, Matthew Latimer and Erik J. Nelson for support with the EXAFS instrumentation and helpful discussions.

Figure 1 | Surface characterization of the Pt_xY nanoparticles before and after ORR activity measurements. (a) Schematic representation of the cluster source. ISS spectrum for Pt_xY 9 nm as-prepared (**b**) and after ORR (**e**). XPS spectra of both the Pt 4f and Y 3d core level region for Pt_xY 9 nm as-prepared (**c, d**) and after ORR (**f, g**) The Pt/Y ratio here is 4 and 15 for as prepared and after ORR. Particle size distributions and representative TEM micrographs for the Pt_xY catalysts of 4 nm (**h**), 5 nm (**i**), 7 nm (**j**) and 9 nm (**k**).

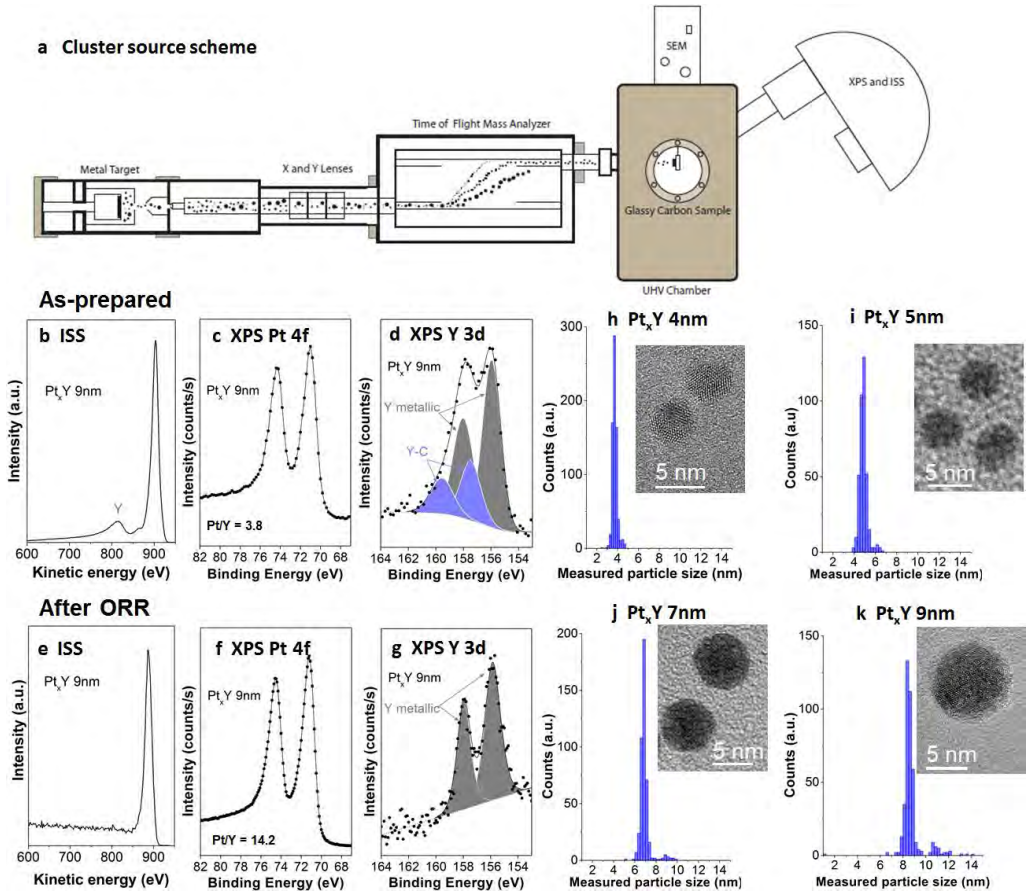

Figure 2 | ORR kinetic current densities and mass activities of the Pt_xY nanoparticles at 0.9 V recorded at 50 mVs^{-1}, 1,600 rpm and 23 ± 1 °C in O_2-saturated 0.1 M $HClO_4$, taken from the anodic cycle. For comparison, the previously published mass and specific activities of pure Pt nanoparticles are also plotted.[40] Each data point corresponds to the mean value from at least three independent activity tests; the error bar shows the standard deviation. The ORR activities were extracted from the anodic polarization scan and corrected for mass transport limitations. The Pt surface area (cm^2_{Pt}) was determined by CO stripping. The amount of Pt deposited in each electrode was measured with a quartz crystal microbalance for the Pt_xY catalyst, while for the pure Pt samples was estimated as reported in[40]. The Pt_3Y pc data corresponds to a sputter cleaned extended surface of polycrystalline Pt_3Y, tested under the same conditions.[11]

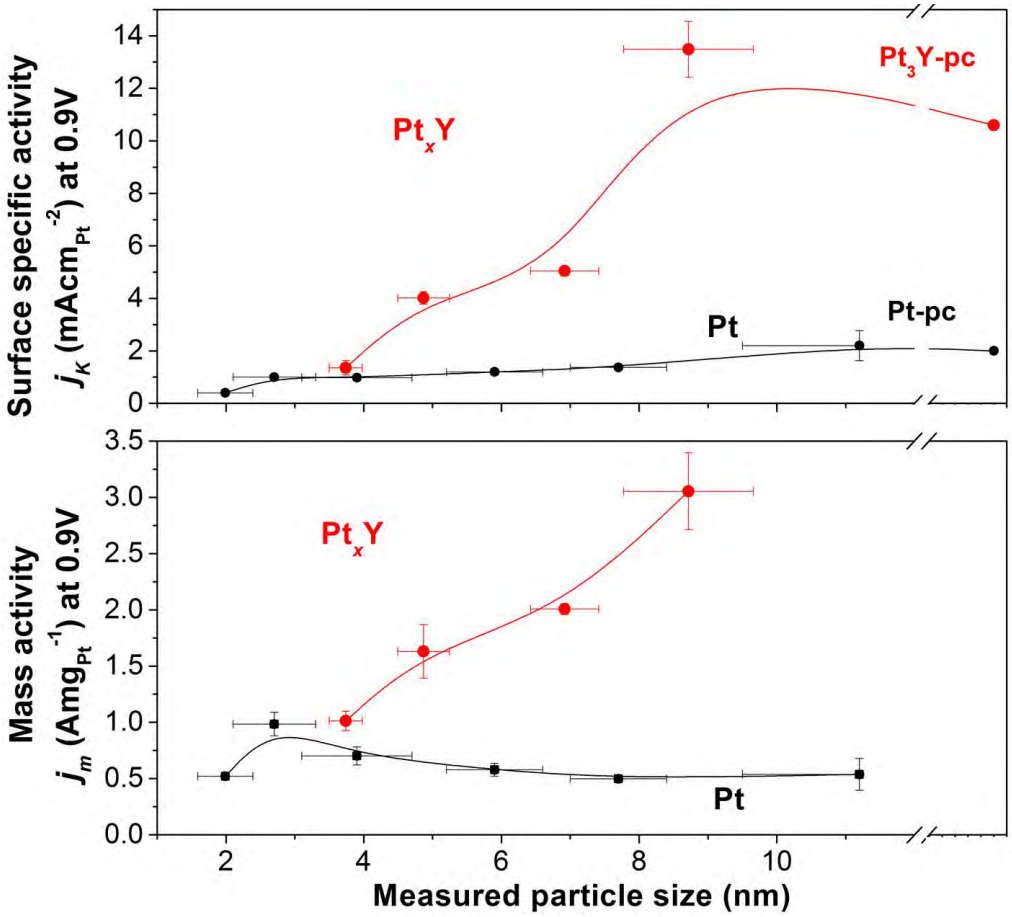

Figure 3 | HAADF-STEM images (left) and Y, Pt and combined Pt+Y X-ray EDS elemental maps (right) for Pt_xY 9 nm. (a) Pt_xY 9 nm as-prepared and **(b)** Pt_xY 9 nm after ORR. Pt and Y EDS intensity line profiles extracted from the spectrum image data cube along with the purple line drawn on the HAADF image are also shown. The thickness of the Pt-rich region varies around the nanoparticles. We estimated the Pt-shell thickness of the nanoparticles by extracting ten line profiles across each particle of (b), obtaining a value of 1.0 ± 0.3 nm.

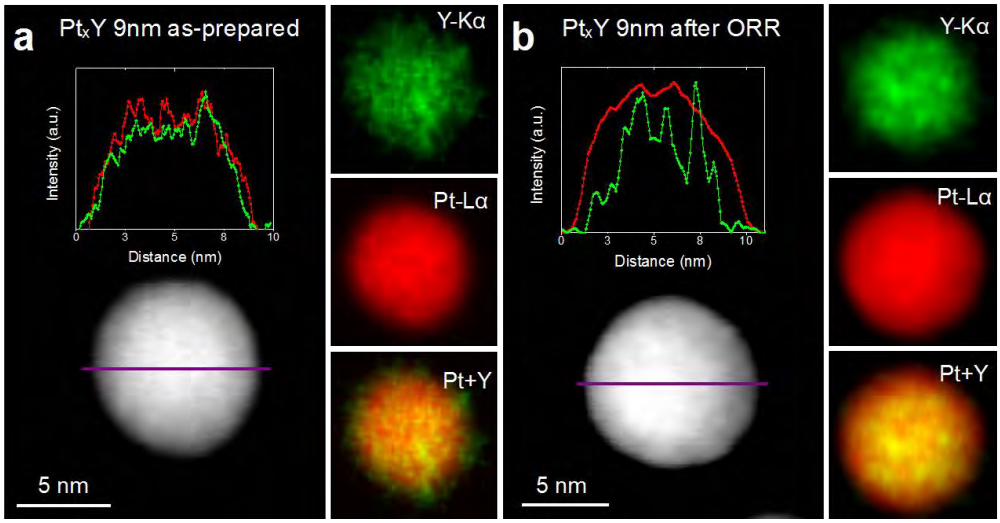

Figure 4 | X-ray Absorption Spectroscopy (XAS) analysis. Average nearest neighbor Pt-Pt distance measured by EXAFS as a function of the particle size for both as-prepared (black) and after ORR (red) recorded on Pt_xY. The line is to guide the eye. To compare, we carried out EXAFS measurements on as-prepared (blue) and electrochemically tested (orange) Pt nanoparticles. We also measured on a Pt foil (grey) in order to have a reference.

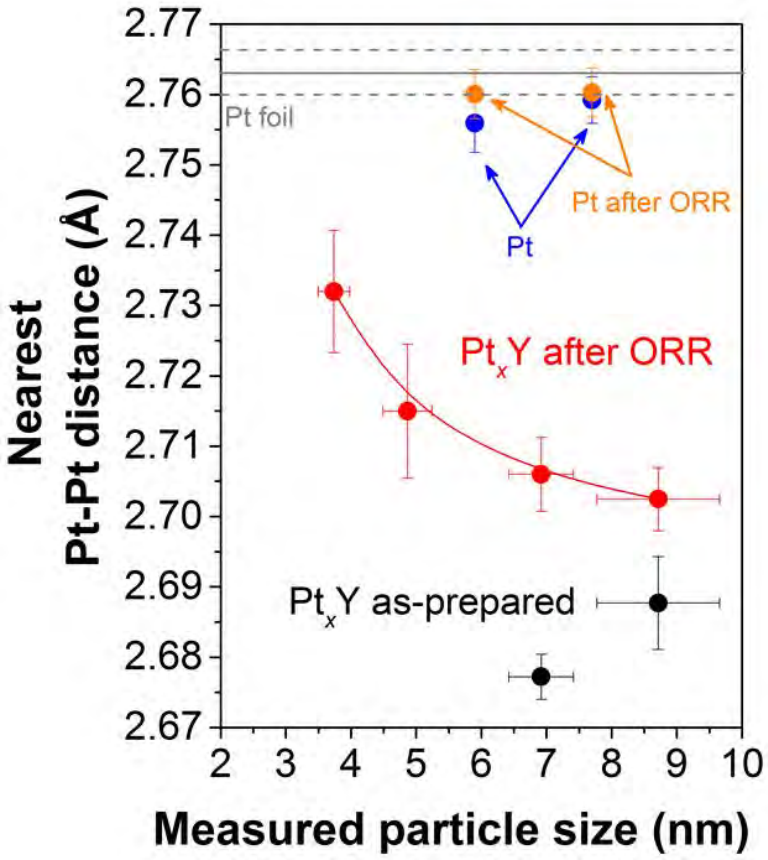

Figure 5 | Surface specific activity, extracted from Fig. 2, as a function of the compressive strain in Pt_xY, relative to bulk Pt, based on the data shown in Fig. 4. The continuous line serves to guide the eye.

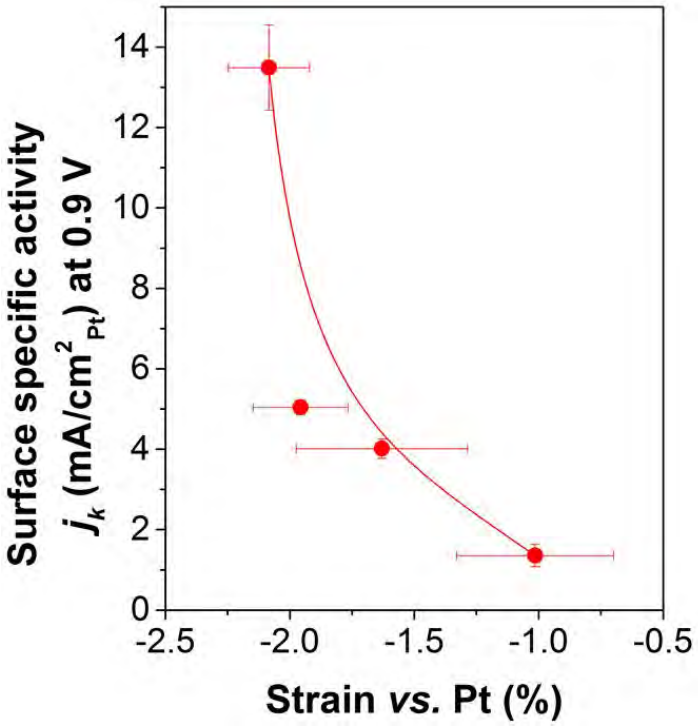

1 Gasteiger, H. A., Kocha, S. S., Sompalli, B. & Wagner, F. T. Activity benchmarks and requirements for Pt, Pt-alloy, and non-Pt oxygen reduction catalysts for PEMFCs. *Appl. Catal. B-Environ.* **56**, 9-35 (2005).

2 Gasteiger, H. A. & Markovic, N. M. Just a Dream-or Future Reality? *Science* **324**, 48-49 (2009).

3 Stephens, I. E. L., Bondarenko, A. S., Grønbjerg, U., Rossmeisl, J. & Chorkendorff, I. Understanding the oxygen reduction reaction on platinum and its alloys. *Energy Environ. Sci.* **5**, 6744-6762 (2012).

4 Debe, M. K. Electrocatalyst approaches and challenges for automotive fuel cells. *Nature* **486**, 43-51, doi:10.1038/nature11115 (2012).

5 Wagner, F. T., Lakshmanan, B. & Mathias, M. F. Electrochemistry and the Future of the Automobile. *J. Phys. Chem. Lett.* **1**, 2204-2219 (2010).

6 Chen, S., Gasteiger, H. A., Hayakawa, K., Tada, T. & Shao-Horn, Y. Platinum-Alloy Cathode Catalyst Degradation in Proton Exchange Membrane Fuel Cells: Nanometer-Scale Compositional and Morphological Changes. *J. Electrochem. Soc.* **157**, A82-A97 (2010).

7 Maillard, F. *et al.* Durability of Pt(3)Co/C nanoparticles in a proton-exchange membrane fuel cell: Direct evidence of bulk Co segregation to the surface. *Electrochemistry Communications* **12**, 1161-1164, doi:10.1016/j.elecom.2010.06.007 (2010).

8 Greeley, J. *et al.* Alloys of platinum and early transition metals as oxygen reduction electrocatalysts. *Nature Chemistry* **1**, 552-556 (2009).

9 Stamenkovic, V. R. *et al.* Improved oxygen reduction activity on $Pt_3Ni(111)$ via increased surface site availability. *Science* **315**, 493-497 (2007).

10 Stephens, I. E. L., Bondarenko, A. S., Bech, L. & Chorkendorff, I. Oxygen electroreduction activity and X-ray photoelectron spectroscopy of alloys of platinum and early transition metals. *ChemCatChem* **4**, 341-349 (2012).

11 Escudero-Escribano, M. *et al.* Pt_5Gd as a highly active and stable catalyst for oxygen electroreduction. *J. Am. Chem. Soc.* **134**, 16476-16479 (2012).

12 Johannesson, G. H. *et al.* Combined electronic structure and evolutionary search approach to materials design. *Physical Review Letters* **88**, 255506 (2002).

13 Jong Yoo, S. *et al.* Enhanced stability and activity of Pt-Y alloy catalysts for electrocatalytic oxygen reduction. *Chemical Communications* **47**, 11414-11416 (2011).

14 Hwang, S. J. *et al.* Role of Electronic Perturbation in Stability and Activity of Pt-Based Alloy Nanocatalysts for Oxygen Reduction. *J. Am. Chem. Soc.* **134**, 19508-19511, doi:10.1021/ja307951y (2012).

15 Sanchez Casalongue, H. *et al.* Direct observation of the oxygenated species during oxygen reduction on a platinum fuel cell cathode. *Nat. Commun.* (in press).

16 Toda, T., Igarashi, H., Uchida, H. & Watanabe, M. Enhancement of the electroreduction of oxygen on Pt alloys with Fe, Ni, and Co. *J. Electrochem. Soc.* **146**, 3750-3756 (1999).

17 Stamenkovic, V. R., Mun, B. S., Mayrhofer, K. J. J., Ross, P. N. & Markovic, N. M. Effect of surface composition on electronic structure, stability, and electrocatalytic properties of Pt-transition metal alloys: Pt-skin versus Pt-skeleton surfaces. *J. Am. Chem. Soc.* **128**, 8813-8819 (2006).

18 Yang, R. Z., Strasser, P. & Toney, M. F. Dealloying of Cu(3)Pt (111) Studied by Surface X-ray Scattering. *J. Phys. Chem. C* **115**, 9074-9080, doi:10.1021/jp111978m (2011).

19 Stephens, I. E. L. *et al.* Tuning the Activity of Pt(111) for Oxygen Electroreduction by Subsurface Alloying. *J. Am. Chem. Soc.* **133**, 5485-5491, doi:10.1021/ja111690g (2011).

20 Strasser, P. *et al.* Lattice-strain control of the activity in dealloyed core-shell fuel cell catalysts. *Nature Chemistry* **2**, 454-460 (2010).

21 Wang, D. L. *et al.* Structurally ordered intermetallic platinum-cobalt core-shell nanoparticles with enhanced activity and stability as oxygen reduction electrocatalysts. *Nature Materials* **12**, 81-87, doi:10.1038/nmat3458 (2013).
22 Johansson, T. *et al.* Pt Skin Versus Pt Skeleton Structures of Pt3Sc as Electrocatalysts for Oxygen Reduction. *Top. Catal.*, 1-10 (2013).
23 Nørskov, J. K. *et al.* Origin of the overpotential for oxygen reduction at a fuel-cell cathode. *Journal of Physical Chemistry B* **108**, 17886-17892 (2004).
24 Kitchin, J. R., Nørskov, J. K., Barteau, M. A. & Chen, J. G. Role of strain and ligand effects in the modification of the electronic and chemical properties of bimetallic surfaces. *Physical Review Letters* **93**, 156801 (2004).
25 Calle-Vallejo, F., Martinez, J. I., Garcia-Lastra, J. M., Rossmeisl, J. & Koper, M. T. M. Physical and Chemical Nature of the Scaling Relations between Adsorption Energies of Atoms on Metal Surfaces. *Physical Review Letters* **108**, doi:11610310.1103/PhysRevLett.108.116103 (2012).
26 Mavrikakis, M., Hammer, B. & Nørskov, J. K. Effect of strain on the reactivity of metal surfaces. *Physical Review Letters* **81**, 2819-2822 (1998).
27 Cordero, B. *et al.* Covalent radii revisited. *Dalton Trans.*, 2832-2838, doi:10.1039/b801115j (2008).
28 Pourbaix, M. *Atlas of Electrochemical Equilibria in Aqueous Solutions*. Second edn, (National Association of Corrosion Engineers, 1974).
29 Nishanth, K. G., Sridhar, P. & Pitchumani, S. Enhanced oxygen reduction reaction activity through spillover effect by Pt–Y(OH)3/C catalyst in direct methanol fuel cells. *Electrochemistry Communications* **13**, 1465-1468, doi:http://dx.doi.org/10.1016/j.elecom.2011.09.021 (2011).
30 Jeon, M. K. & McGinn, P. J. Carbon supported Pt–Y electrocatalysts for the oxygen reduction reaction. *Journal of Power Sources* **196**, 1127-1131, doi:10.1016/j.jpowsour.2010.08.048 (2011).
31 Luczak, F. J. & Landsman, D. A. Fuel cell cathode catalyst alloy-comprising noble metal, cobalt and a transition metal. United States patent 4677092-A (1987).
32 Mukerjee, S. & Srinivasan, S. ENHANCED ELECTROCATALYSIS OF OXYGEN REDUCTION ON PLATINUM ALLOYS IN PROTON-EXCHANGE MEMBRANE FUEL-CELLS. *J. Electroanal. Chem.* **357**, 201-224, doi:10.1016/0022-0728(93)80380-z (1993).
33 van der Vliet, D. F. *et al.* Mesostructured thin films as electrocatalysts with tunable composition and surface morphology. *Nature Materials* **11**, 1051-1058, doi:10.1038/nmat3457 (2012).
34 Cui, C. H., Gan, L., Heggen, M., Rudi, S. & Strasser, P. Compositional segregation in shaped Pt alloy nanoparticles and their structural behaviour during electrocatalysis. *Nature Materials* **12**, 765-771, doi:10.1038/nmat3668 (2013).
35 Snyder, J., Fujita, T., Chen, M. W. & Erlebacher, J. Oxygen reduction in nanoporous metal-ionic liquid composite electrocatalysts. *Nature Materials* **9**, 904-907, doi:10.1038/nmat2878 (2010).
36 Liu, W. *et al.* Bimetallic aerogels: high-performance electrocatalysts for the oxygen reduction reaction. *Angewandte Chemie (International ed. in English)* **52**, 9849-9852, doi:10.1002/anie.201303109 (2013).
37 Sasaki, K. *et al.* Highly stable Pt monolayer on PdAu nanoparticle electrocatalysts for the oxygen reduction reaction. *Nat. Commun.* **3**, doi:10.1038/ncomms2124 (2012).
38 Wang, C. *et al.* Design and Synthesis of Bimetallic Electrocatalyst with Multilayered Pt-Skin Surfaces. *J. Am. Chem. Soc.* **133**, 14396-14403, doi:10.1021/ja2047655 (2011).
39 Nesselberger, M. *et al.* The effect of particle proximity on the oxygen reduction rate of size-selected platinum clusters. *Nature Materials* **12**, 919-924, doi:10.1038/nmat3712 (2013).
40 Perez-Alonso, F. J. *et al.* The effect of size on the oxygen electroreduction activity of mass-selected platinum nanoparticles. *Angewandte Chemie International Edition* **51**, 4641-4643 (2012).

41 Li, Z. Y. *et al.* Structures and optical properties of 4-5 nm bimetallic AgAu nanoparticles. *Faraday Discussions* **138**, 363-373, doi:10.1039/b708958a (2008).
42 Yin, F., Wang, Z. W. & Palmer, R. E. Controlled Formation of Mass-Selected Cu-Au Core-Shell Cluster Beams. *J. Am. Chem. Soc.* **133**, 10325-10327, doi:10.1021/ja201218n (2011).
43 Von Issendorff, B. & Palmer, R. E. A new high transmission infinite range mass selector for cluster and nanoparticle beams. *Review of Scientific Instruments* **70**, 4497-4501 (1999).
44 Li, D. G. *et al.* Surfactant Removal for Colloidal Nanoparticles from Solution Synthesis: The Effect on Catalytic Performance. *ACS Catalysis* **2**, 1358-1362, doi:10.1021/cs300219j (2012).
45 Solla-Gullon, J., Montiel, V., Aldaz, A. & Clavilier, J. Electrochemical characterisation of platinum nanoparticles prepared by microemulsion: how to clean them without loss of crystalline surface structure. *J. Electroanal. Chem.* **491**, 69-77, doi:10.1016/s0022-0728(00)00306-5 (2000).
46 Cuenya, B. R., Baeck, S. H., Jaramillo, T. F. & McFarland, E. W. Size- and support-dependent electronic and catalytic properties of Au-0/Au3+ nanoparticles synthesized from block copolymer micelles. *J. Am. Chem. Soc.* **125**, 12928-12934, doi:10.1021/ja036468u (2003).
47 Reichl, R. & Gaukler, K. H. An Investigation of Air-grown Yttrium Oxide andExperimental Determination of the Sputtering Yield and the Inelastic Mean Free Path. *Applied Surface Science* **26**, 196-210 (1986).

48 Shao-Horn, Y. *et al.* Instability of supported platinum nanoparticles in low-temperature fuel cells. *Top. Catal.* **46**, 285-305 (2007).
49 Choi, S. I. *et al.* Synthesis and Characterization of 9 nm Pt-Ni Octahedra with a Record High Activity of 3.3 A/mg(Pt) for the Oxygen Reduction Reaction. *Nano Lett.* **13**, 3420-3425, doi:10.1021/nl401881z (2013).
50 Nesselberger, M. *et al.* The Particle Size Effect on the Oxygen Reduction Activity of Pt Catalyts: Influence of Electrolyte and Relation to Single Crystal Models. *J. Am. Chem. Soc.* **133**, 17428-17433, doi:10.1021/ja207016u (2011).

Understanding the trends in activity and stability of Pt-based cathode electrocatalysts for low-temperature fuel cells

María Escudero-Escribano, Paolo Malacrida, Ulrik Grønbjerg, Vladimir Tripkovic, Jan Rossmeisl, Ifan E.L. Stephens, Ib Chorkendorff

Department of Physics, Technical University of Denmark, 2800 Kgs. Lyngby, Denmark

Abstract

A combination of electrochemical experiments, X-ray characterisation techniques and theoretical modelling has been used to study the trends in activity and stability of alloys of Pt and lanthanides and alkaline earth metals as electrocatalysts for the oxygen reduction reaction (ORR). Pt_5Tb presents the highest ORR activity ever measured for a sputter-cleaned polycrystalline Pt-alloy, showing a 6-fold activity enhancement over pure polycrystalline Pt. All the Pt-alloys studied show at least a 3-fold enhancement in activity, being more active than traditionally reported alloys of Pt and late transition metals in the polycrystalline form. Angle-resolved X-ray photoelectron spectroscopy (AR-XPS) measurements confirm that, in all cases, a Pt overlayer with a thickness of few Pt layers is formed after electrochemistry. Accordingly, the effect of alloying Pt is to impose strain onto the Pt overlayer. Moreover, the experimental activity of the Pt-alloy cathode electrocatalysts ***versus*** the bulk ***a*** lattice parameter measured by X-ray diffraction (XRD) shows a volcano relationship with the top of the volcano close to Pt_5Tb. All the reported candidates are not only very active, but also highly stable. Furthermore, we show, for the first time, the trends in stability for Pt-alloys catalysts for the ORR, the stability decreasing as the compressive strain increases. On the basis of the AR-XPS experiments, a model for the estimation of the thickness of the Pt overlayer is developed .It shows that the thickness of the overlayer after the stability test increases as the bulk lattice parameter decreases (i.e., the Pt-Pt distance of the Pt overlayer decreases), in agreement with our experimental results. Therefore, this work demonstrates that we can engineer not only the activity but also the stability of our materials by tuning the Pt-Pt distance of the Pt overlayer.